



AFRL-RY-WP-TR-2010-1259

**BEAM SWITCHING OF AN Nd:YAG LASER USING
DOMAIN-ENGINEERED PRISMS IN MAGNESIUM-
OXIDE-DOPED CONGRUENT LITHIUM NIOBATE**

Jonathan W. Evans

University of Dayton

AUGUST 2010

Interim Report

Approved for public release; distribution unlimited.

See additional restrictions described on inside pages

STINFO COPY

**AIR FORCE RESEARCH LABORATORY
SENSORS DIRECTORATE
WRIGHT-PATTERSON AIR FORCE BASE, OH 45433-7320
AIR FORCE MATERIEL COMMAND
UNITED STATES AIR FORCE**

NOTICE AND SIGNATURE PAGE

Using Government drawings, specifications, or other data included in this document for any purpose other than Government procurement does not in any way obligate the U.S. Government. The fact that the Government formulated or supplied the drawings, specifications, or other data does not license the holder or any other person or corporation; or convey any rights or permission to manufacture, use, or sell any patented invention that may relate to them.

This report was cleared for public release by the USAF 88th Air Base Wing (88 ABW) Public Affairs Office (PAO) and is available to the general public, including foreign nationals. Copies may be obtained from the Defense Technical Information Center (DTIC) (<http://www.dtic.mil>).

AFRL-RY-WP-TR-2010-1259 HAS BEEN REVIEWED AND IS APPROVED FOR PUBLICATION IN ACCORDANCE WITH ASSIGNED DISTRIBUTION STATEMENT.

*//Signature//

KENNETH L. SCHEPLER
Work Unit Manager
Electro-Optical Countermeasures Technology
Branch
Electro-Optical Sensor Technology Division

*//Signature//

JOHN F. CARR, Chief
Electro-Optical Countermeasures Technology
Branch
Electro-Optical Sensor Technology Division
Sensors Directorate

This report is published in the interest of scientific and technical information exchange, and its publication does not constitute the Government's approval or disapproval of its ideas or findings.

*Disseminated copies will show “//Signature//” stamped or typed above the signature blocks.

REPORT DOCUMENTATION PAGE				Form Approved OMB No. 0704-0188	
<p>The public reporting burden for this collection of information is estimated to average 1 hour per response, including the time for reviewing instructions, searching existing data sources, gathering and maintaining the data needed, and completing and reviewing the collection of information. Send comments regarding this burden estimate or any other aspect of this collection of information, including suggestions for reducing this burden, to Department of Defense, Washington Headquarters Services, Directorate for Information Operations and Reports (0704-0188), 1215 Jefferson Davis Highway, Suite 1204, Arlington, VA 22202-4302. Respondents should be aware that notwithstanding any other provision of law, no person shall be subject to any penalty for failing to comply with a collection of information if it does not display a currently valid OMB control number. PLEASE DO NOT RETURN YOUR FORM TO THE ABOVE ADDRESS.</p>					
1. REPORT DATE (DD-MM-YY) August 2010		2. REPORT TYPE Interim		3. DATES COVERED (From - To) 26 August 2008 – 30 June 2010	
4. TITLE AND SUBTITLE BEAM SWITCHING OF AN Nd:YAG LASER USING DOMAIN-ENGINEERED PRISMS IN MAGNESIUM-OXIDE-DOPED CONGRUENT LITHIUM NIOBATE				5a. CONTRACT NUMBER In-house	
				5b. GRANT NUMBER	
				5c. PROGRAM ELEMENT NUMBER 62204F	
6. AUTHOR(S) Jonathan W. Evans				5d. PROJECT NUMBER 2003	
				5e. TASK NUMBER 12	
				5f. WORK UNIT NUMBER 20031225	
7. PERFORMING ORGANIZATION NAME(S) AND ADDRESS(ES) By: University of Dayton For: Electro-Optical Countermeasures Technology Branch (AFRL/RJW) Electro-Optical Sensor Technology Division Air Force Research Laboratory, Sensors Directorate Wright-Patterson Air Force Base, OH 45433-7320 United States Air Force				8. PERFORMING ORGANIZATION REPORT NUMBER AFRL-RY-WP-TR-2010-1259	
9. SPONSORING/MONITORING AGENCY NAME(S) AND ADDRESS(ES) Air Force Research Laboratory Sensors Directorate Wright-Patterson Air Force Base, OH 45433-7320 Air Force Materiel Command United States Air Force				10. SPONSORING/MONITORING AGENCY ACRONYM(S) AFRL/RJW	
				11. SPONSORING/MONITORING AGENCY REPORT NUMBER(S) AFRL-RY-WP-TR-2010-1259	
12. DISTRIBUTION/AVAILABILITY STATEMENT Approved for public release; distribution unlimited.					
13. SUPPLEMENTARY NOTES PAO Case Number: 88ABW 10-2128; Clearance Date: 13 Apr 2010. This report contains color. This report is a Masters Thesis written by a University of Dayton (Dayton, OH) Masters candidate.					
14. ABSTRACT In this work, a novel electro-optic beam switch (EOBS) is designed, fabricated and demonstrated. The EOBS presented in this work is designed for a Nd:YAG laser operating at $\lambda = 1064$ nm and is demonstrated to achieve >750 microns of beam translation at switching rates of up to 3 Hz. The EOBS consists of a series of electronically controlled prisms fabricated by ferroelectric domain inversion in an electro-optic crystal wafer. The prisms are arranged such that positive angular deflections are counterbalanced by subsequent negative angular deflections. The result is discrete beam translation with no angular deflection. Also in this work, an algorithm for designing optimal beam translation geometries is developed. Five of the resulting geometric designs are then fabricated in 5 mol% magnesium oxide doped congruent lithium niobate (5%MgO:CLN). The performance of one particular geometry is modeled in detail and analyzed experimentally. The EOBS is used to demonstrate wavelength tuning of a near-infrared laser system using a selectable optical parametric generation (OPG) grating.					
15. SUBJECT TERMS electro-optic switching, beam steering, nonlinear optics, integrated optics, geometric optics, electro-optic devices					
16. SECURITY CLASSIFICATION OF:			17. LIMITATION OF ABSTRACT: SAR	18. NUMBER OF PAGES 202	19a. NAME OF RESPONSIBLE PERSON (Monitor) Kenneth L. Schepler 19b. TELEPHONE NUMBER (Include Area Code) N/A
a. REPORT Unclassified	b. ABSTRACT Unclassified	c. THIS PAGE Unclassified			

TABLE OF CONTENTS

List of Illustrations.....	v
List of Tables.....	x
Acknowledgements	xii
Chapter 1 – Introduction.....	1
1.1 Motivation.....	1
1.2 Project Background.....	2
1.3 Overview of Thesis.....	3
1.4 Formatting.....	3
Chapter 2 – Theory and Background	4
2.1 The Electro-Optic Effect	4
2.2 Three-Wave Mixing	6
2.3 Crystal Domain Engineering.....	16
2.4 Gaussian Beam Propagation	19
Chapter 3 – Electro-Optic Beam Switch and OPG Design	21
3.1 Material Considerations	21
3.2 Geometric Considerations.....	26
3.3 Final Device Design	40
3.4 Fabrication	42
3.5 System Controls.....	45
Chapter 4 – Modeling EOBS Performance with <i>LIGHTS</i>	47
4.1 Finite Difference Method Beam Propagation.....	47
4.2 Beam Propagation Analysis	48
Chapter 5 – Experimental Observations.....	66
5.1 First Generation EOBS Chip Performance.....	66
5.2 Second Generation EOBS Chip Performance.....	81
5.3 Switched OPG.....	94
5.4 System Limitations	97
Chapter 6 – Conclusions	102
6.1 Project Summary.....	102
6.2 Future Work	103
6.3 A Guide to Related Work	105
6.4 Closing Remarks.....	108
References.....	109
Appendix A – A Catalog of FDM Beam Propagation Simulation Results	113
A.1 The Performance of All Channels at the Design Point	113
A.2 Channel 1 Performance under Non-Design Conditions.....	118
Appendix B – Voltage Compensation for Changes in Environmental Variables	146
Appendix C – Error Analysis for Translation Measurements	148
Appendix D – Equipment and Vendor Index	157
Appendix E – A Catalog of MATLAB Code	159
Gayer_Sellmeier.m.....	159
QPM_TuningCurve.m.....	160
Optimal_5pMgOCLN_EOBS_Spec.m	162

Build_GaussianBeam.m	166
LIGHTS_Analysis.m	168
BeamProp_Results_Import.m.....	169
Plot_CenterofAmplitude.m.....	172
Build_EOBS.m.....	174
Two_Point_Trajectory.m.....	177
HDF5_Spiricon_FrameStats.m.....	180
Propagation_of_Errors.m.....	183

LIST OF ILLUSTRATIONS

Figure 1.1 – Zero net angular deflection beam steering by cascaded EO-modulated prisms.	1
Figure 1.2 – The switched OPG concept.....	2
Figure 2.1 – The phasematching efficiency curve	12
Figure 2.2 – Birefringent phasematching [$o \rightarrow e + e$].	14
Figure 2.3 – Noncollinear phasematching.	14
Figure 2.4 – The effective nonlinearity profile of a typical QPM grating.	15
Figure 2.5 – An illustration of the optical parametric generation (OPG) process.....	16
Figure 2.6 – A bare, z-cut crystal substrate.....	17
Figure 2.7 – The crystal wafer with a photoresist pattern.	17
Figure 2.8 – Liquid electrode entrenchment of the photoresist pattern.	17
Figure 2.9 – Poling of the crystal wafer.	18
Figure 2.10 – Selective domain inversion of the crystal wafer.....	18
Figure 2.11 – A periodically poled QPM grating.	19
Figure 2.12 – The Geometry of a Gaussian Laser Beam.....	20
Figure 3.1 – The refractive index of 5%MgO:CLN.....	23
Figure 3.2 – Quasi-phasematched OPG output for a $\lambda_1 = 1.064 \mu m$ pump beam as a function of grating period Λ	25
Figure 3.3 – An electro-optic beam switch in the ON state.....	26
Figure 3.4 – The unit cell representation a beam steering prism.....	27
Figure 3.5 – A geometric ray tracing of an incident beam.	27
Figure 3.6 – Two cascaded unit cells.	28
Figure 3.7 – A two-stage translation channel of 2K unit cells.	31
Figure 3.8 – The geometry of the N^{th} unit cell of Stage 1.	32
Figure 3.9 – The geometry of the N^{th} unit cell of Stage 2.	33
Figure 3.10 – The geometry of the transition cell.	34
Figure 3.11 – Solutions of Equation (3.43) for overall translation of the steered beam.	35
Figure 3.12 – (Left) A single prism with length L . (Right) Two prisms with length L	36
Figure 3.13 – An illustration of a typical gradient-type beam deflector.	36
Figure 3.14 – The overall translation as a function of α for $D_0 = 160 \mu m$	37
Figure 3.15 – The field of solutions shown only as a function of α	38
Figure 3.16 – The solutions to Equation (3.53) for $\alpha = 30^\circ$	39
Figure 3.17 – An image of the CAD specification of the EOBS chip.	41
Figure 3.18 – The OPG grating design.....	42
Figure 3.19 – The 5%MgO:CLN wafer with inverted crystal domains.	42
Figure 3.20 – Domain inversion in 5%MgO:CLN [steering prisms].	43
Figure 3.21 – Domain inversion in 5%MgO:CLN [OPG gratings].	43
Figure 3.22 – The poled region is diced away from the rest of the wafer.	43
Figure 3.23 – Anti-reflective coatings were added to the polished entrance and exit facets.	44
Figure 3.24 – The finished EOBS chip with gold electrodes.....	44
Figure 3.25 – A completed EOBS chip.....	44
Figure 3.26 – A thermally annealed chip.	45
Figure 3.27 – A completed OPG chip.....	45

Figure 3.28 – A functional diagram of EOBS controls.	45
Figure 3.29 – A photograph of the experimental setup for controlling the EOBS chip.	46
Figure 4.1 – Diffraction of a Gaussian beam as simulated in <i>LIGHTS</i>	48
Figure 4.2 – Refraction of a Gaussian beam as simulated in <i>LIGHTS</i>	48
Figure 4.3 – The refractive index profile of EOBS Channel 1.	49
Figure 4.4 – The FDM beam propagation simulation of EOBS Channel 1.	50
Figure 4.5 – The center of amplitude beampath.	51
Figure 4.6 – The refractive indices of 5%MgO:CLN as a function of temperature.	53
Figure 4.7 – A composite of simulated beam paths at various device temperatures.	54
Figure 4.8 – Plot of numerical simulation of EOBS performance at $T=50^{\circ}\text{C}$	54
Figure 4.9 – The refractive indices as a function of the electro-optic coefficient.	55
Figure 4.10 – Simulated beam paths for several values of the electro-optic coefficient. ...	56
Figure 4.11 – A plot of the numerical simulation of EOBS performance at $r'_{33} = 80\% \cdot r_{33}$	57
Figure 4.12 – The refractive indices as a function of wavelength.	58
Figure 4.13 – Simulated beam paths for wavelengths $\lambda = 500\text{ nm}$ to $\lambda = 1500\text{ nm}$	59
Figure 4.14 – Plot of the numerical simulation of EOBS performance at $\lambda = 1500\text{ nm}$	60
Figure 4.15 – Plot of the numerical simulation of EOBS performance at $\lambda = 500\text{ nm}$	60
Figure 4.16 – The refractive indices as a function of applied voltage.	62
Figure 4.17 – Simulated beam paths for voltages $V = -900\text{ Volts}$ to $V = -1200\text{ Volts}$	63
Figure 4.18 – Simulated beam paths for voltages $V = 500\text{ Volts}$ to $V = -400\text{ Volts}$	63
Figure 4.19 – Simulated beam paths for voltages $V = -500\text{ Volts}$ to $V = -1500\text{ Volts}$. ..	64
Figure 4.20 – Simulated beam propagation for voltage $V = -1500\text{ Volts}$	65
Figure 5.1 – The poled prisms of First Generation Chip 1 exhibit excellent quality.	66
Figure 5.2 – The poled prisms of First Generation Chip 2 exhibit poor quality.	66
Figure 5.3 – The aluminum bottom of the chip mount for the first generation chips.	67
Figure 5.4 – The mounting assembly for the first generation EOBS chips.	67
Figure 5.5 – The experimental setup for characterizing the EOBS.	68
Figure 5.6 – A conceptual illustration of the characterization of an EOBS chip.	68
Figure 5.7 – Damage from dielectric breakdown of the air between the top electrode of FCG-1 and the aluminum mount.	69
Figure 5.8 – The beamspot at $V_{\text{applied}} = 0\text{ Volts}$ (Left) and $V_{\text{applied}} = -100\text{ Volts}$ (Right). ..	69
Figure 5.9 – The beamspot at $V_{\text{applied}} = -200\text{ Volts}$ (Left) and $V_{\text{applied}} = -300\text{ Volts}$ (Right).	70
Figure 5.10 – A photograph of FGC-1 immediately after it shattered.	70
Figure 5.11 – The temporal temperature profile of the thermal annealing of FGC-2.	71
Figure 5.12 – FGC-2 after the thermal annealing process.	72
Figure 5.13 – The experimental setup for measuring the effective electro-optic coefficient.	73
Figure 5.14 – A conceptual illustration of the characterization of an EOBS chip.	73
Figure 5.15 – Beam trajectories calculated from two center of amplitude points.	75
Figure 5.16 – The trajectory of the steered beam in response to an applied voltage.	76
Figure 5.17 – The geometry of steered beams in an arbitrary Cartesian coordinate system.	77

Figure 5.18 – Simulated values of angular beam deflection imparted by EOBS Channel 1 and experimental values of angular beam deflection imparted by FGC-2 Channel 1.	79
Figure 5.19 – A photograph of FGC-2 immediately after it was broken.	81
Figure 5.20 – The aluminum bottom of the second generation EOBS chip mount.	82
Figure 5.21 – The second generation EOBS chip mounting assembly.	82
Figure 5.22 – Second Generation Chip #1	83
Figure 5.23 – Second Generation Chip #2	83
Figure 5.24 – The poled prisms of SGC-1 exhibit excellent domain quality.	84
Figure 5.25 – The poled prisms of SGC-2 exhibit excellent domain quality.	84
Figure 5.26 – A typical frame-averaged image of the steered beam.	85
Figure 5.27 – A typical data frame after Gaussian filtering.	87
Figure 5.28 – The beam location of a distorted beamspot.	88
Figure 5.29 – Simulated values of angular beam deflection imparted by EOBS Channel 1 and experimental values of angular beam deflection imparted by SGC-1 Channel 1.	89
Figure 5.30 – Damage from bulk dielectric breakdown of SGC-1.	90
Figure 5.31 – Simulated values of angular beam deflection imparted by EOBS Channel 1 and experimental values of angular beam deflection imparted by SGC-2 Channel 1.	91
Figure 5.32 – Simulated values of angular beam deflection imparted by EOBS Channel 1 and experimental values of angular beam deflection imparted by SGC-2 Channel 1.	92
Figure 5.33 – The steered spot is translated by $\sim 770 \mu m$	94
Figure 5.34 – The OPG chip mount.	95
Figure 5.35 – The setup used to evaluate the OPG chip performance.	95
Figure 5.36 – Signal output from both OPG gratings.	96
Figure 5.37 – The switched OPG system.	97
Figure 5.38 – A simple low-pass filter model of the EOBS system.	98
Figure 5.39 – The squarewave response of the system equivalent circuit at $f = 160 kHz$	99
Figure 5.40 – The squarewave response of the system equivalent circuit at $f = 20 kHz$	100
Figure 6.1 – A modified dual-grating switched OPG system.	104
Figure 6.2 – Monolithic two-bit wavelength multiplexer.	106
Figure 6.3 – A conceptual diagram for a switched CW/mode-locked laser cavity.	107
Figure 6.4 – A conceptual diagram for a single-oscillator multiple-emitter laser system.	107
Figure A.1 – The optical field of a Gaussian beam propagating through Channel 1.	114
Figure A.2 – The center of amplitude beampath of a Gaussian beam in Channel 1.	114
Figure A.3 – The optical field of a Gaussian beam propagating through Channel 2.	115
Figure A.4 – The center of amplitude beampath of a Gaussian beam in Channel 2.	115
Figure A.5 – The optical field of a Gaussian beam propagating through Channel 3.	116
Figure A.6 – The center of amplitude beampath of a Gaussian beam in Channel 3.	116
Figure A.7 – The optical field of a Gaussian beam propagating through Channel 4.	117
Figure A.8 – The center of amplitude beampath of a Gaussian beam in Channel 4.	117
Figure A.9 – The optical field of a Gaussian beam propagating through Channel 5.	118
Figure A.10 – The center of amplitude beampath of a Gaussian beam in Channel 5.	118

Figure A.11 – A Gaussian beam propagating through Channel 1 at $T = 0^{\circ}\text{C}$	119
Figure A.12 – A Gaussian beam propagating through Channel 1 at $T = 5^{\circ}\text{C}$	120
Figure A.13 – A Gaussian beam propagating through Channel 1 at $T = 10^{\circ}\text{C}$	120
Figure A.14 – A Gaussian beam propagating through Channel 1 at $T = 15^{\circ}\text{C}$	121
Figure A.15 – A Gaussian beam propagating through Channel 1 at $T = 20^{\circ}\text{C}$	121
Figure A.16 – A Gaussian beam propagating through Channel 1 at $T = 25^{\circ}\text{C}$	122
Figure A.17 – A Gaussian beam propagating through Channel 1 at $T = 30^{\circ}\text{C}$	122
Figure A.18 – A Gaussian beam propagating through Channel 1 at $T = 35^{\circ}\text{C}$	123
Figure A.19 – A Gaussian beam propagating through Channel 1 at $T = 40^{\circ}\text{C}$	123
Figure A.20 – A Gaussian beam propagating through Channel 1 at $T = 45^{\circ}\text{C}$	124
Figure A.21 – A Gaussian beam propagating through Channel 1 at $T = 50^{\circ}\text{C}$	124
Figure A.22 – A Gaussian beam propagating through Channel 1 at $r'_{33} = 0.80 \cdot r_{33}$	125
Figure A.23 – A Gaussian beam propagating through Channel 1 at $r'_{33} = 0.85 \cdot r_{33}$	126
Figure A.24 – A Gaussian beam propagating through Channel 1 at $r'_{33} = 0.90 \cdot r_{33}$	126
Figure A.25 – A Gaussian beam propagating through Channel 1 at $r'_{33} = 0.95 \cdot r_{33}$	127
Figure A.26 – A Gaussian beam propagating through Channel 1 at $r'_{33} = r_{33}$	127
Figure A.27 – A Gaussian beam with $\lambda = 500 \text{ nm}$ propagating through Channel 1.	128
Figure A.28 – A Gaussian beam with $\lambda = 600 \text{ nm}$ propagating through Channel 1.	129
Figure A.29 – A Gaussian beam with $\lambda = 700 \text{ nm}$ propagating through Channel 1.	129
Figure A.30 – A Gaussian beam with $\lambda = 800 \text{ nm}$ propagating through Channel 1.	130
Figure A.31 – A Gaussian beam with $\lambda = 900 \text{ nm}$ propagating through Channel 1.	130
Figure A.32 – A Gaussian beam with $\lambda = 1000 \text{ nm}$ propagating through Channel 1.	131
Figure A.33 – A Gaussian beam with $\lambda = 1064 \text{ nm}$ propagating through Channel 1.	131
Figure A.34 – A Gaussian beam with $\lambda = 1100 \text{ nm}$ propagating through Channel 1.	132
Figure A.35 – A Gaussian beam with $\lambda = 1200 \text{ nm}$ propagating through Channel 1.	132
Figure A.36 – A Gaussian beam with $\lambda = 1300 \text{ nm}$ propagating through Channel 1.	133
Figure A.37 – A Gaussian beam with $\lambda = 1400 \text{ nm}$ propagating through Channel 1.	133
Figure A.38 – A Gaussian beam with $\lambda = 1500 \text{ nm}$ propagating through Channel 1.	134
Figure A.39 – A Gaussian beam propagating through Channel 1 at $V_{\text{applied}} = 500 \text{ Volts}$.135	
Figure A.40 – A Gaussian beam propagating through Channel 1 at $V_{\text{applied}} = 400 \text{ Volts}$.135	
Figure A.41 – A Gaussian beam propagating through Channel 1 at $V_{\text{applied}} = 300 \text{ Volts}$.136	
Figure A.42 – A Gaussian beam propagating through Channel 1 at $V_{\text{applied}} = 200 \text{ Volts}$.136	
Figure A.43 – A Gaussian beam propagating through Channel 1 at $V_{\text{applied}} = 100 \text{ Volts}$.137	
Figure A.44 – A Gaussian beam propagating through Channel 1 at $V_{\text{applied}} = 0 \text{ Volts}$... 137	
Figure A.45 – A Gaussian beam propagating through Channel 1 at $V_{\text{applied}} =$ –100 Volts.	138
Figure A.46 – A Gaussian beam propagating through Channel 1 at $V_{\text{applied}} =$ –200 Volts.	138
Figure A.47 – A Gaussian beam propagating through Channel 1 at $V_{\text{applied}} =$ –300 Volts.	139
Figure A.48 – A Gaussian beam propagating through Channel 1 at $V_{\text{applied}} =$ –400 Volts.	139
Figure A.49 – A Gaussian beam propagating through Channel 1 at $V_{\text{applied}} =$ –500 Volts.	140

Figure A.50 – A Gaussian beam propagating through Channel 1 at $V_{applied} =$ –600 Volts.	140
Figure A.51 – A Gaussian beam propagating through Channel 1 at $V_{applied} =$ –700 Volts.	141
Figure A.52 – A Gaussian beam propagating through Channel 1 at $V_{applied} =$ –800 Volts.	141
Figure A.53 – A Gaussian beam propagating through Channel 1 at $V_{applied} =$ –900 Volts.	142
Figure A.54 – A Gaussian beam propagating through Channel 1 at $V_{applied} =$ –1000 Volts.	142
Figure A.55 – A Gaussian beam propagating through Channel 1 at $V_{applied} =$ –1100 Volts.	143
Figure A.56 – A Gaussian beam propagating through Channel 1 at $V_{applied} =$ –1200 Volts.	143
Figure A.57 – A Gaussian beam propagating through Channel 1 at $V_{applied} =$ –1300 Volts.	144
Figure A.58 – A Gaussian beam propagating through Channel 1 at $V_{applied} =$ –1400 Volts.	144
Figure A.59 – A Gaussian beam propagating through Channel 1 at $V_{applied} =$ –1500 Volts.	145
Figure C.1 – The geometry of the four-point determination of angular deflection.....	148

LIST OF TABLES

Table 2.1 – A contracted index notation legend.	5
Table 3.1 – A comparison of the properties of electro-optic crystals.	21
Table 3.2 – The Sellmeier coefficients of 5%MgO:CLN.	22
Table 3.3 – The final design parameters of each steering channel.	41
Table 4.1 – A summary of FDM beam propagation results.	52
Table 4.2 – The output characteristics of steered beams of various wavelengths	61
Table 5.1 – Beam deflection data taken with the <i>Spiricon</i> beam profiling camera	11
Table 5.2 – Beam deflection data for SGC-1 at positive values of $V_{applied}$	11
Table 5.3 – Beam deflection data for SGC-2 at positive values of $V_{applied}$	11
Table 5.4 – The ratio R at positive values of $V_{applied}$	11
Table 5.5 – Beam deflection data for SGC-2 at negative values of $V_{applied}$	11
Table A.1 – The final design parameters of each channel.	113
Table C.1 – The experimental data and uncertainty values (Center of Amplitude)	149
Table C.2 – The experimental data and uncertainty values (Gaussian Filter).	149
Table C.3 – The worst-case scenario analysis of angular experimental error.	154
Table E.1 – The content of Index.mat and Index_Trials.mat.	168
Table E.2 – The content of Points.mat.	180

Pro gloriam Dei et testimonium Christi

ACKNOWLEDGEMENTS

This thesis project was made possible through the generous support of many people. Specifically, I would like thank my advisor, Dr. Peter Powers, for providing his expertise in nonlinear optics. I would also like to thank Dr. Kenneth Schepler for encouraging me to develop the electro-optic beam switch concept, and for his innumerable technical insights. Furthermore, I would like to thank Dr. Andrew Sarangan for helping to develop numerical models for this project.

Additional thanks to Dr. Patrick Berry for countless hours of lab technique demonstration and to Mr. Matthew Cocuzzi for providing direct mentorship and guidance. Without these men, the experiment would not have been realized. Thanks also to Dr. Rita Peterson and Mr. Charles Phelps for helping me to learn my way around the laboratory.

I would like to extend my thanks to Dr. Philip Battle and the rest of the staff at *AdvR Inc.* for their dedication and support throughout the EOBS fabrication process and to Mr. John McCurdy, who helped me to build portions of this experiment.

I would also like to thank my closest friends and family for keeping my spirits up through this effort and my parents, Denny and Nancy Evans, in particular for their emotional support. Most importantly, I thank my beloved wife, Pamela, for her unconditional support and unfailing commitment. Without her, I could not have found the will to start, let alone finish, this daunting task.

Chapter 1 – INTRODUCTION

1.1 Motivation

Precisely controlled laser beam deflection capability is of great importance to laser enabled technologies such as laser radar, industrial marking, optical disk tracking [1], free-space optical communication, and laser missile countermeasures. For years, mirrors mounted on mechanical gimbals [2], galvanometers [3], or servo systems [1] have been used to steer laser beams in such systems. These mechanical beam steering systems are subject to inertial effects such as mirror deformation, external vibration [3], and wear. In contrast, non-inertial means of beam steering such as Acousto-Optic (AO) and Electro-Optic (EO) beam deflectors are not subject to such effects [2,3].

EO beam steering devices are typically more compact [2], exhibit much faster response times [2,4], and consume less power [2,4] than their mechanical counterparts. Furthermore, by design, EO beam steering devices often consist of more than one steering surface/boundary. Each surface/boundary permits additional beam control. Thus, in principle, EO beam steering devices can exhibit a greater degree of control over the optical path of a laser beam than can a single-surface, mechanically actuated mirror. Consequently, EO deflectors are ideal for applications for which precise beam control is required over a relatively small angular range.

One means of fabricating 'prism-type' [5] EO deflectors is by domain engineering of ferroelectric crystals [6]. Such deflectors are well developed and have been optimized [7,8] for maximum angular deflection of a laser beam. These optimal prism-type EO deflectors have been suggested as the basis for optical switching regimes [4,9]. Further investigation by Krishnamurthi et al. has employed beam propagation method (BPM) simulations to verify optical switch design [9]; yet, to-date, the author is unaware of any attempt to fabricate such switches.

This work presents a novel prism-type EO beam steering device. Two complimentary steering structures are designed to deflect then and counter-deflect a laser beam (see Figure 1.1).

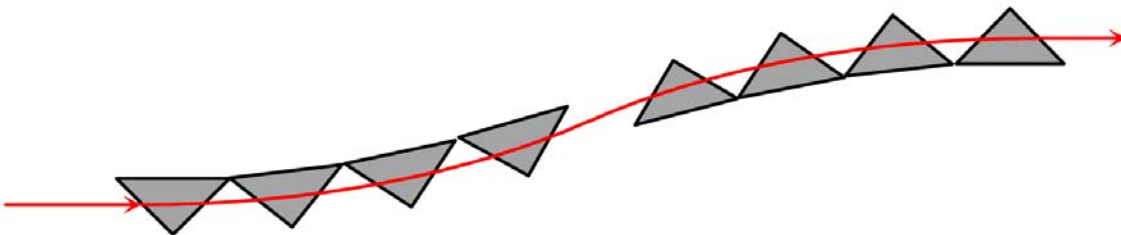


Figure 1.1 – Zero net angular deflection beam steering by cascaded EO-modulated prisms.

The refractive index of the prisms which constitute the Electro-Optic Beam Switch (EOBS) can be electrically modulated (via the linear electro-optic effect) such that the prisms can be effectively turned on and off. A beam propagating through this device when it is in the OFF state experiences only the phase delay of propagation. However, a beam propagating through this device when it is in the ON state is translated some distance perpendicular to its direction of propagation and experiences zero overall angular deflection. Thus, the EOBS can be used to switch a beam between

subsequent optics. This functionality describes a single-bit free-space multiplexer. The current work details the design, optimization, fabrication, and evaluation of an EOBS. The EOBS is designed and optimized for maximum translation of a $\lambda = 1.064 \mu\text{m}$ laser beam, and is fabricated in a z-cut, 5 mol% magnesium oxide doped congruent lithium niobate (5%MgO:CLN) wafer. The EOBS is demonstrated, and its performance evaluated in terms of angular deviation, overall translation, and maximum switching rate.

1.2 Project Background

This project grew out of an effort to develop a rapidly tunable, solid-state, mid-infra-red (MIR) laser source. This waveband requirement is due to the atmospheric transmission windows (3-5 μm , 8-12 μm). Few solid-state direct sources exist in the MIR waveband. Consequently, nonlinear optical (NLO) techniques are often employed to convert near-infra-red (NIR) laser radiation to MIR wavelengths. This process can be temperature tuned, but this tuning mechanism is imprecise, slow, and severely limited by the geometry of the NLO crystal. Alternatively, this work considers a combination of beam steering and NLO techniques to switch the output wavelength of a laser source on demand.

One particular NLO process, optical parametric generation (OPG), can be used to split photons of a given energy into two photons of lesser energies and longer wavelengths. The resulting photon pair may assume any wavelength combination which satisfies conservation of energy and conservation of momentum for the three photon system.

A more detailed discussion of OPG is offered in *Section 2.2.3*; it will suffice for now to say that OPG is a very inefficient process which can be made efficient for a particular combination of wavelengths using a technique known as “quasi-phasematching” (QPM). QPM can be accomplished in lithium niobate using a ferroelectric domain reversed ‘grating’ fabricated by electric field poling [10]. The spatial period Λ of this grating determines which combination of fields will satisfy the phasematching condition:

$$\Delta k = 2\pi \left(\frac{n_2}{\lambda_2} + \frac{n_3}{\lambda_3} - \frac{n_1}{\lambda_1} + \frac{1}{\Lambda} \right) = 0$$

Consequently, the value of Λ will determine the output wavelength combinations which will dominate the OPG process. Thus, in principle, the rapid reconfiguration of such gratings could be used to change the output wavelength(s) of a laser system. However, the poling process requires high voltages and wafer processing steps which are prohibitively difficult to implement *in situ*.

The EOBS described in *Section 1.1* was proposed as a means of rapidly switching a pump beam between two or more wavelength-conversion gratings of different periods (See Figure 1.2).

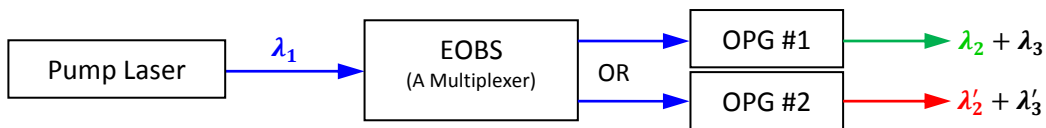


Figure 1.2 – The switched OPG concept.

This work provides proof of concept for rapidly switched OPG technology. Here, an EOBS design in periodically-poled 5%MgO:CLN is demonstrated to steer a laser beam with wavelength $\lambda = 1.064 \mu\text{m}$. This proof of concept provides the basis for extending the technology to the MIR waveband. In theory, broadly tunable MIR sources such as Cr^{2+} switched between OPG gratings made of MIR-transparent NLO materials such as orientation-patterned gallium arsenide (OPGaAs) could form the basis for broadly tunable, solid-state sources of coherent radiation [11, 12].

Both, the electro-optic effect used to steer the beam and the OPG process used to convert the wavelength of the laser radiation are rapid processes. Thus, in principle, the chief factor limiting the maximum switching speed will be the RC time constant of the EOBS system itself. Additionally, it should be noted that although integrated beam steering structures and QPM gratings have been fabricated on the same wafer [5,13], this is the first work which uses the beam steering functionality to tune the wavelength of the emitted radiation.

1.3 Overview of Thesis

Chapter 2 presents an overview of the theoretical concepts which are used to analyze the behavior of the EOBS. Four sections address separate topics: the electro-optic effect, three-wave mixing, domain engineering of crystals, and Gaussian beam propagation.

Chapter 3 details the design of the EOBS. The geometric and physical constraints affecting the design are considered and the critical parameters of the device are optimized. Five sections address separate topics: the selection of the electro-optic material, the geometric optimization of the beam steering channels, the final design of the EOBS, device fabrication, and the control regime.

Chapter 4 explains the use of finite difference method (FDM) beam propagation software to simulate the propagation of a Gaussian beam through an EOBS. The performance of an EOBS under various environmental conditions is evaluated. Two sections address separate topics: finite difference method theory, and simulation results.

Chapter 5 reports the experimental procedures used to evaluate the performance of the EOBS. Four sections address separate topics: the setup of beam switching experiments, beam translation measurements, switched OPG, and system limitations.

Chapter 6 offers conclusions concerning of the success of the research and makes suggestions for future work enabled by the EOBS device.

1.4 Formatting

Additionally, references are noted by brackets, e.g. [321]. MATLAB code is referenced by brackets and an 'M,' e.g. [M321]. A catalog of MATLAB code used in this work is available in *Appendix E*. Vendors are referenced by brackets and a 'V,' e.g. [V321]. Figures, tables, and equations are referenced by chapter and order of appearance therein. Thus, "Equation (1.2)" refers to the second equation in Chapter 1.

CHAPTER 2 – THEORY AND BACKGROUND

2.1 The Electro-Optic Effect

The electro-optic effect is a coupling between an electric field within a material and its refractive index. This effect is exhibited by some crystalline materials that lack inversion symmetry. As is common of many crystal phenomena, the coupling is dependent on the orientation of the electric field and the tensor properties of the material.

2.1.1 The First Order Electro-Optic Effect

Recall that for electromagnetic phenomena in the MKS system of units, the electric displacement \vec{D} and the electric field \vec{E} are related:

$$\vec{D} = \epsilon_0 \vec{\epsilon} \vec{E} \quad (2.1)$$

where, ϵ_0 is the vacuum permittivity, and $\vec{\epsilon}$ is the relative permittivity tensor. Assuming that the crystal posses a natural, well-defined coordinate system; the relative permittivity tensor of that crystal can be written:

$$\vec{\epsilon} = \begin{bmatrix} \epsilon_x & 0 & 0 \\ 0 & \epsilon_y & 0 \\ 0 & 0 & \epsilon_z \end{bmatrix} \quad (2.2)$$

The inverse of Equation (2.1) is:

$$\vec{E} = \frac{1}{\epsilon_0} \vec{B} \vec{D} \quad (2.3)$$

where:

$$\vec{B} = \begin{bmatrix} \epsilon_x^{-1} & 0 & 0 \\ 0 & \epsilon_y^{-1} & 0 \\ 0 & 0 & \epsilon_z^{-1} \end{bmatrix} = \begin{bmatrix} \frac{1}{n_x^2} & 0 & 0 \\ 0 & \frac{1}{n_y^2} & 0 \\ 0 & 0 & \frac{1}{n_z^2} \end{bmatrix} \quad (2.4)$$

represents the unperturbed state of the crystal lattice.

The applied electric field \vec{E} can be seen to represent a deformation of this tensor to state \vec{B}' :

$$\vec{B}' = \vec{B} + \Delta \vec{B} \quad (2.5)$$

where:

$$\Delta \vec{B}_{ij} = \sum_k r_{ijk} E_k \quad (2.6)$$

Or, using Einstein notation:

$$\Delta \vec{B}_{ij} = \vec{r}_{ijk} \vec{E}_k \quad (2.7)$$

where \vec{r}_{ijk} is known as the “electro-optic tensor.” It has been shown that, if the medium is lossless and lacks optical activity, the tensor can be assumed to be symmetric. This symmetry allows for contracted index notation, shown in Table 2.1.

Table 2.1 – A contracted index notation legend.

i,j	Contracted
11	1
22	2
33	3
23	4
13	5
12	6

So, for example $r_{12k} \equiv r_{21k} \rightarrow r_{6k}$. Thus, the contracted electro-optic tensor is:

$$\vec{r}_{ij} = \begin{bmatrix} r_{11} & r_{12} & r_{13} \\ r_{21} & r_{22} & r_{23} \\ r_{31} & r_{32} & r_{33} \\ r_{41} & r_{42} & r_{43} \\ r_{51} & r_{52} & r_{53} \\ r_{61} & r_{62} & r_{63} \end{bmatrix} \quad (2.8)$$

It is important to note that contracted tensors do not obey traditional tensor transformation and multiplication properties. The contracted index notation is therefore a conceptual tool and not a precise mathematical description and the results of these operations must be interpreted within the context of the contracted notation.

It is plainly seen that the electro-optical tensor describes the change in the magnitude of the principal indices of refraction and the orientation of the principal optical axes. So, under the influence of an electric field $\vec{E}_k = [E_x \ E_y \ E_z]$:

$$\Delta \vec{B}_{ij} = \vec{r}_{ijk} \vec{E}_k = \begin{bmatrix} r_{11} & r_{12} & r_{13} \\ r_{21} & r_{22} & r_{23} \\ r_{31} & r_{32} & r_{33} \\ r_{41} & r_{42} & r_{43} \\ r_{51} & r_{52} & r_{53} \\ r_{61} & r_{62} & r_{63} \end{bmatrix} \begin{bmatrix} E_x \\ E_y \\ E_z \end{bmatrix} = \begin{bmatrix} r_{11}E_x + r_{12}E_y + r_{13}E_z \\ r_{21}E_x + r_{22}E_y + r_{23}E_z \\ r_{31}E_x + r_{32}E_y + r_{33}E_z \\ r_{41}E_x + r_{42}E_y + r_{43}E_z \\ r_{51}E_x + r_{52}E_y + r_{53}E_z \\ r_{61}E_x + r_{62}E_y + r_{63}E_z \end{bmatrix} \quad (2.9)$$

which, in standard index notation is:

$$\Delta \vec{B}_{ij} = \begin{bmatrix} r_{11}E_x + r_{12}E_y + r_{13}E_z & r_{61}E_x + r_{62}E_y + r_{63}E_z & r_{51}E_x + r_{52}E_y + r_{53}E_z \\ r_{61}E_x + r_{62}E_y + r_{63}E_z & r_{21}E_x + r_{22}E_y + r_{23}E_z & r_{41}E_x + r_{42}E_y + r_{43}E_z \\ r_{51}E_x + r_{52}E_y + r_{53}E_z & r_{41}E_x + r_{42}E_y + r_{43}E_z & r_{31}E_x + r_{32}E_y + r_{33}E_z \end{bmatrix} \quad (2.10)$$

Finding the eigenvectors of this tensor would yield the new principal axes in terms of the original coordinate system. Finding the eigenvalues of the tensor would yield the expression for the modified indices of refraction (which apply in the new coordinate system). This calculation is not performed for the general case, but is shown for 3m crystals in particular in *Section 3.1.2*.

2.1.2 Second Order Effects

The relationship between an electric field and the material polarization it drives is:

$$\vec{P}_i = \epsilon_0 \chi_{ij} \vec{E}_j \quad (2.11)$$

where \vec{P} is the polarization induced by the optical field and χ is the electric susceptibility. Assuming that high order responses are weaker than low order responses, the Taylor series representation is [14]:

$$P_i = \epsilon_0 (\chi_{ij} E_j + 2\chi_{ijk} E_j E_k + 4\chi_{ijkl} E_j E_k E_l + \dots) \quad (2.12)$$

with each successive term being a small correction to the linear term. For conceptual purposes, these terms can be parameterized:

$$\vec{P}_{total} = \vec{P}^{(I)} + \vec{P}^{(II)} + \vec{P}^{(III)} + \dots \quad (2.13)$$

which can be written more simply as:

$$\vec{P}_{total} = \vec{P}^{(L)} + \vec{P}^{(NL)} \quad (2.14)$$

where $\vec{P}^{(L)}$ is the linear polarization and $\vec{P}^{(NL)}$ is the total non-linear polarization.

2.2 Three-Wave Mixing

Optical parametric generation (OPG) is a process whereby a single photon of a particular wavelength is converted into two photons of longer wavelengths. Since OPG is a spontaneous process, it has a large bandwidth. To describe it properly, one must account for all the possible frequency combinations that satisfy energy and momentum conservation. In reality, not all frequency pairings are needed, only those pairings within the phasematching bandwidth have an appreciable contribution.

It is possible to describe OPG by calculating the phase matching bandwidth of an optical parametric amplifier (OPA). An OPA amplifies the input signal by ‘stimulating’ a pump photon to split into a signal photon and an idler photon at the difference frequency between the pump and signal. The OPG process can be considered to be a noise-seed OPA that starts with input signals at many frequencies which are then amplified. In the small signal limit, these processes are independent, and their efficiency is determined by the OPA gain and the phase matching conditions.

These three wave mixing processes are coupled to the second order polarization of the medium in which they occur. Accordingly, in *Section 2.2.1*, the physical conditions required for efficient OPA (and, by extension, OPG) are derived from a consideration of

the electromagnetic interaction of optical fields with material polarizations containing second order terms.

2.2.1 The Phasematching Condition

Consider the Maxwell-Faraday equation:

$$\vec{\nabla} \times \vec{E} = -\frac{\partial \vec{B}}{\partial t} \quad (2.15)$$

Taking the curl of both sides of Equation (2.15) yields:

$$\vec{\nabla} \times (\vec{\nabla} \times \vec{E}) = -\frac{\partial (\vec{\nabla} \times \vec{B})}{\partial t} = -\frac{\partial (\vec{\nabla} \times \mu \vec{H})}{\partial t} \quad (2.16)$$

Substituting in Ampere's Law (assume $\vec{J}_f = 0$) yields:

$$\vec{\nabla} \times (\vec{\nabla} \times \vec{E}) = -\mu \frac{\partial (\vec{\nabla} \times \vec{H})}{\partial t} = -\mu \frac{\partial \left(\vec{J}_f + \frac{\partial \vec{D}}{\partial t} \right)}{\partial t} = -\mu \frac{\partial^2 \vec{D}}{\partial^2 t} \quad (2.17)$$

The left side of Equation (2.17) can be evaluated:

$$\vec{\nabla} \times (\vec{\nabla} \times \vec{E}) = \vec{\nabla}(\vec{\nabla} \cdot \vec{E}) - \nabla^2 \vec{E} \quad (2.18)$$

Under the assumption the material is homogeneous ($\vec{\nabla} \cdot \vec{E} = 0$), Equation (2.18) becomes:

$$\vec{\nabla} \times (\vec{\nabla} \times \vec{E}) = -\nabla^2 \vec{E} \quad (2.19)$$

Substituting Equation (2.17) into Equation (2.19) and assuming the material is non-magnetic ($\mu = \mu_0$) yields:

$$\nabla^2 \vec{E} = \mu_0 \frac{\partial^2 \vec{D}}{\partial^2 t} \quad (2.20)$$

which is the electromagnetic wave equation for a plane wave in a dielectric medium. Substituting the constitutive relationship, $\vec{D} = \epsilon_0 \vec{E} + \vec{P}_{total}$, into Equation (2.20) yields:

$$\nabla^2 \vec{E} = \mu_0 \epsilon_0 \frac{\partial^2 \vec{E}}{\partial t^2} + \mu_0 \frac{\partial^2 \vec{P}_{total}}{\partial t^2} \quad (2.21)$$

which can be written more explicitly as:

$$\nabla^2 \vec{E} = \mu_0 \epsilon_0 \frac{\partial^2 \vec{E}}{\partial t^2} + \mu_0 \frac{\partial^2 \vec{P}^{(L)}}{\partial t^2} + \mu_0 \frac{\partial^2 \vec{P}^{(NL)}}{\partial t^2} \quad (2.22)$$

From this form of the wave equation, a system of three coupled differential equations can be found which describe the evolution of the fields as they propagate. So, to find the differential equation describing the evolution of the electric field of the pump beam, it is assumed that all fields involved in this interaction take the form of plane waves.

Recall that, for plane waves traveling along the z-axis, the electric field expression can be written:

$$\vec{E}_1 = \frac{1}{2} [A_1(z) e^{i(k_1 z - \omega_1 t + \phi_1)} + c.c.] \hat{p}_1 \quad (2.23)$$

where \hat{p}_1 is a unit vector in an arbitrary direction and $A_1(z)$ is the complex amplitude of the electric field of the pump beam. Recalling that $\vec{P} = \epsilon_0 \vec{\chi} \vec{E}$, the linear polarization term becomes:

$$\vec{P}^{(L)} = \frac{1}{2} \epsilon_0 [\chi^{(I)} A_1(z) e^{-i\omega_1 t} + c.c.] \hat{p}_1 \quad (2.24)$$

where $\chi^{(I)}$ is the first order susceptibility.

Because the nonlinear responses are weak, the resulting processes are assumed to be independent, and the $\vec{P}^{(NL)}$ term in Equation (2.22) can be written in terms of only one specific process, instead of in general terms for all processes. Here, the sum frequency generation ($\omega_1 = \omega_2 + \omega_3$) process is considered. The standard frequency convention ($\omega_1 > \omega_2 > \omega_3$), is used. The nonlinear (second order) term for this process can be written as:

$$\vec{P}^{(II)}(\omega_1) = \frac{1}{2} [2\epsilon_0 d_{123} \vec{E}_2 \vec{E}_3 e^{-i\omega_1 t} + c.c.] \hat{p}_1 \quad (2.25)$$

where $d_{123} = \frac{1}{2} \chi_{123}$. The complex magnitude of this expression is [15]:

$$\vec{P}^{(NL)} = 2\epsilon_0 d_{eff} A_2(z) A_3(z) e^{i((k_2 + k_3)z - \omega_1 t)} \hat{p}_1 \quad (2.26)$$

where d_{eff} is a scalar quantity known as the “effective nonlinearity” of the interaction. Mathematically, d_{eff} takes the form of a sum of the products of the values of the quadratic susceptibility tensor \vec{d} and the geometric considerations of a specific process. So, from Equation (2.22):

$$\nabla^2 A_1(z) e^{i(k_1 z - \omega_1 t + \phi_1)} \hat{p}_1 = \frac{\mu_0 \epsilon_0}{2} \frac{\partial^2}{\partial t^2} [A_1(z) e^{i(k_1 z - \omega_1 t + \phi_1)}] \hat{p}_1 \quad (2.27)$$

$$\begin{aligned}
& + \frac{\mu_0 \epsilon_0}{2} \frac{\partial^2}{\partial t^2} [\chi^{(1)} A_1(z) e^{-i\omega_1 t}] \hat{p}_1 \\
& + 2\mu_0 \epsilon_0 d_{eff} A_2(z) A_3(z) e^{i((k_2+k_3)z - \omega_1 t)} \hat{p}_1
\end{aligned}$$

Under the assumption that the fields are monochromatic, the complex amplitudes thereof become time-independent, so substituting $\mu_0 \epsilon_0 = \frac{1}{c^2}$ into Equation (2.27) and letting $\frac{\partial}{\partial t} \rightarrow -i\omega_1$ yields:

$$\begin{aligned}
& \nabla^2 A_1(z) e^{ik_1 z} e^{-i\omega_1 t} \hat{p}_1 \\
& = \left[-\frac{\omega_1^2}{c^2} A_1(z) e^{ik_1 z} e^{-i\omega_1 t} - \frac{\omega_1^2}{c^2} \chi^{(1)} A_1(z) e^{ik_1 z} e^{-i\omega_1 t} \right. \\
& \quad \left. - 2 \frac{\omega_1^2}{c^2} d_{eff} A_2(z) A_3(z) e^{i((k_2+k_3)z - \omega_1 t)} \right] \hat{p}_1
\end{aligned} \tag{2.28}$$

where the phase ϕ has been discarded. Substituting $1 + \chi^{(1)} = n^2$ into Equation (2.28) and rearranging the terms yields:

$$\begin{aligned}
& \left[\nabla^2 A_1(z) e^{ik_1 z} e^{-i\omega_1 t} + \frac{\omega_1^2 n^2}{c^2} A_1(z) e^{ik_1 z} e^{-i\omega_1 t} \right] \hat{p}_1 \\
& = \left[-2 \frac{\omega_1^2}{c^2} d_{eff} A_2(z) A_3(z) e^{i(k_2+k_3)z} e^{-i\omega_1 t} \right] \hat{p}_1
\end{aligned} \tag{2.29}$$

For the sake of simplifying this derivation, it can be assumed that the field will be driven in the same direction as the nonlinear polarization. Thus, the vector nature can be discarded and Equation (2.29) becomes:

$$\begin{aligned}
& \nabla^2 A_1(z) e^{ik_1 z} e^{-i\omega_1 t} + \frac{\omega_1^2 n^2}{c^2} A_1(z) e^{ik_1 z} \\
& = -2 \frac{\omega_1^2}{c^2} d_{eff} A_2(z) A_3(z) e^{i(k_2+k_3)z} e^{-i\omega_1 t}
\end{aligned} \tag{2.30}$$

The case of collinear plane waves has already been assumed so $\nabla^2 \rightarrow \frac{\partial^2}{\partial z^2}$. So:

$$\begin{aligned}
& \frac{\partial^2}{\partial z^2} A_1(z) e^{ik_1 z} e^{-i\omega_1 t} + \frac{\omega_1^2 n^2}{c^2} A_1(z) e^{ik_1 z} + c. c. \\
& = -2 \frac{\omega_1^2}{c^2} d_{eff} A_2(z) A_3(z) e^{i(k_2+k_3)z} e^{-i\omega_1 t} + c. c.
\end{aligned} \tag{2.31}$$

Note that the complex conjugate terms of Equation (2.31) can be dropped with no loss of generality. So, evaluating the derivatives yields:

$$\left\{ \frac{\partial^2}{\partial z^2} [A_1(z)] + 2ik_1 \frac{\partial}{\partial z} [A_1(z)] + i^2 k_1^2 A_1(z) + \frac{\omega_1^2 n^2}{c^2} A_1(z) \right\} e^{ik_1 z} e^{-i\omega_1 t} =$$

$$= -2 \frac{\omega_1^2}{c^2} d_{eff} A_2(z) A_3(z) e^{i(k_2+k_3)z} e^{-i\omega_1 t} \quad (2.32)$$

If the envelope A_1 is assumed to vary slowly, then $ik \frac{\partial A}{\partial z} \gg \frac{\partial^2 A}{\partial z^2}$, and $\frac{\partial^2 A}{\partial z^2} \rightarrow 0$. Thus:

$$\left\{ 2ik_1 \frac{\partial}{\partial z} [A_1(z)] - k_1^2 A_1(z) + \frac{\omega_1^2 n^2}{c^2} A_1(z) \right\} e^{ik_1 z} e^{-i\omega_1 t}$$

$$= -2 \frac{\omega_1^2}{c^2} d_{eff} A_2(z) A_3(z) e^{i(k_2+k_3)z} e^{-i\omega_1 t} \quad (2.33)$$

Substituting $k_1^2 = \frac{\omega_1^2 n^2}{c^2}$ into Equation (2.33) yields:

$$ik_1 \frac{\partial}{\partial z} [A_1(z)] e^{ik_1 z} e^{-i\omega_1 t} = - \frac{\omega_1^2}{c^2} d_{eff} A_2(z) A_3(z) e^{i(k_2+k_3)z} e^{-i\omega_1 t} \quad (2.34)$$

The time dependence terms $e^{-i\omega_1 t}$ cancel and rearranging yields:

$$\frac{\partial}{\partial z} [A_1(z)] = i \frac{\omega_1^2}{k_1 c^2} d_{eff} A_2(z) A_3(z) e^{i(k_2+k_3-k_1)z} \quad (2.35)$$

Substituting $\Delta k = k_2 + k_3 - k_1$ yields:

$$\frac{\partial}{\partial z} [A_1(z)] = i \frac{\omega_1^2}{k_1 c^2} d_{eff} A_2(z) A_3(z) e^{i\Delta k z} \quad (2.36)$$

which describes the evolution of the pump field over time as it propagates in the z -direction. By following similar arguments, the expressions for the signal and idler beams can be found to have similar forms [16]:

$$\frac{\partial}{\partial z} [A_2(z)] = i \frac{\omega_2^2}{k_2 c^2} d_{eff} A_1(z) A_3^*(z) e^{-i\Delta k z} \quad (2.37)$$

$$\frac{\partial}{\partial z} [A_3(z)] = i \frac{\omega_3^2}{k_3 c^2} d_{eff} A_1(z) A_2^*(z) e^{-i\Delta k z} \quad (2.38)$$

This system of coupled partial differential equations describes the three-wave mixing process.

Recall the definition of intensity:

$$I_m(z) = \frac{c\epsilon_0 n_m}{2} A_m(z) A_m^*(z) \quad (2.39)$$

Thus, the variation of the intensity of the optical field of a beam is given by:

$$\frac{\partial}{\partial z} [I_m(z)] = \frac{c\epsilon_0 n_m}{2} \left(A_m^*(z) \frac{\partial}{\partial z} [A_m(z)] + A_m(z) \frac{\partial}{\partial z} [A_m^*(z)] \right) \quad (2.40)$$

Substituting Equation (2.36) into Equation (2.40) yields:

$$\begin{aligned} \frac{\partial}{\partial z} [I_1(z)] &= \frac{c\epsilon_0 n_m}{2} \frac{\omega_1^2}{k_1 c^2} d_{eff} (iA_1^*(z)A_2(z)A_3(z)e^{i\Delta kz} + c.c.) \\ &= \frac{1}{2} \epsilon_0 \omega_1 d_{eff} (iA_1^*(z)A_2(z)A_3(z)e^{i\Delta kz} + c.c.) \\ &= -\epsilon_0 \omega_1 d_{eff} \text{Im}(A_1^*(z)A_2(z)A_3(z)e^{i\Delta kz}) \\ &= \epsilon_0 \omega_1 d_{eff} \text{Im}(A_1(z)A_2^*(z)A_3^*(z)e^{-i\Delta kz}) \end{aligned} \quad (2.41)$$

Likewise, substituting Equations (2.37) and (2.38) into Equation (2.40) and performing similar steps yields:

$$\frac{\partial}{\partial z} [I_2(z)] = -\epsilon_0 \omega_2 d_{eff} \text{Im}(A_2^*(z)A_1(z)A_3^*(z)e^{-i\Delta kz}) \quad (2.42)$$

$$\frac{\partial}{\partial z} [I_3(z)] = -\epsilon_0 \omega_1 d_{eff} \text{Im}(A_3^*(z)A_1(z)A_2^*(z)e^{-i\Delta kz}) \quad (2.43)$$

Equations (2.41), (2.42), and (2.43) can be readily combined by direct substitution. Recognizing the common factor $-\epsilon_0 \text{Im}(A_3^*(z)A_1(z)A_2^*(z)e^{-i\Delta kz})$ the relationship between the three fields becomes:

$$-\frac{\partial}{\partial z} [I_1(z)] = \frac{\partial}{\partial z} [I_2(z)] = \frac{\partial}{\partial z} [I_3(z)] = -\epsilon_0 \text{Im}(A_3^*(z)A_1(z)A_2^*(z)e^{-i\Delta kz}) \quad (2.44)$$

Or more explicitly:

$$\frac{\partial}{\partial z} [I_1(z)] = -\frac{\partial}{\partial z} [I_2(z)] = -\frac{\partial}{\partial z} [I_3(z)] \quad (2.45)$$

The equalities shown in (2.45) are known as the “Manley-Rowe relations” for the nonlinear process. These equalities describe the coupling of the pump, signal, and idler intensities. Thus, it is seen that, due to the nonlinear susceptibility of the material, power can flow between pump, signal, and idler fields at different wavelengths.

Now recall that it has been assumed that the processes which couple different frequencies are weak. Thus, for the case of two co-aligned lasers, the amplitude of the electric fields will be relatively constant over the whole length of the interaction. This concept is called the “undepleted pump approximation.” Under this approximation, the spatial dependence of the amplitude of the undepleted fields disappears, leaving only the equation for the electric field of the idler beam:

$$\frac{\partial}{\partial z} [A_3(z)] = i \frac{\omega_3^2}{k_3 c^2} d_{eff} A_1 A_2^* e^{-i\Delta k z} = i \frac{\omega_3}{n_3 c} d_{eff} A_1 A_2^* e^{-i\Delta k z} \quad (2.46)$$

Integrating both sides of Equation (2.46) yields:

$$\int \frac{\partial}{\partial z} [A_3(z)] \partial z = \int_0^L i \frac{\omega_3}{n_3 c} d_{eff} A_1 A_2^* e^{i\Delta k z} \partial z \quad (2.47)$$

So the complex amplitude of the field is:

$$\begin{aligned} A_3 &= \frac{\omega_3}{\Delta k n_3 c} A_1 A_2^* (e^{i\Delta k L} - 1) \\ &= \frac{\omega_3}{\Delta k n_3 c} d_{eff} A_1 A_2^* e^{\frac{i\Delta k L}{2}} \left(e^{\frac{i\Delta k L}{2}} - e^{-\frac{i\Delta k L}{2}} \right) \\ &= \frac{i 2 \omega_3}{\Delta k n_3 c} d_{eff} A_1 A_2^* e^{\frac{i\Delta k L}{2}} \sin\left(\frac{\Delta k L}{2}\right) \\ &= \frac{i \omega_3 L}{n_3 c} d_{eff} A_1 A_2^* e^{\frac{i\Delta k L}{2}} sa\left(\frac{\Delta k L}{2}\right) \end{aligned} \quad (2.48)$$

where the definition $sa(x) = \frac{\sin(x)}{x}$ has been used. Substituting into the definition of average intensity, $I_3 = \frac{c n_3 \epsilon_0}{2} |A_3|^2$, yields:

$$I_3 = \frac{\omega_3^2 L^2 \epsilon_0}{2 n_3 c} d_{eff}^2 |A_1|^2 |A_2|^2 sa^2\left(\frac{\Delta k L}{2}\right) \quad (2.49)$$

Figure 2.1 shows a plot of the normalized function $I_3(\Delta k)$.

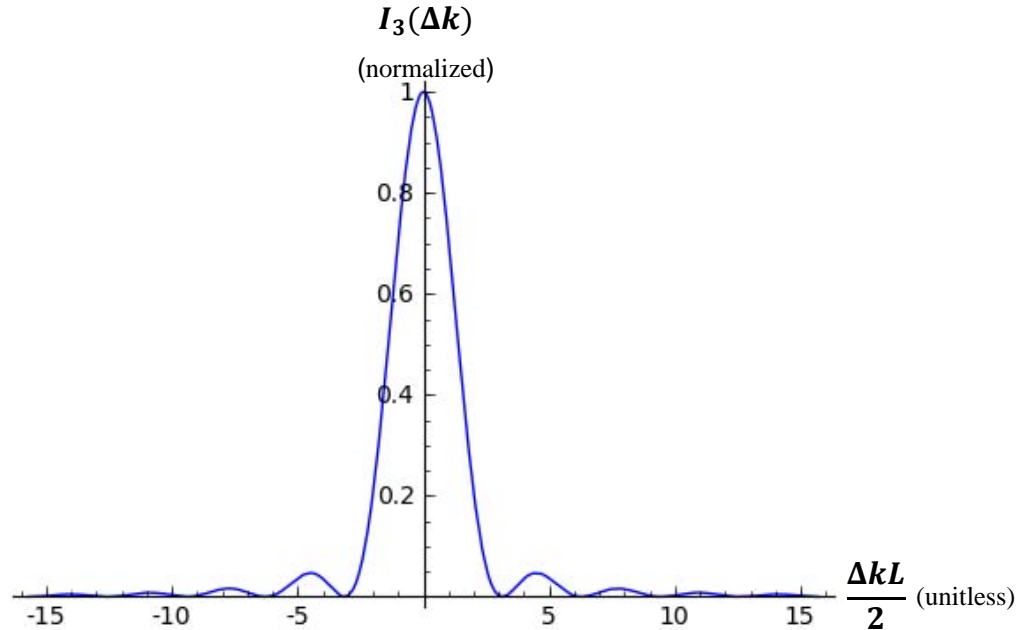


Figure 2.1 – The phasematching efficiency curve.

It is clear that the highest idler intensity is achieved when:

$$\Delta k = k_2 + k_3 - k_1 = 0 \quad (2.50)$$

which is known as the “phasematching condition.” Measurable output is only expected when the phasematching condition is satisfied within the acceptance band shown in Figure 2.1. The phasematching bandwidth is then the full-width half-maximum (FWHM) value of the main lobe of the efficiency envelope:

$$BW_{\Delta k} = FWHM \left\{ sa^2 \left(\frac{\Delta k L}{2} \right) \right\} \quad (2.51)$$

which is the region where:

$$-2.783 < \Delta k L < 2.783 \quad (2.52)$$

When this condition is satisfied, the weak non-linear process becomes efficient and wavelength conversion effects can be observed. Experimentally, the output bandwidth of the OPG process follows this functional dependence.

2.2.2 Dispersion and the k -vector Mismatch

In general, for any quantum process, energy must be conserved:

$$\Delta E = E_3 + E_2 - E_1 = hc \left(\frac{1}{\lambda_2} + \frac{1}{\lambda_3} - \frac{1}{\lambda_1} \right) = 0 \quad (2.53)^1$$

So, in the classical limit, energy will be conserved in the optical fields involved in the process and the wavelengths of these fields must satisfy the relationship:

$$\frac{1}{\lambda_1} = \frac{1}{\lambda_2} + \frac{1}{\lambda_3} \quad (2.54)$$

Equation (2.54) imposes a fundamental limitation on the nonlinear process. If this equation is not satisfied, the interaction between λ_1 , λ_2 , and λ_3 is non-physical.

Now, recall the phasematching condition:

$$\Delta k = \vec{k}_2 + \vec{k}_3 - \vec{k}_1 = 0$$

Substituting $k_m = \frac{2\pi n_m}{\lambda_m}$ yields:

$$\Delta k = 2\pi \left(\frac{n_2}{\lambda_2} + \frac{n_3}{\lambda_3} - \frac{n_1}{\lambda_1} \right) = 0 \quad (2.55)$$

¹ The sign of each term is determined by the particular process under consideration.

where $n_m = n(\lambda_m)$. So it follows that if the medium is dispersionless ($n_1 = n_2 = n_3$), that the phasematching condition and the energy conservation condition are simultaneously satisfied. However, in general, the index of refraction of the conversion medium is wavelength dependent ($n = n(\lambda)$); thus $n_1 \neq n_2 \neq n_3$. The consequence of this dispersion is that Equation (2.55) is not satisfied when the combination of λ_1 , λ_2 , and λ_3 satisfy the conservation of energy equation (Equation (2.53)).

Experimentally, simultaneous satisfaction of the conservation and phasematching relationships can be achieved using three separate techniques. The first technique, known as “birefringent phasematching,” is accomplished by using a birefringent nonlinear crystal as the conversion medium. In such crystals, the index of refraction is polarization dependent. These crystals typically have an angularly dependent extraordinary index of refraction. By adjusting the angle of incident light relative to the optical axis of the crystal, the phasematching equation can be satisfied and the process becomes efficient. Figure 2.2 shows the geometry of this interaction.

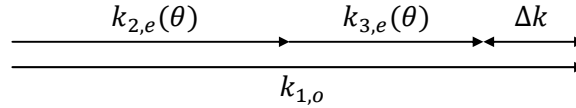


Figure 2.2 – Birefringent phasematching [$o \rightarrow e + e$].

The second technique, known as “non-collinear phasematching,” compensates for the k-vector mismatch between field components with changes to the propagation direction of the incident beams. Figure 2.3 shows the geometry of this interaction.

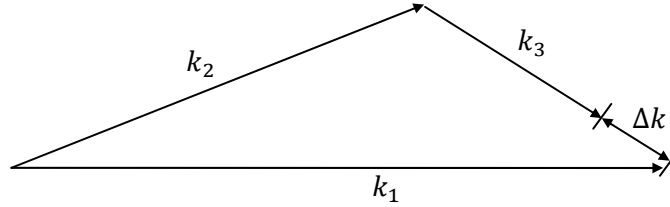


Figure 2.3 – Noncollinear phasematching.

Birefringent and noncollinear phasematching techniques are not employed in this work, and thus, are not explored in detail in this discussion. The third technique is the aforementioned quasi-phase matching (QPM) which can be accomplished in ferroelectric crystals by fabricating (via electric field poling) a period structure in a nonlinear crystal. The periodic inversion of the crystal structure induces a periodic reversal of the effective nonlinearity d_{eff} that compensates for the phase mismatch of the interaction [17]. This periodic structure is typically referred to as an “OPG grating;” however, there is no modulation of the refractive index, only inversion of the even-ordered susceptibilities of the material. For a three-wave-mixing process, this can be thought of as a periodic reversal of the effective nonlinearity d_{eff} .

Figure 2.4 shows the grating geometry, the actual fabrication is discussed in Section 2.3.

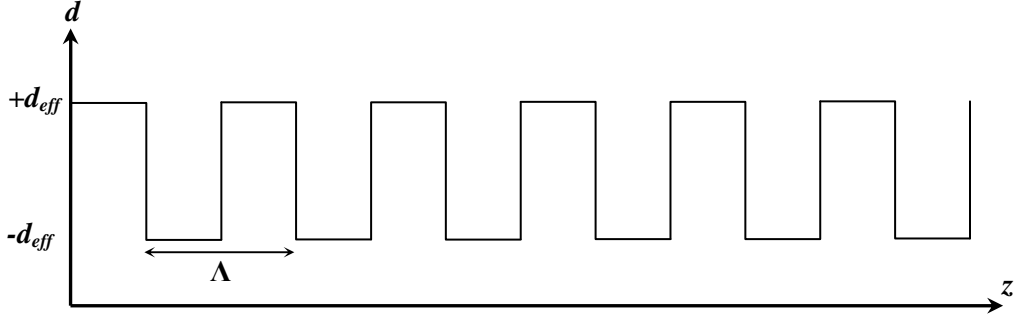


Figure 2.4 – The effective nonlinearity profile of a typical QPM grating.

The QPM grating has an intrinsic k-vector of $k_{grating} = \pm \frac{2\pi}{\Lambda} m$, where m is the order of the QPM interaction [15]. For this discussion, the order is assumed to be $m = 1$. Thus the phasematching condition becomes:

$$\Delta k = 2\pi \left(\frac{n_2}{\lambda_2} + \frac{n_3}{\lambda_3} - \frac{n_1}{\lambda_1} + \frac{1}{\Lambda} \right) = 0 \quad (2.56)$$

Thus, the grating period Λ becomes a means of compensating for material dispersion and allowing the nonlinear interaction to simultaneously satisfy the energy conservation condition and the phasematching condition. Thus, quasi-phasematching allows the nonlinear process to become efficient and significant out power is expected at the idler wavelength.

2.2.3 Optical Parametric Generation

Optical parametric generation (OPG) is essentially a broad-band OPA process. Like OPA, OPG allows the mixing of fields of different wavelengths. The chief difference between the processes is that OPG involves only a pump beam and relies on noise to provide a signal seed.² Conceptually, the process can be thought of as a single pump photon splitting into two photons of lower energies, and therefore, longer wavelengths ($\lambda_1 \rightarrow \lambda_2 + \lambda_3$). Figure 2.5 illustrates the OPG process.

² It is actually quite difficult to derive the OPG expression when only the pump field is present. Vacuum fluctuations are often invoked to explain the presence of a signal field. This signal field is amplified as the OPG process intensifies and the idler field is generated as a result of the mixing of the pump and signal fields. Conceptually, this process can be thought of as the sum frequency generation (SFG) process operating in reverse; thus, Equation (2.49) presents the coupling between the three waves. A more detailed explanation is available in [15].

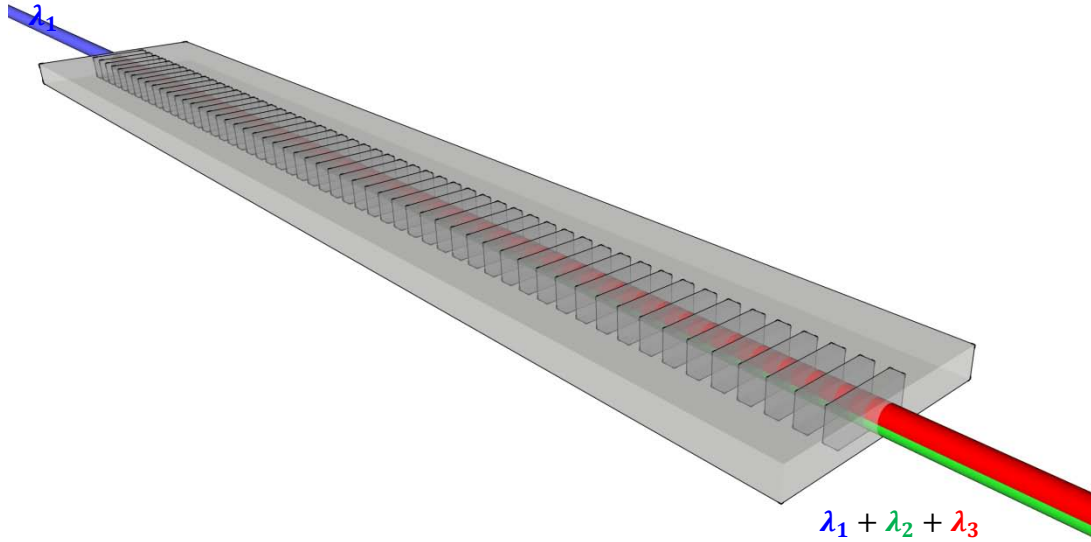


Figure 2.5 – An illustration of the optical parametric generation (OPG) process.

Because no strong signal field is present, the signal wavelength is unconstrained. Thus, the dominant signal and idler wavelength pair is, in effect, determined by the poling period Λ . Thus, the process can be ‘tuned’ by simply selecting a poling period which leads to a process which is most efficient ($\Delta k = 0$) at the desired signal or idler wavelength. Selecting specific signal and idler wavelengths will be addressed in more detail in *Section 3.1.3*.

Physically, the pump field will have finite spectral width. Thus, λ_1 can be thought of as the mean-value of the spectral content of the pump field. For a typical OPG grating, whose length L is on the order of a few centimeters, the phasematching bandwidth of the process is wider than the spectral content of the pump laser. Thus, all of the spectral content of the pump beam can be utilized in the OPG process. Consequently, the signal and idler beams will also have finite-spectral width.

The EOBS developed in this work was designed to switch a pump beam between two OPG gratings (see Figure 1.2) with poling periods Λ_1 and Λ_2 . If $\Lambda_1 \neq \Lambda_2$ the wavelength of the signal and idler beams emerging from each grating will be different. Appropriate filters allow the separation of the signal and/or idler beam from the residual pump beam. Thus, such a system is essentially a single bit wavelength multiplexer.

2.3 Crystal Domain Engineering

OPG gratings and prism-type beam steering devices can be fabricated by electric field poling of ferroelectric materials. The poling process results in selectively reversed crystal domains [10]. The process begins with a bare, z-cut crystal substrate (Figure 2.6).



Figure 2.6 – A bare, z-cut crystal substrate.

Using standard photolithography techniques, the surface of the substrate is covered in photoresist. Using a mask to shade the section of the wafer which is not to be poled, the resist is exposed to ultra-violet (UV) light. The photoresist is UV sensitive and the exposed region can be rinsed away, leaving the region to be poled as a bare surface (Figure 2.7).

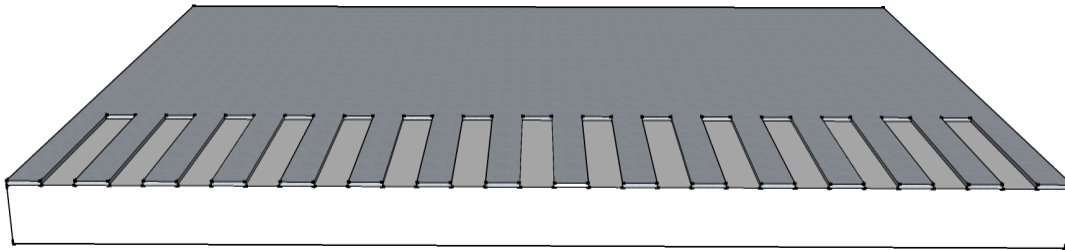


Figure 2.7 – The crystal wafer with a photoresist pattern.

The patterned wafer is then placed in a jig, which is filled with lithium chloride, which functions as a liquid electrode (alternatively, sputtered metal electrodes can be used). The electrolyte fills the valleys between the features of the photoresist (Figure 2.8)

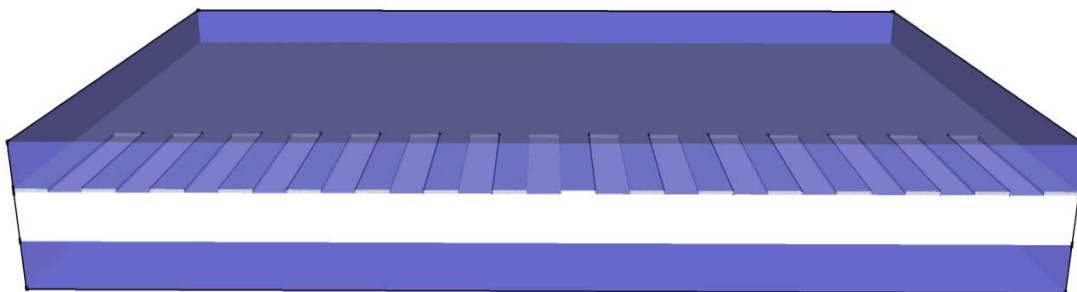


Figure 2.8 – Liquid electrode entrenchment of the photoresist pattern.

High voltage is applied across the top and bottom electrodes. The photoresist reduces the current flow across the wafer; thus, the current is higher where the surface is bare. The voltage is increased until the field across the bare portion of the wafer exceeds the coercive field of the crystal (Figure 2.9).

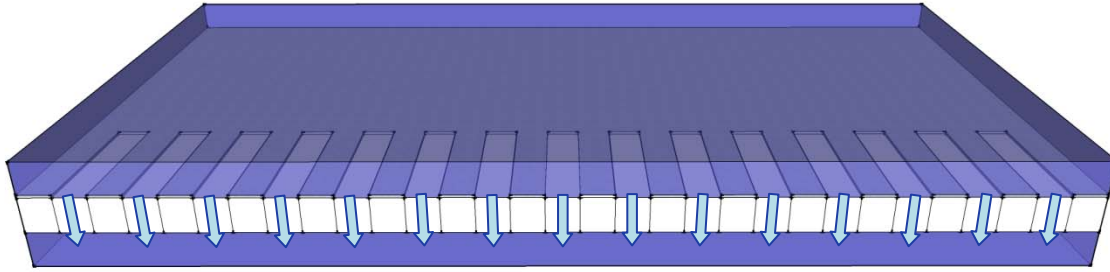


Figure 2.9 – Poling of the crystal wafer.

When the applied field exceeds the coercive field, the ions in the crystal begin to drift (Figure 2.10). The result of this drift current is that the unit cell of the crystal is inverted along the applied field in the exposed regions. When the electric field is turned off, the domain inversion remains. Conceptually, the inverted regions can be thought of as having been cut out of the crystal and reinserted upside-down.

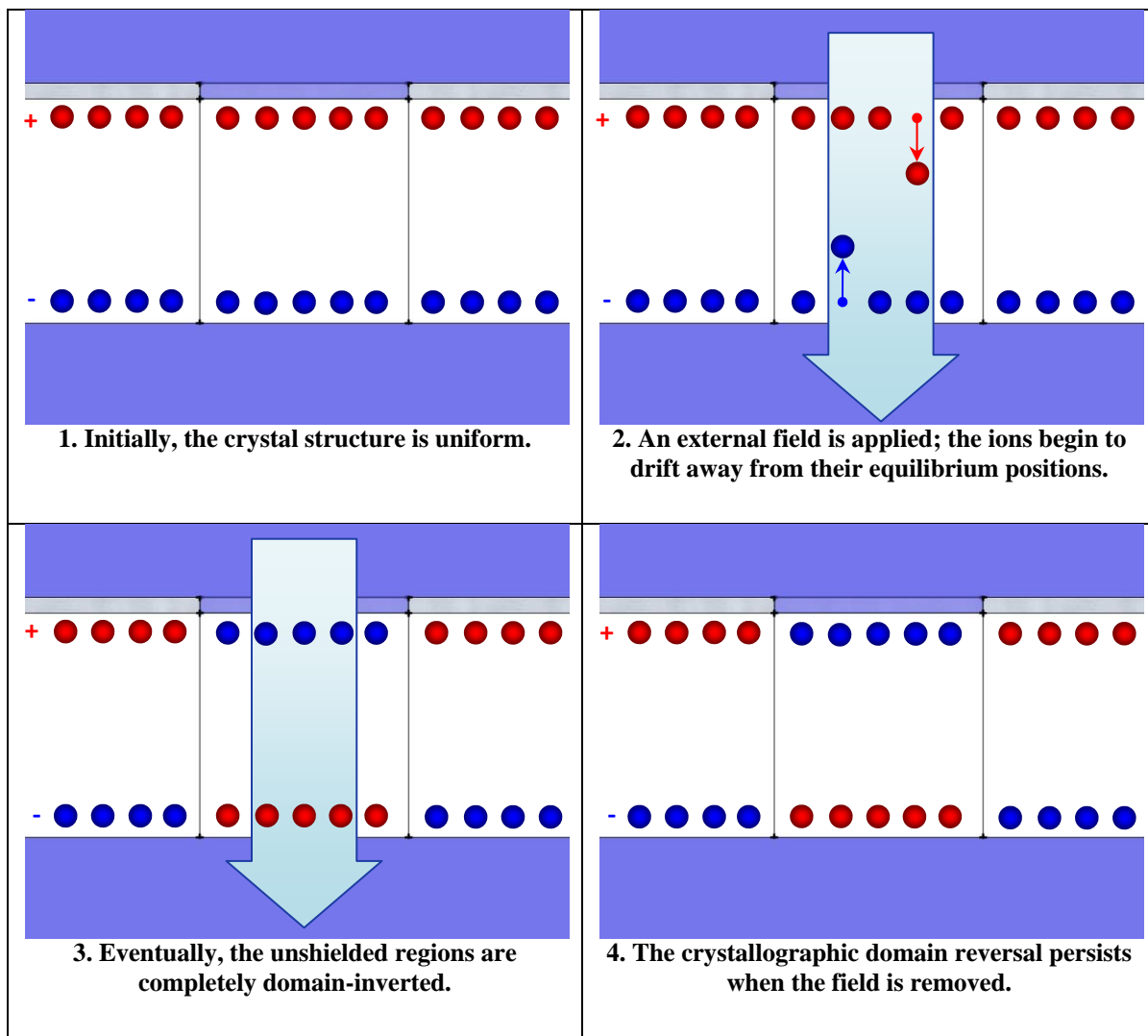


Figure 2.10 – Selective domain inversion of the crystal wafer.

The electrolyte is drained and the remaining photoresist is exposed and rinsed away. The crystal now has inverted crystal domains where the original exposure was not shaded (Figure 2.11).

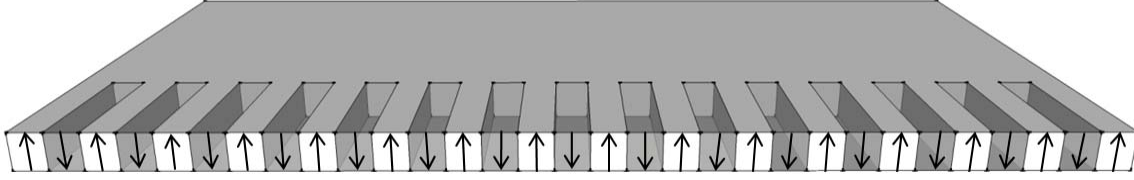


Figure 2.11 – A periodically poled QPM grating.

This periodic structure imparts the $\frac{2\pi}{\Lambda}$ factor in Equation (2.56), which leads to efficient nonlinear conversion of laser radiation. The geometry of the inverted domains need not be periodic as shown, but can be defined arbitrarily. For instance, the geometry of the beam steering prisms presented in this work is not periodic.

2.4 Gaussian Beam Propagation

Recall the electromagnetic wave equation (Equation (2.20)):

$$\nabla^2 \vec{E} = \mu_0 \frac{\partial^2 \vec{D}}{\partial t^2}$$

It can be shown [14 pp. 24-27] that one of the solutions to the electric field wave equation takes the form of a Gaussian function:

$$E(r, x) = E_0 \frac{w_0}{w(z)} \cdot e^{-\frac{r^2}{w^2(z)}} \cdot e^{-ik \left(z + \frac{r^2}{2R(z)} - \frac{\tan^{-1}(\frac{z_0}{z})}{k} \right)} \quad (2.57)$$

where:

$$R(z) = z \left[1 + \left(\frac{z_R}{z} \right)^2 \right] \quad (2.58)$$

$$w^2(z) = w_0^2 \left[1 + \left(\frac{z}{z_R} \right)^2 \right] \quad (2.59)$$

$$z_R = \frac{\pi w_0^2}{\lambda} \quad (2.60)$$

$R(z)$ is the radius of curvature of the phase front of the beam, $w(z)$ is the radius of the beam away from the axis of propagation, and z_R is the Rayleigh range.

Figure 2.12 shows the geometry of a typical Gaussian laser beam.

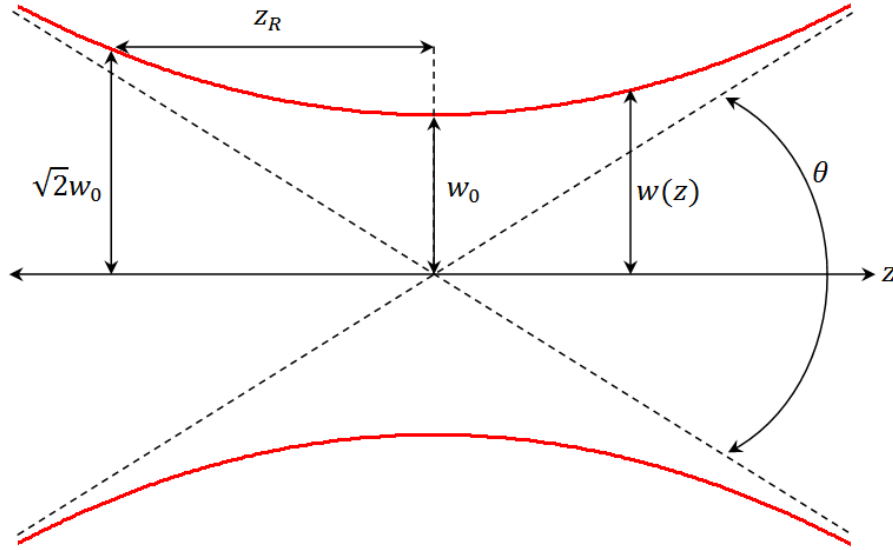


Figure 2.12 – The Geometry of a Gaussian Laser Beam

Thus, assuming that the location of the beam waist is at $z = 0$, the beam diameter at any point along the axis of propagation can be calculated:

$$D(z) = 2w_0 \left(\left[1 + \left(\frac{z\lambda}{n\pi w_0^2} \right)^2 \right] \right)^{\frac{1}{2}} \quad (2.61)$$

It will be shown in *Section 3.2.1* that the diffraction of Gaussian beams will directly impact the steering performance of EOBS designs.

CHAPTER 3 – ELECTRO-OPTIC BEAM SWITCH AND OPG DESIGN

3.1 Material Considerations

3.1.1 Material Selection

One of the engineering constraints placed upon crystal selection was that both the EO beam steering structures and OPG gratings be fabricated in the same wafer. Fabricating both structures on a single wafer reduces the material and poling costs by a factor of two. Consequently, the material chosen must simultaneously exhibit a strong electro-optic coefficient (r_{33}), a strong effective nonlinearity (d_{eff}), and the ability to be readily poled. Relatively few materials exhibit all three characteristics. Thus, material selection for the EOBS was straightforward.

Due to the aforementioned material constraints, the most common materials used for both EO beam steering and QPM are z-cut lithium tantalate and z-cut lithium niobate. Large (76 mm diameter), z-cut wafers of these crystals are readily available in congruent and stoichiometric forms.

It will be shown in Section 3.1.2 that the change in refractive index used to steer the beam obeys the proportionality $\Delta n \propto n^3 r_{33}$. Thus the relative performance of lithium tantalate and lithium niobate can be considered in terms of the refractive index n and the electro-optic coefficient r_{33} . Table 3.1 shows the parameters of interest to index modulation in an electro-optic crystal.

Table 3.1 – A comparison of the properties of electro-optic crystals.

	Stoichiometric Lithium Tantalate	Stoichiometric Lithium Niobate	Congruent Lithium Tantalate	Congruent Lithium Niobate
r_{33} [pm/Volt] ³ @ $\lambda = 0.6328 \mu\text{m}$	30.5 [18]	~29.5 [19]	30.0 [20]	~31.5 [19]
n_e @ $\lambda = 1.064 \mu\text{m}$	2.1336 [21]	2.1435 [22] ⁴	2.1377 [21]	2.1556 [23]
$n_e^3 r_{33}$ [pm/Volt]	296.25	295.52	293.04	315.52

It is clear from the calculation of $n_e^3 \cdot r_{33}$ for each material, that only marginal steering improvements can be achieved by selecting one material over another.

³ The wavelength dependence of r_{33} is complicated, and data is generally unavailable at $\lambda = 1.064 \mu\text{m}$. Typically, Miller's rule is used to estimate the dispersion in r_{33} , however an exact value requires a measurement at $\lambda = 1.064 \mu\text{m}$. Furthermore, measurements of this value may vary based on the type of measurement technique used (interferometry [19] or deflection calibration [18]), the type of electrode used [20], and the mechanical means of securing the material [24]. It is not surprising that literature values for these coefficients vary somewhat. Thus, it is common to say that the electro-optic coefficient is nominally $r_{33} = 30.8 \text{ pm/Volt}$ [24]. This value will be assumed for all following calculations involving 5%MgO:CLN. Fortunately, as will be seen in Equation (3.10), the effect of deviations from the nominal r_{33} value on Δn can be easily compensated for by increasing the applied voltage (see Equation (3.10))

⁴ This value is actually measured for 1 mol% Mg-doped SLN. Nakamura *et al.* [25] showed that the extraordinary refractive index n_e of SLN is unaffected by MgO doping levels < 4.6 mol%.

Consequently, other experimental factors dominated the choice of EO crystal used to fabricate the EOBS.

Crystals were purchased through *AdvR Inc.* [V1] of Bozeman, Montana. Dr. Phillip Battle of *AdvR Inc.* recommended the use of 5 mol% magnesium oxide doped congruent lithium niobate (5%MgO:CLN) due to its resilience against photo-refractive damage (PRD) [26]. The added protection against PRD afforded by the magnesium-oxide doping eliminates the need to operate the EOBS at elevated temperatures (~100°C) in order to thermally anneal away PRD. Thus, this choice allows the EOBS to be operated without external heating, simplifying the experiment. Thus, the EOBS was designed to be fabricated in 5%MgO:CLN.

The extraordinary index of refraction of 5%MgO:CLN [22] is given by:

$$n_e^2(\lambda, T) = a_1 + b_1 f + \frac{a_2 + b_2 f}{\lambda^2 - (a_3 + b_3 f)^2} + \frac{a_4 + b_4 f}{\lambda^2 - a_5^2} - a_6 \lambda^2 \quad (3.1)$$

where, $f = (T - 24.5)(T + 570.82)$. Note that the index of refraction of 5%MgO:CLN is both wavelength and temperature dependent. The Sellmeier coefficients for Equation (3.1) are shown in Table 3.2.

Table 3.2 – The Sellmeier coefficients of 5%MgO:CLN.

$a_1 = 5.756$
$a_2 = 0.0983$
$a_3 = 0.2020$
$a_4 = 189.32$
$a_5 = 12.52$
$a_6 = 0.0132$
$b_1 = 2.860 \times 10^{-6}$
$b_2 = 4.700 \times 10^{-8}$
$b_3 = 6.113 \times 10^{-8}$
$b_4 = 1.516 \times 10^{-4}$

Figure 3.1 shows a plot [M1] of the extraordinary index as a function of wavelength. Note that 5%MgO:CLN is highly dispersive in the visible and NIR wavebands.

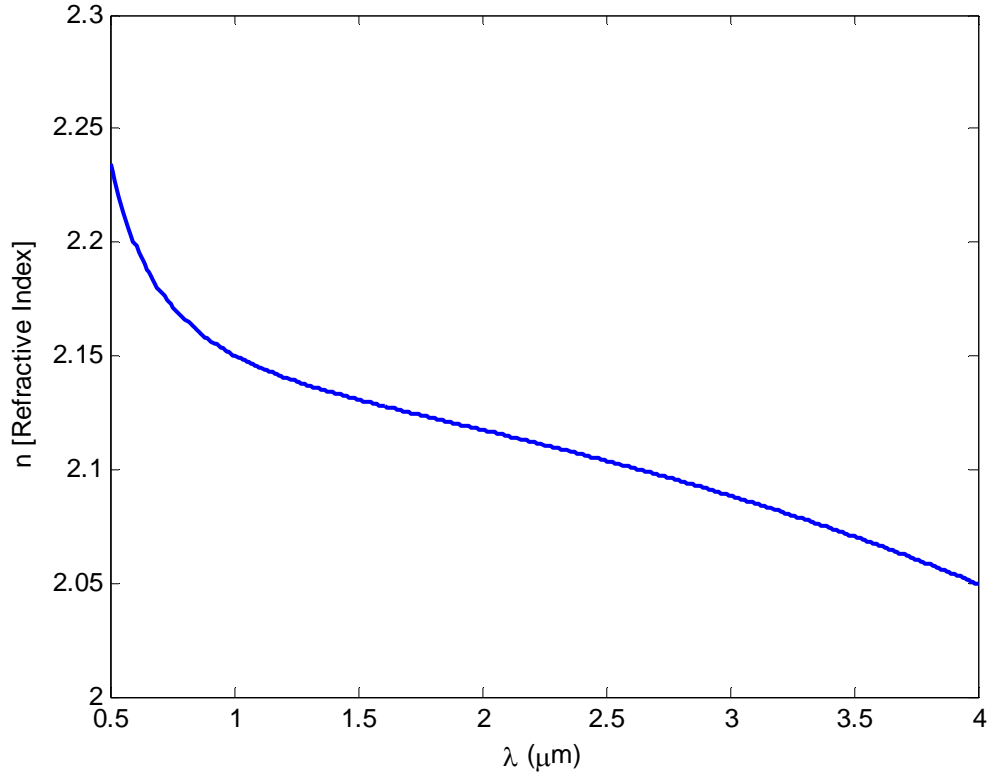


Figure 3.1 – The refractive index of 5%MgO:CLN.

Thus:

$$n_e(1.064 \mu\text{m}, 20^\circ\text{C}) = 2.1468 \quad (3.2)$$

3.1.2 Electro-Optic Modulation in CLN

The refractive index of 5%MgO:CLN transforms according to the manner shown in Section 2.1.1. Consider, that CLN is of crystal class 3m (trigonal symmetry), and has an electro-optical tensor [27 p. 308]:

$$\vec{r}_{ij} = \begin{bmatrix} 0 & -r_{22} & r_{13} \\ 0 & r_{22} & r_{13} \\ 0 & 0 & r_{33} \\ 0 & r_{51} & 0 \\ r_{51} & 0 & 0 \\ -r_{22} & 0 & 0 \end{bmatrix} \quad (3.3)$$

Consider the case of 5%MgO:CLN with a field \vec{E} applied along the z-axis.

$$\Delta \vec{B} = \begin{bmatrix} 0 & -r_{22} & r_{13} \\ 0 & r_{22} & r_{13} \\ 0 & 0 & r_{33} \\ 0 & r_{51} & 0 \\ r_{51} & 0 & 0 \\ -r_{22} & 0 & 0 \end{bmatrix} \begin{bmatrix} 0 \\ 0 \\ E_z \end{bmatrix} = \begin{bmatrix} E_z r_{13} \\ E_z r_{13} \\ E_z r_{33} \\ 0 \\ 0 \\ 0 \end{bmatrix} \quad (3.4)$$

Or, in standard index form:

$$\Delta \vec{B} = \begin{bmatrix} E_z r_{13} & 0 & 0 \\ 0 & E_z r_{13} & 0 \\ 0 & 0 & E_z r_{33} \end{bmatrix} \quad (3.5)$$

So,

$$\begin{aligned} \vec{B}' &= \vec{B} + \Delta \vec{B} = \begin{bmatrix} \frac{1}{n_x^2} & 0 & 0 \\ 0 & \frac{1}{n_y^2} & 0 \\ 0 & 0 & \frac{1}{n_z^2} \end{bmatrix} + \begin{bmatrix} E_z r_{13} & 0 & 0 \\ 0 & E_z r_{13} & 0 \\ 0 & 0 & E_z r_{33} \end{bmatrix} \\ &= \begin{bmatrix} \frac{1}{n_x^2} + E_z r_{13} & 0 & 0 \\ 0 & \frac{1}{n_y^2} + E_z r_{13} & 0 \\ 0 & 0 & \frac{1}{n_z^2} + E_z r_{33} \end{bmatrix} \end{aligned} \quad (3.6)$$

Thus, it is seen that the effect is to change the magnitudes of the principal refractive indices without changing the orientation of the principal axes. So, for the z-axis index:

$$\begin{aligned} \frac{1}{n_z'^2} &= \frac{1}{n_z^2} + E_z r_{33} \\ \therefore n_z &= n_z' \cdot (1 + n_z^2 \cdot E_z r_{33})^{\frac{1}{2}} \end{aligned} \quad (3.7)$$

Assuming that r_{33} is small, and applying the binomial approximation:

$$\begin{aligned} n_z &\approx n_z' \cdot \left(1 + \frac{n_z^2 \cdot E_z r_{33}}{2} \right) \\ \therefore n_z' &\approx n_z - \frac{n_z' n_z^2 E_z r_{33}}{2} \end{aligned} \quad (3.8)$$

Assuming that $n_z \approx n'_z$:

$$\begin{aligned} n'_z &\approx n_z - \frac{n_z^3 E_z r_{33}}{2} \\ \therefore \Delta n_z &= n'_z - n_z \approx -\frac{n_z^3 E_z r_{33}}{2} \end{aligned} \quad (3.9)$$

So, under the influence of a voltage $V_{applied}$ applied across a crystal of thickness Z , the index of refraction becomes:

$$n'_e(\lambda, V, T, r_{33}) = n_e(\lambda, T) - \frac{1}{2} r_{33} n_e^3(\lambda, T) \cdot \frac{V}{Z} \quad (3.10)$$

3.1.3 Quasi-Phasematching in 5%MgO:CLN

Substituting Equation (3.1) into Equation (2.56) gives the expression for Δk in 5%MgO:CLN. This expression relates the optimal period for the first order OPG interaction and the wavelength output of the OPG process. The expression is cumbersome, and does not provide analytical insight. The plot [M2] of this expression (Figure 3.2) is sufficient to understand the role of grating period on the output of the OPG process.

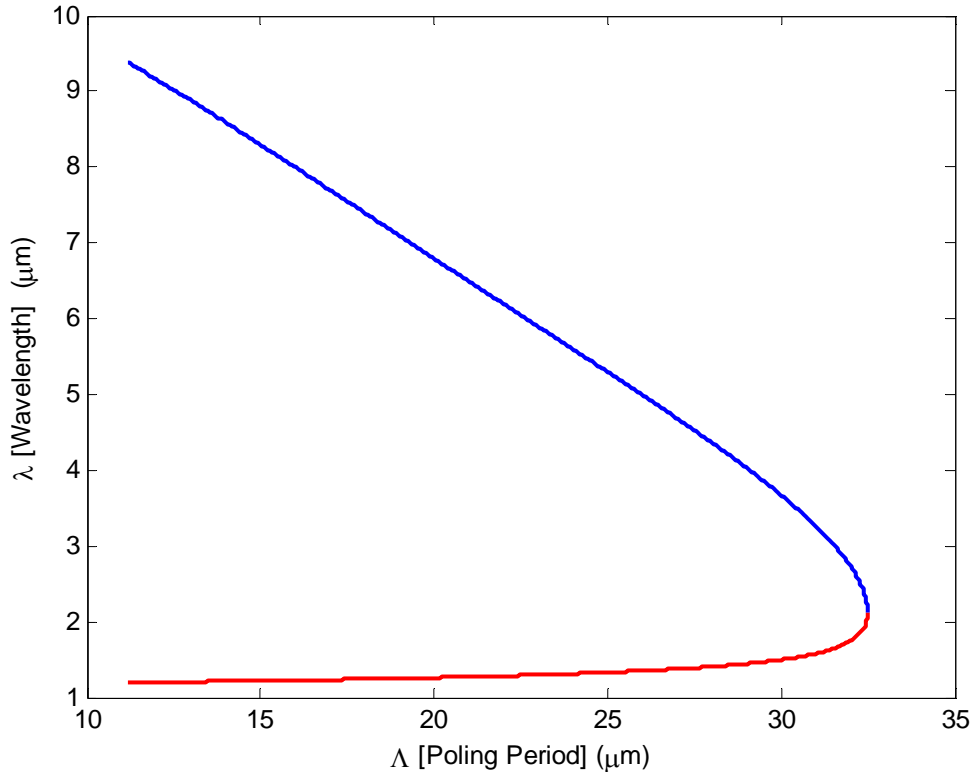


Figure 3.2 – Quasi-phasematched OPG output for a $\lambda_1 = 1.064 \mu m$ pump beam as a function of grating period Λ (λ_2 :Red, λ_3 :Blue).

Recall that the EOBS was designed to facilitate wavelength selection by switching a pump beam between two OPG gratings. The grating periods were chosen, based on this graph, to be $\Lambda_1 = 29.0 \mu m$ and $\Lambda_2 = 31.0 \mu m$. Thus it can be predicted from Figure 3.2 that for the $\lambda_1 = 1.064 \mu m$ pump:

$$\begin{aligned}\Lambda_1 = 29.0 \mu m &\rightarrow \lambda_2 = 1.444 \mu m \text{ \& } \lambda_3 = 3.273 \mu m \\ \Lambda_2 = 31.0 \mu m &\rightarrow \lambda_2 = 1.577 \mu m \text{ \& } \lambda_3 = 4.040 \mu m\end{aligned}$$

3.2 Geometric Considerations

3.2.1 Crystal Domain Geometry Optimization

Recall from *Section 1.1* that the EOBS is intended to translate an incident beam with no overall angular deflection. Also recall from *Section 3.1.2* that the electro-optic effect is weak, and will only result in fourth decimal place changes in the refractive index of the 5%MgO:CLN crystal. Thus, the angular deflections imparted by each prism will be very small. Thus, it is not a trivial task to design a series of prisms that will impart appreciable translation to the incident beam. Consequently, the geometry of prisms must be analyzed in terms of the geometry of the incident beam and optimized to maximally deflect it. Multiple geometries were designed so that beams of different quality and size could be accommodated. Five of these steering ‘channels’, as well as two OPG gratings, were fabricated in parallel on a single 5%MgO:CLN wafer. Thus, a five channel EOBS chip and a two grating wavelength conversion chip were fabricated from each wafer.

Each steering channel is divided into two stages. In order to accomplish beam translation with no overall angular deflection, each prism in the first stage is paired with a prism in the second stage which undoes the deflection imparted by its partner. This concept is illustrated in Figure 3.3.

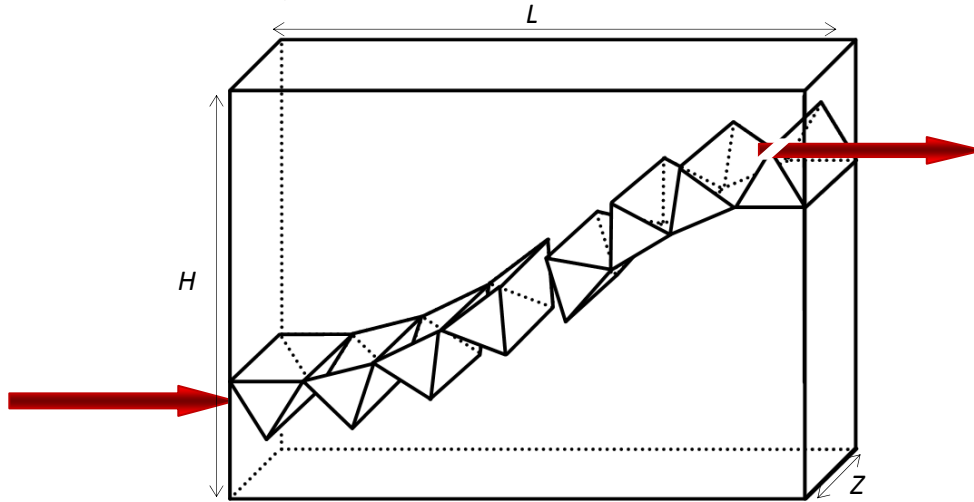


Figure 3.3 – An electro-optic beam switch in the ON state.

Each stage of an EOBS channel was modeled as a series of cascaded unit cells. Figure 3.4 shows the unit cell geometry used to represent each beam steering prism.

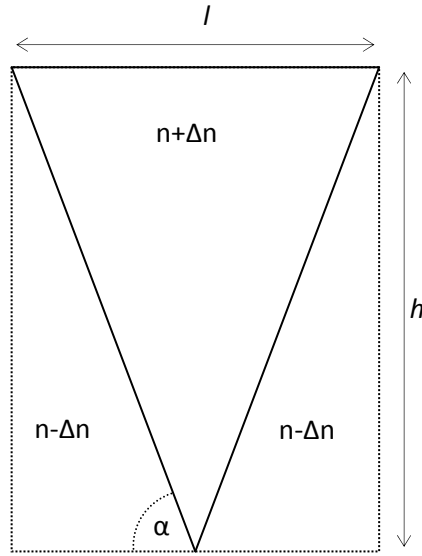


Figure 3.4 – The unit cell representation a beam steering prism.

Figure 3.5 shows a ray tracing of an incident beam propagating through such a cell. It can be clearly seen that each cell imparts a translation Y and angular deflection β to the input ray.

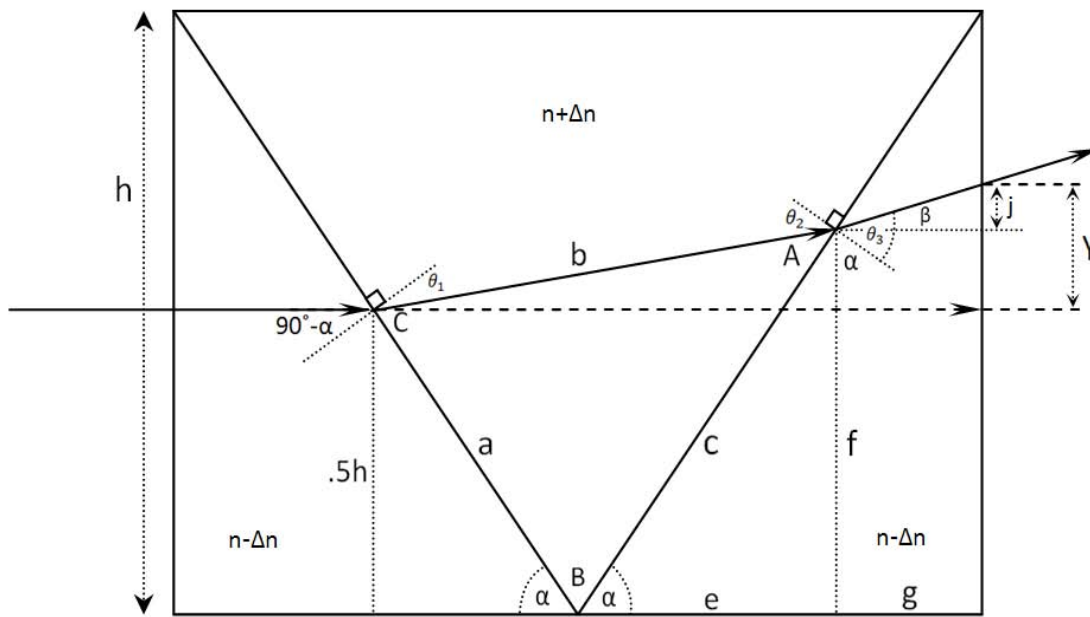


Figure 3.5 – A geometric ray tracing of an incident beam.

Unit cells of this type can be cascaded to form larger deflection structures. Two such cells are shown in Figure 3.6.

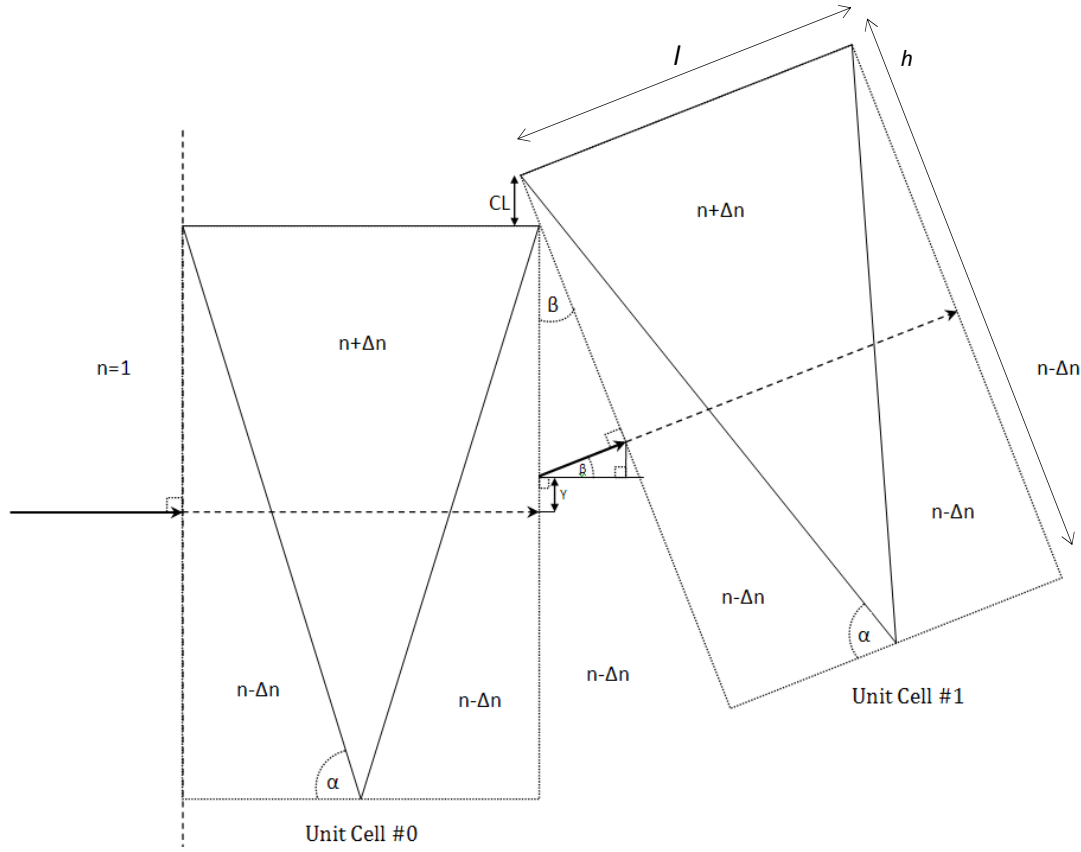


Figure 3.6 – Two cascaded unit cells.

Each successive unit cell is rotated by an angle β so that the output ray of the previous cell is normally incident upon the following cell. Each unit cell is also raised by a compensation distance CL in order that the incident beam will be centered with respect to the front face of each unit cell.

Recall that the electro-optic coefficient r_{33} is generally small ($\sim \text{pm/V}$) and thus, Δn is also small. Consequently, the angular deflection imparted by each prism, and thus the overall translation imparted by the entire channel, is also small. However, the angular deflection imparted to the beam can be enhanced by applying a large electric field across the EOBS chip. However, the control voltage may not be arbitrarily large. If the applied voltage induces an electric field across the wafer which exceeds the coercive field of the crystal, it will begin to pole, irreversibly damaging it. Thus, the control voltage constituting the ‘ON State’ was constrained to be $V_{\text{applied}} = \pm 1 \text{ [kV]}$. The coercive field of 5%MgO:CLN is $\sim 6.8 \text{ kV/mm}$ [28], which, for a $Z = 0.5 \text{ mm}$ wafer, corresponds to a poling voltage of:

$$V_{\text{poling}} = E_c Z = 6.8 \left[\frac{\text{kV}}{\text{mm}} \right] \cdot 0.5 \text{ mm} = 3.4 \text{ kV} \quad (3.11)$$

Thus it is not likely that the EOBS will be damaged at $V_{\text{applied}} = \pm 1 \text{ [kV]}$.

Now, recall Equation (3.2):

$$n_e(1.064 \mu m, 20^\circ C) = 2.1468$$

Thus, for a $Z = 0.5 \text{ mm}$ wafer:

$$\Delta n = -\frac{1}{2} r_{33} n_e^3 \frac{V}{Z} = -\frac{1}{2} 30.8 \times 10^{-12} \cdot 2.1468^3 \frac{-1000}{5 \times 10^{-4}} = 3.0475 \times 10^{-4} \quad (3.12)$$

and:

$$n_{prism} = n_e(1.064 \mu m, 20^\circ C) + \Delta n_e = 2.14714 \quad (3.13)$$

$$n_{background} = n_e(1.064 \mu m, 20^\circ C) - \Delta n_e = 2.14654 \quad (3.14)$$

From analysis of Figure 3.5, a symbolic expression for the angular deflection β , and the translation Y , can be derived as functions of α, n, Δ , and h by applying Snell's Law at each dielectric interface and combining equations.

From Snell's law at first interface:

$$\theta_1 = \sin^{-1} \left(\frac{n - \Delta n}{n + \Delta n} \sin(90^\circ - \alpha) \right) \quad (3.15)$$

Geometrically:

$$\theta_2 = 90^\circ - (180^\circ - (90^\circ - \theta_1) - (180^\circ - 2\alpha)) = 180^\circ - \theta_1 - 2\alpha \quad (3.16)$$

From Snell's law at second interface:

$$\theta_3 = \sin^{-1} \left(\frac{n + \Delta n}{n - \Delta n} \sin(\theta_2) \right) \quad (3.17)$$

Thus, from Figure 3.5:

$$\beta = \theta_3 + \alpha - 90^\circ \quad (3.18)$$

$$Y = g \cdot \tan \beta + f - .5h \quad (3.19)$$

where,

$$a = 0.5h \cdot \csc(\alpha) \quad (3.20)$$

$$B = 180^\circ - 2\alpha \quad (3.21)$$

$$C = 90^\circ - \theta_1 \quad (3.22)$$

$$A = 180^\circ - B - C \quad (3.23)$$

$$c = \frac{\sin C}{\sin A} \quad (3.24)$$

$$e = c \cdot \cos \alpha \quad (3.25)$$

$$f = c \cdot \sin \alpha \quad (3.26)$$

$$g = h \cdot \cot \alpha - e \quad (3.27)$$

$$j = g \cdot \tan \beta \quad (3.28)$$

From Figure 3.6:

$$CL = [.5h - (.5h - Y) \cos(\beta)] \cdot \cos(\beta) \quad (3.29)$$

In order to constrain the equations governing the performance of the device to two free variables, it is necessary to parameterize h in terms of other variables. The steered beam will diffract as it propagates, and it is crucial that the beam not intersect the top and bottom faces of the unit cell. Choosing an adequate height for the unit cell will ensure that the beam does not overfill the steering prisms.

Given the fact that the maximum deflection angle of prism-type electro-optic deflectors are typically small, it is reasonable to assume that the EOBS will impart, at most, ~1 mm of overall translation to the steered beam (the results of this computation as shown in Figure 3.11 shows that this assumption is reasonable). So, the effective propagation distance is:

$$L_{eff} = \frac{L + 1000}{n} [\mu m] \quad (3.30)$$

Allowing a factor of $\sqrt{2}$ (or roughly 41%) margin of error on the exit face of the final unit cell of the channel, and assuming the beam waist of the laser will be located at the center of the channel, the height of the cell is then:

$$h = 2\sqrt{2}w(z) = 2\sqrt{2}w_0 \sqrt{1 + \left(\frac{M^2(L + 1000)\lambda}{2w_0^2\pi n} \right)^2} \quad (3.31)$$

The length of the unit cell is then:

$$l = 2 \cdot h \cdot \cot(\alpha) = 4\sqrt{2}w_0 \sqrt{1 + \left(\frac{M^2(L + 1000)\lambda}{2w_0^2\pi n} \right)^2} \cot(\alpha) \quad (3.32)$$

Thus, the maximum number of unit cells of length l which can fit into length L is⁵:

$$Num \approx \left\lfloor \frac{L}{l} \right\rfloor = \left\lfloor \frac{L}{4\sqrt{2}w_0 \sqrt{1 + \left(\frac{M^2(d + 1000)\lambda}{2w_0^2\pi n} \right)^2} \cot(\alpha)} \right\rfloor \quad (3.33)$$

Iff: $\beta \ll 90^\circ - \alpha$

As M^2 increases, fewer cells can fit into the steering channel. As a result, the maximum translation distance of the channel decreases. Thus, it is desirable that the steered laser have high beam quality. Two Nd:YAG lasers were available for this

⁵ Note here that $\lfloor x \rfloor = \text{floor}(x)$.

experiment; each was quoted to have “near-Gaussian” beam quality. The first, a *Teem Photonics Nanopulse* microchip laser [V2], was measured to have a beam quality of $M^2 = 1.76$. The second, a *Spectra-Physics T-series* DPSS laser [V3], was measured to have a beam quality of $M^2 = 1.305$. Consequently, most EOBS channels were designed under the assumption that $M^2 = 1.76$. Thus, the EOBS design should tolerate changes in beam quality in the range: $1 < M^2 < 1.76$. Individual channel specifications are addressed in great detail in *Section 3.3.1*.

The two stage EOBS channel must contain an even number of unit cells. Thus the maximum number of unit cells comprising a channel is⁶:

$$K = \frac{Num - Num \setminus 2}{2} \quad (3.34)$$

Figure 3.7 shows a diagram of a pure translation channel.

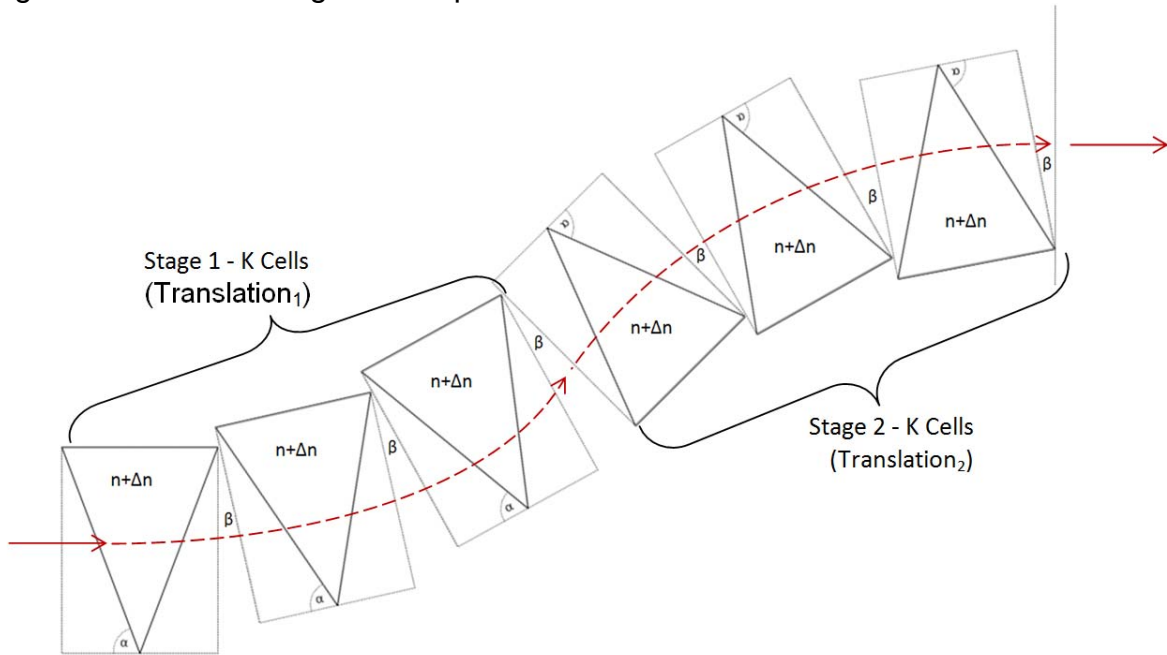


Figure 3.7 – A two-stage translation channel of 2K unit cells.

⁶ Note here that $x \setminus 2$ denotes modulo-2 division of x .

Consider translation of a beam through the N^{th} unit cell of Stage 1 (Figure 3.8):

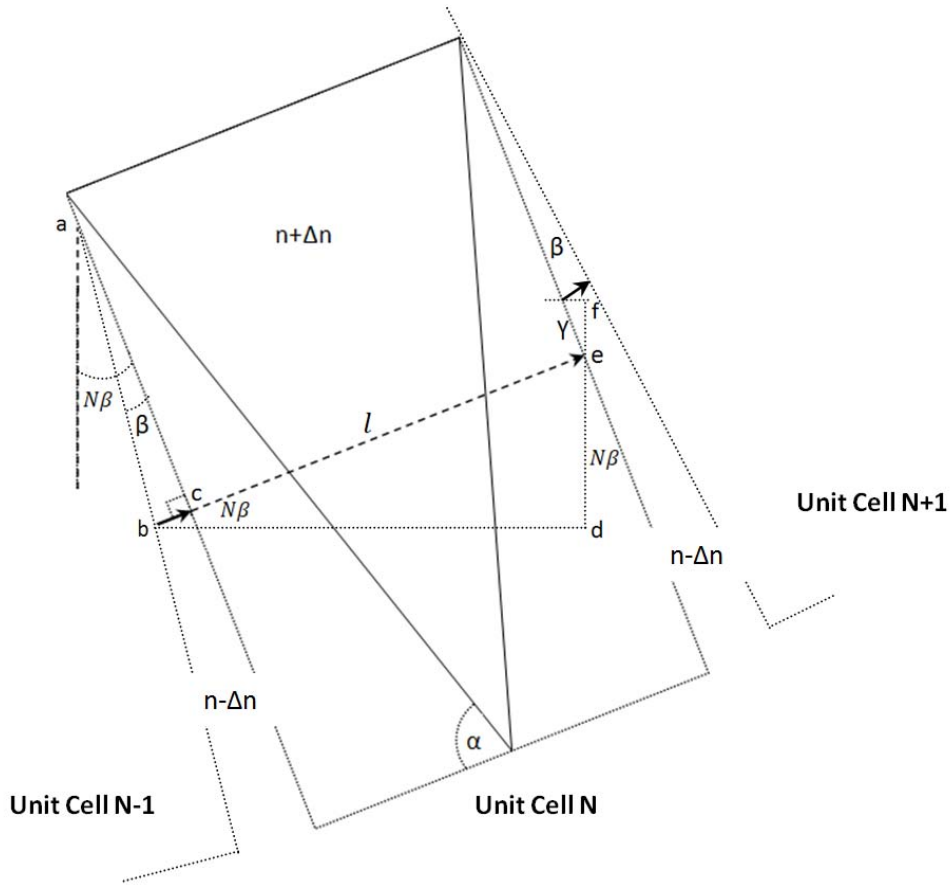


Figure 3.8 – The geometry of the N^{th} unit cell of Stage 1.

From Figure 3.8:

$$\overline{ab} = .5h - Y \quad (3.35)$$

$$\overline{bc} = \overline{ab} \cdot \sin(\beta) \quad (3.36)$$

$$\overline{be} = \overline{bc} + l \quad (3.37)$$

$$\overline{de} = \overline{be} \cdot \sin(N\beta) \quad (3.38)$$

$$\overline{ef} = Y \cdot \cos(N\beta) \quad (3.39)$$

Combining the above equations the translation of the beam due to propagation from the rear face of a particular unit cell to the rear face of the next unit cell is:

$$\begin{aligned} \text{Translation} &= \overline{de} + \overline{ef} \\ &= Y \cdot \cos(N\beta) + (l + (.5h - Y) \cdot \sin(\beta)) \cdot \sin(N\beta) \end{aligned} \quad (3.40)$$

Consider translation of a beam through the N^{th} unit cell of Stage 2 (Figure 3.9):

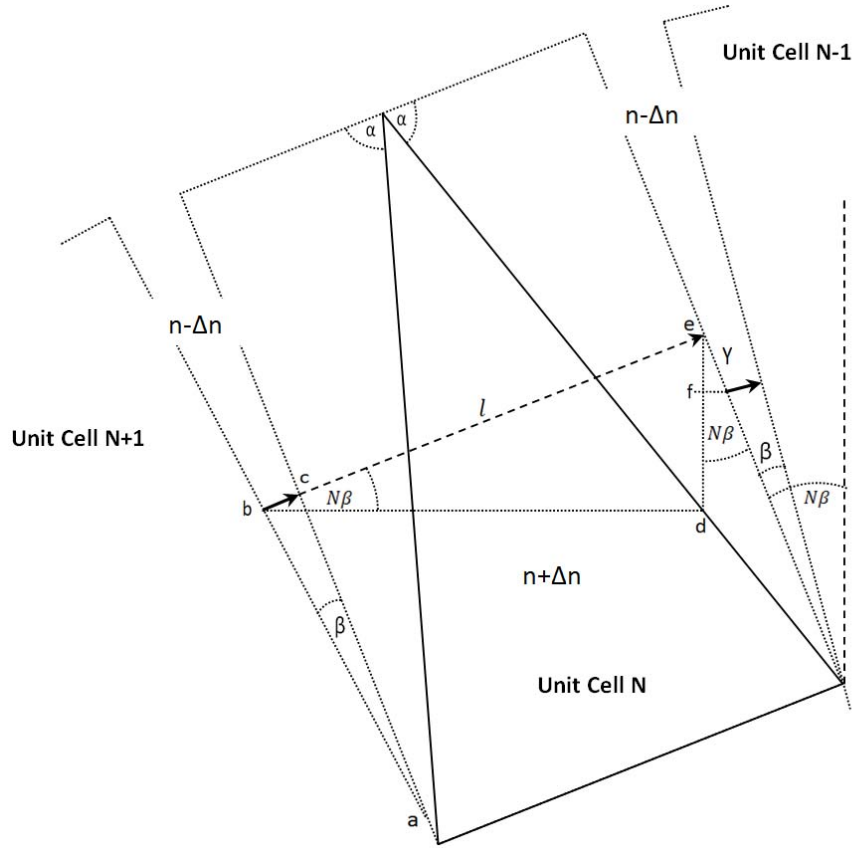


Figure 3.9 – The geometry of the N^{th} unit cell of Stage 2.

From Figure 3.9:

$$\overline{ab} = .5h - Y \quad (3.41)$$

$$\overline{bc} = \overline{ab} \cdot \sin(\beta) \quad (3.42)$$

$$\overline{be} = \overline{bc} + l \quad (3.43)$$

$$\overline{de} = \overline{be} \cdot \sin(N\beta) \quad (3.44)$$

$$\overline{ef} = Y \cdot \cos(N\beta) \quad (3.45)$$

Combining the above equations the translation of the beam due to propagation from the rear face of a particular unit cell to the rear face of the next unit cell is:

$$\begin{aligned} \text{Translation} &= \overline{de} - \overline{ef} \\ &= -Y \cdot \cos(N\beta) + (l + (.5h - Y) \cdot \sin(\beta)) \cdot \sin(N\beta) \end{aligned} \quad (3.46)$$

From Figure 3.7, it can be seen that the K^{th} unit cell of Stage 2 is uniquely positioned, creating adjacent angles which are opposite in sense. Thus, the translation of a beam through this ‘transition’ cell is considered here.

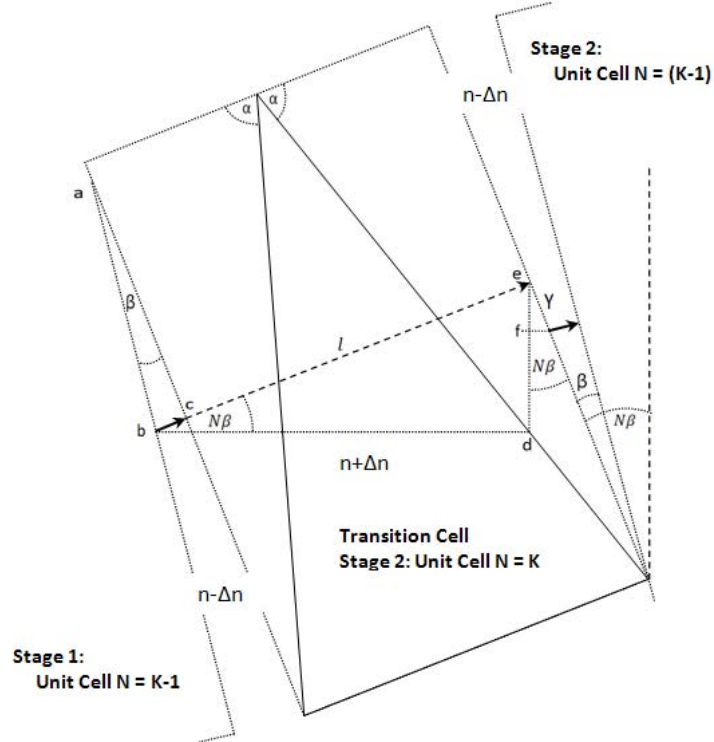


Figure 3.10 – The geometry of the transition cell.

From Figure 3.10:

$$\overline{ab} = .5h - Y \quad (3.47)$$

$$\overline{bc} = \overline{ab} \cdot \sin(\beta) \quad (3.48)$$

$$\overline{be} = \overline{bc} + l \quad (3.49)$$

$$\overline{de} = \overline{be} \cdot \sin(N\beta) \quad (3.50)$$

$$\overline{ef} = Y \cdot \cos(N\beta) \quad (3.51)$$

Combining the above equations the translation of the beam due to propagation from the rear face of a particular unit cell to the rear face of the next unit cell is:

$$\begin{aligned} \text{Translation} &= \overline{de} - \overline{ef} \\ &= -Y \cdot \cos(N\beta) + (l + (.5h - Y) \cdot \sin(\beta)) \cdot \sin(N\beta) \end{aligned} \quad (3.52)$$

Note that this is the same expression for the translation in all other Stage 2 cells. Thus, the overall translation can be calculated by:

$$\begin{aligned} \text{Translation}_{\text{total}} &= \text{Translation}_1 + \text{Translation}_2 \\ &= \sum_{N=0}^{K-1} [Y \cdot \cos(N\beta) + (length + (.5 \cdot height - Y) \cdot \sin(\beta)) \cdot \sin(N\beta)] \\ &\quad + \sum_{N=1}^K [-Y \cdot \cos(N\beta) + (length + (.5 \cdot height - Y) \cdot \sin(\beta)) \cdot \sin(N\beta)] \end{aligned} \quad (3.53)$$

$Translation_{total}$ can be maximized by allowing the steering channel to be as long as is possible. The largest 5%MgO:CLN wafers available for poling were 3" in diameter, and a 5 mm margin for wafer handling had to be left around the edge of the circular wafer. Thus the maximum channel length was $L \approx 66 \text{ mm}$.

By substituting Equations (3.30) and (3.31) into Equation (3.53), $Translation_{total}$ becomes an expression with only two free variables: α & D_0 . Analytically, this expression is intractably complicated, but can be constructed numerically without difficulty in MATLAB [V4, M3]. Figure 3.11 shows the field of solutions to this expression. Note that this field of solutions is generated by allowing the unit cell height h to change to barely accommodate the steered beam by the ~40% margin previously discussed [p. 42]. Also note that while the each channel is optimized for a specific laser; each will, in principle, accommodate any laser beam which fits within the input aperture of the channel and does not diffract too quickly.

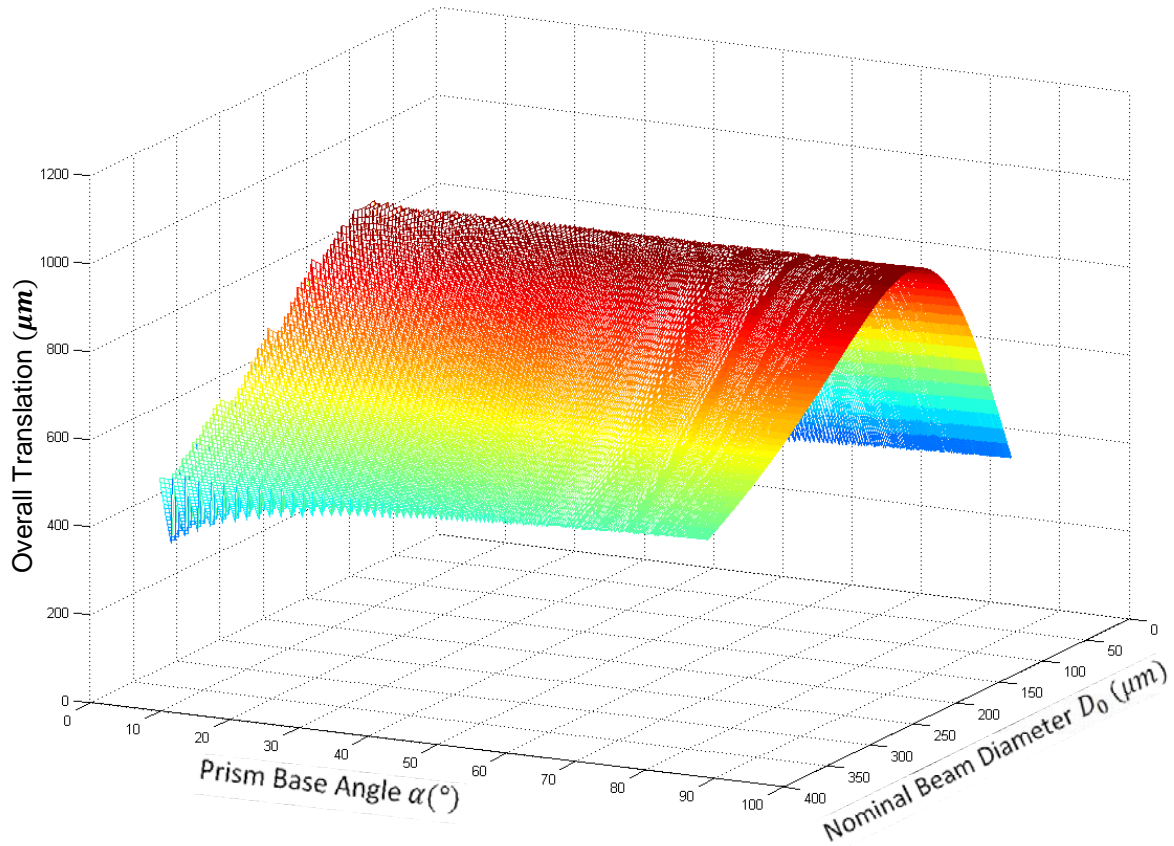


Figure 3.11 – Solutions of Equation (3.43) for overall translation of the steered beam.

It is interesting to note that the behavior of the device is independent of α , especially at large values of α . However, this is not particularly surprising; it is well established that prism-type deflectors are equivalent to the gradient-type deflectors of the same length [4,9]. It is instructive to consider the reason this behavior is expected. Figure 3.12 (left) shows a single prism with a length of L . Figure 3.12 (Right) shows two prisms whose combined lengths are equal to L . It will not be proven in this discussion,

but it can be seen from Snell's Law that these structures are equivalent as beam deflectors.

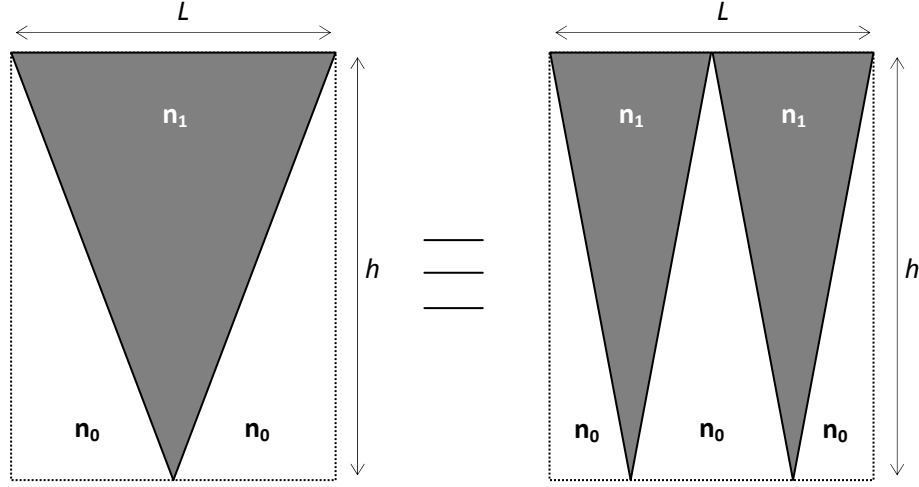


Figure 3.12 – (Left) A single prism with length L . (Right) Two prisms with length L .

The equivalence holds for any integer number N of prisms whose combined length is L . Thus a 'gradient-type' beam deflector can be thought of as the limiting case as $N \rightarrow \infty$. Figure 3.13 shows the concept of an arbitrarily large number of prisms within space L forming a gradient-type beam deflector which is equivalent to the deflectors in Figure 3.12.

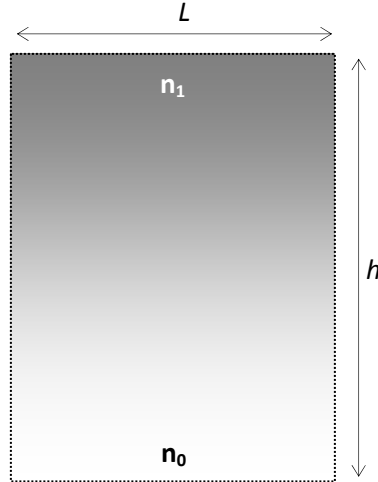


Figure 3.13 – An illustration of a typical gradient-type beam deflector.

Similarly, for the EOBS, as $\alpha \rightarrow \frac{\pi}{2}$ the overall steering effect approaches a limiting value. This behavior is more clearly seen by observing the overall translation at a specific value of D . Figure 3.14 shows the overall translation as a function of α for $D_0 = 160 \mu m$.

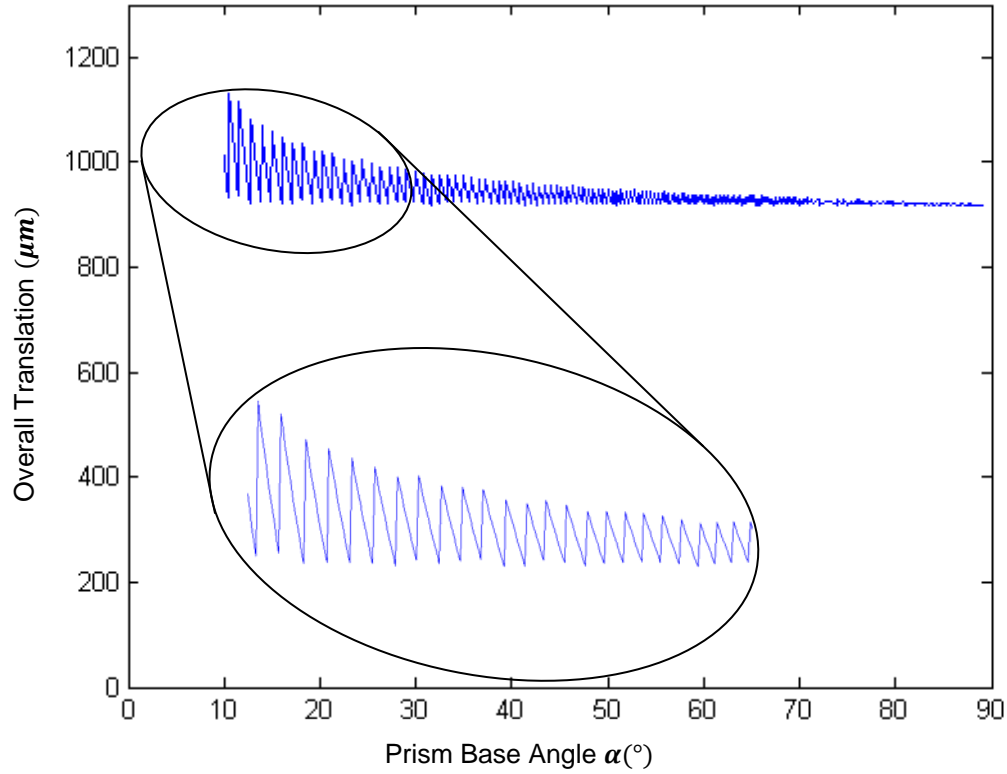


Figure 3.14 – The overall translation as a function of α for $D_0 = 160 \mu m$.

Note that in Figure 3.14, the overall translation experiences discrete jumps for small values of α . These jumps occur where α becomes just large enough to permit another pair of cells to fit within the steering channel. The downward sloping segments represent solutions for which the number of cells remains constant. Note that, as a consequence of Snell's Law, increasing the value of α for a given number of cells decreases the steering performance of the EOBS.

From Figure 3.11, there is clearly an optimal beam waist for which to design an EOBS channel. Figure 3.15 shows that for nearly all values of α , the most optimal beam diameter for which to design is $D_0 = 160 \mu m$.

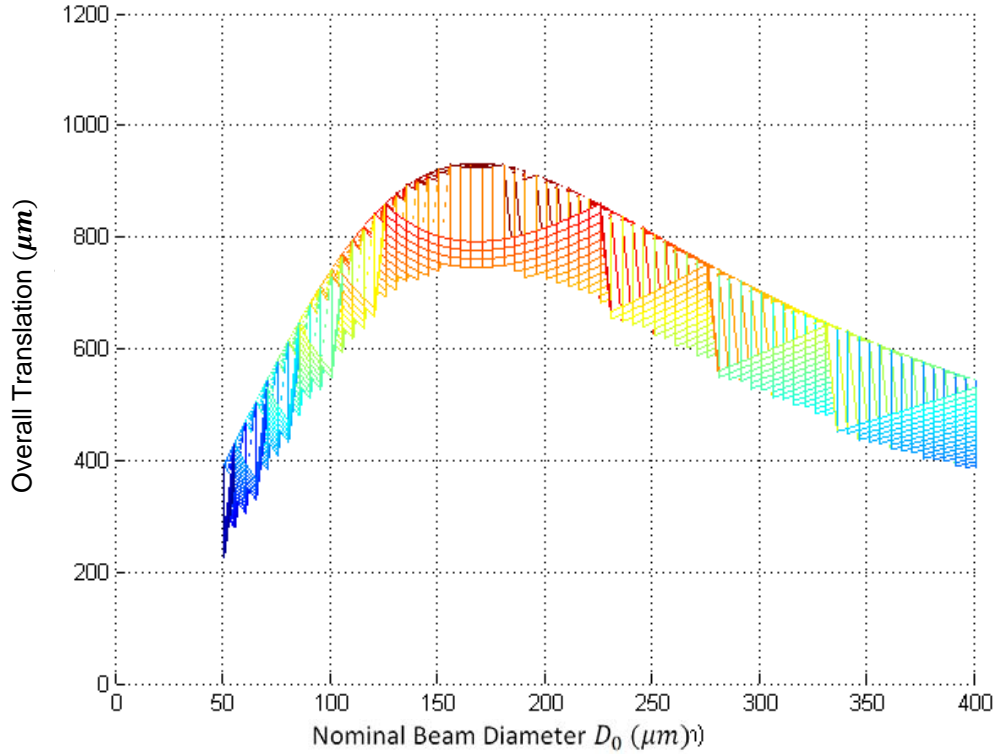


Figure 3.15 – The field of solutions shown only as a function of α .

At $D_0 = 160 \mu m$, the number of cells (all with a common α) which can fit into a channel of finite length is maximized.⁷ If the EOBS were designed for $D_0 > 160 \mu m$, the number of cells in a beam steering channel would decrease due to the overall width of the beam (despite its relative collimation). If the EOBS were designed for $D_0 < 160 \mu m$, the number of cells in a beam steering channel would decrease due to increase beam diffraction.

For the sake of experimental flexibility, five solutions to Equation (3.53) were fabricated as five separate channels on the EOBS chip. This flexibility allows the fabrication of channels that are not truly optimal, but which will be more tolerant of variations in beam waist. Thus, it was not necessary to meticulously adjust the focusing characteristics of the beam such that D_0 be equal to $160 \mu m$. Section 3.3.1 will show the design specifications for these channels in greater detail.

MATLAB was used to record the design details corresponding to the most optimal solutions of Equation (3.53) as well as solutions of particular interest to the author [M3]. Solutions were calculated for input variables α & D , with domains $10^\circ \leq \alpha \leq 89.9^\circ$ (0.1° resolution) and $50 \mu m \leq D < 400 \mu m$ ($10 \mu m$ resolution).

Dr. Battle of AdvR Inc. recommended that the poled features be design to have domain edges which accommodate the natural tendency of CLN to form hexagonal domains. Thus, noting that the performance of the EOBS is independent of the value of α , it was specified that $\alpha \approx 30^\circ$. The result of poling along natural domain directions of the crystal should be an increase in the domain fidelity of the poled regions of the

⁷ It should be noted, that this is due to the overall size of the unit cell changing and thus the equivalence principle demonstrated in **Figure 3.12** does not apply.

device. Figure 3.16 shows the cross-section of solutions to Equation (3.53) for $\alpha = 30^\circ$ as a function of D_0 . Clearly, many solutions exist which will yield $Translation_{total} > 700 \mu m$. This amount of steering will be more than sufficient to ensure that beams with beamwaist diameters $150 \mu m < D_0 < 200 \mu m$ will have well-defined output states (the output beamspots do not overlap).

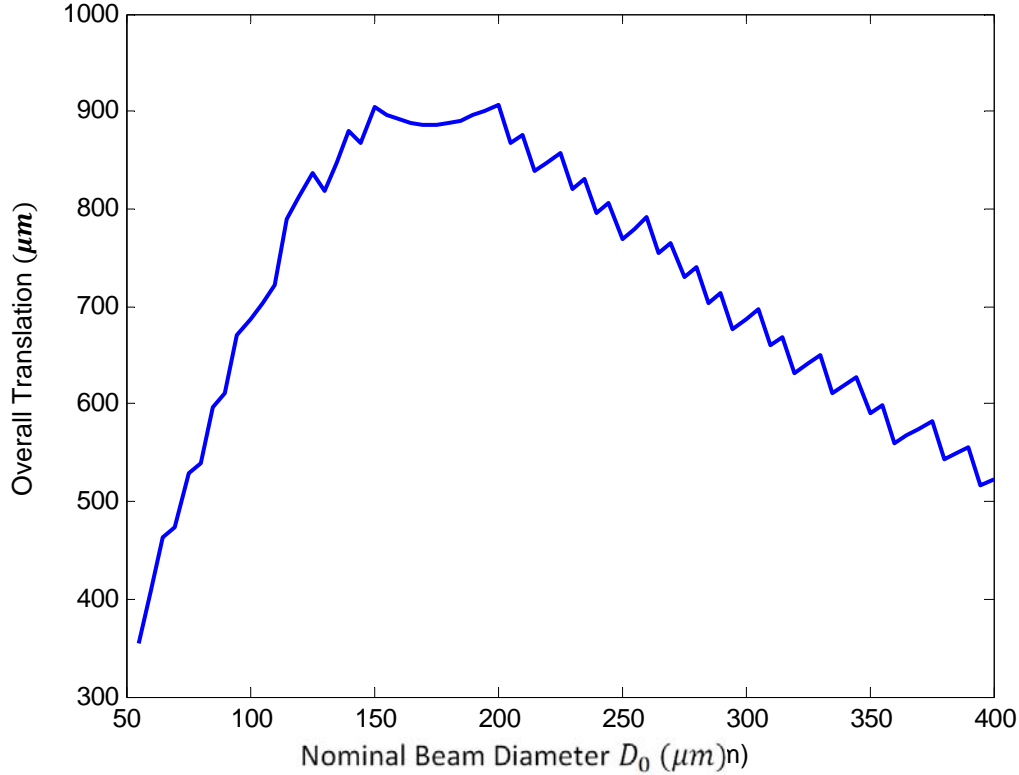


Figure 3.16 – The solutions to Equation (3.53) for $\alpha = 30^\circ$.

3.2.2 Channel Losses

From Figure 3.5, the Fresnel losses due to reflection at the prism interfaces can be calculated:

$$\begin{aligned}
 R_{internal} &= 1 - T_{total}^{Num} = 1 - (T_1 T_2)^{Num} = 1 - [(1 - R_1)(1 - R_2)]^{Num} \\
 &= 1 - \left[\left(1 - \left(\frac{\sin(\theta_1 - (90^\circ - \alpha))}{\sin(\theta_1 + 90^\circ - \alpha)} \right)^2 \right) \left(1 - \left(\frac{\sin(\theta_3 - \theta_2)}{\sin(\theta_3 + \theta_2)} \right)^2 \right) \right]^{Num} \quad (3.54)
 \end{aligned}$$

where Num is the number of unit cells in the device and R and T are the reflection and transmission coefficients at each interface respectively.

Due to the small value of Δn , the internal losses due to Fresnel reflection are negligible. Recall from Equation (3.2) that $n_e(1.064 \mu m, 20^\circ C) = 2.1468$ and, from Equation (3.12), that $\Delta n_e = 3.0475 \times 10^{-4}$. For the transverse electric case, which will have a greater reflection coefficient than the transverse magnetic case, it can be seen that:

From $n_{background} \rightarrow n_{prism}$:

$$R_s(60^\circ) = \left[\frac{n_1 \cos(\theta_1) - n_2 \sqrt{1 - \left(\frac{n_1}{n_2} \sin(\theta_1)\right)^2}}{n_1 \cos(\theta_1) + n_2 \sqrt{1 - \left(\frac{n_1}{n_2} \sin(\theta_1)\right)^2}} \right]^2 = 3.2187 \times 10^{-7} \quad (3.55)$$

From $n_{prism} \rightarrow n_{background}$:

$$R_s(60^\circ) = \left[\frac{n_2 \cos(\theta_1) - n_1 \sqrt{1 - \left(\frac{n_1}{n_2} \sin(\theta_1)\right)^2}}{n_2 \cos(\theta_1) + n_1 \sqrt{1 - \left(\frac{n_1}{n_2} \sin(\theta_1)\right)^2}} \right]^2 = 3.230 \times 10^{-7} \quad (3.56)$$

Thus, even for the case of over 1000 unit cells the predicted internal loss is on the order of $R \approx 1 \times 10^{-4}$. Thus, internal losses were not considered as a factor in the design.

3.3 Final Device Design

3.3.1 Selection of Final Translation Channel Candidates

The EOBS device was designed to consist of five independent translation channels. Each channel was constructed from prisms of slightly different geometries. As mentioned in Section 3.2.1, MATLAB was used to calculate the overall translation for the field of solutions corresponding to input variables α & D , with domains $10^\circ \leq \alpha \leq 89.9^\circ$ and $50 \mu m \leq D \leq 400 \mu m$ [M3].

The twenty-five most optimal prism geometries for which $\alpha = 30.0^\circ$ were recorded. Two of these geometries were selected for fabrication on the EOBS chip. The first (Channel 1), corresponding to a relatively large beam waist $D_0 = 250 \mu m$, was calculated to achieve $775.16 \mu m$ overall translation. The second geometry (Channel 3), corresponding to a slightly smaller beam waist $D_0 = 155 \mu m$, was calculated to achieve $913.52 \mu m$ overall translation.

A third geometry (Channel 4) was selected by the same method as Channels 1 & 3, but a value of $M^2 = 1$ was assumed in order to maximize overall translation. The most optimal choice given that $\alpha = 30^\circ$, was $D_0 = 165 \mu m$. This geometry was calculated to achieve $1044.60 \mu m$ overall translation.

A fourth geometry (Channel 2) was selected from the relaxed constraint that $\alpha > 20^\circ$ (and $M^2 = 1$)⁸. The most optimal geometry satisfying this constraint was found to be $\alpha = 22.9^\circ$, $D_0 = 140 \mu m$. This geometry was calculated to achieve $1071.52 \mu m$ overall translation.

The fifth geometry (Channel 5) was designed as an attempt to integrate an EOBS with OPG in the same channel. Thus, 20 mm of the channel was dedicated to two OPG gratings, the remaining 46 mm were used for an EOBS. The most optimal geometry given $\alpha = 30.0^\circ$ and $M^2 = 1.76$ was $D_0 = 170 \mu m$, which was calculated to achieve $Translation_{Total} = 497.25 \mu m$.

⁸ There was some concern that this channel would not pole well due to the value of $\alpha = 22.9^\circ$ not corresponding to the natural domains of CLN. However, when the device was poled, the quality of the poling of this channel did not seem to be degraded in any way.

Table 3.3 shows the calculated design parameters for each of these channels.

Table 3.3 – The final design parameters of each steering channel.⁹

Channel Number	D (μm)	α ($^\circ$)	Translation (μm)	Number of Cells	h (μm)	l (μm)	CL (μm)	Beta ($^\circ$)
1	250	30	775.16	48	392.57	1359.89	0.67224	0.056695
2	140	22.9	1071.52	48	290.39	1374.89	0.92859	0.077519
3	185	30	913.52	56	339.90	1177.46	0.58206	0.056695
4	165	30	1044.60	64	297.58	1030.86	0.50959	0.056695
5	170	30	497.25	44	299.69	1038.16	0.51320	0.056695

The parameters shown in Table 3.3 were readily used to generate a CAD drawing of the device. *TurboCAD 15 Deluxe* [V5] was used to generate prism shapes and to position and align them according to the design parameters and the algorithm outlined in Section 3.2. Figure 3.17 shows the CAD spec that was used to fabricate the EOBS.

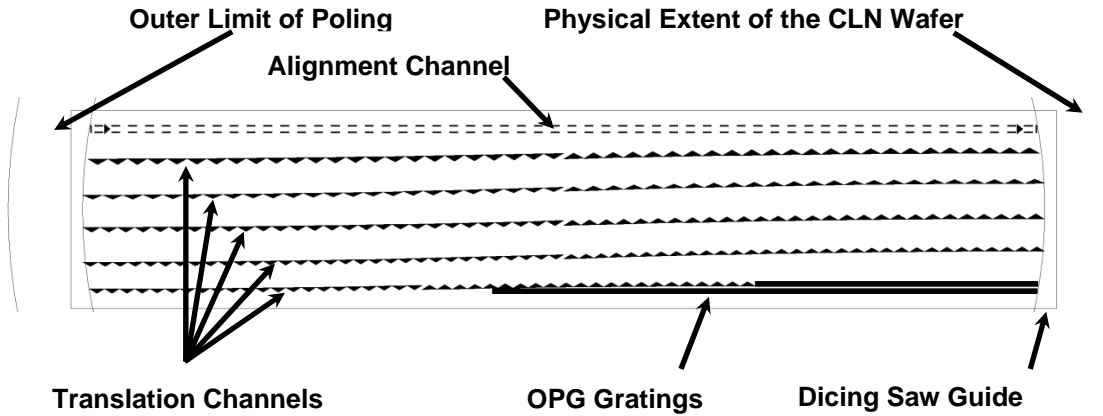


Figure 3.17 – An image of the CAD specification of the EOBS chip.

The cascaded prism structures and the fiducial alignment structures are each centered within a 2.0 mm wide channel. A pair of OPG gratings was also designed as shown in Figure 3.18. The dimensions of the gratings were specified such that any of the steering channels could switch between these gratings.

⁹ After the EOBS chip was fabricated, a small typographical error was noted in the Sellmeier Equation expression programmed in MATLAB. The result of this error was a -0.28% deviation in the value of the refractive index at $\lambda = 1.064 \mu\text{m}$ and $T = 20^\circ\text{C}$. Appendix B offers an argument that this deviation may be compensated for by allowing the control voltage to be $V_{\text{applied}} = -1000 \text{ Volts} \left(\frac{1}{1-0.0028} \right)^2 = -1005.6 \text{ Volts}$.

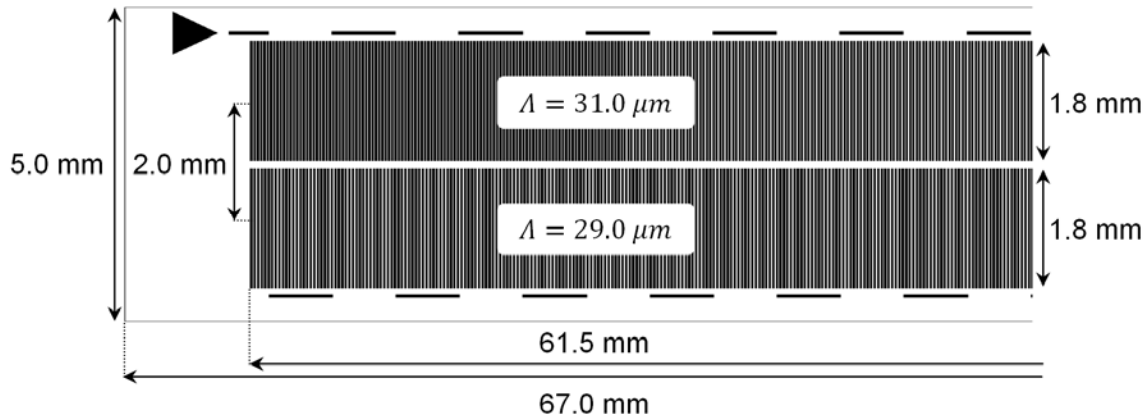


Figure 3.18 – The OPG grating design.

3.4 Fabrication

3.4.1 Fabrication of the EOBS and OPG Gratings

Fabrication began with a bare crystal substrate. The crystal was coated in photoresist and a photomask generated from the CAD spec shown in Figure 3.17 was used to selectively develop the resist. The poling technique illustrated in Section 2.3 was applied. The wafer then contained inverted crystal domains as shown in Figure 3.19.

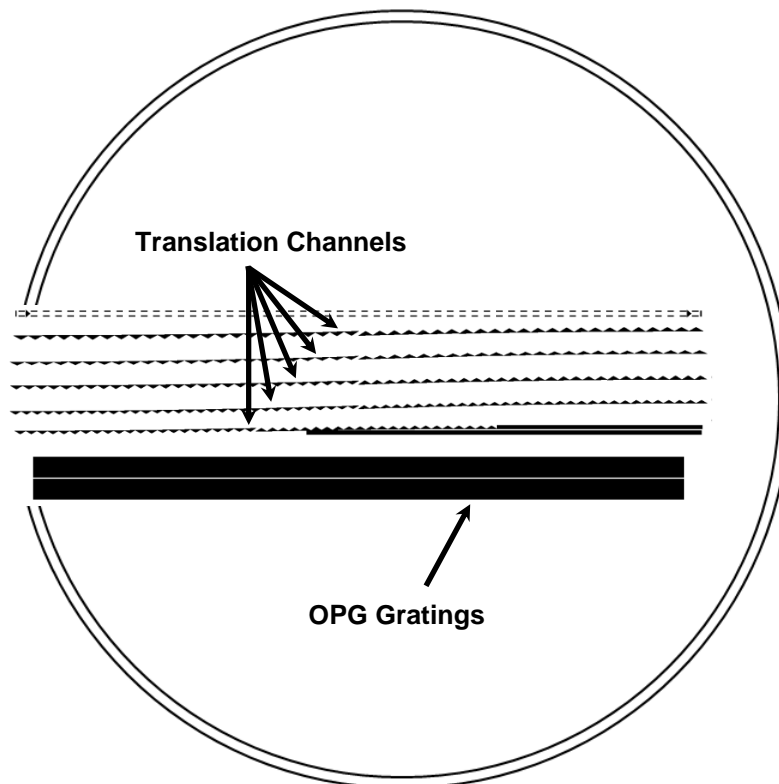


Figure 3.19 – The 5%MgO:CLN wafer with inverted crystal domains (black).

After the poling process was complete, the surface was etched with hydrofluoric acid to reveal the quality of the poling. Figure 3.20 shows the triangular prism domains of the EOBS. Note that these triangular regions exhibit excellent domain quality.

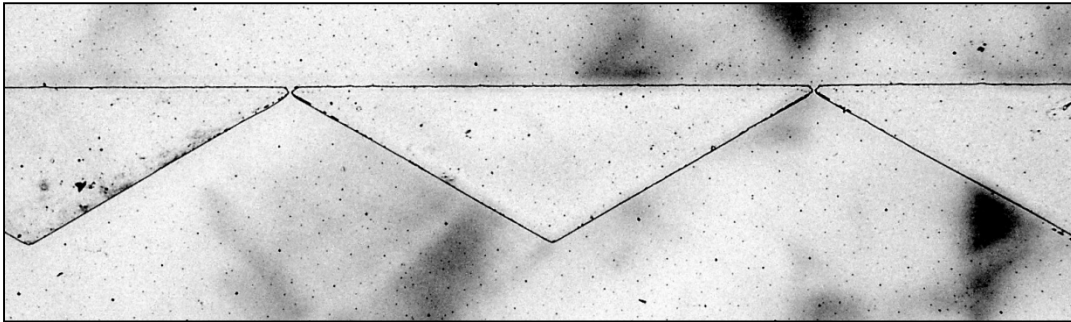


Figure 3.20 – Domain inversion in 5%MgO:CLN [steering prisms].

Figure 3.21 shows two OPG gratings fabricated side-by-side. Note that these gratings are slightly over-poled, which is expected to reduce the conversion efficiency [17].

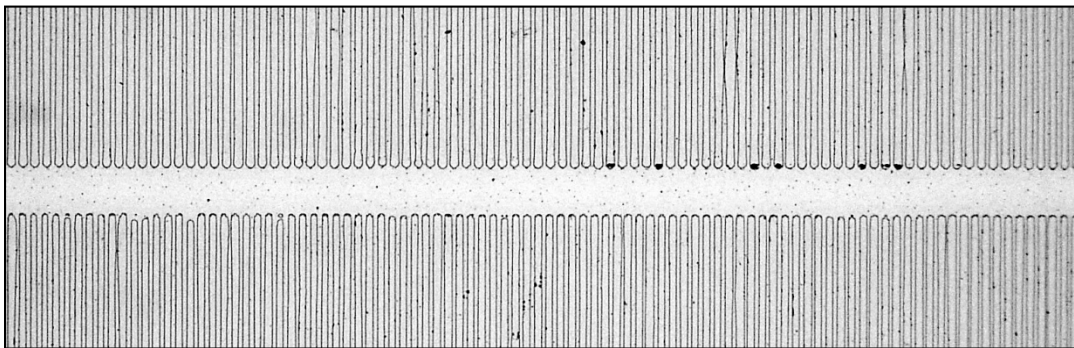


Figure 3.21 – Domain inversion in 5%MgO:CLN [OPG gratings].

After the wafer is poled, the poled region is then diced away from the wafer as shown in Figure 3.22.

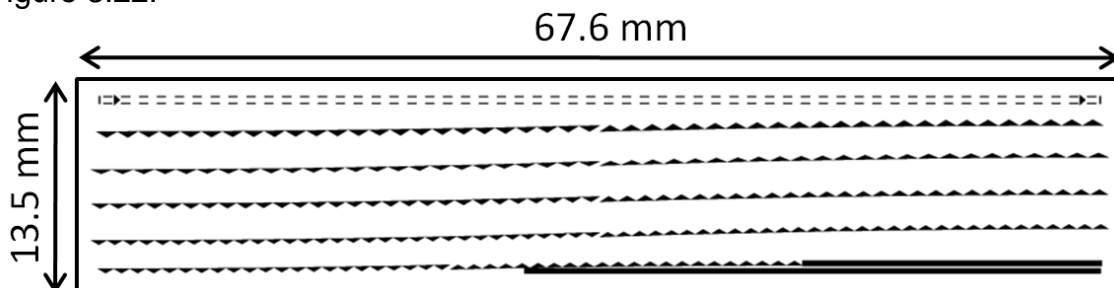


Figure 3.22 – The poled region is diced away from the rest of the wafer.

The entrance and exit facets are polished to create a minimally scattering surface as shown in Figure 3.23. The entrance and exit facets are anti-reflection coated in order to reduce Fresnel reflection as shown in Figure 3.23.



Figure 3.23 – Anti-reflective coatings were added to the polished entrance and exit facets.

The Fresnel losses without the coatings are calculated to be:

$$R_{s,p} = \left(\frac{n_1 - n_2}{n_1 + n_2} \right)^2 = \left(\frac{1 - 2.1468}{1 + 2.1468} \right)^2 = 13.28\% \quad (3.57)$$

These losses would be significant, especially if the EOBS were to be placed in an optical cavity.

The edges of the top and bottom surfaces of the device are masked to prevent the metal from forming an electrical short around the edges of the device. Then, 100Å of chromium and 500Å of gold are sputtered onto the front and back surfaces of the device. These planes of metal form the control electrodes for the device. The mask is removed, and the chip is now complete (Figure 3.24 & Figure 3.25)



Figure 3.24 – The finished EOBS chip with gold electrodes.

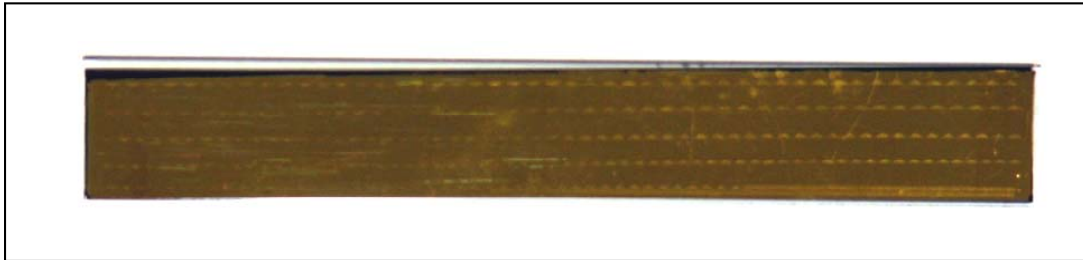


Figure 3.25 – A completed EOBS chip.

For reasons explained in Section 5.1.2, some of the fabricated chips had to be thermally annealed at $T = 550^\circ\text{C}$ overnight. This resulted in tarnishing of the gold electrodes. Electrode resistance of the annealed chips was $R_{\text{electrode}} < 1\Omega$. Figure 3.26

shows a composite image of one of the annealed chips as seen under slight magnification.

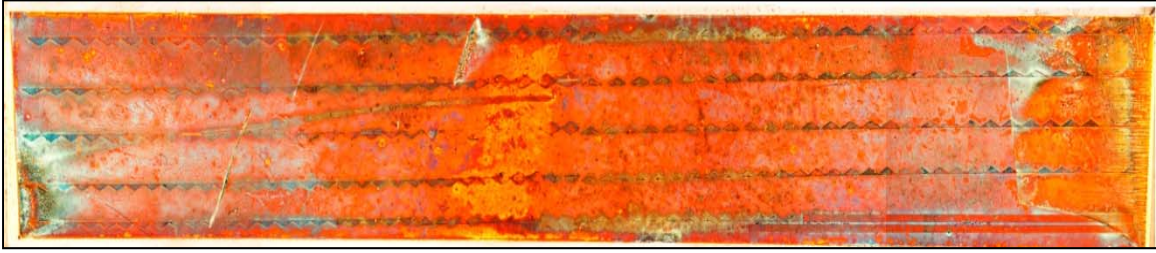


Figure 3.26 – A thermally annealed chip.

Figure 3.27 shows a completed OPG Chip with two gratings of periods $\Lambda = 29.0 \mu m$ and $\Lambda = 31.0 \mu m$.

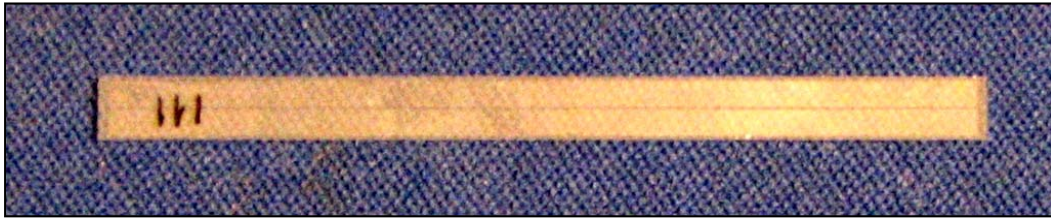


Figure 3.27 – A completed OPG chip.

3.5 System Controls

The hardware design for the controlling EOBS was straightforward. A *Power Designs TW5005D* power supply [V6] functioned as a voltage source. And an *EMCO C30N* negative high-voltage amplifier [V7] ($G \approx 625 \text{ Volts/Volt}$) was used to amplify the signal to $V_{\text{applied}} = -1005.6 \text{ Volts}$, which was applied directly to the EOBS. When an AC signal was needed, a *Hewlett Packard 3325B* function generator [V8] was used. Positive voltage steering was accomplished using a *Trek 50/750* HV amplifier [V9]. Figure 3.28 illustrates the setup.

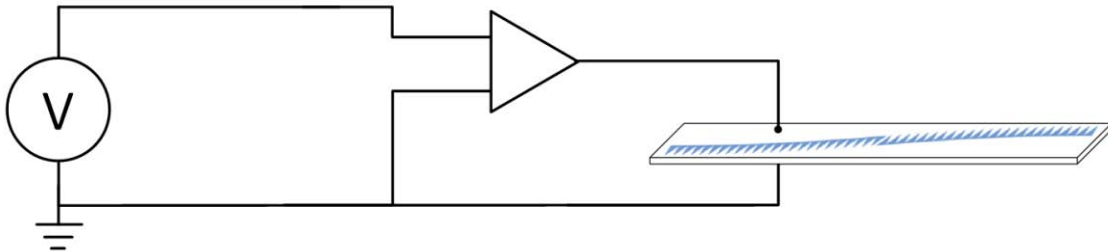


Figure 3.28 – A functional diagram of EOBS controls.

A photograph of the experimental setup is shown in Figure 3.29.

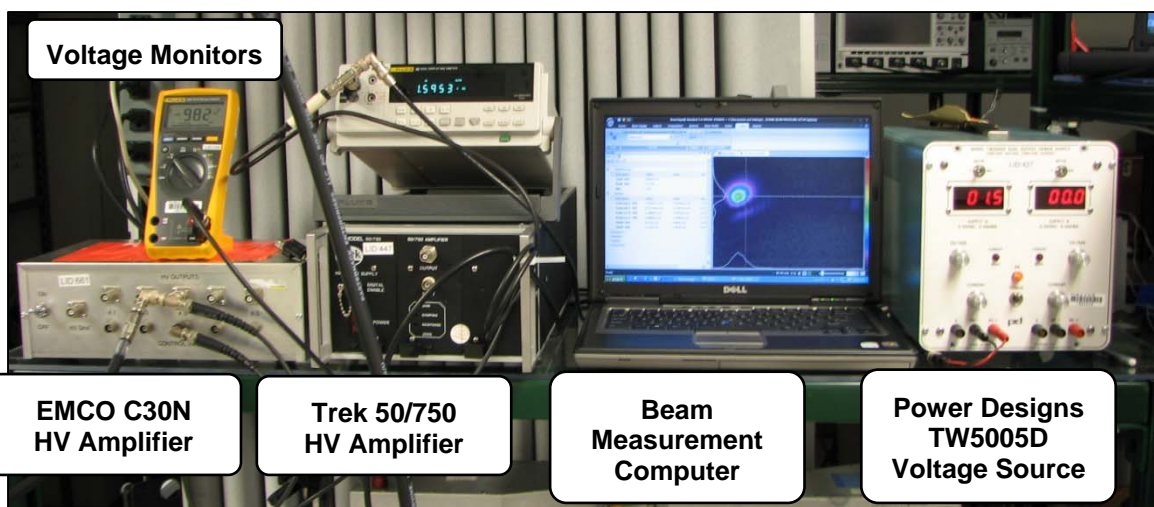


Figure 3.29 – A photograph of the experimental setup for controlling the EOBS chip.

CHAPTER 4 – MODELING EOBS PERFORMANCE WITH *LIGHTS*

4.1 *Finite Difference Method Beam Propagation*

The attentive reader should recognize that the ray analysis used in *Section 3.2.1* can be used to calculate an optimal EOBS geometry from a consideration of the physical constraints of the design. Thus, if the value of a given physical parameter is changed and the analysis is repeated, the result is the most optimal design geometry given the change. This is not, however, a prediction of the effect of that change on the performance of the original design. The ray analysis techniques of *Section 3.2.1* do not easily permit investigation into the effect(s) of perturbations to the physical parameters considered in the design process on the performance of the EOBS design.

Wave analysis of light propagating through EOBS channels provided important insight into the performance of the EOBS design. First, modeling the wave behavior of a beam propagating through Channel 1 verified the validity of the ray analysis performed in *Section 3.2.1*. Substantial discrepancies between ray and wave analyses would have been an indicator that the geometry of the problem was not properly considered during the design process or that ray analysis was not a valid tool for analyzing this problem. Second, simulating the propagation of a laser beam through each EOBS steering channel design elucidated the extent to which attempts to contain the beam within each channel would be successful.

LIGHTS [29] is a software implementation of a finite difference method (FDM) partial differential equation (PDE) solver and can be used to simulate the propagation of light through a device with an arbitrary refractive index profile. The FDM beam propagation implemented in *LIGHTS* is a direct discretization of Maxwell's wave equation, and can capture the diffractive and refractive effects most affecting the design of the EOBS and other problems in integrated optical design.

The user can define the geometry of an arbitrary refractive profile in two or three dimensions. The user also defines the geometry of the light source. The propagation vector is assumed to be the +z-direction. The source and the refractive index data are sampled according to user defined resolution criteria. Appropriate boundary conditions are assumed and the sampled meshes are used to solve the transverse components of the wave equation under the slowly varying envelope approximation. The problem is computationally simplified by applying the Alternating Direction Implicit (ADI) method of solving PDEs [30 p. 64] and the computations are performed on a high-performance, 64-bit, parallel processing data cluster. Thus, complex beam propagation simulations can be performed in only a few minutes.

Figure 4.1 shows that the FDM beam propagation simulation captures the wave nature of light responsible for the Gaussian beam propagation profile shown in *Section 2.4*.

Figure 4.2 shows that the FDM beam propagation simulation captures the wave nature of light responsible for the refraction of light at dielectric interfaces according to Snell's Law. Note that some computational artifacts can be seen propagating away from the prism in Figure 4.2. These artifacts contain a miniscule amount of 'energy' compared to the Gaussian beam and do not contribute appreciably to subsequent behavior of the simulation.

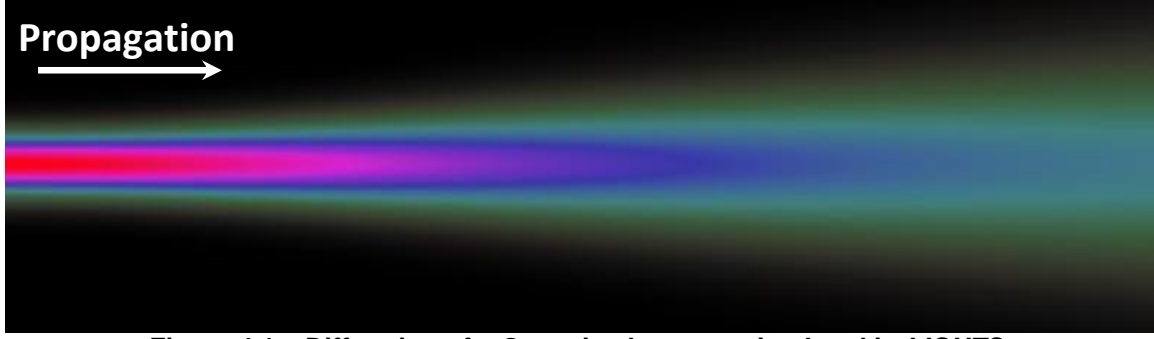


Figure 4.1 – Diffraction of a Gaussian beam as simulated in *LIGHTS*.

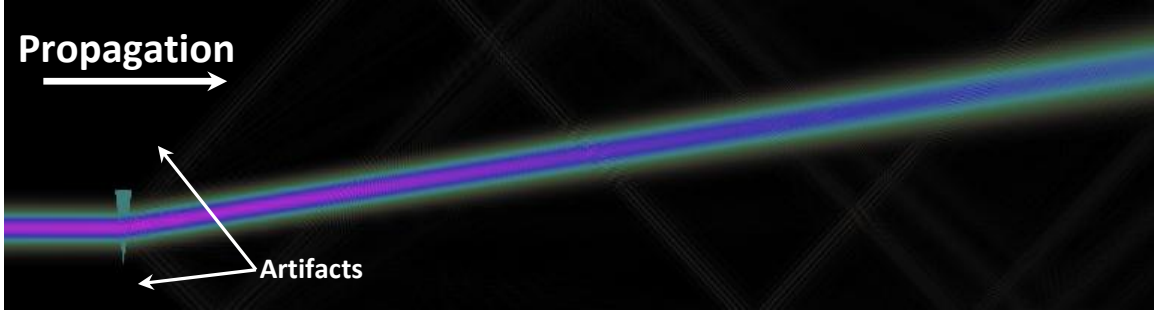


Figure 4.2 – Refraction of a Gaussian beam as simulated in *LIGHTS*.

4.2 Beam Propagation Analysis

4.2.1 Software Setup

The only physical quantities taken into consideration by the FDM algorithm implemented in *LIGHTS* are the position-dependent optical field, and the position-dependent refractive index. Thus, *LIGHTS* enables the user to visualize the interaction of light with objects with arbitrary refractive index profiles. Consequently, even though there is no direct way to program *LIGHTS* to consider the electro-optic effect, this effect can be simulated because it is directly coupled to the refractive index profile used in the simulation. By extension, *LIGHTS*, enables the user to simulate the effects of changes in any variable which can be coupled to the refractive index. Recall Equation (3.10):

$$n'_e(\lambda, V, T, r_{33}) = n_e(\lambda, T) - \frac{1}{2} r_{33} n_e^3(\lambda, T) \cdot \frac{V}{L}$$

Because n'_e is coupled to applied voltage, wavelength, temperature, and the electro-optic coefficient, *LIGHTS* can be used to assess the effect of changes of these parameters on the performance of EOBS channels.

Also recall that, due to ferroelectric domain inversion, the sign of the electro-optic coefficient is inverted within the prismatic regions ($r_{33} \rightarrow -r_{33}$). Thus, inside the triangular prisms the refractive index is:

$$n_{prism} = n_e(\lambda, T) - \frac{1}{2} r_{33} n_e^3(\lambda, T) \cdot \frac{V}{L} \quad (4.1)$$

And outside the triangular prisms the refractive index is:

$$n_{background} = n_e(\lambda, T) + \frac{1}{2}r_{33}n_e^3(\lambda, T) \cdot \frac{V}{L} \quad (4.2)$$

where $n_e(\lambda, T)$ is given by Equation (3.1):

$$n_e^2 = a_1 + b_1f + \frac{a_2 + b_2f}{\lambda^2 - (a_3 + b_3f)^2} + \frac{a_4 + b_4f}{\lambda^2 - a_5^2} - a_6\lambda^2$$

where $f = (T - 24.5)(f + 580.82)$ and the sellmeier coefficients are given in Table 3.2.

The index of refraction profile of EOBS Channel 1 (see Table 3.3) can be seen in Figure 4.3.

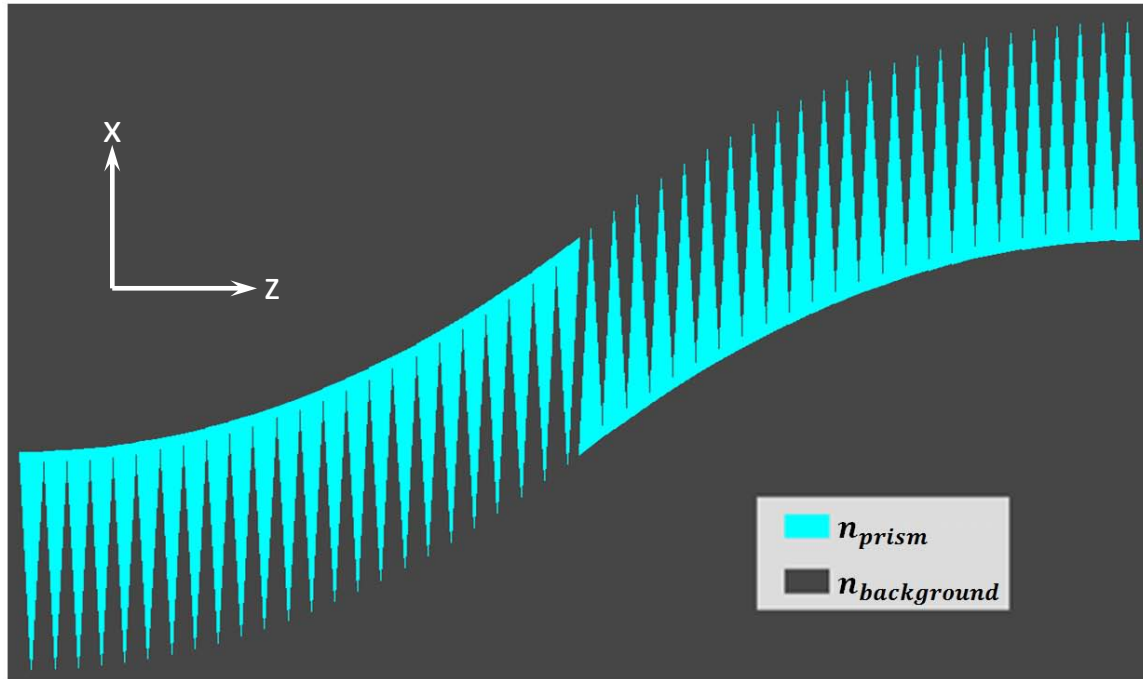


Figure 4.3 – The refractive index profile of EOBS Channel 1.

Recall that Channel 1 was designed to translate a near-Gaussian beam with quality $M^2 = 1.76$ and wavelength $\lambda = 1.064 \mu m$. The electro-optic coefficient was assumed to be $r_{33} = 30.8 pm/V$. The error-corrected control voltage was $V = -1005.6 Volts$, and the device was designed to work at room temperature ($T = 20^\circ C$). Under these conditions:

$$n_{prism} = n_e(\lambda, T) - \frac{1}{2}r_{33}n_e^3(\lambda, T) \cdot \frac{V}{L} = 2.1471447$$

$$n_{background} = n_e(\lambda, T) + \frac{1}{2}r_{33}n_e^3(\lambda, T) \cdot \frac{V}{L} = 2.1465352$$

The positions of the steering prisms and these refractive index values were uploaded to *LIGHTS*. The input field was generated in MATLAB [M4] as a converging Gaussian beam with wavelength $\lambda = 1.064 \mu m$. The optimal beamwaist diameter

calculated for each design (see Table 3.3) was used and the beamwaist location assumed to be $z_0 = 33000 \mu m$ (the geometric center of the channel). Numerical amplitude and phase profiles of the focused beam were uploaded to lights. Figure 4.4 shows the results of the *LIGHTS* simulation.

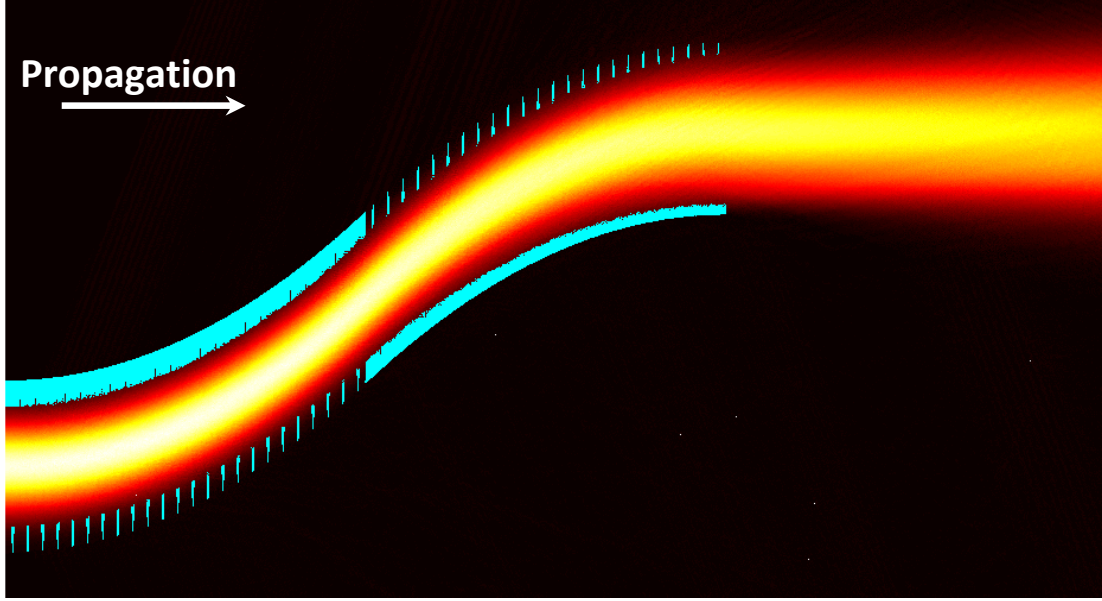


Figure 4.4 – The FDM beam propagation simulation of EOBS Channel 1 (idea conditions).
[Prisms – Cyan; Laser – Red/Yellow]

EOBS Channel 1 was designed to contain all of the optical energy within the $1/e^2$ width of the Gaussian beam. Note that Figure 4.4 only shows field values $A > \frac{A_{max}}{e^2}$. Thus it is clear that EOBS Channel 1 will deliver at least 87.5% of the input energy, and probably more, to its output.

4.2.2 Comparison of Wave Analysis (*LIGHTS*) with Ray Analysis (*MATLAB*)

MATLAB [M5] was used to calculate the center of amplitude of each ‘vertical’ line using the standard formula:

$$x_{centroid} = \frac{\sum_x E(x, z) \cdot x}{\sum_x E(x, z)} \Bigg|_z \quad (4.3)$$

The propagation path of the center of amplitude is shown in Figure 4.5. The indicated region was used to calculate beam steering statistics.

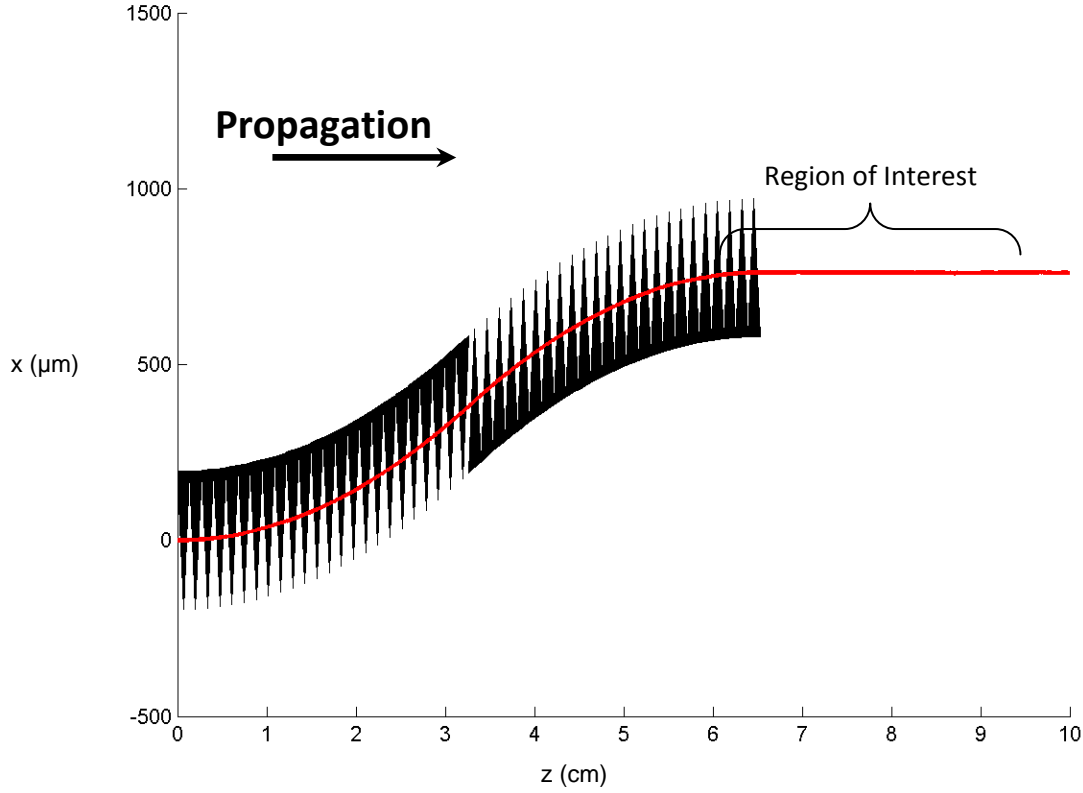


Figure 4.5 – The center of amplitude beampath [red].

From Figure 4.5, it is clear that the center of amplitude beam path is directly through the center of the steering channel. From the center of amplitude data, the overall translation was calculated to be $Translation_{total} = 769.66 \pm 0.366 \mu m$.

The deflection angle of the beam in air was calculated to be:

$$\theta_{deflection} = \arcsin\left(\frac{n_{CLN}}{n_{air}} \sin\left(\arctan\left(\frac{x_{centroid}(z_2) - x_{centroid}(z_1)}{z_2 - z_1}\right)\right)\right) \quad (4.4)$$

$$= -0.0569^\circ = -0.99 \text{ mrad}$$

Which is on the order of the angular divergence of the beam:

$$\theta_{divergence} = \arcsin\left(\frac{n_{CLN}}{n_{air}} \sin\left(\arctan\left(\frac{w(z_2) - w(z_1)}{z_2 - z_1}\right)\right)\right) \quad (4.5)$$

$$= 0.4869^\circ = 8.50 \text{ mrad}$$

Recall that the overall translation value predicted from ray analysis is $Translation_{total} = 775.16 \mu m$ with a nominal output angle of $\theta_{output} = 0^\circ$. Thus, the angular deviation of the simulated beam from the ideal design value is small and the agreement between calculated and simulated overall translation values is close:

$$\%Difference = \frac{Translation_{simulation} - Translation_{design}}{Translation_{design}} = 0.71\% \quad (4.6)$$

Not surprisingly, ray analysis was shown to be an accurate approximation to the wave behavior of a propagating beam.

Similar results were obtained for all five EOBS steering channels. The results of these FDM beam propagation simulations are contained in *Appendix A*. Table 4.1 shows a summary of FDM beam propagation simulation results as well as the ray analysis predictions for EOBS Channels 1-5.

Table 4.1 – A summary of FDM beam propagation results.

Name	Calculated Translation	Simulated Translation	Simulated Output Angle	%Difference
Channel 1	775.16 μm	769.66 \pm 0.37 μm	-0.1035°	0.71%
Channel 2	1071.52 μm	1049.07 \pm 0.61 μm	-1.2526°	2.01%
Channel 3	913.52 μm	903.77 \pm 0.51 μm	-0.5303°	1.07%
Channel 4	1044.60 μm	1022.38 \pm 0.41 μm	-0.7509°	2.12%
Channel 5	497.25 μm	491.06 \pm 0.61 μm	-0.8184°	1.24%

4.2.3 Trends in the Effects of Changing Physical Parameters

Wave propagation simulations were constructed to analyze the effect of single parameter changes on the steering performance of EOBS Channel 1. The effect of uniform fluctuations in device temperature and deviations of the electro-optic coefficient from the specified value were investigated. The suitability of Channel 1 to steer beams with wavelengths from $\lambda = 500 \text{ nm}$ to $\lambda = 1500 \text{ nm}$ was examined. The steering behavior of Channel 1 as the applied voltage varies from $V_{applied} = 500 \text{ Volts}$ to $V_{applied} = -1500 \text{ Volts}$ was simulated.

Figure 4.6, Figure 4.9, Figure 4.12, and Figure 4.16 show the coupling of the physical trends which were analyzed to the refractive indices n_{prism} and $n_{background}$.

The Effect of Device Temperature:

Recall that the index of refraction of 5%MgO:CLN is temperature dependent and consider that the temperature of the EOBS is likely to fluctuate with room temperature. Thus, it is prudent to simulate the effect of such fluctuations on the performance of the EOBS. Figure 4.6 shows the coupling of device temperature to the extraordinary refractive index of 5%MgO:CLN at ambient temperatures from 0°C to 50°C in intervals of 5 C°.

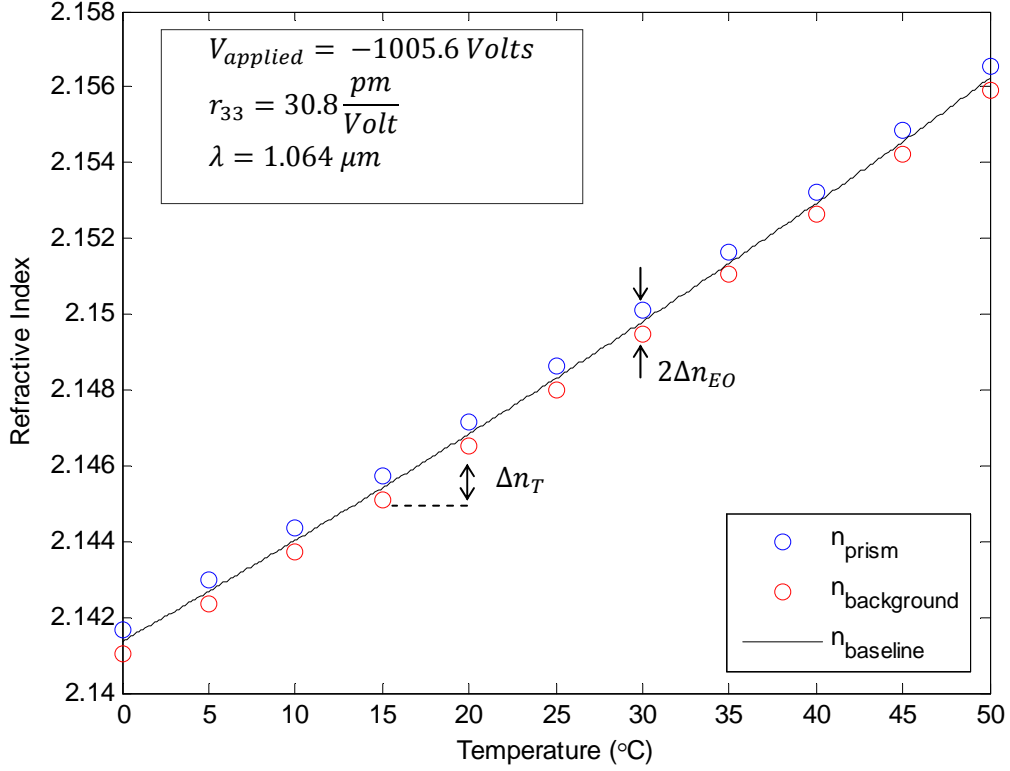


Figure 4.6 – The refractive indices of 5%MgO:CLN as a function of temperature.

From Figure 4.6, note that Δn_T is on the same order as Δn_{EO} and that n_{prism} and $n_{background}$ vary in the same direction with respect to temperature. Thus, the effect of the EOBS temperature on its steering performance was expected to be small.

Figure 4.7 shows a plot of the center of amplitude beam paths corresponding to each point shown in Figure 4.6. By inspection, the various paths do not vary significantly. Clearly, the overall effect of device temperature is negligible.

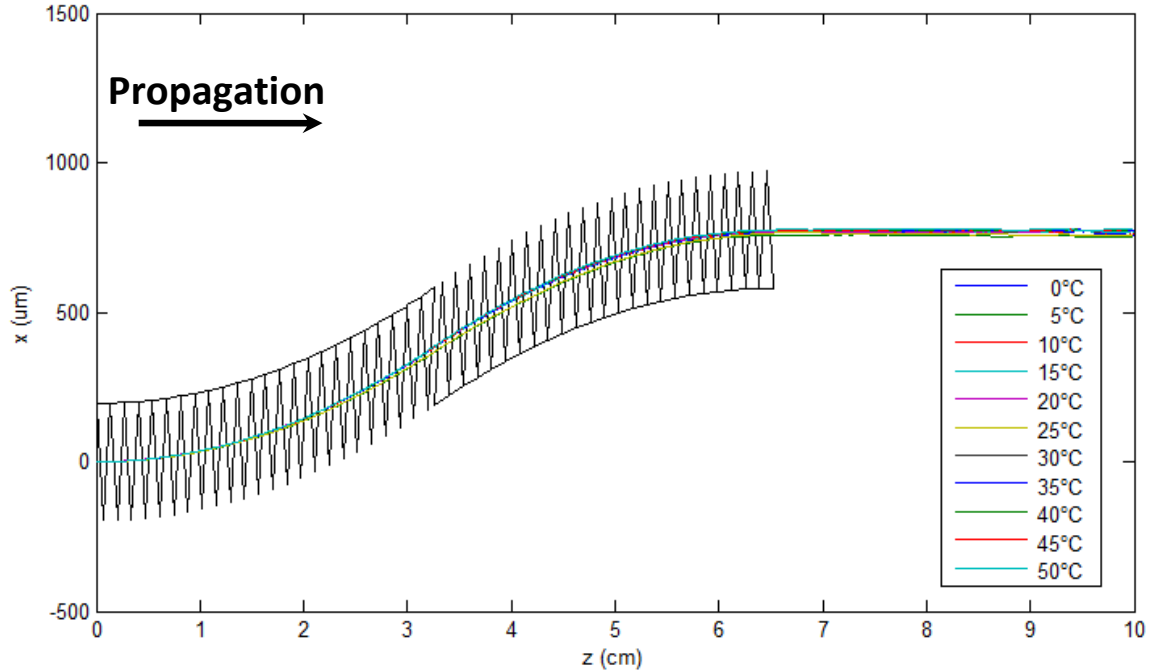


Figure 4.7 – A composite of simulated beam paths at various device temperatures.

Figure 4.8 clearly shows that, for the extreme case of $T = 50^{\circ}\text{C}$, the device performance is practically indistinguishable from the design case (Figure 4.4). An entire catalog of images of the numerical FDM beam propagation simulations performed for this thesis is contained in *Appendix A*.¹⁰

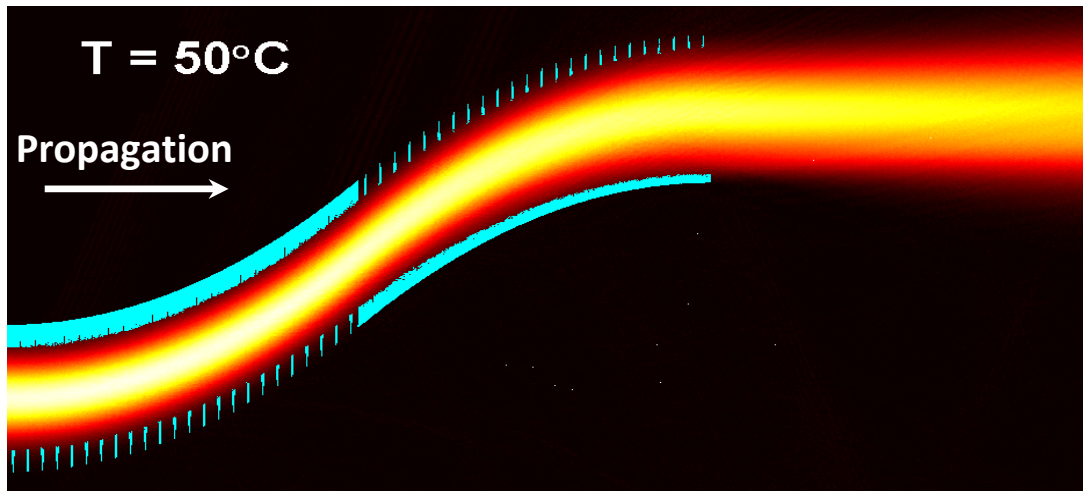


Figure 4.8 – Plot of numerical simulation of EOBS performance at $T=50^{\circ}\text{C}$.

The Effect of Deviations in the Electro-Optic Coefficient:

Recall that the electro-optic coefficient r_{33} couples electrical excitation to modulation of the index of refraction of 5%MgO:CLN and consider that the electro-optic

¹⁰ For the sake of succinctness, only simulations which demonstrate physical trends or exemplify behavior radically different from the desired behavior will be included in the main body of the text.

coefficient of that material is specified at the wavelength $\lambda = 632.8 \text{ nm}$ of a helium-neon laser. The value of the electro-optic constant has been shown to be wavelength dependent [18,19]. Thus, since the EOBS is designed to steer beams with wavelength $\lambda = 1.064 \mu\text{m}$, it is prudent to simulate the effect of deviations of the electro-optic coefficient from the specified value on the performance of the EOBS. Figure 4.9 illustrates the coupling of the electro-optic coefficient r'_{33} to the extraordinary refractive index of 5%MgO:CLN at values from $80\% \cdot r_{33}$ to $100\% \cdot r_{33}$ in intervals of 5%.

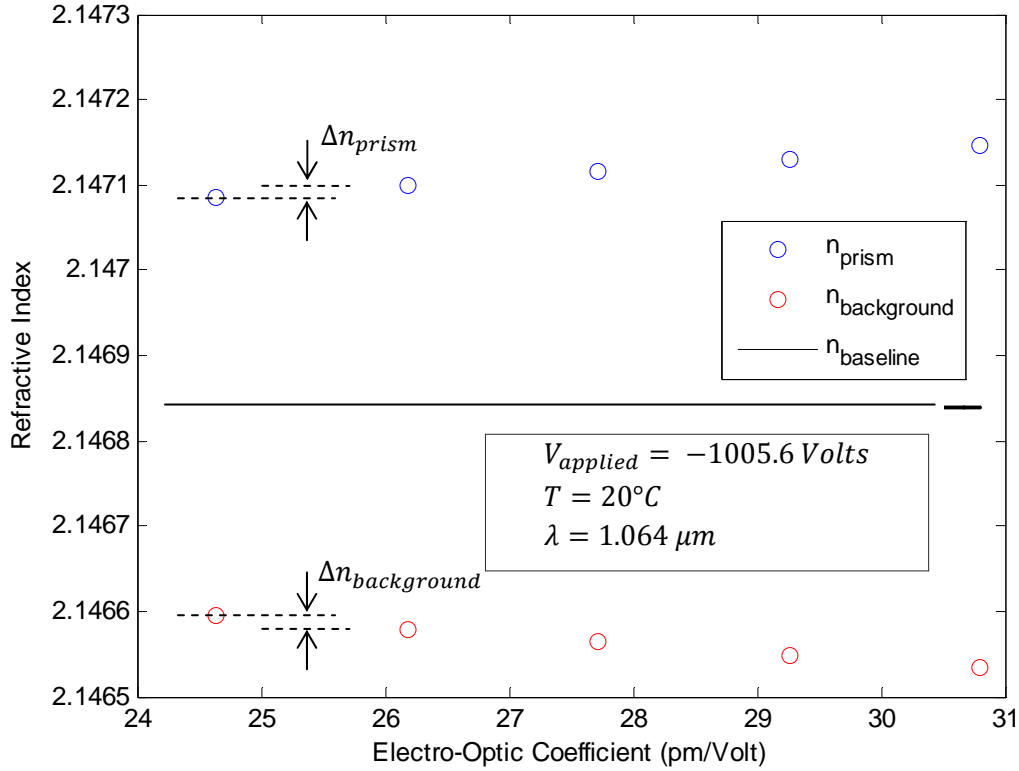


Figure 4.9 – The refractive indices as a function of the electro-optic coefficient.

From Figure 4.9, note that n_{prism} and $n_{background}$ vary in opposite directions with respect to the electro-optic coefficient r'_{33} . Thus, the effect of deviations of the electro-optic coefficient from its specified value may be significant even though Δn_{prism} and $\Delta n_{background}$ are small.

Figure 4.10 shows a plot of the center of amplitude path corresponding to different values of r'_{33} ¹¹. Upon first inspection, the paths do not seem to differ very much. In this case, the center of amplitude of the simulated beam does not represent the behavior of the beam nearly as well as in the ideal case.

¹¹ Only values lower than the nominal value $r_{33} = 30.8 \frac{\text{pm}}{\text{Volt}}$ were considered because it seemed likely that, due to electro-optic dispersion effects [19], r_{33} would be smaller at $\lambda = 1.064 \mu\text{m}$ than at $\lambda = 632.8 \text{ nm}$, where it is typically measured. Furthermore, changes in the value of r_{33} are numerically equivalent to changes in $V_{applied}$, thus it is possible to understand the consequences of underestimating the value of r_{33} by considering simulations where $V_{applied} < -1000 \text{ Volts}$ [pp. 82-85].

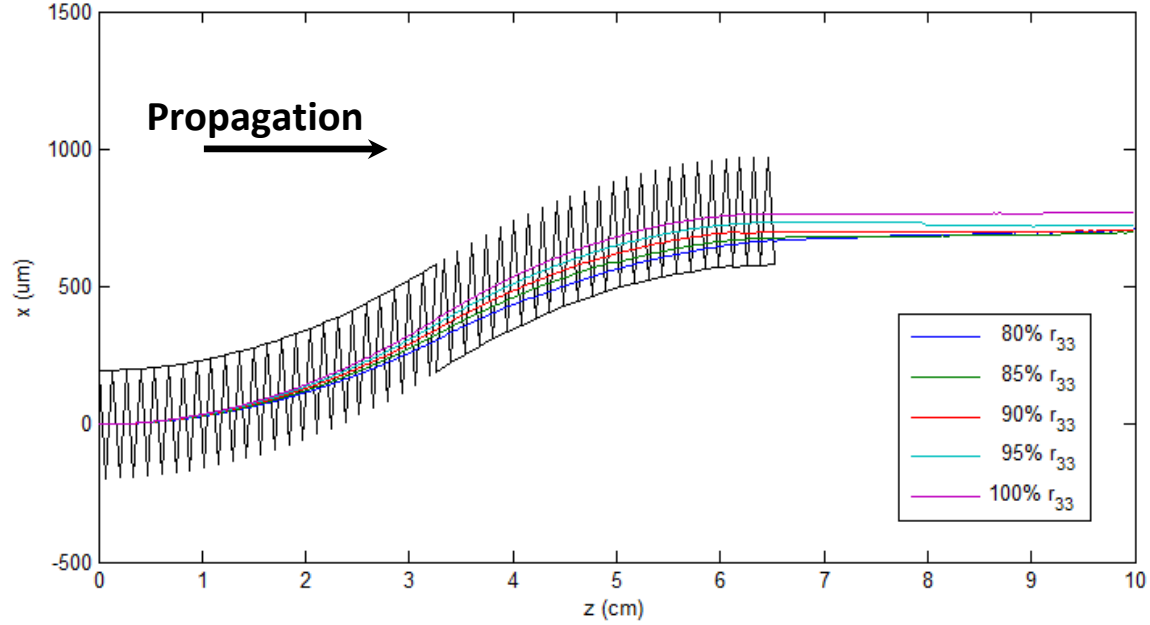


Figure 4.10 – Simulated beam paths for several values of the electro-optic coefficient.

Figure 4.11 clearly shows that, for the extreme case of $r'_{33} = 80\% \cdot r_{33}$, the device performance does deteriorate significantly from the design case (Figure 4.4). It is clear that the beam is under-steered and, consequently, intersects the bottom edge of the second stage of the EOBS steering channel. The slight positive index difference between the prisms and the background material causes total internal reflection (TIR), effects which cause the majority of the input energy to leave through the output face of the EOBS channel, but the quality is significantly deteriorated. Furthermore, the center of amplitude of the beam travels at a significant angle with respect to the optic axis. Thus, it is doubtful that this beam would be useful in the far-field.

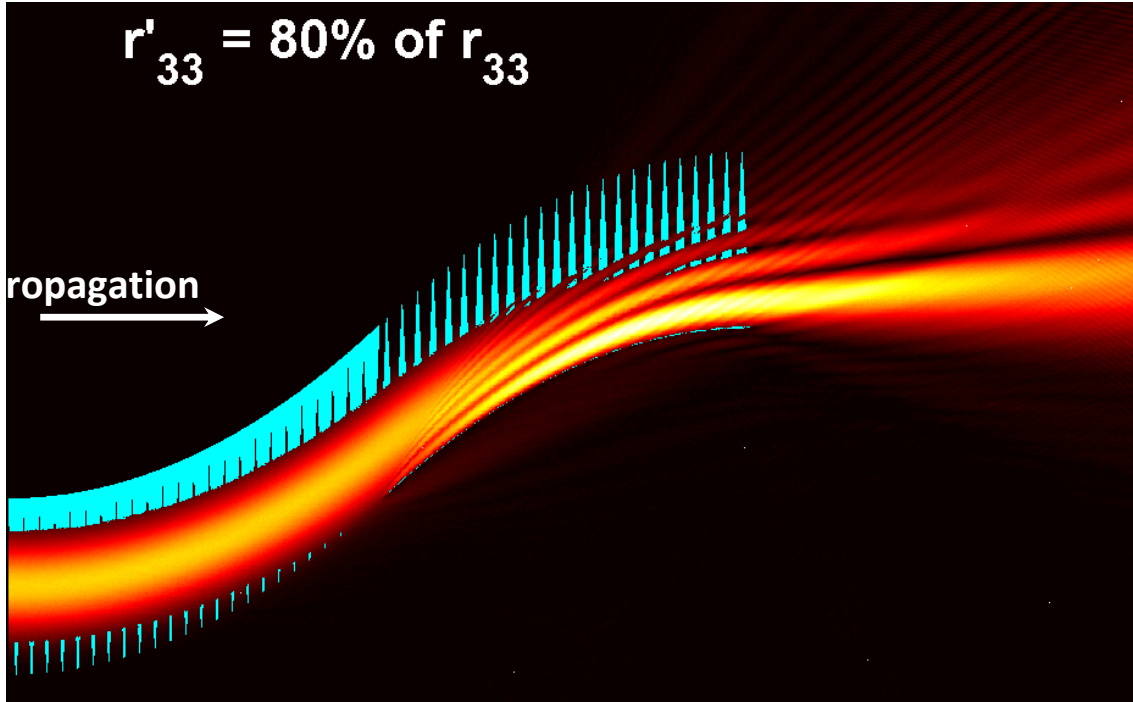


Figure 4.11 – A plot of the numerical simulation of EOBS performance at $r'_{33} = 80\% \cdot r_{33}$.

Again, the numerical FDM beam propagation results of each case are contained in *Appendix A*. From these simulations, it is clear that the kind of deterioration that is shown in Figure 4.11 is evident with less severity in cases where the deviation of the electro-optic coefficient from the specified value is also less severe.

EOBS Performance at Non-Design Wavelengths:

The EOBS designed in this work was designed to steer beams with wavelength $\lambda = 1.064 \mu m$. In principle, the EOBS will perform similarly at nearby wavelengths. However, recall that 5%MgO:CLN is highly dispersive in the visible and near-IR wavebands. Thus, it is prudent to evaluate the suitability of the EOBS to steer beams of various wavelengths. Figure 4.12 illustrates the coupling of the wavelength λ to the extraordinary refractive index of 5%MgO:CLN at values from $\lambda = 500 nm$ to $\lambda = 1500 nm$ in intervals of $\Delta\lambda = 100 nm$.

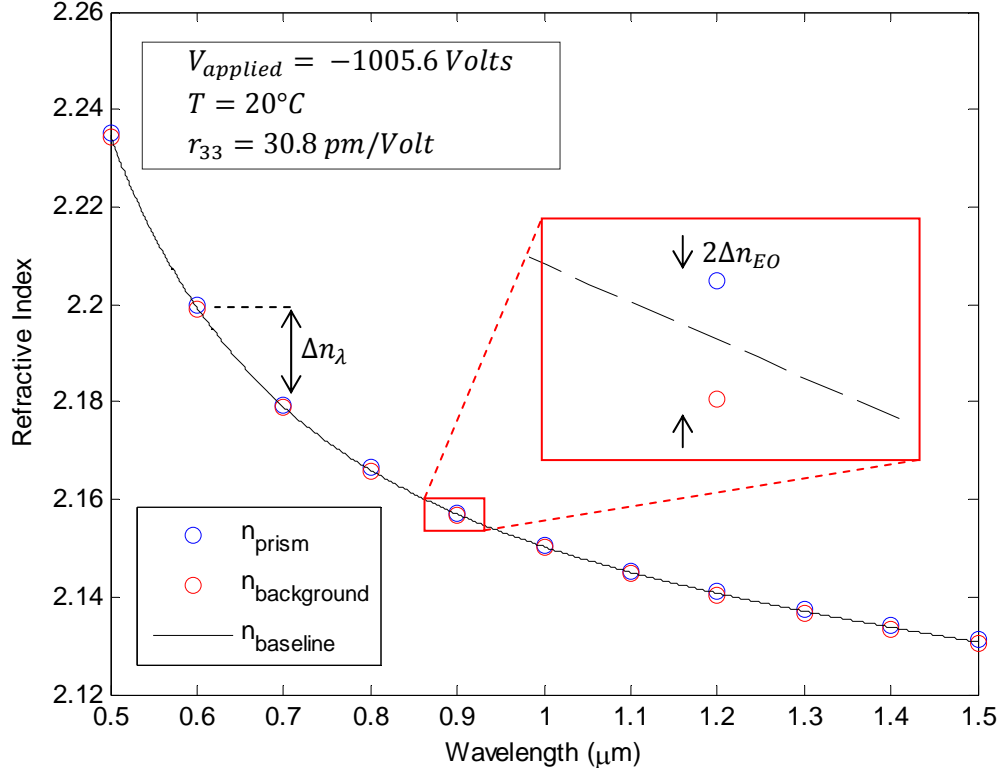


Figure 4.12 – The refractive indices as a function of wavelength.

From Figure 4.12, note that $\Delta n_\lambda \gg 2\Delta n_{EO}$. Thus, the effect of the material dispersion will dominate the small changes in refractive index allowed by the electro-optic effect. Thus, this EOBS was expected to be unsuitable for wavelengths far from the design wavelength.

Figure 4.13 shows a plot of the center of amplitude paths for $\lambda = 500 \text{ nm}$ to $\lambda = 1500 \text{ nm}$. Somewhat surprisingly, Channel 1 performed adequately in simulations at all wavelengths considered.

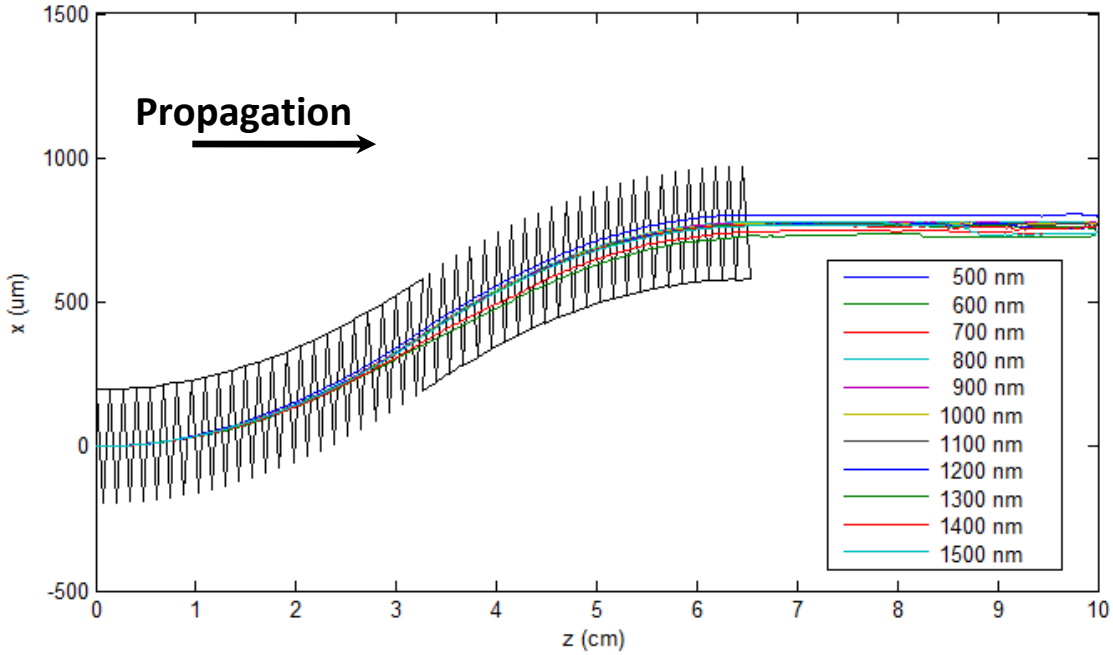


Figure 4.13 – Simulated beam paths for wavelengths $\lambda = 500 \text{ nm}$ to $\lambda = 1500 \text{ nm}$.

Figure 4.14 shows that, for the extreme case of $\lambda = 1500 \text{ nm}$, the steering performance of Channel 1 is similar to the design case (Figure 4.4). Similarly, Figure 4.15 shows that, for the extreme case of $\lambda = 500 \text{ nm}$, the steering performance of Channel 1 is similar to the design case (Figure 4.4), though some light leakage can be observed. The noisy spatial profile of the steered beam is a consequence of this leakage. It is unclear whether this leakage is physical or only an artifact of the FDM computation. Again, the results of the FDM beam propagation of each case are contained in *Appendix A*.

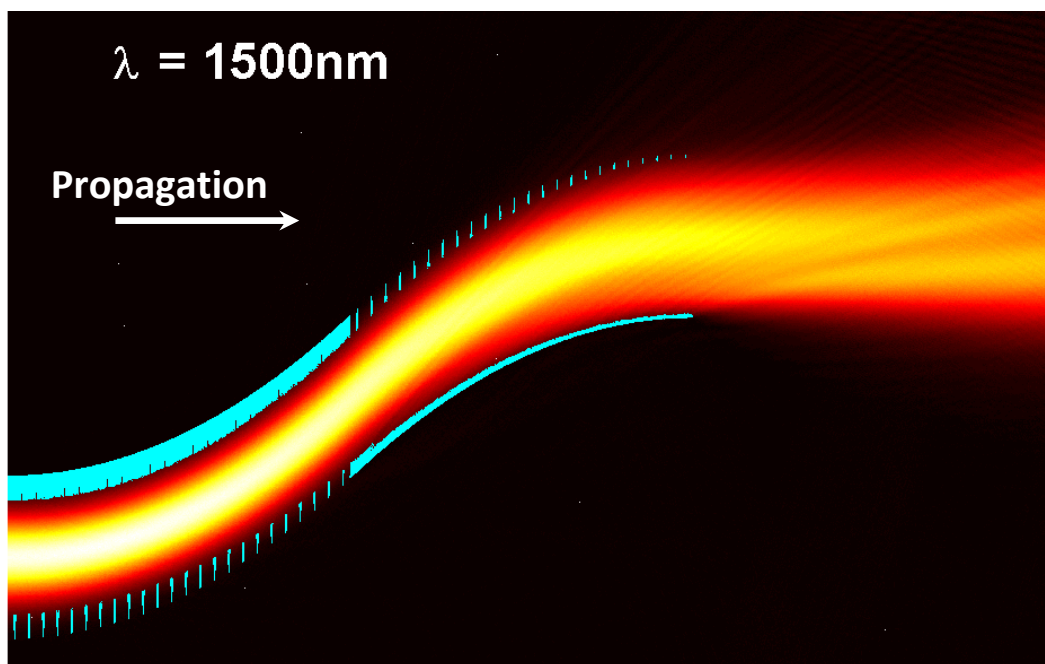


Figure 4.14 – Plot of the numerical simulation of EOBS performance at $\lambda = 1500\text{ nm}$.

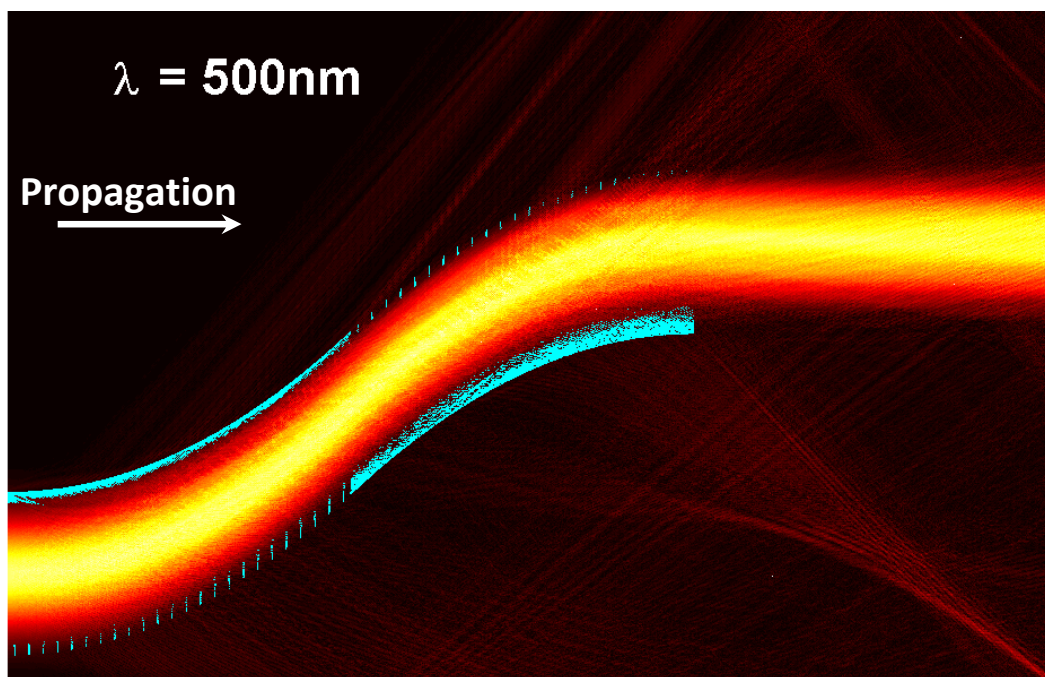


Figure 4.15 – Plot of the numerical simulation of EOBS performance at $\lambda = 500\text{ nm}$.

Table 4.2 – The output characteristics of steered beams of various wavelengths

Wavelength	Simulated Translation	Simulated Output Angle	%Deviation from $\lambda = 1064 \text{ nm}$
500 nm	$801.88 \pm 0.42 \text{ } \mu\text{m}$	-0.3182°	4.19%
600 nm	$733.62 \pm 5.12 \text{ } \mu\text{m}$	-6.3383°	-4.68%
700 nm	$747.64 \pm 1.50 \text{ } \mu\text{m}$	-1.2801°	-2.86%
800 nm	$778.26 \pm 0.37 \text{ } \mu\text{m}$	0.1766°	1.12%
900 nm	$775.04 \pm 0.68 \text{ } \mu\text{m}$	-0.3000°	0.70%
1000 nm	$772.43 \pm 0.18 \text{ } \mu\text{m}$	0.1528°	0.36%
1064 nm	$769.66 \pm 0.37 \text{ } \mu\text{m}$	-0.1035°	-
1100 nm	$769.29 \pm 0.65 \text{ } \mu\text{m}$	-0.9230°	-0.05%
1200 nm	$766.09 \pm 0.57 \text{ } \mu\text{m}$	-1.2398°	-0.46%
1300 nm	$763.26 \pm 1.54 \text{ } \mu\text{m}$	-2.4300°	-0.83%
1400 nm	$760.32 \pm 0.92 \text{ } \mu\text{m}$	-3.0271°	-1.21%
1500 nm	$761.86 \pm 1.48 \text{ } \mu\text{m}$	-3.7742°	-1.01%

Table 4.2, shows a few trends in EOBS performance. Beams with wavelengths shorter than the design wavelength typically experience more overall translation than the channel was designed to impart. Conversely, beams with wavelengths longer than the design wavelength typically experience less overall translation than the channel was designed to impart. Moreover the angular deflection imparted to the beam increases with increased deviation from the design wavelength. Two notable exceptions to these trends are the $\lambda = 600 \text{ nm}$ and $\lambda = 700 \text{ nm}$ cases. The factors contributing to these exceptions are not immediately clear.

In principle, it is possible to compensate for the effects of dispersion by adjusting the control voltage V_{applied} . This concept is explored in further detail in *Appendix B*.

EOBS Performance at Non-Design Voltages:

The EOBS was designed to be electrically modulated between two steering states. Thus, only two voltage states were considered during the design process, OFF: $V_{\text{applied}} = 0 \text{ Volts}$ and ON: $V_{\text{applied}} = -1000 \text{ Volts}$. Any voltage amplifier used to modulate the EOBS between voltage states is going to have a finite rise/fall time during which the applied voltage will sweep through the range of voltages between states. Thus it seems prudent to simulate the steering response of the EOBS within this range of voltages.

For the sake of comprehensiveness, the response of the device was simulated at voltages from $V_{\text{applied}} = -1500 \text{ Volts}$ to $V_{\text{applied}} = 500 \text{ Volts}$. Figure 4.16 illustrates the coupling of the applied voltage V_{applied} to the extraordinary refractive index of 5%MgO:CLN at values within this range in intervals of $\Delta V = 100 \text{ Volts}$.

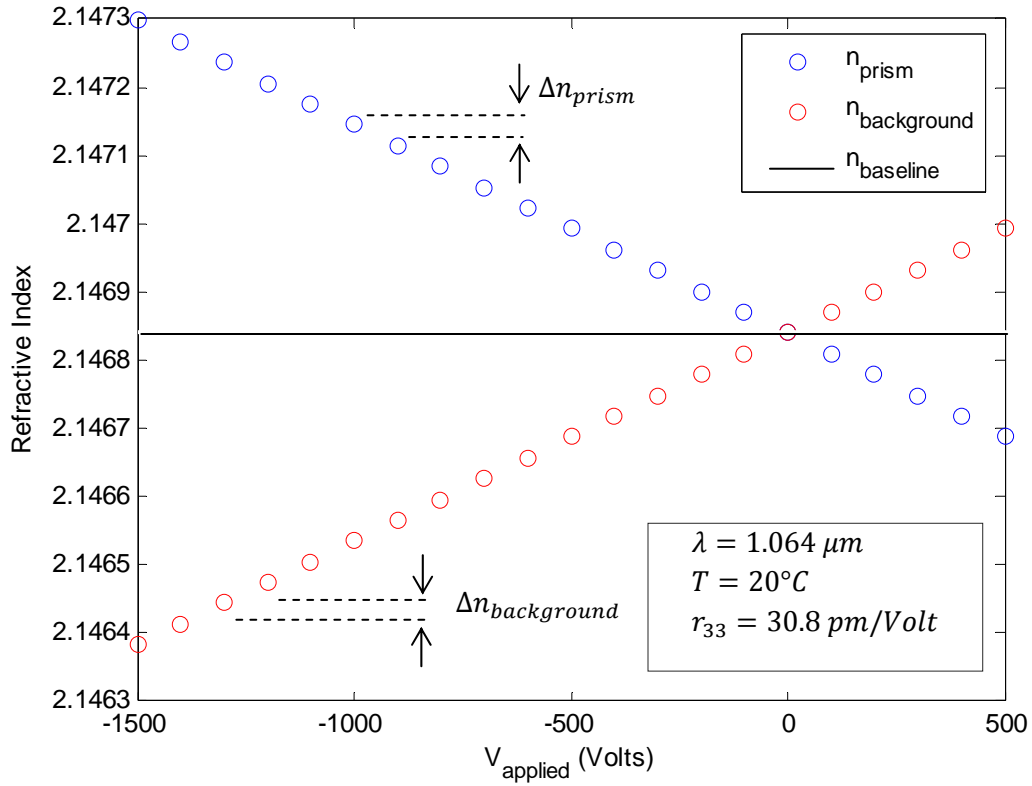


Figure 4.16 – The refractive indices as a function of applied voltage.

From Figure 4.16, note that n_{prism} and $n_{\text{background}}$ vary in opposite directions with respect to the applied voltage V_{applied} . The linear variation of n_{prism} and $n_{\text{background}}$ with opposite slope is qualitatively similar to the situation considered when evaluating the effects of deviations in the electro-optic coefficient from the specified value. Thus, the FDM beam propagation results corresponding to $-1000 \text{ Volts} < V_{\text{applied}} < -800 \text{ Volts}$ are expected to be similar to the simulations shown in Figure 4.10 (where $80\% \cdot r_{33} < r'_{33} < r_{33}$).

Figure 4.17 shows a plot of the center of amplitude path for $V_{\text{applied}} = -900 \text{ Volts}$ to $V_{\text{applied}} = -1200 \text{ Volts}$. By inspection, the paths of these beams are similar to the design case with slight differences in the overall translation.

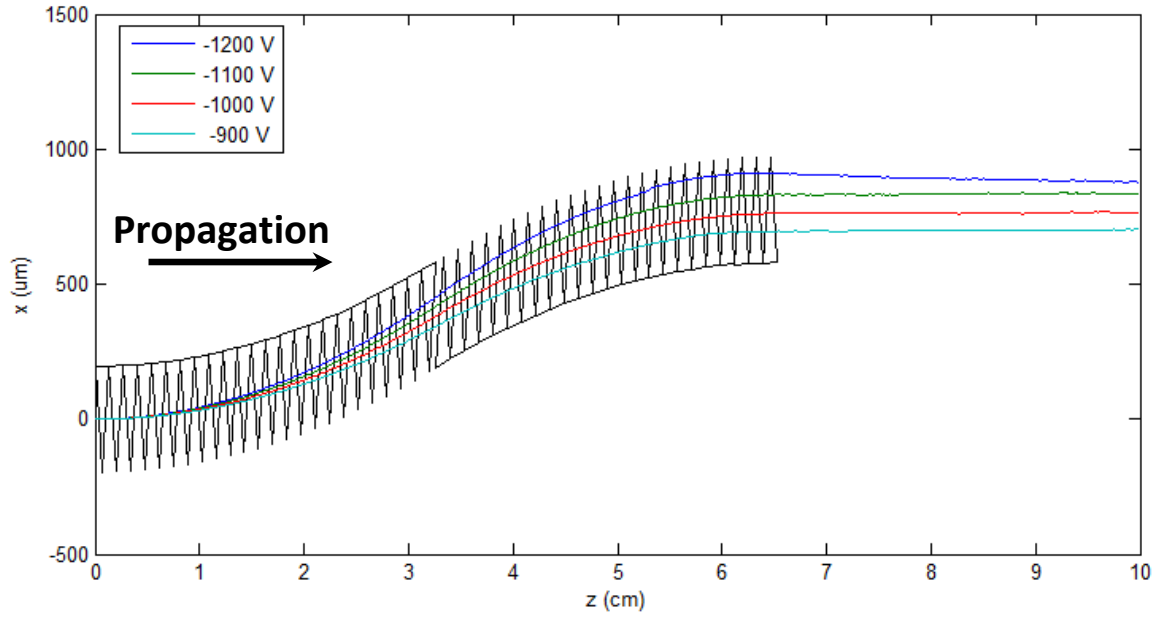


Figure 4.17 – Simulated beam paths for voltages $V = -900$ Volts to $V = -1200$ Volts.

Figure 4.18 shows a plot of the center of amplitude path for $V_{applied} = 500$ Volts to $V_{applied} = -400$ Volts. By inspection, the behavior of this EOBS in this range of voltages is basically that of a voltage-controlled beam deflector.

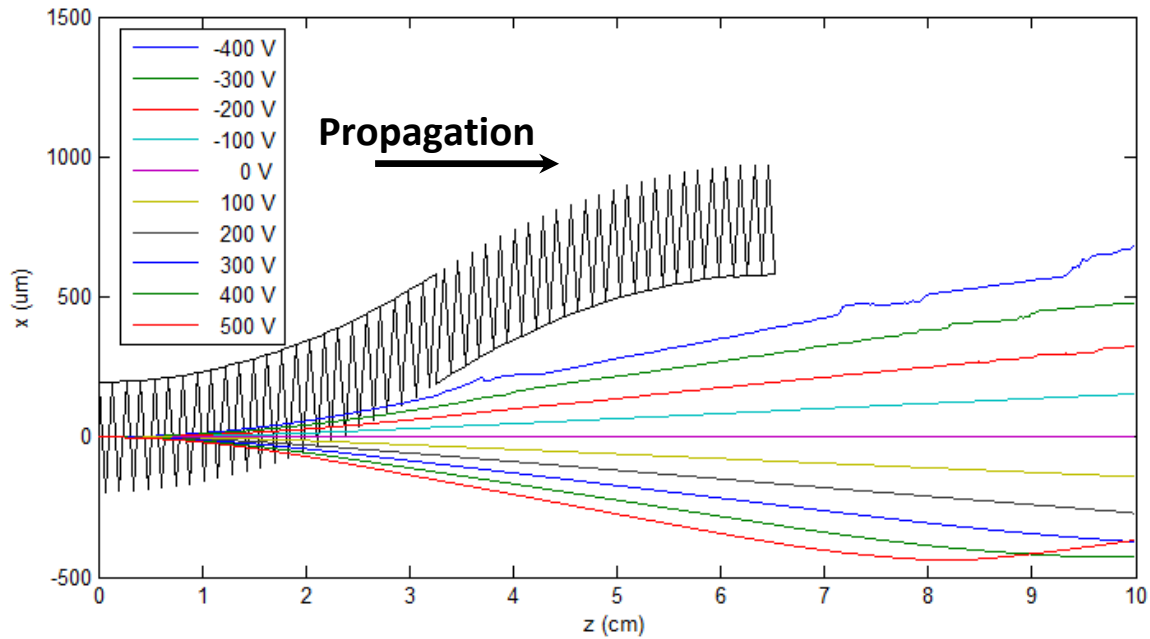


Figure 4.18 – Simulated beam paths for voltages $V = 500$ Volts to $V = -400$ Volts .
[False Reflection Effects at Edge of the Simulation Space can be Seen at the Bottom-Right Corner of the Image.]

Figure 4.19 shows a plot of the center of amplitude path for $V_{applied} = -500$ Volts to $V_{applied} = -800$ Volts and for $V_{applied} = -1300$ Volts to $V_{applied} = -1500$ Volts. The

behavior of the center of amplitude is seen to be quite erratic. The beam path, as described by the center of amplitude location, is not particularly meaningful in these cases. A catalog of the results of FDM beam propagation simulations for each case can be found in *Appendix A*.

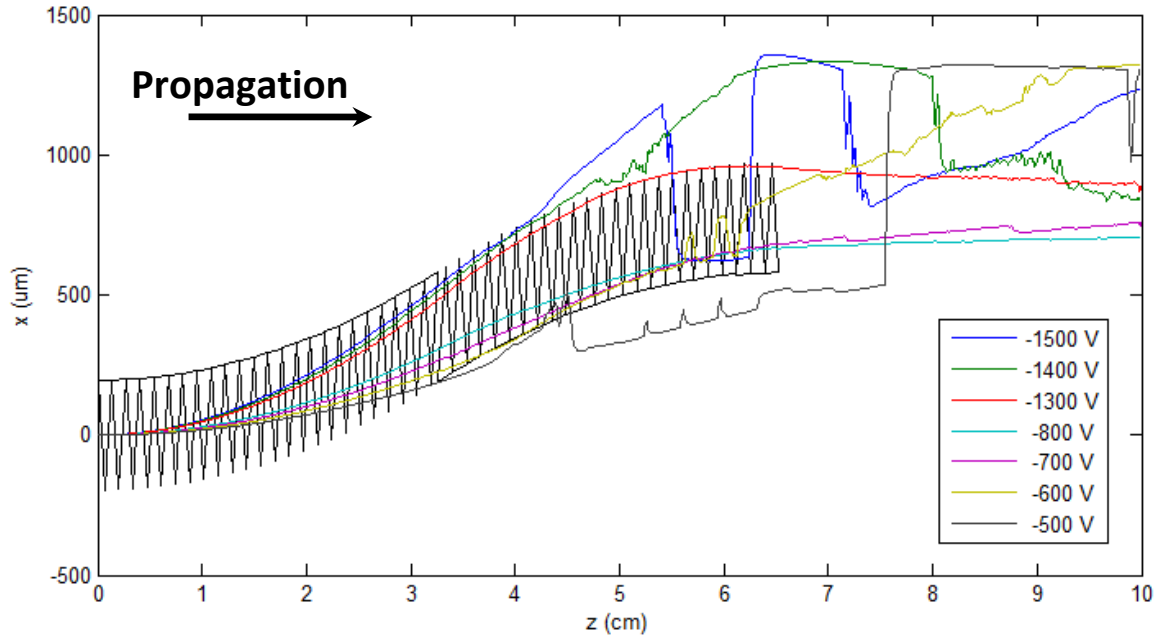


Figure 4.19 – Simulated beam paths for voltages $V = -500$ Volts to $V = -1500$ Volts
[In some cases, the center of amplitude is not descriptive of the beam path.]

Figure 4.20 clearly shows that, for the extreme case of $V_{\text{applied}} = -1500$ Volts, the beam is oversteered such that it intersects the top of the EOBS steering channel. Some of the beam experiences TIR effects in the lower stage of the EOBS and is then guided out through the upper stage. The result is two psuedo-parallel output beams which propagate at a severe angle relative to the optic axis of the device. Note that the reflection of the beam at the image boundary is an artifact of the simulation limit and is not physical.

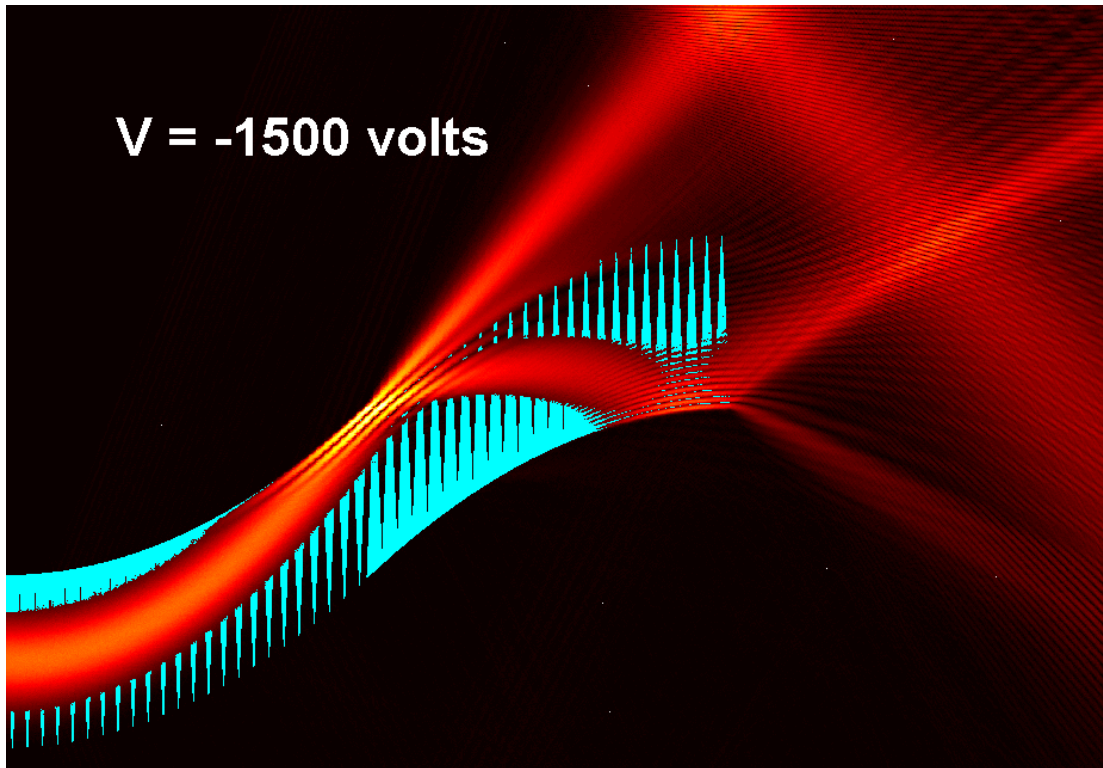


Figure 4.20 – Simulated beam propagation for voltage $V = -1500$ Volts.
[False reflection effects at edge of the simulation space can be seen at the top edge of the image.]

CHAPTER 5 – EXPERIMENTAL OBSERVATIONS

5.1 First Generation EOBS Chip Performance

5.1.1 Qualitative Observations of the First Generation EOBS Chips

Poled Domain Fidelity:

A pair of EOBS chips were fabricated from 5%MgO:CLN wafers purchased from *Crystal Technology, Inc.* [V10]. One of these chips, 'First Generation Chip #1,' had excellent domain fidelity. The other, 'First Generation Chip #2' exhibited comparably poor domain quality. Figure 5.1 and Figure 5.2 show the relative domain quality of these chips.



Figure 5.1 – The poled prisms of First Generation Chip 1 exhibit excellent quality.



Figure 5.2 – The poled prisms of First Generation Chip 2 exhibit poor quality.
[The discoloration is due to tarnishing of the gold electrode.]

First Generation Chip #1 (FGC-1) was expected to exhibit steering behavior that would closely resemble the beam propagation simulation performed in Chapter 4. First Generation Chip #2 (FCG-2) was not expected to perform well at all due to relatively poor domain quality.

Electrical Concerns:

The bulk electrical resistance of FGC-1 was measured to be $R_{FGC-1} = 1.8 \text{ M}\Omega$. The bulk electrical resistance of FCG-2 was measured to be $R_{FCG-2} = 1.5 \text{ M}\Omega$. According to Dr. Phil Battle of *AdvR Inc.*, metalized 5%MgO:CLN chips typically exhibit bulk electrical resistances $R \approx 1 \text{ G}\Omega$, that is, they are typically considered to be capacitors. He was surprised to hear that this chip exhibited such a low resistance.

5.1.2 Characterization of the First Generation EOBS Chips

Experimental Setup:

FGC-1 was placed into a mounting system designed to accurately position an EOBS chip within an optical experiment and to deliver the high-voltage control signal to the chip. The bottom of the mount was machined from a block of aluminum. The surface that contacts the chip was covered in indium foil to provide good electrical and thermal conductivity between the chip and the mount. This mount was designed to secure the EOBS chip and to serve as the grounding contact for the bottom electrode of the chip. Figure 5.3 shows an isometric view of the aluminum mount.

The upper mount was machined from a piece of clear plastic. This piece was designed to be bolted to the top of the aluminum chip mount and to house the high-

voltage BNC connector which delivers the control voltage to the EOBS chip. The EOBS mounting system was designed to be bolted to a six-axis stage so that the EOBS chip could be precisely positioned on an optical table. Figure 5.4 shows an isometric view of the whole mounting assembly.

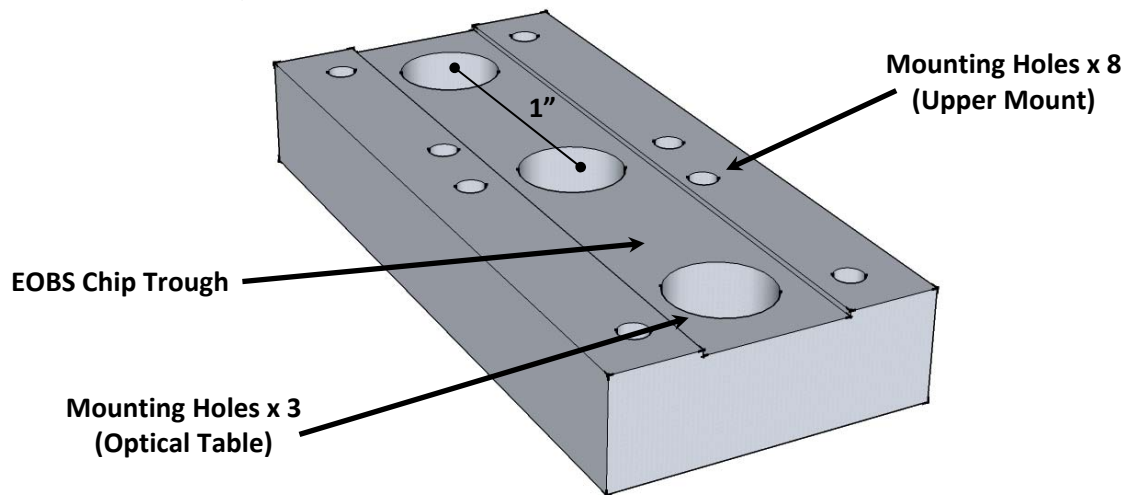


Figure 5.3 – The aluminum bottom of the chip mount for the first generation chips.

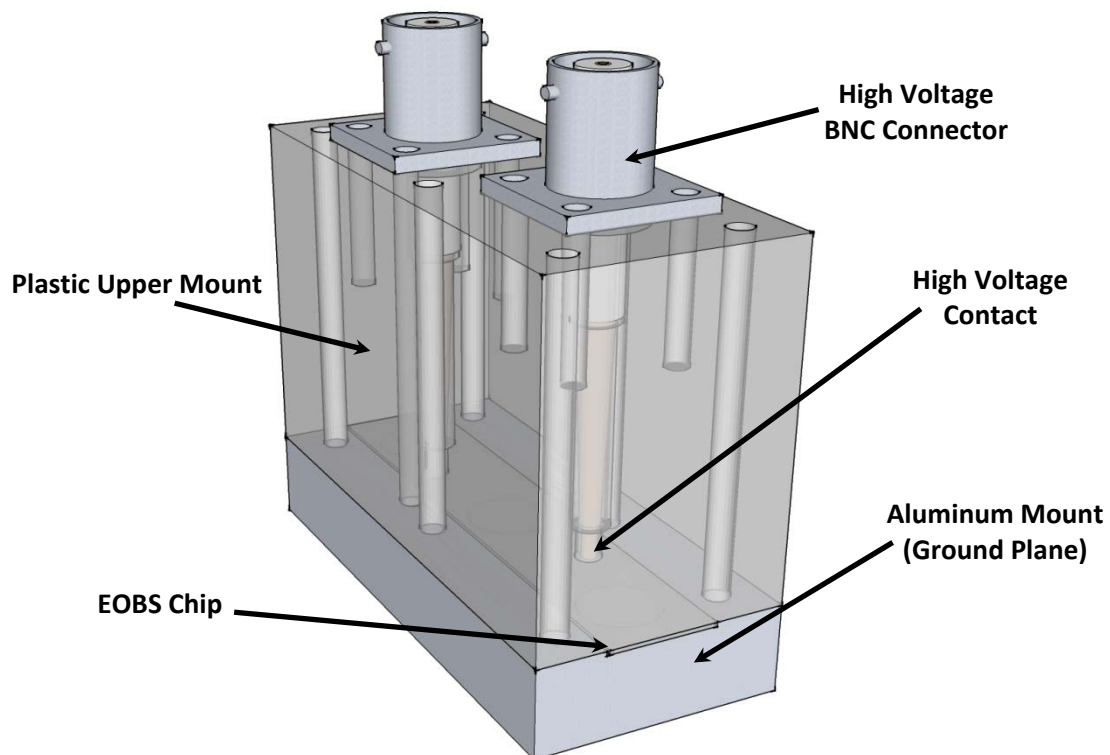


Figure 5.4 – The mounting assembly for the first generation EOBS chips.

FGC-1 was mounted as shown and placed into a characterization setup as shown in Figure 5.5.

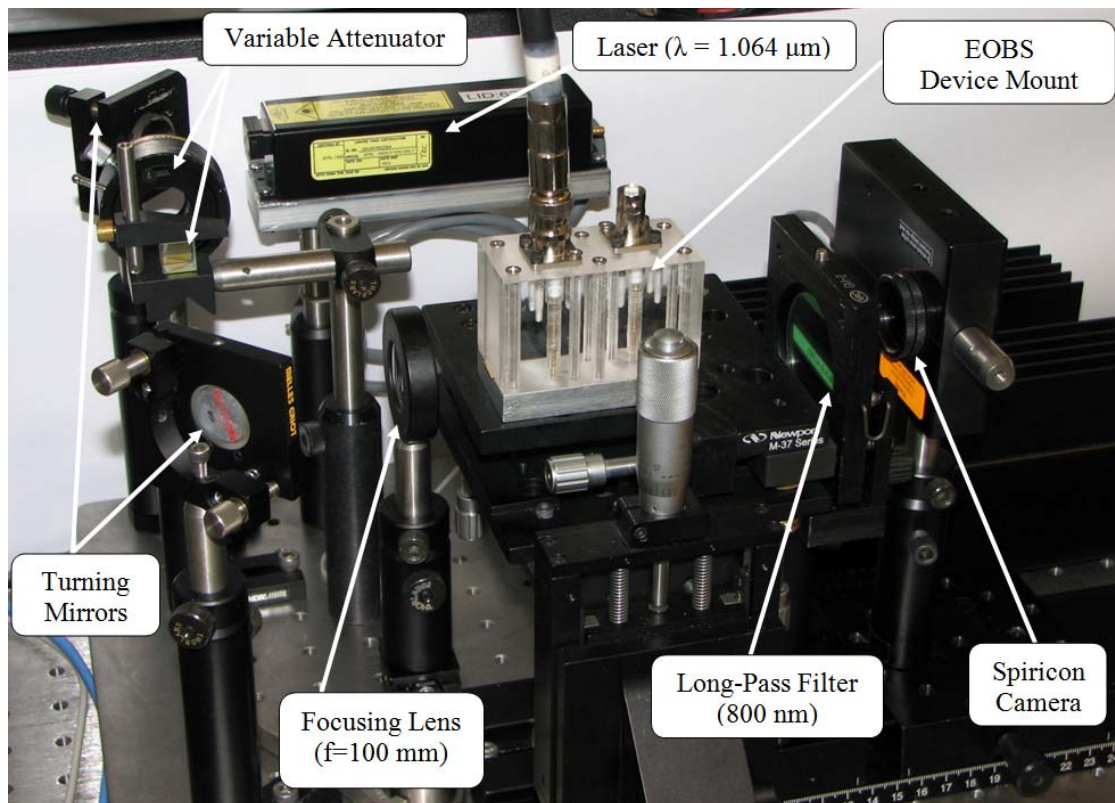


Figure 5.5 – The experimental setup for characterizing the EOBS.

The goal of this experiment was to characterize the response of FGC-1 by measuring the angular deflection imparted to the beam at applied voltages $0 \text{ Volts} < V_{\text{applied}} < -1000 \text{ Volts}$ in intervals of 100 volts (see Figure 5.6).

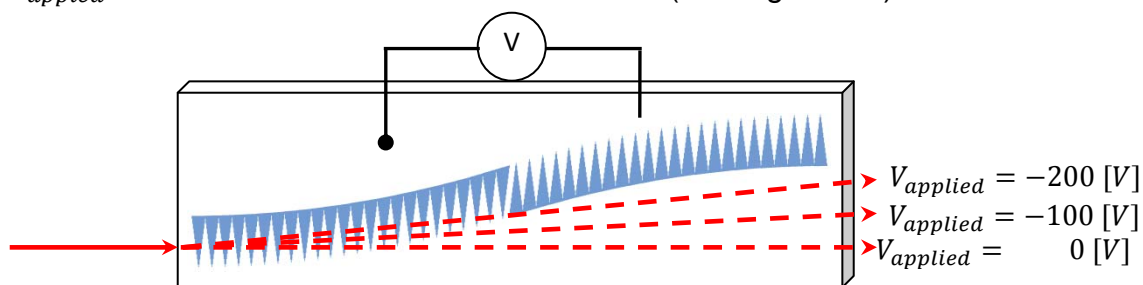


Figure 5.6 – A conceptual illustration of the characterization of an EOBS chip.

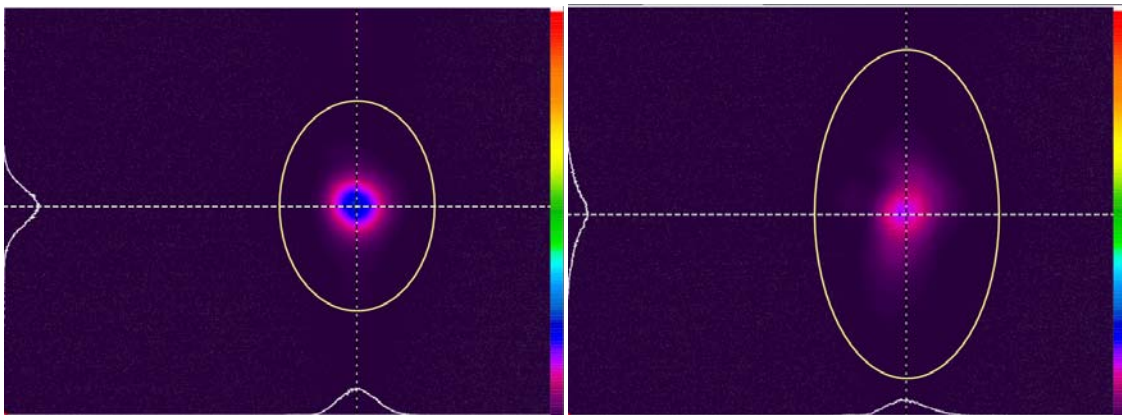
Qualitative Observations:

At $V_{\text{applied}} \approx -300 \text{ Volts}$ dielectric breakdown of the air between the gold electrode of the FCG-1 and the aluminum mount occurred. Figure 5.7 shows some vaporization to the chrome/gold electrode as a result of this breakdown.

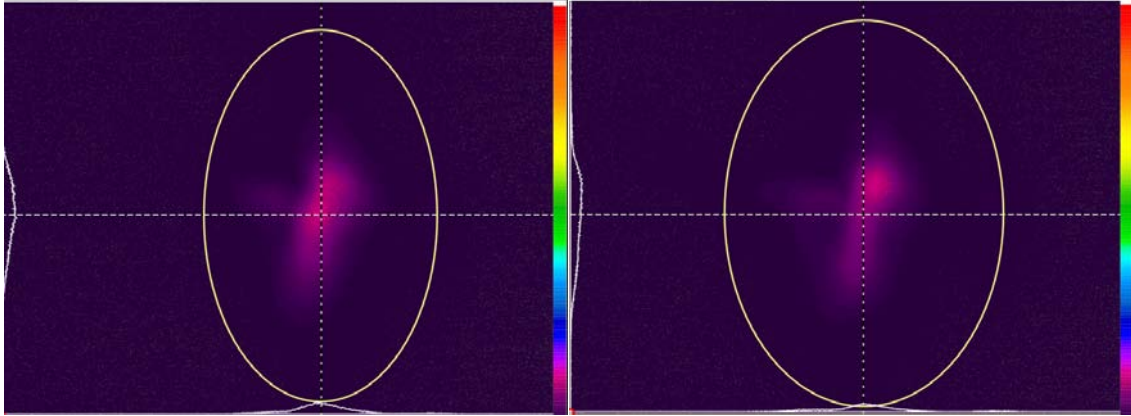


Figure 5.7 – Damage from dielectric breakdown of the air between the top electrode of FGC-1 and the aluminum mount.

Pieces of optical fiber were added as dielectric spacers between the edge of the chip and the inner edges of the aluminum mount to prevent dielectric breakdown of the air between them. Voltages as ‘large’ as $V = -1.3\text{ kV}$ were applied without dielectric breakdown. FGC-1 was aligned with the system shown in Figure 5.5 such that the beam went through Channel 1. Pictures of the output beam were collected at applied voltages $0\text{ Volts} < V_{\text{applied}} < -300\text{ Volts}$ in increments of 100 volts. Severe degradation of beam quality was observed over time (see Figure 5.8 and Figure 5.9).



**Figure 5.8 –The beamspot at $V_{\text{applied}} = 0\text{ Volts}$ (Left) and $V_{\text{applied}} = -100\text{ Volts}$ (Right).
[Note that each beam has a roughly Gaussian cross-section.]**



**Figure 5.9 – The beamspot at $V_{\text{applied}} = -200 \text{ Volts}$ (Left) and $V_{\text{applied}} = -300 \text{ Volts}$ (Right).
[Note that the Gaussian profile of the spot has deteriorated.]**

As seen in Figure 5.8 and Figure 5.9, the beam began to steer in the appropriate direction. However, after a short time, a great deal of beam distortion was observed. The applied voltage was ‘reduced’ to $V_{\text{applied}} = 0 \text{ Volts}$, and the distortion remained. The laser was turned off and the chip left to rest for an hour. The laser was turned back on and the beam distortion had disappeared. It seems likely that thermal lensing induced by the $P = V^2/R$ heating in the crystal was responsible for the distortion.

After allowing the device to rest, the laser was turned on and the applied voltages was ‘increased’ to $V_{\text{applied}} = -300V$. The distortion seen in Figure 5.8 and Figure 5.9 was not observed. The deflection angle of the output beam steering was demonstrated to vary proportionally to applied voltage. However, the EOBS chip suddenly and audibly shattered (Figure 5.10) at $V_{\text{applied}} \approx -800 \text{ Volts}$. This voltage had been achieved previously without incident, so it seems likely that the shattering was not due exclusively to the application of high voltage.

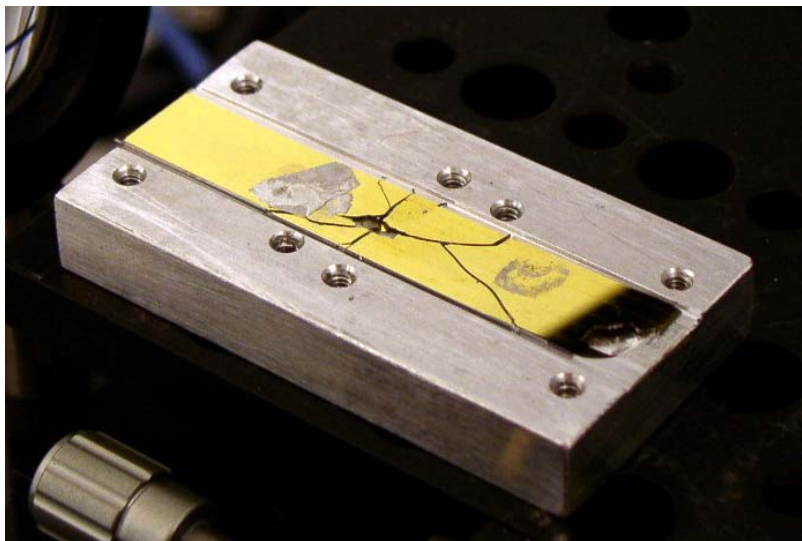


Figure 5.10 – A photograph of FGC-1 immediately after it shattered.

It has been hypothesized that non-uniform ohmic heating, due to the crystal's low resistance, caused enough stress within the crystal lattice that the chip shattered. It is unknown whether the resistance of the chip was uniform, or if the low resistance of the chip could be attributed to a few isolated regions of relatively high electrical conductivity. If such regions were created during the fabrication process, then the $P = V^2/R$ heating would have been non-uniform. Furthermore, the presence of mounting holes in the aluminum mount may have contributed to the development of a temperature gradient between regions of the crystal which were thermally isolated and regions of the crystal which were in strong thermal contact with the aluminum mount. Consequently, mitigation of ohmic heating (see Section 5.2.1) became a priority in the next iteration of EOBS chip and mount design.

Saving the EOBS Concept:

Due to the loss of FGC-1 and the poor domain quality of FGC-2, research proceeded along two parallel paths. First, an order was placed with *AdvR Inc.* for a second generation of EOBS chips. This topic is discussed in further detail in Section 5.2.1. Second, beam steering experimentations continued with FGC-2 in place of FGC-1.

Dr. Battle suggested, based on experience with 5%MgO:CLN devices at *AdvR Inc.*, that annealing FGC-2 would increase the bulk electrical resistance to $R_{FGC-2} \approx 1G\Omega$; this is a three order-of-magnitude increase in bulk resistance. As a consequence, the effects of $P = V^2/R$ heating should be minimized.

FGC-2 was sent to Dr. Sarangan of the University of Dayton. The chip was placed in an annealing oven and the temperature was increased by 25 C°/hour. The oven temperature was held at 550°C overnight. The temperature was lowered at the same rate. Figure 5.11 shows the temperature settings and anneal times for the EOBS chip. Note that the oven temperature had to be controlled manually, so there are multiple temperature settings which were held overnight.

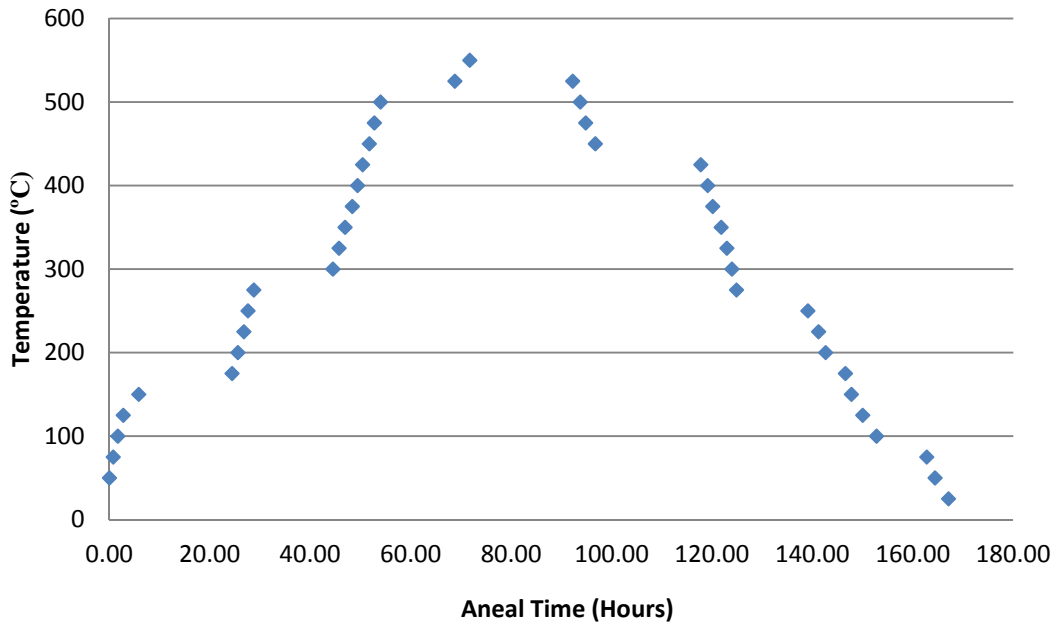


Figure 5.11 – The temporal temperature profile of the thermal annealing of FGC-2.

After the long thermal anneal the bulk electrical resistance of FGC-2 was high enough that it appeared as an ‘open-load’ to a *Fluke 45* multi-meter [V11]. From the multi-meter manual, the maximum resistance that the multi-meter can measure is $R = 300\text{ M}\Omega$. Thus, the bulk electrical resistance of the device is known to be $R_{FGC-2} > 300\text{ M}\Omega$. The gold electrodes of FGC-2 were tarnished, but the surface resistance of the electrode was measured to be $R_{surface} \approx 0.2\ \Omega$. Figure 5.12 shows FGC-2 after the thermal anneal.

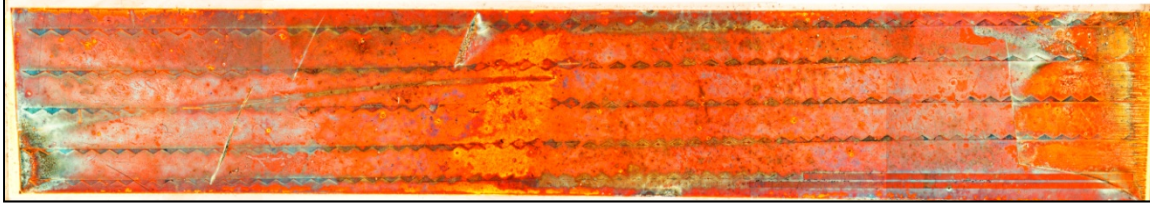


Figure 5.12 – FGC-2 after the thermal annealing process.

FGC-2 Steering Performance

The experimental setup for characterizing EOBS chips was modified slightly. The system was reconfigured to allow OPG stages to be added to the beam path after the EOBS chip. Because the OPG process requires a strong pump laser, the *Nanopulse*¹² laser was replaced with a *Spectra-Physics T-Series*¹³ laser. The opto-mechanics of the previous setup also had to be spread out over wider area on the optical table to allow space for the additional OPG stages. Figure 5.13 shows the setup used to evaluate FGC-2.

¹² $\Delta t_{pulse} = 0.7\text{ ns}$, $P_{avg} = 36.3\text{ mW}$, $P_{peak} = 7.57\text{ kW}$, $PRF = 6.85\text{ kHz}$

¹³ $\Delta t_{pulse} = 31.9\text{ ns}$, $P_{avg} > 1\text{ W}$, $P_{peak} > 3.1\text{ kW}$, $PRF = 10\text{ kHz}$

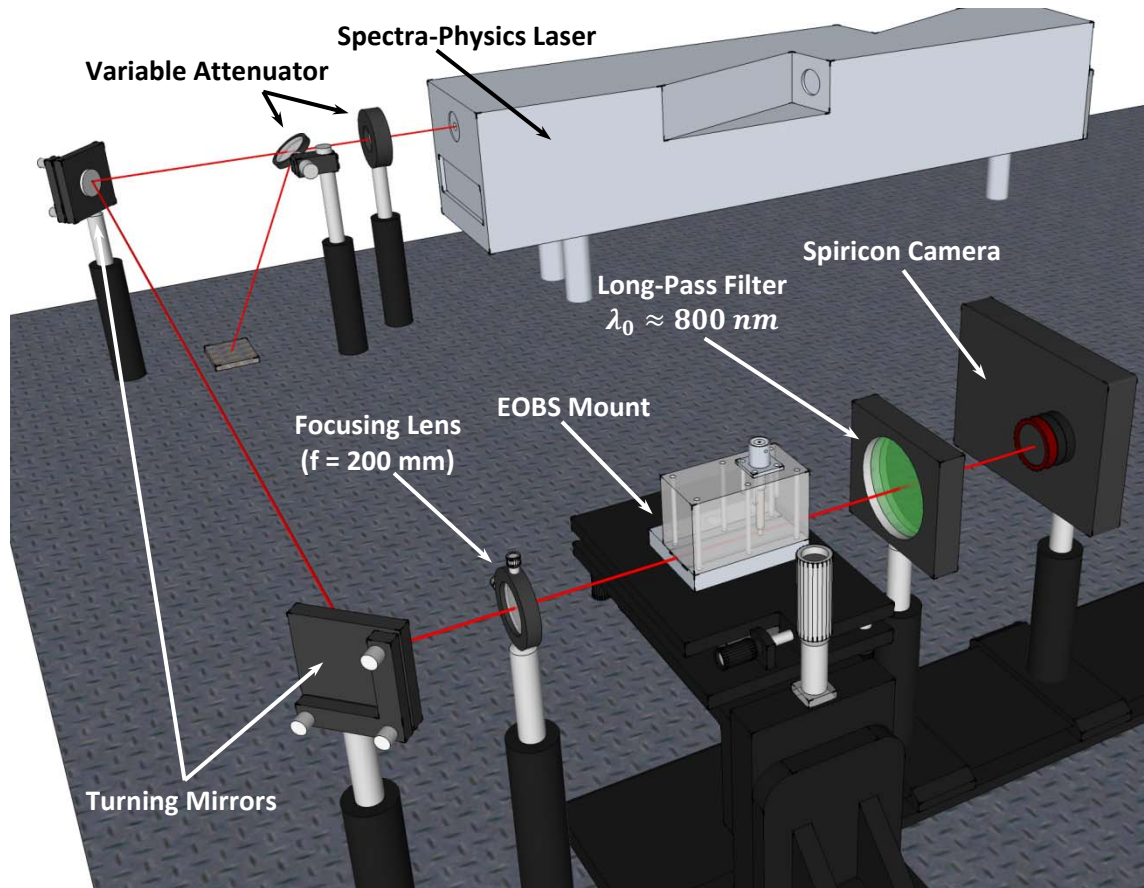


Figure 5.13 – The experimental setup for measuring the effective electro-optic coefficient.

FGC-2 was placed into the experimental setup. Unlike FGC-1, FGC-2 was modulated with positive voltages (see Figure 5.14).

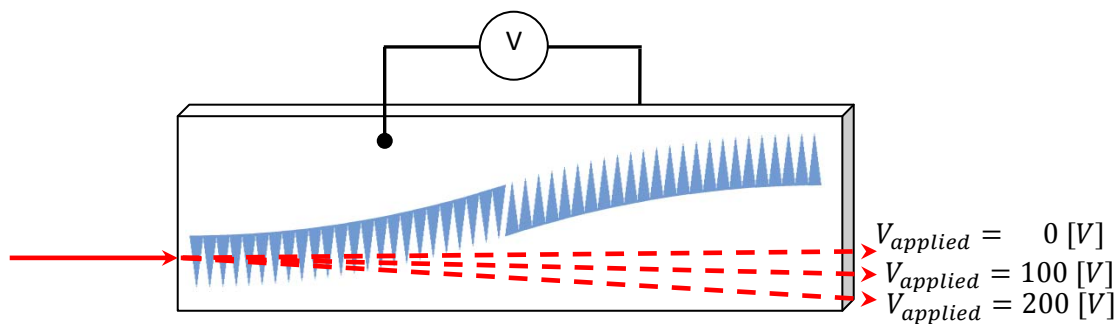


Figure 5.14 – A conceptual illustration of the characterization of an EOBS chip.

A *Spiricon SP620U* beam-profiling camera [V12] and *Beam-Gage* software were used to capture and average fifty frames of beam data for each case from $V_{\text{applied}} = 0$ Volts to $V_{\text{applied}} = 500$ Volts in increments of 100 Volts. For each applied voltage case, the beamspot location was recorded at two points, z_1 and z_2 , along the optic axis of the system. Table 5.1 shows the measured center of amplitude (CoA) data.

Table 5.1 – Beam deflection data taken with the *Spiricon* beam profiling camera.

Applied Voltage (Volts)	At $z_1 = 19$ cm				At $z_2 = 20$ cm			
	x-dimension (μm)		y-dimension (μm)		x-dimension (μm)		y-dimension (μm)	
	CoA Location	CoA StdDev	CoA Location	CoA StdDev	CoA Location	CoA StdDev	CoA Location	CoA StdDev
0.0	1902.934	0.281	870.031	0.328	1881.138	0.365	861.612	0.381
100.5	1992.004	0.332	868.335	0.332	1984.422	0.648	858.976	0.418
199.8	2209.573	0.472	866.203	0.371	2227.686	1.270	856.974	0.453
300.3	2361.056	1.082	865.150	0.452	2411.500	1.250	856.975	0.530
399.6	2576.192	0.856	859.150	0.336	2644.457	1.099	849.290	0.408
499.9	2819.560	0.384	851.805	0.264	2917.980	0.436	842.190	0.336

Using the data in Table 5.1, the straight-line trajectory can be calculated by writing the equation of the line in two-point form:

$$\frac{x - x_1}{x_2 - x_1} = \frac{y - y_1}{y_2 - y_1} = \frac{z - z_1}{z_2 - z_1} \quad (5.1)$$

Rearranging, the line can be written as a function of z :

$$y = (z - z_1) \cdot \frac{y_2 - y_1}{z_2 - z_1} + y_1 \quad (5.2)$$

$$x = (z - z_1) \cdot \frac{x_2 - x_1}{z_2 - z_1} + x_1 \quad (5.3)$$

Figure 5.15 shows the straight-line trajectories as calculated in MATLAB [M6].

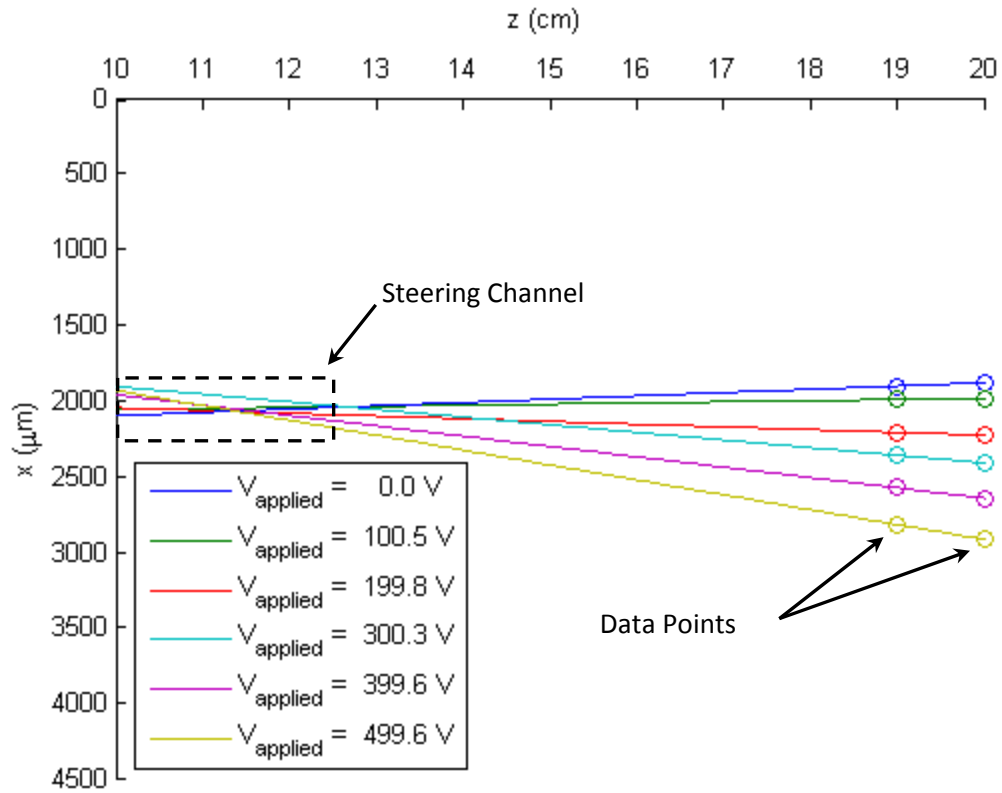


Figure 5.15 – Beam trajectories calculated from two center of amplitude points.

Recall that beam propagation simulation in *LIGHTS* (Chapter 4) predicts negative angular deflection of the beam at positive voltages (see Figure 4.18). Figure 5.16 shows calculated trajectory of the steered beam at discrete intervals of 100 volts.

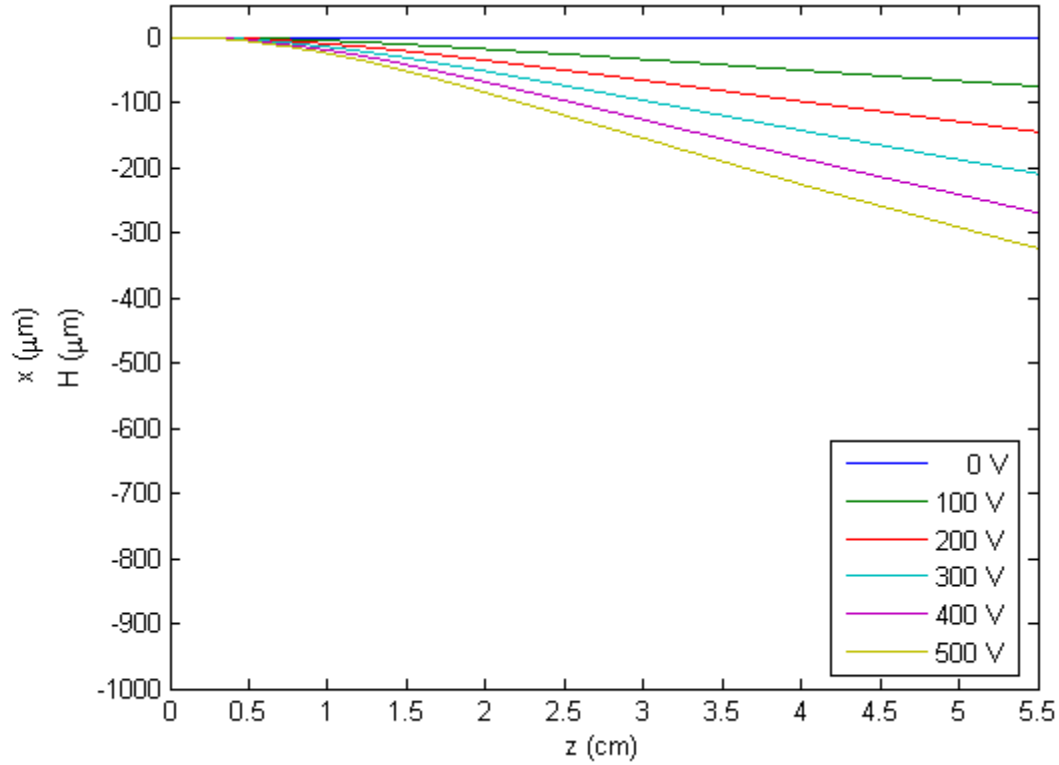


Figure 5.16 – The trajectory of the steered beam in response to an applied voltage. [Simulated in LIGHTS]

Comparing Figure 5.15 and Figure 5.16, it is clear that the measured and calculated trends are qualitatively similar. For a quantitative comparison it is important to consider that the data set shown in Figure 5.15 was taken in air; whereas, the beam propagation simulation is simulating the diffraction of the beam in 5%MgO:CLN.

To compare the experimental behavior of FGC-2 with the predicted behavior of the LIGHTS simulation, the angular deflection of the beam relative to the $V_{applied} = 0 \text{ Volts}$ case was calculated. Consider the geometry of this problem as shown in Figure 5.17.

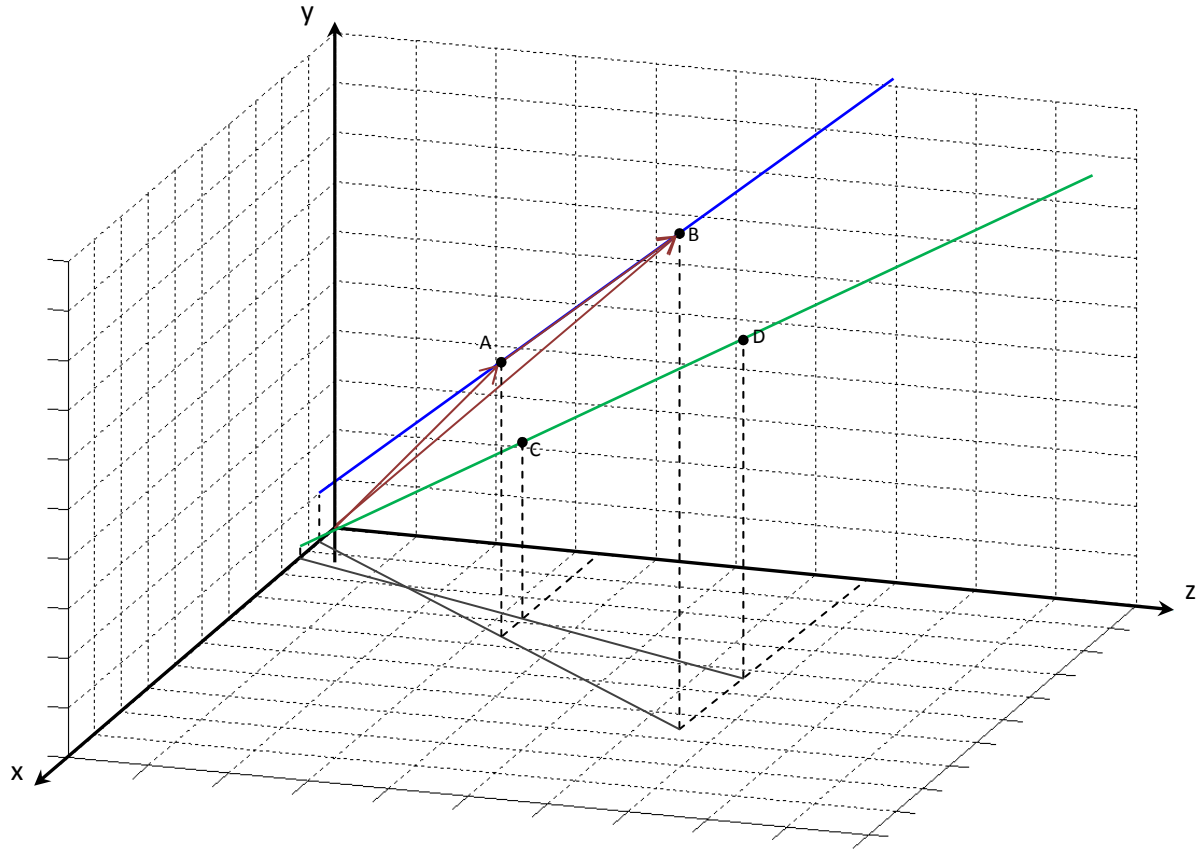


Figure 5.17 – The geometry of steered beams in an arbitrary Cartesian coordinate system.
[Note that, in general, neither \overline{AB} nor \overline{CD} contain the origin.]

Consider two points A and B measured at z_1 and z_2 respectively with $V_{\text{applied}} = 0 \text{ Volts}$. Consider also two points C and D measured at z_1 and z_2 respectively with $V_{\text{applied}} \neq 0 \text{ Volts}$. If the EOBS chip functions as expected, points A, B, C , and D should be co-planar (see Figure 5.16). However, since the location of the intersection of the trajectories is unknown (and may not actually exist), it is more straightforward to calculate the angle between them from a vector treatment of the points A, B, C , and D .

From Figure 5.17:

$$\vec{B} = \vec{A} + \overrightarrow{AB} \quad (5.4)$$

Therefore:

$$\overrightarrow{AB} = \vec{B} - \vec{A} \quad (5.5)$$

Similarly:

$$\overrightarrow{CD} = \vec{D} - \vec{C} \quad (5.6)$$

Recall:

$$\cos \theta = \frac{\vec{AB} \cdot \vec{CD}}{|\vec{AB}| |\vec{CD}|} \quad (5.7)$$

Therefore:

$$\theta = \arccos \left[\frac{\langle x_{AB}, y_{AB}, z_{AB} \rangle \cdot \langle x_{CD}, y_{CD}, z_{CD} \rangle}{\sqrt{x_{AB}^2 + y_{AB}^2 + z_{AB}^2} \times \sqrt{x_{CD}^2 + y_{CD}^2 + z_{CD}^2}} \right] \quad (5.8)$$

where:

$$\psi_{AB} = \psi_B - \psi_A \quad (5.9)$$

where ψ is x, y , or z . Thus, it is straightforward to use MATLAB [M6] to calculate $\theta_{deflection}$ as a discrete function of voltage.

Calculating the deflection angle $\theta_{deflection}$ from the results of the beam propagation simulation is straightforward. For any two points (x_1, z_1) and (x_2, z_2) , which are not in the steering region ($z < 3.0 \text{ mm}$) and which lie on a beam path calculated for a constant value of $V_{applied}$, the steering angle within the EOBS can be found by:

$$\theta_{deflection} = \arctan \left(\frac{x_2 - x_1}{z_2 - z_1} \right) \quad (5.10)$$

This simulation was performed under the assumption that the beam propagates in 5%MgO:CLN. Snell's law can be used to transform the angle inside the crystal to an angle outside the crystal. The free-space deflection angle can be calculated:

$$\theta_{free-space} = \arcsin \left(\frac{n_{5\%MgO:CLN}}{n_{air}} \cdot \sin \left(\arctan \left(\frac{x_2 - x_1}{z_2 - z_1} \right) \right) \right) \quad (5.11)$$

Figure 5.18 shows a plot of the measured deflection angle of the steered beam relative to the $V_{applied} = 0 \text{ Volts}$ case, and a plot of the external deflection angle as calculated in LIGHTS.

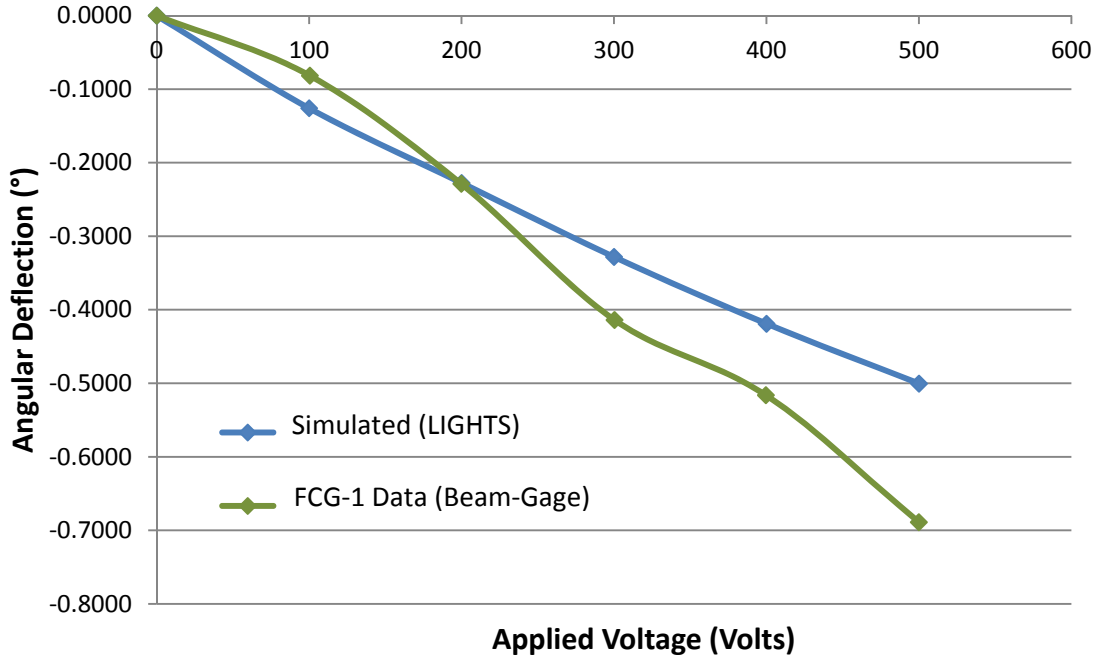


Figure 5.18 – Simulated values of angular beam deflection imparted by EOBS Channel 1 and experimental values of angular beam deflection imparted by FGC-2 Channel 1.

If each prism within the steering channel ‘sees’ the same electrical and optical environment, the simulated and experimental voltage response curves should have similar shapes. Thus, the responses of these channels can be compared in terms of an effective electro-optic coefficient $r_{33,eff}$. If $r_{33,eff} > r_{33,assumed}$ the data curve should be scaled to the left of the simulation curve. Conversely, if $r_{33,eff} < r_{33,assumed}$ the data curve should be scaled to the right of the simulation curve. From Figure 5.18, the relationship between $r_{33,assumed}$ and $r_{33,eff}$ is unclear. It is, however, clear that $r_{33,assumed}$ and $r_{33,eff}$ are on the same order of magnitude.

If $r_{33,assumed} \neq r_{33,eff}$, the EOBS can still be made to function properly by adjusting the ON-state voltage V_{ON} . Recall that the shift in the refractive index of each prism is given by Equation (3.10):

$$n'_e(\lambda, V, T, r_{33}) = n_e(\lambda, T) - \frac{1}{2} r_{33} n_e^3(\lambda, T) \cdot \frac{V}{Z}$$

By inspection, Δn is linearly dependant on the electro-optic coefficient r_{33} and the applied voltage $V_{applied}$. Thus, any uncertainty in the value of r_{33} that arises due to dispersion of the electro-optic coefficient (r_{33} is slightly wavelength dependent [19] and was measured at $\lambda = 632.8 \text{ nm}$; whereas the steered laser has a wavelength $\lambda = 1.064 \mu\text{m}$) can be exactly compensated for by adjusting the applied voltage (this concept is explored in greater detail in *Appendix B*).

However, if the value of r_{33} is too highly overestimated when the EOBS is designed, the $V_{applied}$ required to compensate for the reduction in r_{33} may be so large that the coercive field E_c of the 5%MgO:CLN chip will be exceeded. If a $V_{applied} > Z \cdot E_c$

is applied to the EOBS, it will (most likely) destroy the carefully engineered domains responsible for deflecting the beam. The coercive field of 5%MgO:CLN is $E_c \approx 6.8 \text{ kV/mm}$ [28]. Consequently, for an EOBS chip of thickness $Z = 0.5 \text{ mm}$, the maximum permissible applied voltage is $V_{\text{applied,max}} = \pm 3200 \text{ Volts}$. Thus, it seems unlikely that compensatory control voltages would induce electric fields which exceed the coercive field.

Beam Quality Observations:

Due to the relatively poor quality of the poled domains (see Figure 5.2), the quality of the steered beam was considerably worse than the unsteered beam. The Gaussian structure of the steered laser spot was somewhat intact, but significant spatial distortion and additional noisy features were evident. However, the shape of the output spot did not change with time. This behavior stands in contrast to FCG-1 (which was not thermally annealed), in which significant beam distortions could be observed to evolve over time when voltage was applied.

The lack of such effects when using the annealed chip is consistent with the theory that the distortion effects observed in FGC-1 were due to nonuniformities in ohmic heating of the chip. This result suggests that thermally annealing future EOBS chips will prevent the recurrence of time-dependant beam distortions like those observed in FGC-1.

Beam switching Observations:

If the EOBS operates as designed, the straight line trajectory of the steered output beam should be parallel to the unsteered output beam. If the optics are all well aligned, then in either the ON or OFF state of the EOBS, the center of amplitude location of the beamspot on the beam-profiling camera should remain the same as the camera moves along the optic axis. Each beamspot should diffract and expand as the output beam propagates away from the EOBS, but the center of amplitude of the beam should not translate. To first order, this kind of behavior was observed with the annealed first generation EOBS chip. At $V_{\text{applied}} = -890 \text{ Volts}$ (significantly lower in magnitude than the design point: $V_{\text{applied}} = -1000 \text{ Volts}$), the output of Channel 1 of the annealed first generation EOBS chip was mostly stationary as the camera was moved along an optical rail over a range of $\sim 10 \text{ cm}$. The separation of the centers of amplitude of the ON and OFF state outputs was also on the order of the expected beam translation, $\sim 750 \text{ }\mu\text{m}$. This visual inspection does not account for deviations of the true optical axis from the rail, but it is another indication that the second generation EOBS chips are likely to perform as designed.

Another Broken Chip:

Unfortunately, while loosening the screws on the chip mount in order to double-check the alignment of the chip, the chip made an audible ‘crack.’ The chip appeared to be unharmed, though the input beam would no longer propagate through it. The chip was successfully removed from its mount and placed under a microscope. When the chip contacted the microscope stage, the chip separated along the small crack which had formed across the chip. Figure 5.19 shows the broken EOBS chip.

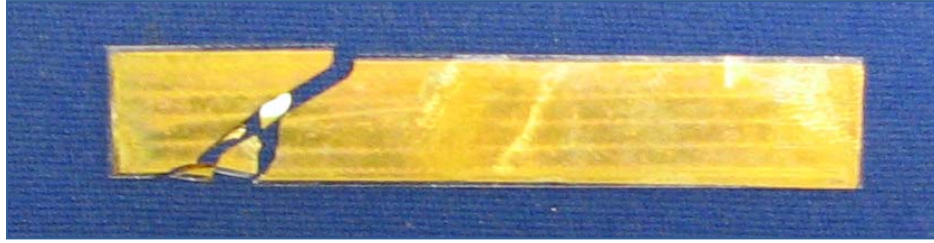


Figure 5.19 – A photograph of FGC-2 immediately after it was broken.

5.2 Second Generation EOBS Chip Performance

5.2.1 Design changes to the Second Generation EOBS Chips

Mitigation of Ohmic Heating:

Dr. Battle reported that only chips manufactured from 5%MgO:CLN wafers from *Crystal Technology, Inc.* exhibited lower-than-expected resistances after poling and metallization. The exact cause of this behavior is unknown, but it was not exhibited in metalized chips manufactured from 5%MgO:CLN wafers from *Yamaju Ceramics Co.* [V13]. *Yamaju*-brand wafers still exhibited bulk electrical resistances $R > 100 M\Omega$ when metalized. Thus, the second generation EOBS chips fabricated from *Yamaju*-brand wafers.

AdvR Inc. began the fabrication of a second pair of EOBS chips. Due to the success of annealing FGC-2, both chips were thermally annealed overnight at 550°C after they were poled. After metallization, the bulk electrical resistances of the chips were measured to be $R_{chip\ 1} \approx 100 M\Omega$ and $R_{chip\ 2} \approx 300 M\Omega$. Only chip #2 was annealed after metallization because it is common for 5%MgO:CLN to shatter under the influence of its own pyroelectricity [31], when heated.

Mitigation of Dielectric Breakdown:

Due to the dielectric breakdown issues experienced with FGC-1 (see Figure 5.10), the second generation chip design included a 3 mm wide bare region between the gold electrodes and the edge of the chip. The addition of this region resulted in a chip design that was 6 mm longer and 6 mm wider than the first generation chip design.

EOBS Chip Mount Redesign:

Because of the increased size of the second generation chips, the EOBS chip mount had to be redesigned and refabricated. The mount was elongated and the chip trough was widened to accommodate the second generation chips. In order to avoid repeating the damage done to FCG-1, the trough depth was increased from 0.5 mm (the nominal thickness of an EOBS chip) to 1.5 mm so that there would be no mechanical clamping of the EOBS chip. Furthermore, the optical table mounting holes were moved outside of the chip trough so that the environment underneath the EOBS chip would be more thermally uniform. Figure 5.20 shows an isometric view of the second generation EOBS chip mount.

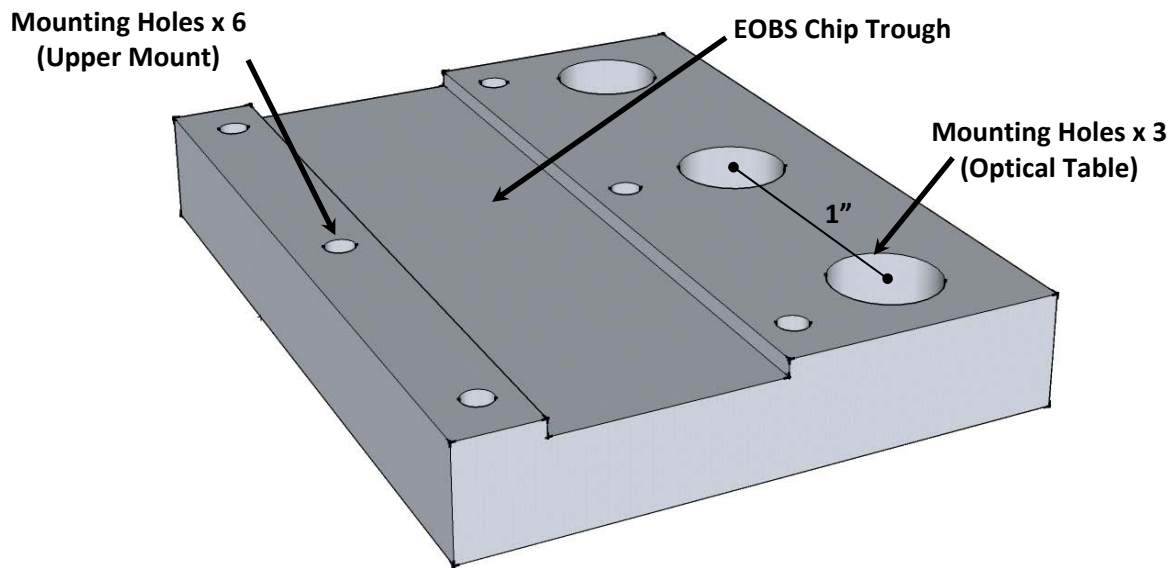


Figure 5.20 – The aluminum bottom of the second generation EOBS chip mount.

The upper portion of the mount was also redesigned and fabricated to fit the second generation EOBS chip mount. Figure 5.21 shows an isometric view of the chip mounting assembly.

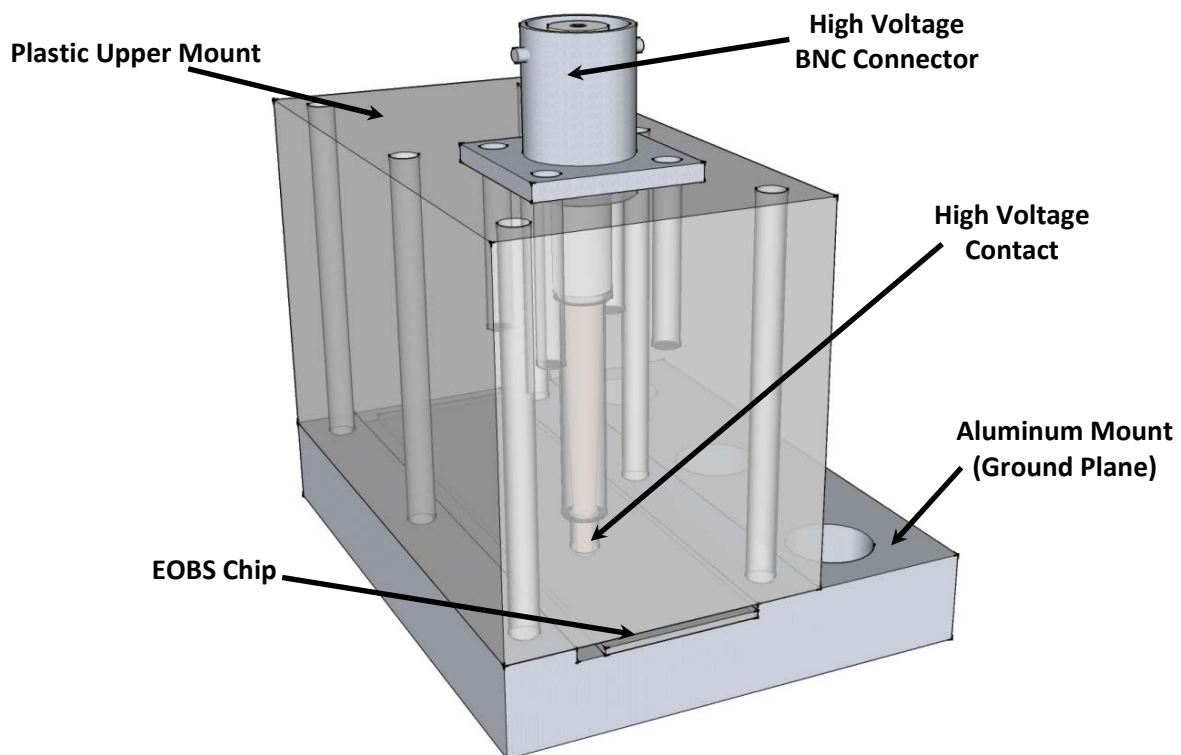


Figure 5.21 – The second generation EOBS chip mounting assembly.

Reduction of Fabrication Costs and Lead Time:

The end facets of the second generation EOBS chips were not AR-coated to lower the overall cost of fabrication. Electing not to include AR-coatings also shortened the fabrication considerably.

5.2.2 Qualitative Observations of the Second Generation EOBS Chips

A second pair of EOBS chips were fabricated from 5%MgO:CLN wafers purchased from *Yamaju Ceramics Co.* Second Generation Chip #1 (SGC-1) was not thermally annealed after metallization. Second Generation Chip #2 (SGC-2) was thermally annealed after metallization. During the annealing process, it suffered a fracture that destroyed three of the five steering channels. This fracture went through the metalized region of the chip; consequently, the edge of the chip had to be coated with nitrocellulose lacquer to prevent dielectric breakdown across the edge of the chip. Figure 5.22 and Figure 5.23 show composite photographs of these chips.

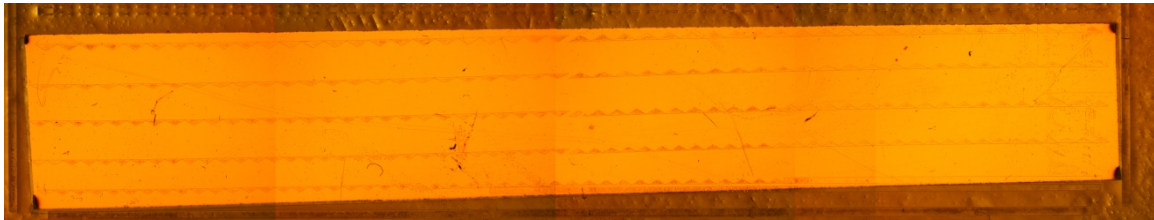


Figure 5.22 – Second Generation Chip #1

[Note that the gold electrode was applied relative to the steering channels and is oriented at an angle relative to the edges of the chip. The channels are completely metalized and steering performance should not be affected.]



Figure 5.23 – Second Generation Chip #2

[Note the missing pieces of the chip on the left.]

Poled Domain Fidelity:

‘Second Generation Chip #1’ and ‘Second Generation Chip #2’ exhibited excellent domain quality. Both Second Generation Chip #1 (SGC-1) and Second Generation Chip #2 (SCG-2) were expected to exhibit steering behavior that would closely resemble the beam propagation simulation performed in Chapter 4. Figure 5.24 and Figure 5.25 shows the relative domain quality of these chips.

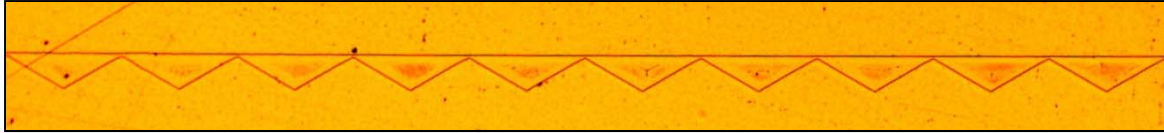


Figure 5.24 – The poled prisms of SGC-1 exhibit excellent domain quality.

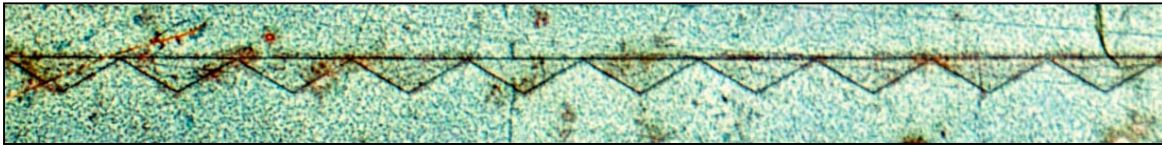


Figure 5.25 – The poled prisms of SGC-2 exhibit excellent domain quality.
[The discoloration is due to tarnishing of the gold electrode.]

Electrical Concerns:

The bulk electrical resistance of SGC-1 was measured to be $R_{SGC-1} = 90.8 \text{ M}\Omega$. The bulk electrical resistance of SCG-2 was measured to be $R_{SCG-2} > 300 \text{ M}\Omega$.

5.2.3 *Characterization of the Second Generation EOBS Chips*

SGC-1 and SCG-2 were both evaluated in the same manner as FGC-2 (See pp. 96, 97). The *Spiricon* beam-profiling camera was used to capture beam data for each case from $V_{\text{applied}} = 0 \text{ Volts}$ to $V_{\text{applied}} = 500 \text{ Volts}$ in increments of 100 Volts. For each of these cases, fifty frames of beam data were recorded at each point, z_1 and z_2 , along the optic axis of the system. MATLAB was employed to perform frame-averaging of the data collected at each point [M7]. Figure 5.26 shows a typical frame-averaged image of the steered beam.

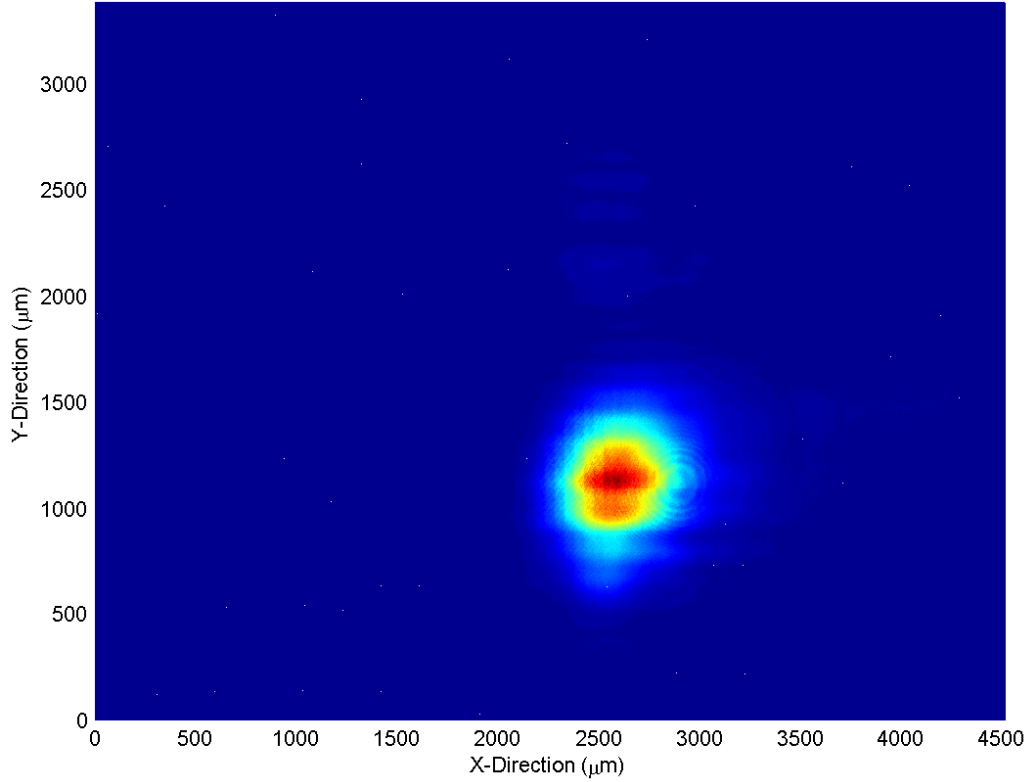


Figure 5.26 – A typical frame-averaged image of the steered beam.

For the ideal case of a perfect Gaussian beam cross-section, the coordinates of the amplitude peak provide an adequate description of the beamspot location in the measurement plane. From Figure 5.26 it is clear that the steered beam was not perfectly Gaussian. Thus, two mathematical techniques were used to determine the coordinates of a single-point which adequately described the location of the steered beam.

The Center of Amplitude Location Technique:

Recall that the standard equation for the center of mass \vec{R} of an object is:

$$\vec{R} = \frac{\sum m_i \vec{r}_i}{\sum m_i} \quad (5.12)$$

where m_i is the mass of the i^{th} particle whose location is \vec{r}_i .
More explicitly:

$$(x_R, y_R) = \left(\frac{\sum_{x,y} [A(x,y) \cdot x]}{\sum_{x,y} [A(x,y)]}, \frac{\sum_{x,y} [A(x,y) \cdot y]}{\sum_{x,y} [A(x,y)]} \right) \quad (5.13)$$

where $A(x,y)$ is the value of the frame-averaged beam data at (x,y) .

Expected Value Filtering Technique:

Recall the discrete convolution equation:

$$g * h = \sum_{x,y} g(\psi, \eta) h(x - \psi, y - \eta) \Delta\psi \Delta\eta \quad (5.14)$$

where $g(x, y)$ is the two-dimensional signal and $h(x, y)$ is the two-dimensional filter envelope. Recall that the steered beam is expected to have a Gaussian cross-section thus an appropriate filter can be expressed:

$$h(x, y) = \frac{1}{\sqrt{2\pi\sigma^2}} e^{-\frac{x^2+y^2}{2\sigma^2}} \quad (5.15)$$

where σ^2 is the variance of the Gaussian distribution. Thus the filtered frame can be expressed:

$$F(x, y) = \sum_{x,y} A(\psi, \eta) \frac{1}{\sqrt{2\pi\sigma^2}} e^{-\frac{(x-\psi)^2+(y-\eta)^2}{2\sigma^2}} \Delta\psi \Delta\eta \quad (5.16)$$

Thus, if the frame-averaged data is convolved with a Gaussian distribution, it will appear more Gaussian than the original frame. Figure 5.27 shows the results of such filtering of the frame shown in Figure 5.26 as performed in MATLAB [M7]. Note that the high spatial frequency features of the original image have been filtered out.

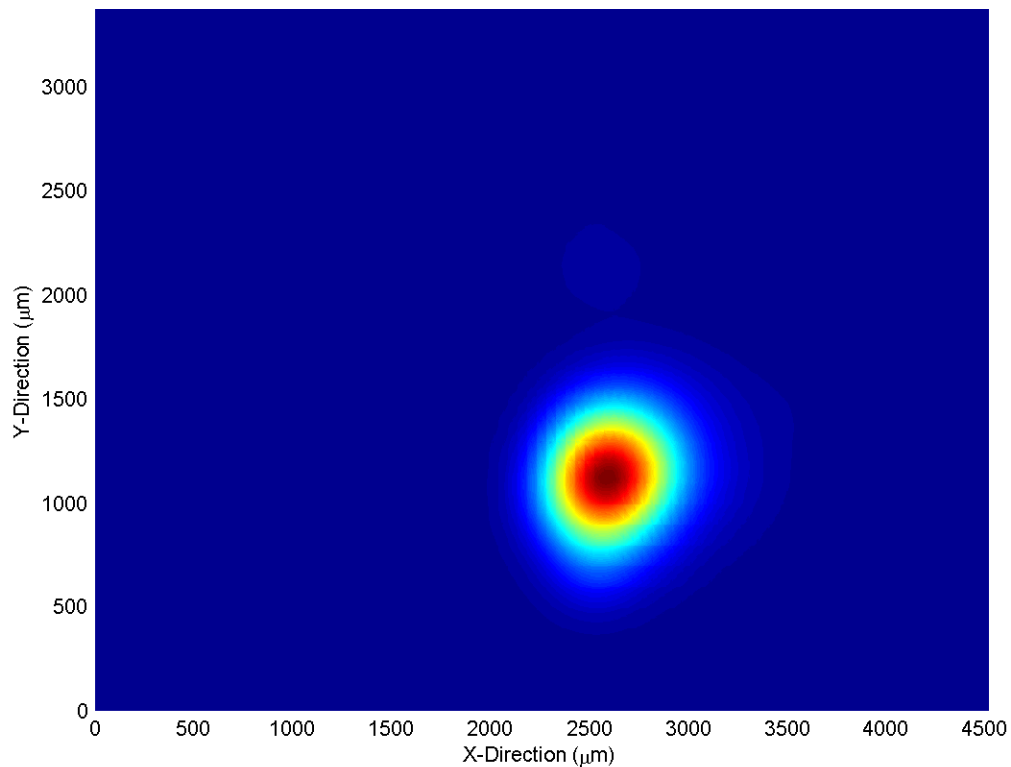


Figure 5.27 – A typical data frame after Gaussian filtering.

The single-point beam location of the original frame is then selected to be the location of the maximum value of the filtered frame.

Beam Locations of Distorted Beamspots

Figure 5.28 shows the single-point beam location of a distorted beam cross-section as determined by three selection methods. The insufficiency of the peak-location method is clearly seen. For the case shown, both the center of amplitude and Gaussian filter methods find the single-point beamspot location to be near the apparent center of the amplitude profile of the beamspot. Further analyses requiring calculation of the beamspot location will utilize and compare both methods.

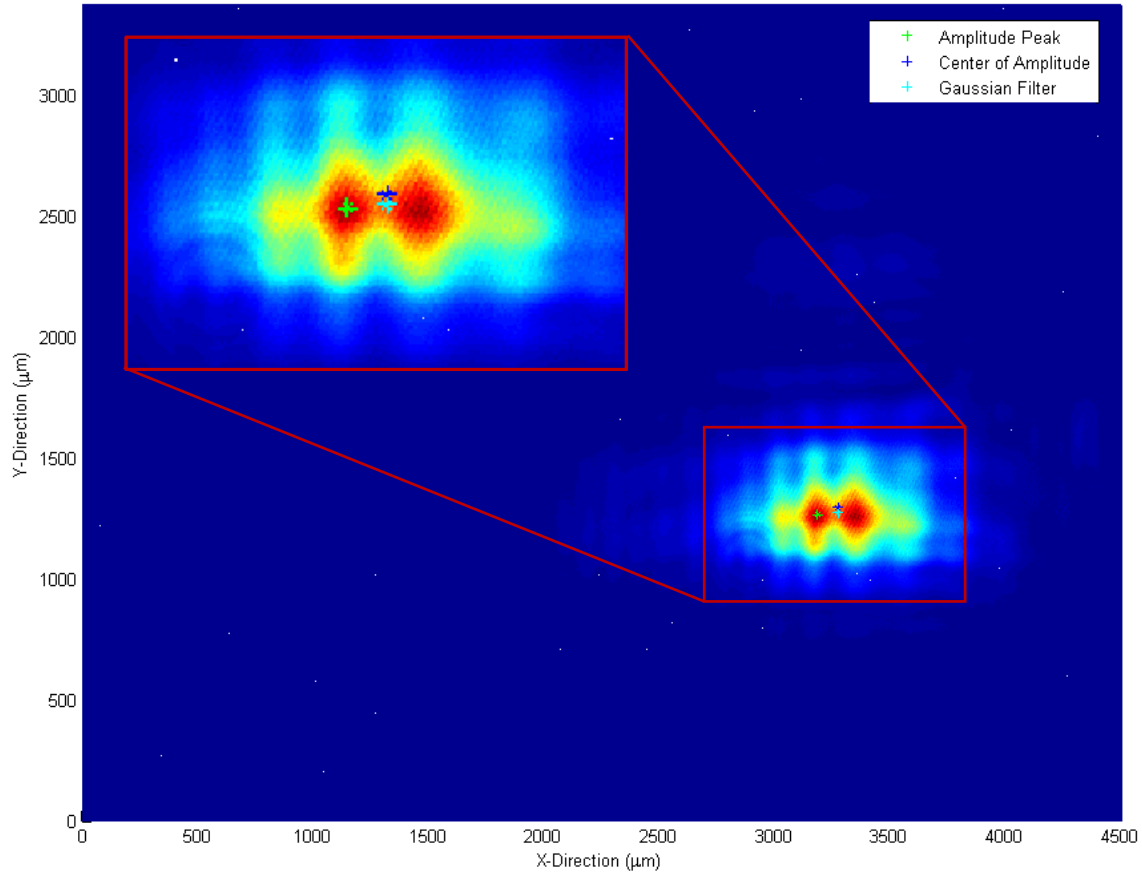


Figure 5.28 – The beam location of a distorted beamspot.

SGC-1 Steering Performance (Positive Voltages)

Table 5.2 shows the single-point beamspot location data for SGC-1 as calculated by the center of amplitude and Gaussian filter methods respectively.

Table 5.2 – Beam deflection data for SGC-1 at positive values of $V_{applied}$.

Applied Voltage (Volts)	Center of Amplitude				Gaussian Filter			
	At $z_1 = 15$ cm		At $z_2 = 16.5$ cm		At $z_1 = 15$ cm		At $z_2 = 16.5$ cm	
	x-dim (μm)	y-dim (μm)	x-dim (μm)	y-dim (μm)	x-dim (μm)	y-dim (μm)	x-dim (μm)	y-dim (μm)
0.0	2339.9	1781.6	2323.9	1872.4	2327.6	1790.8	2305.6	1870.0
99.7	2357.1	1780.9	2348.9	1874.7	2345.2	1790.8	2327.6	1874.4
199.9	2379.9	1785.1	2383.4	1876.8	2367.2	1795.2	2362.8	1874.4
300.1	2408.8	1788.7	2434.6	1881.8	2389.2	1795.2	2411.2	1878.8
400.5	2446.8	1791.9	2495.6	1883.6	2424.4	1799.6	2464.0	1883.2
500.0	2499.4	1809.4	2574.7	1912.0	2481.6	1821.6	2543.2	1918.4

From the data in Table 5.2 the deflection angle relative to the $V_{applied} = 0 \text{ Volts}$ case can be calculated as a discrete function of applied voltage. Figure 5.29 shows a plot of this data compared to the beam propagation simulation.

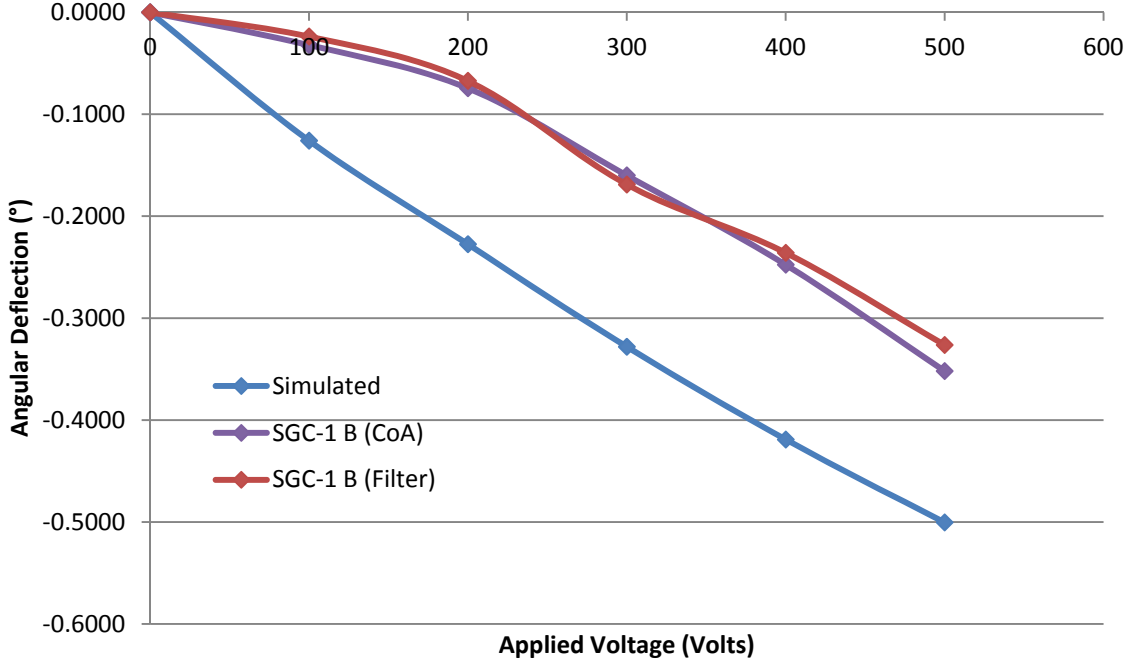


Figure 5.29 – Simulated values of angular beam deflection imparted by EOBS Channel 1 and experimental values of angular beam deflection imparted by SGC-1 Channel 1.

It is clear from Figure 5.29 that the behavior of SGC-1 is qualitatively consistent with the beam propagation simulation. It is also clear that $r_{33,eff} < r_{33,assumed}$.

SGC-1 Steering Performance (Negative Voltages)

SGC-1 experienced dielectric breakdown through the bulk of the crystal at $V_{applied} \approx -700 \text{ Volts}$. The chip could not maintain $V_{applied} < -300 \text{ Volts}$ after this failure. Figure 5.30 shows a photograph of the damage.



Figure 5.30 – Damage from bulk dielectric breakdown of SGC-1.

SGC-2 Steering Performance (Positive Voltages)

Table 5.3 shows the beam location data for SGC-2 as processed by the center of amplitude and expected value filter section methods.

Table 5.3 – Beam deflection data for SGC-2 at positive values of $V_{applied}$.

Applied Voltage (Volts)	Center of Amplitude				Gaussian Filter			
	At $z_1 = 15$ cm		At $z_2 = 16.5$ cm		At $z_1 = 15$ cm		At $z_2 = 16.5$ cm	
	x-dim (μm)	y-dim (μm)	x-dim (μm)	y-dim (μm)	x-dim (μm)	y-dim (μm)	x-dim (μm)	y-dim (μm)
0	2587.5	1373.4	2607.1	1304.6	2556.4	1350.8	2574.0	1280.4
100.5	2727.4	1371.6	2809.9	1302.1	2706	1350.8	2772.0	1280.4
199.7	2854.1	1368.4	2971.9	1299.0	2851.2	1346.4	2930.4	1276.0
300.1	2968.2	1361.5	3123.0	1297.1	2965.6	1346.4	3110.8	1276.0
400.4	3083	1368.4	3273.7	1297.7	3080.0	1346.4	3273.6	1276.0
499.9	3194.1	1361.8	3438.1	1295.5	3203.2	1346.4	3432.0	1276.0

From the data in Table 5.3 the deflection angle relative to the $V_{applied} = 0 \text{ Volts}$ case can be calculated as a discrete function of applied voltage. Figure 5.31 shows a plot of this data compared to the beam propagation simulation.

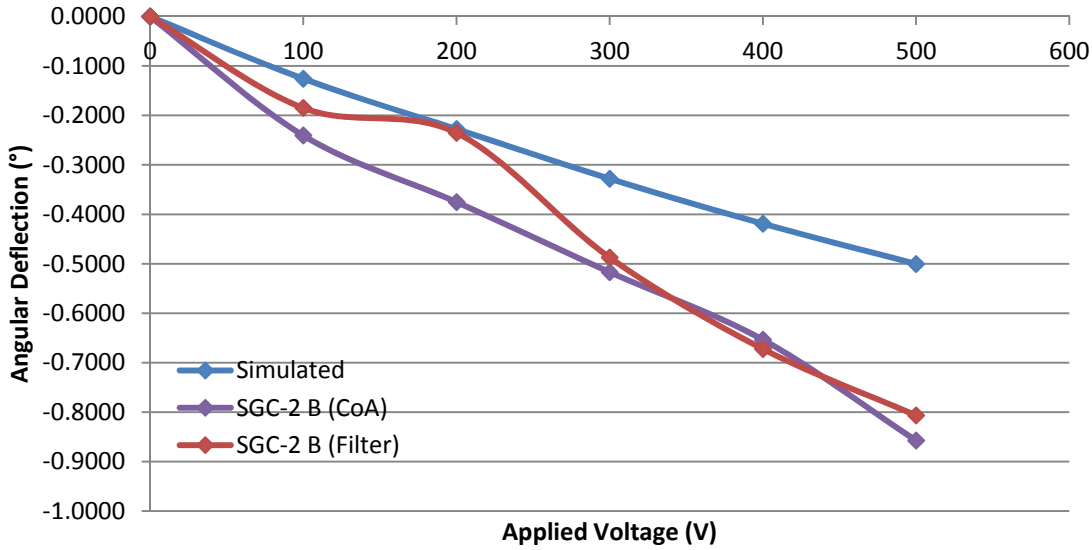


Figure 5.31 – Simulated values of angular beam deflection imparted by EOBS Channel 1 and experimental values of angular beam deflection imparted by SGC-2 Channel 1.

It is clear from Figure 5.31 that the behavior of SGC-2 is qualitatively consistent with the beam propagation simulation. It is also clear that $r_{33,eff} > r_{33,assumed}$. Furthermore, the relationship between r_{33} and $r_{33,eff}$ can be seen to be voltage invariant. Table 5.4 shows the ratio $R = \frac{\theta_{SGC-2 (CoA)}}{\theta_{simulation}}$ of the experimental deflection angles to the simulated deflection angles at $V \neq 0 \text{ Volts}$. Note that the value of R is about the same for all values of the applied voltage.

Table 5.4 – The ratio R at positive values of $V_{applied}$.

Applied Voltage (Volts)	R
100	1.9104
200	1.6494
300	1.5753
400	1.5596
500	1.7133
Average:	1.682

SGC-2 Steering Performance (Negative Voltages)

The experiment to evaluate the steering response of SCG-2 to negative values of $V_{applied}$ was conducted in the same manner as the tests at positive values. Table 5.5 shows the beam location data for SGC-2 as processed by the center of amplitude and expected value filter section methods.

Table 5.5 – Beam deflection data for SGC-2 at negative values of $V_{applied}$.

Applied Voltage (Volts)	Center of Amplitude				Gaussian Filter			
	At $z_1 = 15$ cm		At $z_2 = 16.5$ cm		At $z_1 = 15$ cm		At $z_2 = 16.5$ cm	
	x-dim (μm)	y-dim (μm)	x-dim (μm)	y-dim (μm)	x-dim (μm)	y-dim (μm)	x-dim (μm)	y-dim (μm)
0	2575.2	1362.0	2584.3	1295.5	2547.6	1346.4	2565.2	1267.2
100	2410.2	1356.8	2384.6	1292.9	2376.0	1333.2	2336.4	1258.4
200	2242.9	1357.2	2172.3	1291.3	2226.4	1333.2	2142.8	1258.4
300	2043.6	1358.2	1934.5	1294.7	2046.0	1337.6	1931.6	1254.0
400	1812.6	1360.2	1622.6	1295.3	1821.6	1333.2	1632.4	1249.6
500	1521.2	1364.0	1243.9	1296.4	1504.8	1342.0	1205.6	1249.6
600	485.2	1355.7	1008.0	1314.1	536.8	1333.2	1038.4	1284.8
700	801.5	1401.0	462.5	1329.6	862.4	1386.0	431.2	1298.0
800	1186.6	1420.2	858.2	1393.6	1144.0	1421.2	805.2	1425.6
900	1590.9	1439.8	1449.8	1418.0	1614.8	1430.0	1487.2	1425.6
1000	1919.5	1449.6	1985.5	1417.9	1922.8	1438.8	1971.2	1416.8

From the data Table 5.5 the deflection angle relative to the $V_{applied} = 0$ Volts case can be calculated as a discrete function of applied voltage. Figure 5.32 shows a plot of this data compared to the beam propagation simulation.

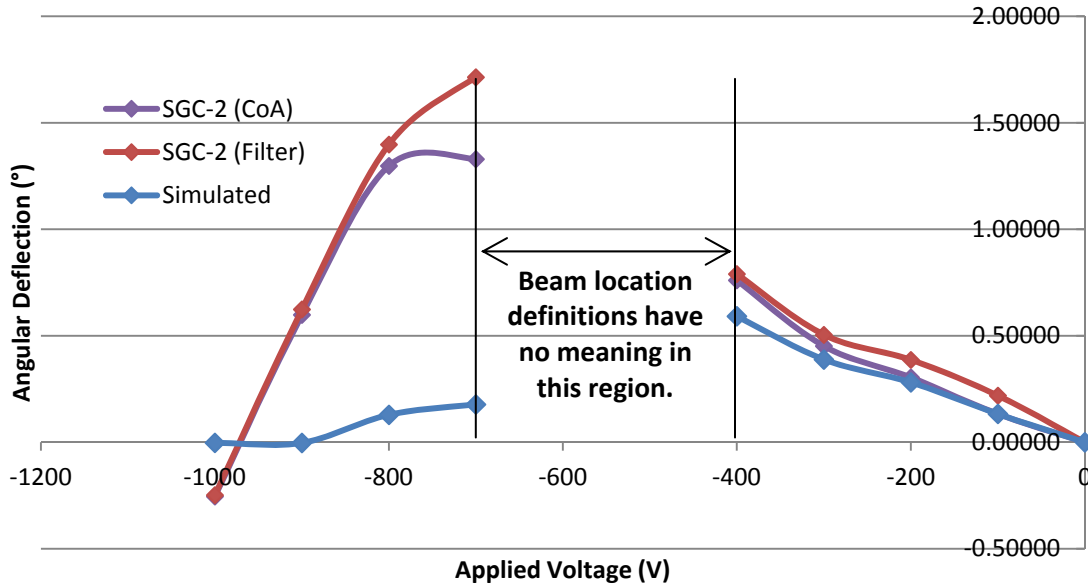


Figure 5.32 – Simulated values of angular beam deflection imparted by EOBS Channel 1 and experimental values of angular beam deflection imparted by SGC-2 Channel 1.

From the extrapolation shown in Figure 5.32, the zero angular deflection point occurs at $V_{applied} \approx 960$ Volts. The two point form of this line can be expressed as:

$$\theta = \frac{\theta_2 - \theta_1}{V_2 - V_1} (V - V_1) + \theta_1 \quad (5.17)$$

So, for $\theta = 0^\circ$:

$$\begin{aligned} -\theta_1 &= \frac{\theta_2 - \theta_1}{V_2 - V_1} (V_{control} - V_1) \\ \therefore -\theta_1 \cdot \frac{V_2 - V_1}{\theta_2 - \theta_1} &= V_{control} - V_1 \\ \therefore V_{control} &= V_1 - \theta_1 \cdot \frac{V_2 - V_1}{\theta_2 - \theta_1} = -970.1 \text{ Volts} \end{aligned} \quad (5.18)$$

Similarly:

$$\Delta x_i = x_{V_2} + \frac{V_{control} - V_1}{V_2 - V_1} (x_{V_2} - x_{V_1}) - x_{V_0} \quad (5.19)$$

And:

$$\Delta y_i = y_{V_2} + \frac{V_{control} - V_1}{V_2 - V_1} (y_{V_1} - y_{V_2}) - y_{V_0} \quad (5.20)$$

From which the overall translation is found to be:

$$Translation_{experiment} = 759.30 \pm 13.87 \mu m^{14} \quad (5.21)$$

Recall from Section 4.2.2:

$$\begin{aligned} Translation_{design} &= 775.16 \mu m \\ Translation_{simulation} &= 769.66 \pm 0.37 \mu m \end{aligned}$$

Thus the fractional error is:

$$\begin{aligned} \%Error_{simulation} &= \frac{Translation_{experiment} - Translation_{simulation}}{Translation_{simulation}} \\ &= 1.35\% \end{aligned} \quad (5.22)$$

$$\%Error_{design} = \frac{Translation_{experiment} - Translation_{design}}{Translation_{design}} = 2.04\% \quad (5.23)$$

Thus, ray tracing, wave simulation, and experiment are seen to agree exceptionally well. The experimental uncertainty is found to be much larger than the simulation uncertainty; this is largely due to the fact that the data was interpolated twice to arrive at the experimental value of $Translation_{experimental}$.

¹⁴ The numerical calculation of experimental error is quite long and has been excluded here in favor of placement in Appendix C. The code can be found in [M8]

The *Spiricon* beam profiling camera was used to capture frame data for $V_{\text{applied}} = 0 \text{ Volts}$ and for $V_{\text{applied}} = V_{\text{control}}$. Figure 5.33 shows that at $V_{\text{applied}} \approx -970 \text{ Volts}$, the beamspot is translated by $\sim 770 \mu\text{m}$.

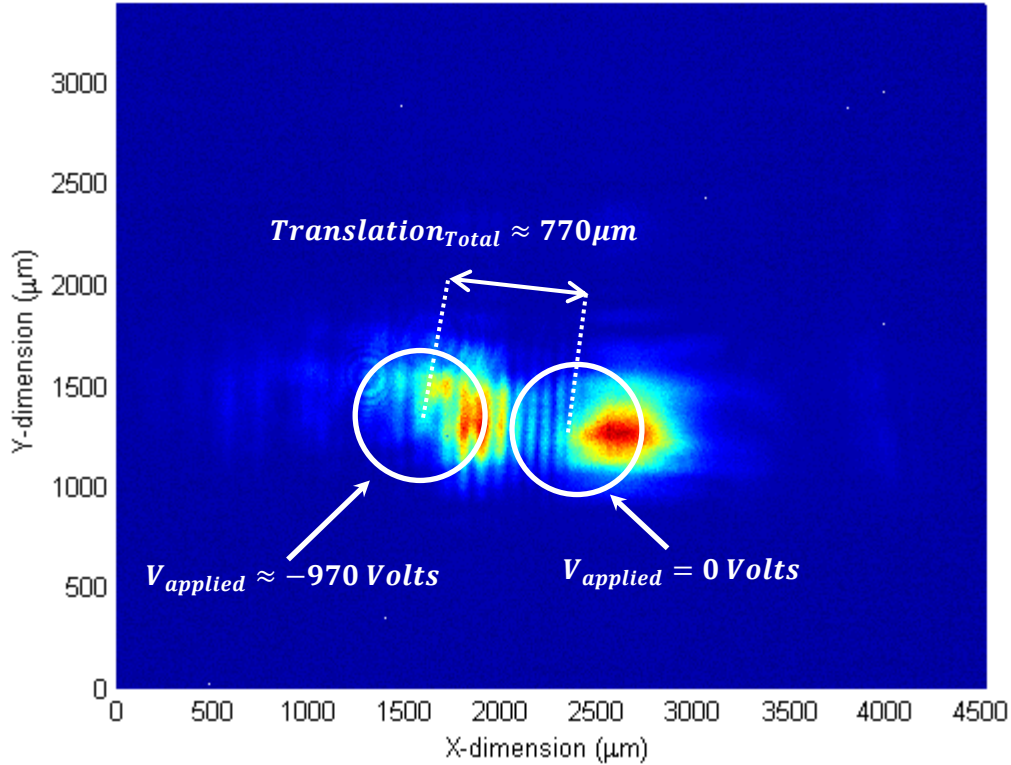


Figure 5.33 – The steered spot is translated by $\sim 770 \mu\text{m}$.

[Note that the steered beampot is distorted in this image; however, the quality improved dramatically when the focusing lens was replaced by a lens with a longer focal length.]

5.3 Switched OPG

5.3.1 The OPG Chip Mount

Experimental evaluation of SGC-2 verifies that EOBS technology is, in principle, a viable means of selecting subsequent optics. However, this analysis is not as compelling as a demonstration of the utility of such switching capabilities. Thus, one objective of the current research was to demonstrate a switched OPG system. To that end, an OPG chip mounting system was designed to be bolted to a six-axis stage so that the OPG chip could be precisely positioned on an optical table. The mount in Figure 5.34 was designed to hold an OPG chip in place.

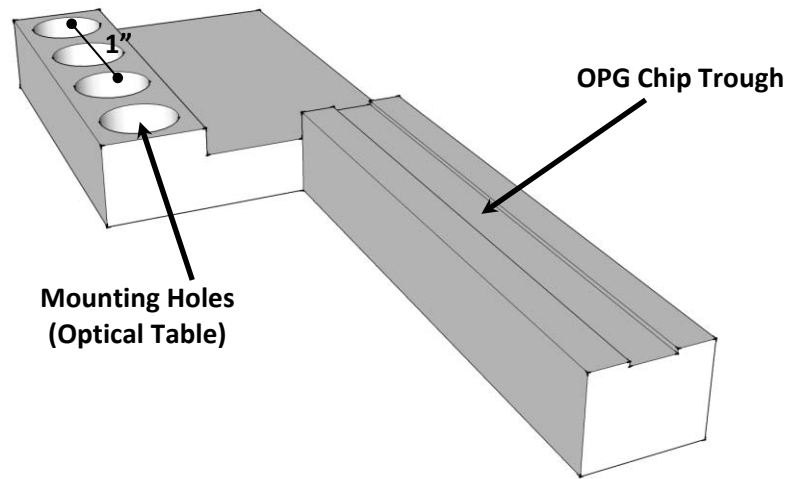


Figure 5.34 – The OPG chip mount.

5.3.2 OPG Chip Performance

It was necessary to demonstrate OPG using the gratings fabricated for this experiment before attempting to use them with the EOBS to demonstrate switched OPG. In order to verify that the OPG grating chip performed as designed, the setup shown in Figure 5.35 was assembled. Recall that the pump wavelength was $\lambda_1 = 1.064 \mu\text{m}$ and that the gratings were designed such that:

$$\begin{aligned}\Lambda_1 = 29.0 \mu\text{m} &\rightarrow \lambda_2 = 1.444 \mu\text{m} \text{ \& } \lambda_3 = 3.273 \mu\text{m} \\ \Lambda_2 = 31.0 \mu\text{m} &\rightarrow \lambda_2 = 1.577 \mu\text{m} \text{ \& } \lambda_3 = 4.040 \mu\text{m}\end{aligned}$$

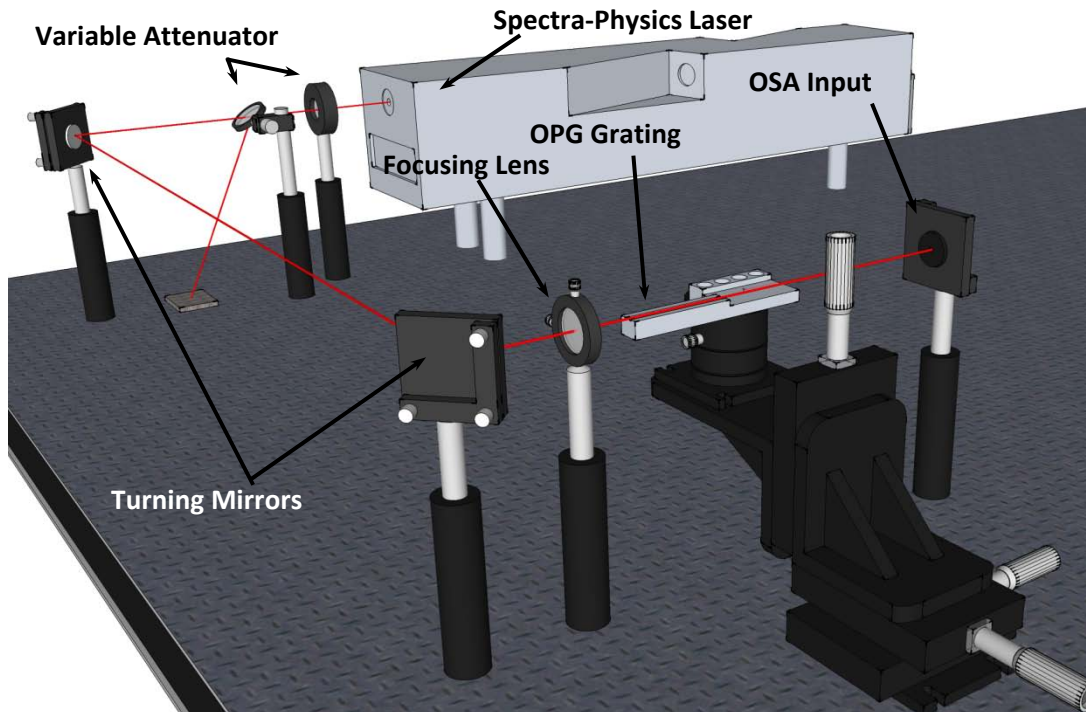


Figure 5.35 – The setup used to evaluate the OPG chip performance.

The OPG grating chip was positioned such that the beamwaist was located in the middle of the chip and the pump beam went directly through one of the gratings. Then the pump power was increased until the signal wavelength became visible on the screen of *Yokogawa AQ6575* optical spectrum analyzer (OSA) [V14]. The grating was then translated such that the pump beam went directly through the second grating.

OPG was successfully demonstrated with both gratings. The output peak corresponding to the $\Lambda = 29.0 \mu\text{m}$ grating was measured at $\lambda_2 = 1451.3 \text{ nm}$ and the peak corresponding to the $\Lambda = 31.0 \mu\text{m}$ grating was measured at $\lambda_3 = 1591.9 \text{ nm}$. These wavelengths agree fairly well with the predicted values calculated in *Section 3.1.3*. Figure 5.36 shows that the signal beams for each of these gratings were visible on the OSA.

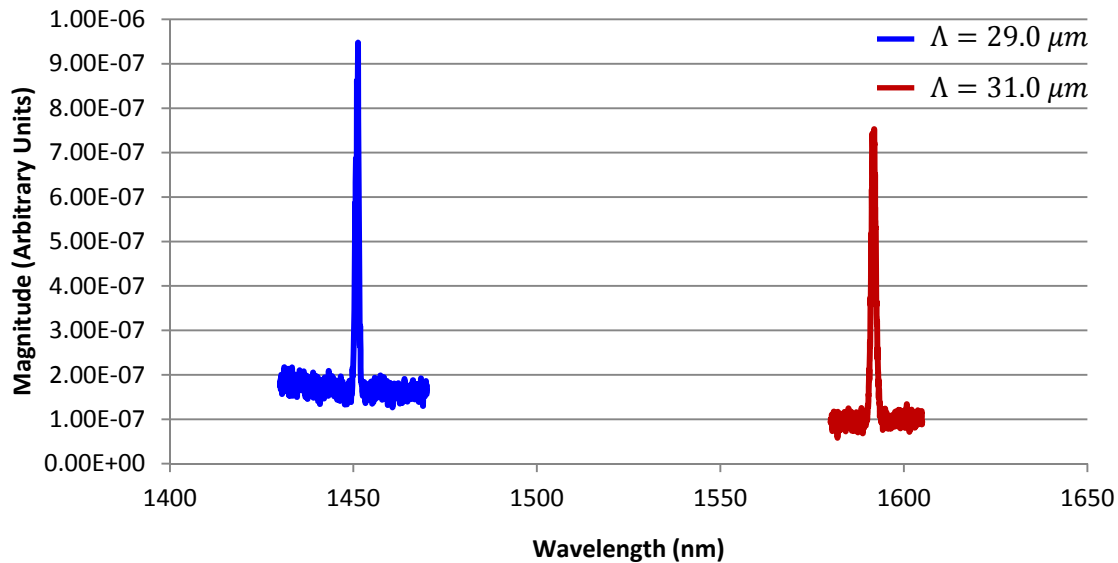


Figure 5.36 – Signal output from both OPG gratings.

5.3.3 Switched OPG System Design

The switched OPG system was assembled as pictured in Figure 5.37.

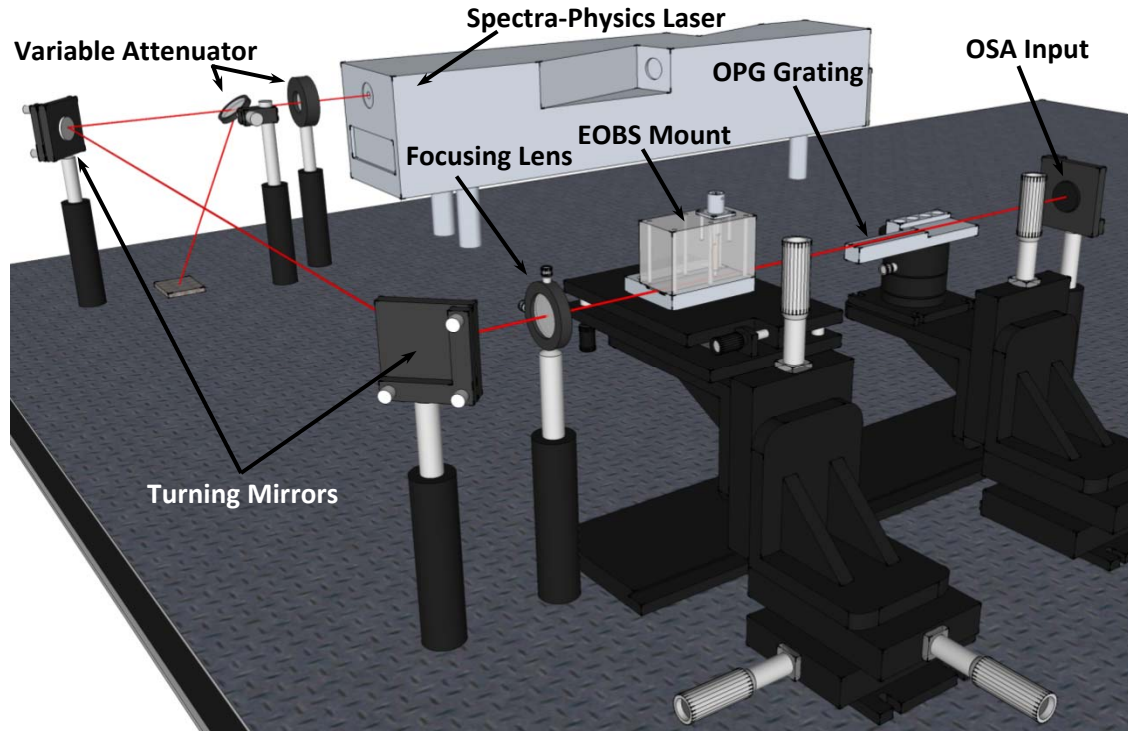


Figure 5.37 – The switched OPG system.

The pump beam was profiled with the *Spiricon* camera. The EOBS mount was then positioned just beyond the location where the beam diameter matched the Channel 1 prism height. The OPG chip was positioned such that pump beam passed through the $\Lambda = 29.0 \mu\text{m}$ grating and the beam waist was near the center of the chip. Due to Fresnel losses at the entrance and exit facets of the EOBS chip, the pump power entering the OPG chip was reduced below the OPG detection threshold. The pump power was increased until the characteristic red output (formed by sum frequency generation [SFG] of the pump and signal beams) was visible.

It was possible to switch the pump beam between the $\Lambda = 29.0 \mu\text{m}$ grating ($V_{\text{applied}} = V_{\text{OFF}}$) and the $\Lambda = 31.0 \mu\text{m}$ grating ($V_{\text{applied}} = V_{\text{ON}}$), but the output of the OPG interaction was not observed in the ON state. Increasing the pump power did not yield measurable power at the signal wavelength. It is not clear why the OPG process did not produce appreciable output with the EOBS in the ON state. It is plausible that distortion of the steered beam contributed to a decrease in conversion efficiency and raised the detection threshold significantly.

5.4 System Limitations

5.4.1 Theoretical Limits to Modulation Speed

Both the electro-optic effect used to steer the beam and the OPG process utilized to generate the signal and pump wavelengths occur at time scales that are far shorter than the times scales at which the control voltage of the EOBS can be modulated. Thus it seems intuitive to assume that the factors limiting the maximum wavelength

modulation frequency will be the rise and fall times of the EOBS chip and the amplifier controlling it.

Electrically, the EOBS design is a parallel plate capacitor. Thus, the capacitance of the EOBS should be:

$$C_{EOBS} = \frac{A\epsilon}{d} = \frac{Lw\epsilon_{33}\epsilon_0}{d} \approx 493 \text{ pF} \quad (5.24)$$

where A is the overlapping area of the electrodes, $L = 66 \text{ mm}$ is the electrode overlap length, $w = 15 \text{ mm}$ is electrode overlap width, $d = 500 \mu\text{m}$ is the distance between the electrodes, $\epsilon_{33} = 28.1$ [32 p. 97]¹⁵ is the relative dielectric permittivity of 5%MgO:CLN in the z-direction, and $\epsilon_0 = 8.8542 \times 10^{-12} \text{ F/m}$ is the vacuum permittivity. The capacitance of SGC-1 was measured to be $C_{SGC-1} \approx 1 \text{ nF}$, which is consistent with the preceding theory. The resistance of SGC-1 was measured to be $R_{SGC-1} > 300 \text{ M}\Omega$. For the sake of this discussion, let $R_{EOBS} \approx 1 \text{ G}\Omega$. Thus the EOBS can be modeled as a low pass filter system such as is shown in Figure 5.38.

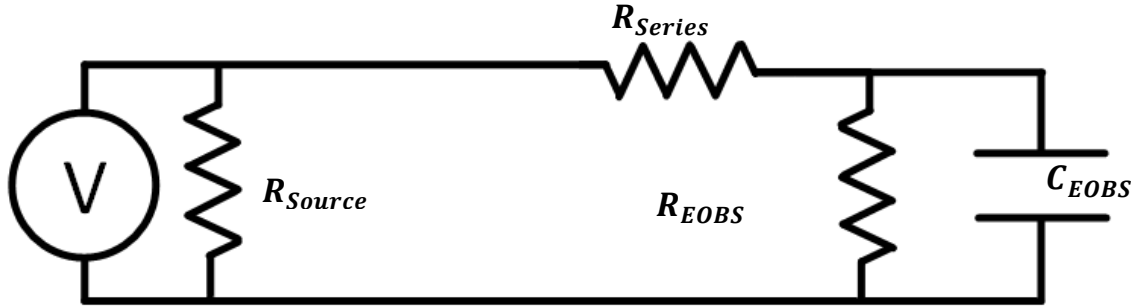


Figure 5.38 – A simple low-pass filter model of the EOBS system.¹⁶

The datasheet of the *EMCO C30N* negative high voltage amplifier used in this system did not include an output impedance specification. However, the value of the parallel resistors R_{source} and R_{EOBS} does not directly affect this analysis. The overall series resistance of the system R_{series} is the combined output resistance of the amplifier, line resistance, and series resistance of the EOBS chip; this value should be small. For the sake of this analysis, the series resistance will be assumed to be $R_{series} \approx 1 \text{ k}\Omega$. Thus, the RC time constant of the system is approximately:

$$\tau_{switching} = R_{series}C_{EOBS} = 1 \mu\text{sec} \quad (5.25)$$

Thus, the 3dB bandwidth of the system is:

¹⁵ Wong [32] presents the dielectric permittivity tensor for LiNbO_3 , it is generally accepted that MgO doping does not dramatically affect the electrical properties of LiNbO_3 . Thus, this value is acceptable for an order-of-magnitude discussion of switching bandwidth.

¹⁶ Because 5%MgO:CLN is a piezoelectric material, this model is deceptively simple and will not totally capture the electrical behavior of the EOBS. Typically, Butterworth-Van Dyke equivalent circuit analysis is used to model the mechanical resonances of such a device [33 p. 127]. This model will suffice to illustrate effects which limit EOBS switching performance.

$$f_{3dB} = \frac{1}{2\pi R_{Series} C_{EOBS}} = 159.2 \text{ kHz} \quad (5.26)$$

It is apparent that the EOBS will not function correctly at the -3dB point, because rail-to-rail modulation of the applied voltage is not possible. To further illustrate this point, the squarewave response of the EOBS system equivalent circuit was calculated using *5Spice* circuit analysis software [V15]. Figure 5.39 clearly shows that, at $f = 160 \text{ kHz}$, the applied voltage does not settle to steady ON or OFF states. Conversely, Figure 5.40 clearly shows that, at $f = 20 \text{ kHz}$, the applied voltage settles into steady ON and OFF states.

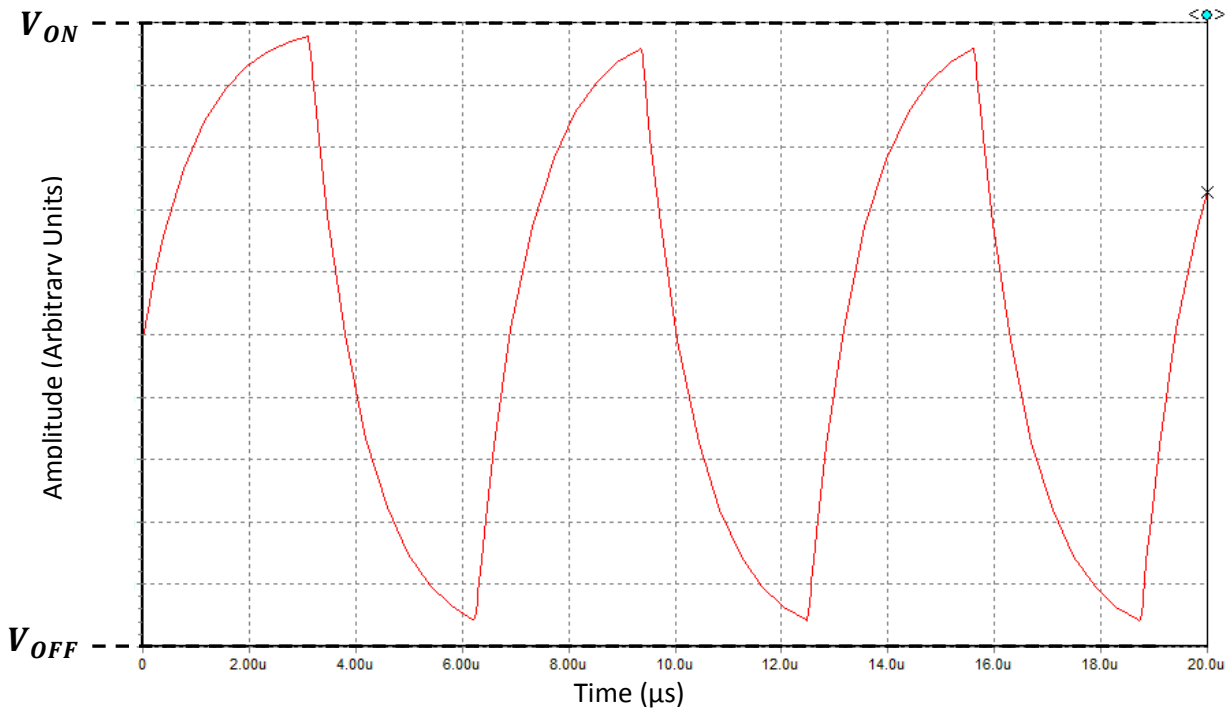


Figure 5.39 – The squarewave response of the system equivalent circuit at $f = 160 \text{ kHz}$.

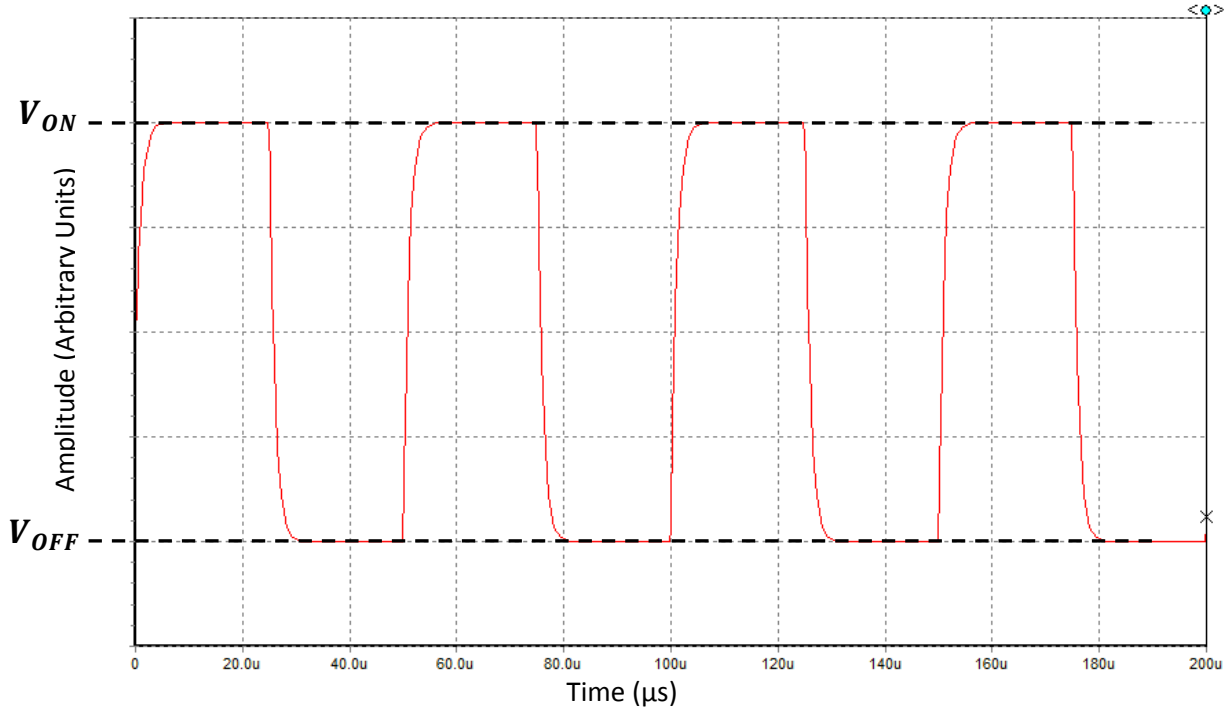


Figure 5.40 – The squarewave response of the system equivalent circuit at $f = 20 \text{ kHz}$.

From the equivalent circuit model, it is clear that the EOBS can sustain rail-to-rail modulation at frequencies of $f < 20 \text{ kHz}$. However, the rated output bandwidth of the C30N amplifier is $f_{\text{max}C30N} = 3 \text{ kHz}$. Thus it is logical to conclude that the system is amplifier limited and $f = 3 \text{ kHz}$ is expected to be the maximum switching frequency of this system.

Admittedly, the RC model presented here is somewhat oversimplified. Dissipation of energy stored in the capacitor through the amplifier circuit, as well as the effects of other loss mechanisms (vibration, heat, etc.), are neglected. Thus, due to the simplicity of this model, it is clear that this calculation only provides a qualitative measure of the maximum modulation frequency of the system.

Note that smaller EO beam deflectors built by *AdvR Inc.* have been demonstrated at frequencies of $\sim 20 \text{ MHz}$ [34]. The surface area of the EOBS design is approximately 40x larger than these deflectors. Thus, the EOBS chip design should, in principle, be capable of switching frequencies of at least 500 kHz. However, due to the limitations of the HV amplifier, the experimental performance was not expected to exceed a few kHz.

5.4.2 Low Frequency Modulation of SGC-1

The switching performance of SGC-1¹⁷ was qualitatively evaluated by measuring the state-to-state transition time. A square-wave control signal modulated between $V_{\text{OFF}} = 0 \text{ Volts}$ and $V_{\text{ON}} = -970 \text{ Volts}$ was applied to SGC-1. The *Spiricon* beam profiling camera was used to record the output of the EOBS at 30fps (see Figure 5.13).

¹⁷ SGC-1 was repaired by *AdvR Inc.* The gold around the breakdown site (**Figure 5.30**) was removed and the damage site coated with nitrocellulose lacquer. Full functionality was restored.

At $f_{modulation} \approx 100 \text{ mHz}$, each state was clearly visible for seconds between each transition. The amount of the time required to move from the ON state to the OFF state was determined by the number of frames between the onset of the switching response and the arrival of the steered beam at the new state. On the average, the ON-OFF transition took place over the course of seven frames. Thus the state-to-state transition time is:

$$T_{ON-OFF} \approx \frac{7 \text{ frames}}{30 \text{ fps}} = 0.233 \text{ sec} \quad (5.27)$$

It was apparent that the $V_{OFF} \rightarrow V_{ON}$ transition occurred more rapidly than the $V_{ON} \rightarrow V_{OFF}$ transition. This transition was typically completed in only one frame. Thus,

$$T_{OFF-ON} < \frac{1 \text{ frames}}{30 \text{ fps}} = 0.033 \text{ sec}$$

Assuming that the state lifetime is required to be at least as long as the longer of the two transition times, it can be concluded that the maximum modulation frequency conservatively estimated to be:

$$f_{max} = \frac{1}{4T_{switching}} = 1.08 \text{ Hz} \quad (5.28)$$

The frequency of the square-wave signal was slowly increased and its effect on the steering performance of the EOBS was observed. The EOBS performed as designed for $f_{modulation} < 3 \text{ Hz}$. However, as $f_{modulation} \rightarrow 4 \text{ Hz}$ (well below the Nyquist frequency of the camera), the steering behavior became erratic. The ON state became very short-lived and the output was seen to scatter in the same sporadic way as shown in FDM beam propagation simulations at $-600 \text{ Volts} > V_{Applied} > -800 \text{ Volts}$. Thus $f_{max} \approx 3 \text{ Hz}$ can be thought of as the maximum modulation frequency of this system. This is almost certainly due to resistive/capacitive effects within the HV amplifier. That is, it is not representative of the fundamental limit of SGC-1.

5.4.3 Qualitative Power Limits

Due the prohibitive cost of the EOBS chips, an optical power failure analysis could not be performed. Consequently, an upper optical energy density limit is not known. However, it should be noted that, in preliminary tests, high pump powers ($>1 \text{ W}$ as measured by the internal power meter of the T-Series Laser) induced some damage within the 5%MgO:CLN. It is unclear what the specific damage mechanism was, though photo-refractive damage is suspected. Thus, if a switched system requires high-power operation, the EOBS may have to be operated at elevated temperatures to mitigate the effects of photo-refractive damage. Recall that the steering performance of the EOBS is virtually unaffected by uniform changes in temperature.

CHAPTER 6 – CONCLUSIONS

6.1 Project Summary

6.1.1 Design and Optimization

Geometric design of the EOBS followed from a geometric analysis of a single-prism unit-cell. The height of each cell was specified to be 140% of the $1/e^2$ beam diameter of the beam at the entrance facet of the EOBS chip. Cells were cascaded such that each cell would impart the same small angular deflection and translation components to the propagating beam. Thus, by construction, steering channels were designed to impart no overall deflection. The performance of such channels was parameterized in terms of two free variables: the beam waist diameter D_0 and the angle α defined by the base of the unit cell and one of the congruent legs of the isosceles triangular prism. The value of the overall translation was calculated for $10^\circ \leq \alpha < 90^\circ$ and $50 \mu\text{m} < D_0 < 400 \mu\text{m}$.

The results of the overall translation calculation happened to be optimal at $D_0 = 160 \mu\text{m}$ and independent of α to within quantization factors brought about by the fact that only even integer values of cells were permitted in a steering channel. The optimal geometry, referred to in this work as “Channel 3,” was designed utilizing $D_0 = 160 \mu\text{m}$ and $\alpha = 30^\circ$ and was calculated to impart $Translation = 913.52 \mu\text{m}$ to the steered beam. Another notable geometry, referred to in this work as “Channel 1,” was designed to be more tolerant of beams with various beam waist sizes by utilizing $D_0 = 255 \mu\text{m}$ and $\alpha = 30^\circ$ and was calculated to impart $Translation_{design} = 775.49 \mu\text{m}$ to the steered beam. This versatile steering channel was the object of study for the majority of the simulations and experiments presented in this work. Five distinct steering channel geometries were selected for simulation and fabrication; these geometries were designated as ‘Channel 1’ through ‘Channel 5.’

6.1.2 Numerical Beam Propagation

Finite difference method beam propagation simulations for Channels 1-5 were implemented in LIGHTS. These simulations enabled the verification of each steering channel design and the exploration of the effect of environmental factors on EOBS performance.

Beam propagation through Channels 1-5 was simulated under design conditions and the simulated steering performance of these geometries was found to have strong agreement with the predications made using the ray analysis to design the channels. For example, Channel 1 was found to impart $Translation_{simulation} = 761.03 \pm 0.48 \mu\text{m}$ to the steered beam.

Beam propagation through Channel 1 was simulated within the temperature range $0^\circ\text{C} \leq T \leq 50^\circ\text{C}$. The performance of the EOBS was found to be relatively insensitive to uniform changes in device temperature.

Beam propagation through Channel 1 was simulated for beams with wavelengths in the range $500 \text{ nm} \leq \lambda \leq 1500 \text{ nm}$. The overall translation imparted to a steered beam was found to be wavelength dependent. It was concluded that dispersive effects could be compensated for by adjusting the ON-state voltage. Thus, in principle, the EOBS chips fabricated for this work can be used to switch beams with wavelengths other than $\lambda = 1.064 \mu\text{m}$.

Beam propagation through Channel 1 was simulated as the applied voltage was varied through the range $-1500 \text{ Volts} \leq V_{\text{applied}} \leq 500 \text{ Volts}$. For cases $-500 \text{ Volts} \leq V_{\text{applied}} \leq 500 \text{ Volts}$ the behavior of the EOBS was the same as an electro-optic angular beam scanner. For cases $-1100 \text{ Volts} \leq V_{\text{applied}} \leq -900 \text{ Volts}$ the output exhibited approximately zero angular deflection. For all other values of V_{applied} , the output of Channel 1 did not resemble a Gaussian beam.

6.1.3 Beam Switching Experiments

The steering response Channel 1 of EOBS chip SCG-2 was measured using beam location measurements for applied voltages $0 \text{ Volts} \geq V_{\text{applied}} \geq -1000 \text{ Volts}$. This data was interpolated to determine that this channel exhibited zero angular deflection behavior at $V_{\text{applied}} = -970.1 \text{ Volts}$. This value was used to find the interpolated value of $\text{Translation}_{\text{experiment}} = 759.01 \pm 15.90 \mu\text{m}$. Thus it is seen that design, simulation, and experiment agree to within a few percent.

The state transition time of beam switching system, was found to be $T_{\text{ON-OFF}} \approx 0.233 \text{ sec}$. The maximum modulation frequency the beam switching system was found to be limited by the HV amplifier. SCG-1 was demonstrated at $f_{\text{max}} = 3 \text{ Hertz}$.

6.1.4 Additional Observations

A few additional observations will aid in the design of next-generation EOBS chips. First, it was discovered in the course of this work that while the thermal annealing step was initially considered optional, that it is, in reality, conclusively necessary. Without this step, the bulk resistance of EOBS chips is sufficiently low that localized ohmic heating will lead to thermo-optic beam distortion. Furthermore, dielectric breakdown through the bulk of the unannealed chips FGC-1 and SGC-1 seems to indicate that annealing is necessary to mitigate the risk of dielectric breakdown. The localized nature of the heating and of the breakdown may be explained by the existence of conduction paths along poled domain boundaries. It is speculated that the thermal annealing process eliminates these conduction paths.

Second, it is also crucial to the design of devices such as the EOBS that a significant margin of nonmetalized substrate be left as a gap between the electrodes and the device mount. The first generation chips did not include this margin and exhibited breakdown between the electrodes and the EOBS mount. The second generation chips were design to have a $\sim 3 \text{ mm}$ gap between the electrodes and the edge of the chip. No surface breakdown was observed in second generation chips.

Finally, it is important to note that even though the EOBS chips were fabricated from 5%MgO:CLN to mitigate photo-refractive damage, some photorefractive damage is believed to have been observed in SCG-2 at high pump fluence. High-power EOBS chips fabricated from 5%MgO:CLN may have to be operated at elevated temperatures.

6.2 Future Work

This work demonstrated a wavelength-agile, solid-state source of coherent NIR radiation. Single-grating switched OPG enabled discrete tuning of the system output between two spectral states. Spectral State ZERO contained $\lambda = 1064 \text{ nm}, 532 \text{ nm}, 1451 \text{ nm}, 3987 \text{ nm}$, and 613.9 nm . Spectral State ONE contained only $\lambda = 1064 \text{ nm}$ and 532 nm . Immediate future work will seek to demonstrate dual-

grating switched OPG. In this regime, Spectral State ONE will consist of $\lambda = 1064\text{ nm}, 532\text{ nm}, 1591\text{ nm}, 3210\text{ nm},$ and 637.7 nm . With the choice of an appropriate filter, and combination of frequencies can be isolated. Most notably, a long pass filter that passes $\lambda > 3000\text{ nm}$ would isolate the idler wavelengths of each interaction. The result would be a discrete, wavelength-agile source of MIR radiation.

Realizing dual-grating switched OPG will require system-level reconstruction of the experiment. The optics must be properly chosen to focus the pump beam such that it will propagate through the EOBS chip without clipping the steering channel and such that the beamwaist location will be beyond the EOBS chip. Performing this design step should lead to improved steered beam quality and enable dual-grating switched OPG. The optimal focusing regime may be require that the pump beam be focused differently in each OPG grating. Figure 6.1 shows a two-branch approach to optimizing the focusing characteristics of each OPG interaction.

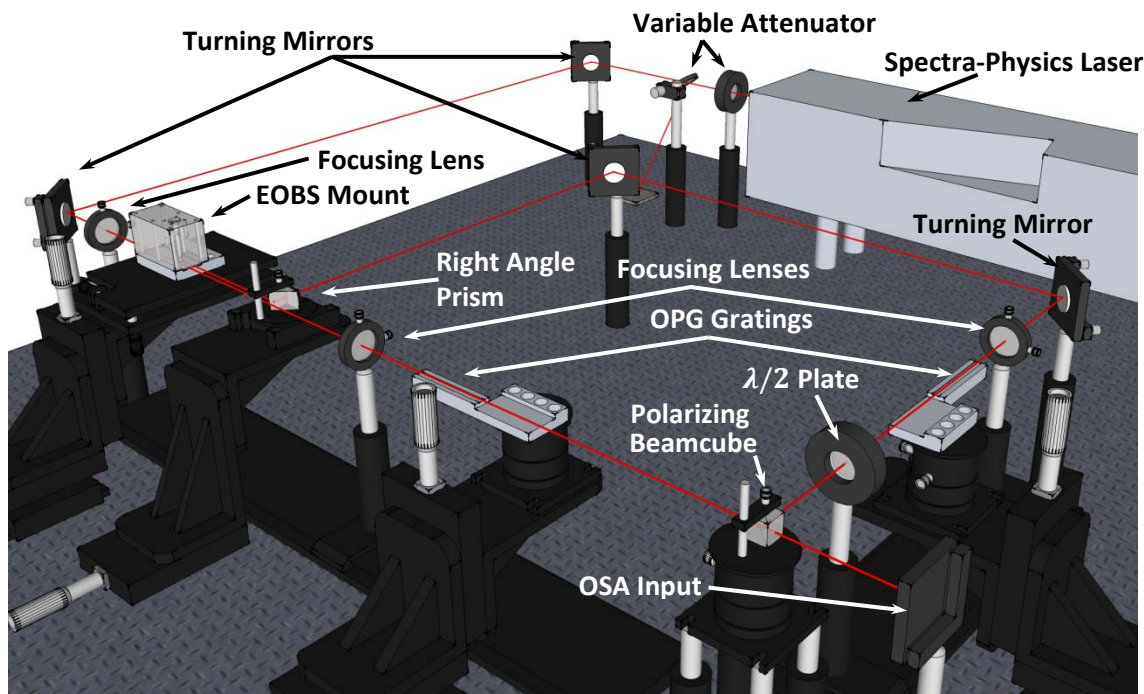


Figure 6.1 – A modified dual-grating switched OPG system.

In this configuration, the unsteered beam would be used to define the primary optic axis of the system. A right-angle prism and two turning mirrors can be positioned such that the steered beam is directed orthogonally to the primary axis. Separate focusing lenses can be used to focus the steered and unsteered beams into OPG gratings with a different poled periods.

The polarization of the signal beam from the second branch would be rotated 90° using a $\lambda/2$ plate. The rotated beam could then be realigned to the primary optical axis with a polarizing beam cube. The combined output could be focused into the fiber input of an OSA.

6.3 A Guide to Related Work

6.3.1 Material Factors

In addition to fabricating an EOBS device and exploring aspects of its performance, this work lays the foundation for EOBS design in general. The optimization routine developed for EOBS devices fabricated from 5%MgO:CLN can easily be extended to other materials. Indeed, several factors motivate the search alternative materials for an EOBS application.

First, the electro-optic coefficient of most materials is small; it is typically on the order of tens of pm/V. Consequently, the index modulation of such materials is small. Thus, the optimization routine developed in this work generated no geometries capable of achieving $Translation_{design} > \sim 1\text{ mm}$. For many applications, this amount of translation is far too small to be of any use. Materials with high electro-optic coefficients would enable much larger beam translations, which would enable beam switching between targets on the centimeter scale typically used in diode-pumped solid state laser cavities. For example, barium titanate ($BaTiO_3$) has an electro-optic coefficient of $r_{51} = 820\text{ pm/V}$; an EOBS manufactured from this material has the potential to exhibit beam translations on the order of $\sim 2\text{ cm}$. The principal limitation with $BaTiO_3$ devices is the fact that the orientation of the electro-optic tensor requires that the modulating voltage be applied along the thin edge of the wafer. Such electro-optically active materials would also allow the devices to be operated at much lower voltages.

Furthermore, materials with flatter dispersion curves would be more suitable for switching wavelengths other than the design wavelength. EOBS designs for steering broad-spectrum tunable sources, such as transition metal ion lasers, would benefit from such a flat dispersion curve to ensure that the switching performance of the EOBS changes minimally as the source is tuned.

Additionally, electro-optical materials exhibiting high refractive indices would also allow greater index modulation and thus greater beam translation. The development of transparent, high-index, flat-dispersion, highly electro-optically active materials which withstand PRD would be immensely helpful to enabling large-translation EOBS devices.

6.3.2 System-Level Improvements

Recall that the maximum modulation frequency achieved using second generation EOBS chips was $\sim 3\text{ Hz}$. This may be the highest achievable switching frequency using a signal generator and the specific high-voltages negative amplifier used in this work. However, the interested controls engineer should be able to improve the step response of the EOBS. The EOBS would first have to be electrically characterized so that a circuit model can be developed. Then an appropriate proportional integral derivative (PID) controller could be developed to minimize the state transition time and increase the maximum modulation frequency.

It should be noted that Muhammad et al. [35] developed an HV power supply specifically for controlling ferroelectric crystal devices.

6.3.3 Monolithic Two-Bit Wavelength Multiplexing

The EOBS was developed to enable rapid selection between two OPG gratings in free space. The elaborate system of opto-mechanics used with the EOBS was tedious to align. It would be far more compelling to integrate the switching and conversion onto

a single compact chip. This chip could be integrated into a fiberized package which would not require alignment. Figure 6.2 shows a conceptual design for a fiberized, single-package, two-bit wavelength multiplexer.

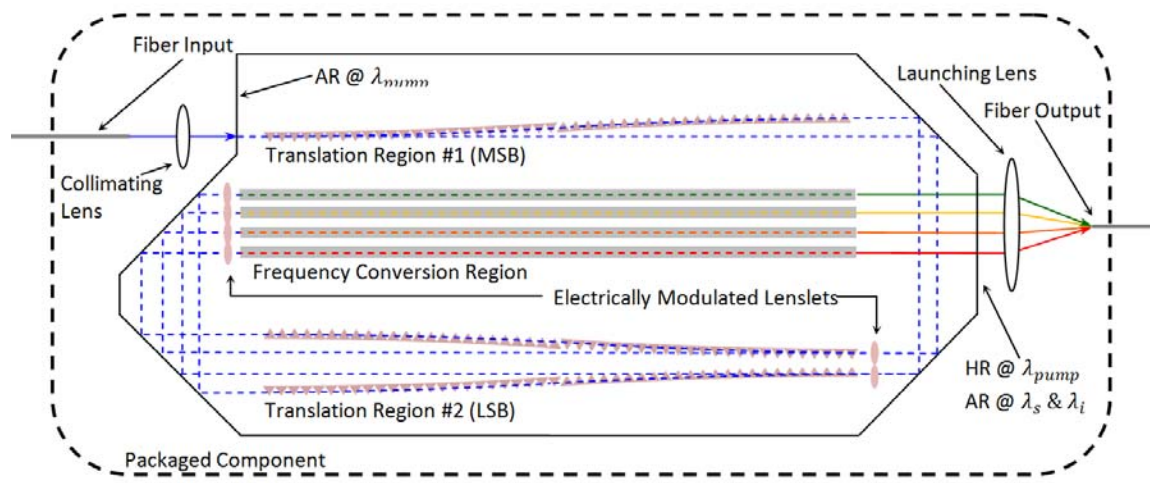


Figure 6.2 – Monolithic two-bit wavelength multiplexer.

6.3.4 Intra-cavity Switching

The EOBS design is, of course, bi-directional. Thus, in principle, an EOBS could be inserted into a laser cavity to enable the rapid reconfiguration of an experiment. For example, the EOBS could be used to select between two separate gain crystals, thus enabling two distinctly different laser outputs. Alternatively, the EOBS could be used between a saturable absorber mirror and an ordinary mirror, thus enabling the user to toggle between continuous-wave (CW) or pulsed output. Figure 6.3 shows a conceptual design for reconfigurable laser cavity.

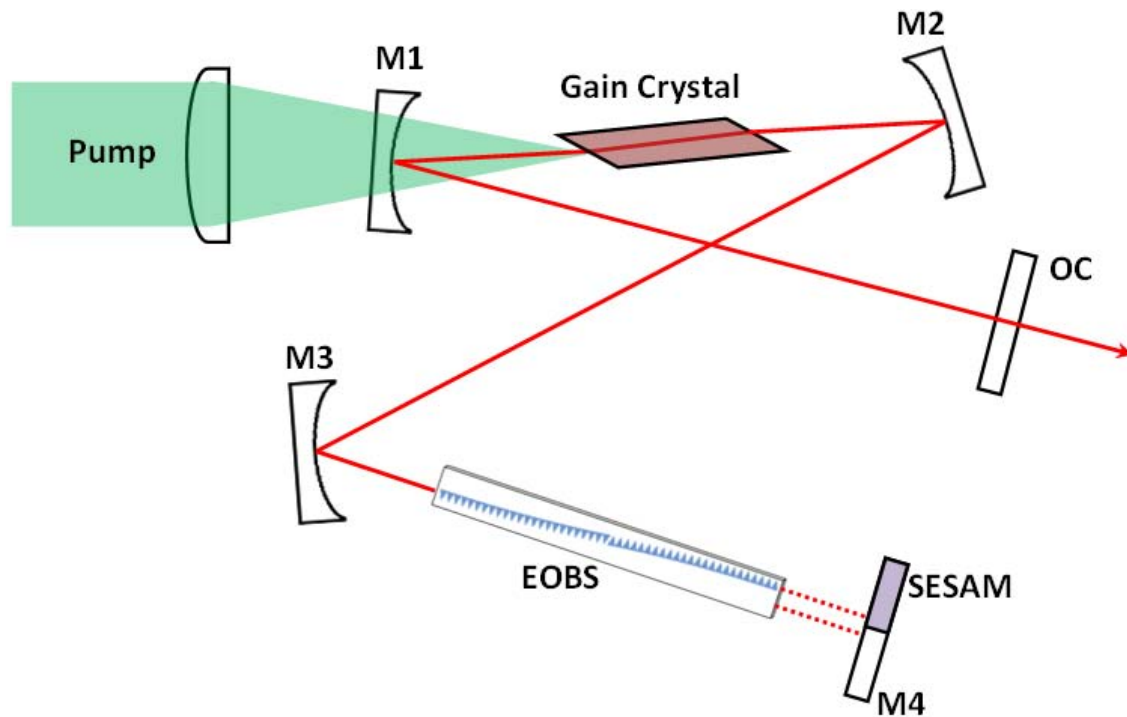


Figure 6.3 – A conceptual diagram for a switched CW/mode-locked laser cavity.

6.3.5 Single-Oscillator Multiple-Emitter Sources

The EOBS would function well as a fiber switch for high optical power applications. The EOBS seems especially useful in applications where size and weight considerations are crucial. A single laser could be coupled to any one of multiple emitter ‘addresses.’ Figure 6.4 shows a conceptual block diagram for such a switch.

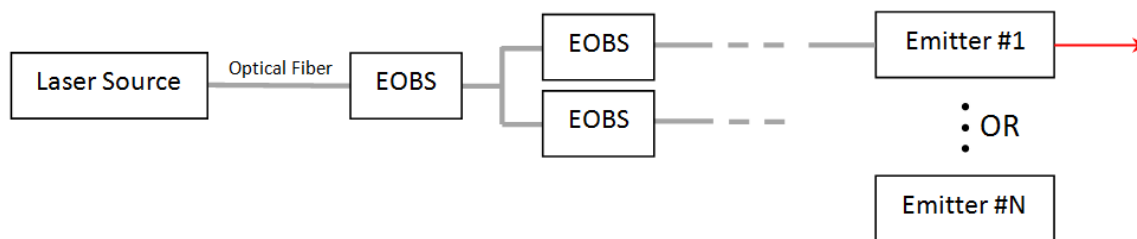


Figure 6.4 – A conceptual diagram for a single-oscillator multiple-emitter laser system.

Airborne laser applications which require laser light to be directed along multiple axes would especially benefit from the ability to rapidly select an output emitter for one laser source. This would reduce the number of sources to one and reduce the overall size and weight of the laser system. This reduction in size and weight would allow additional technologies to be included in weight-constrained aircraft.

6.4 Closing Remarks

In conclusion, the EOBS concept presented in this work was successfully transitioned from a geometric design to a tangible device and was experimentally demonstrated to perform as designed. The EOBS is a viable technology that has the potential to enable a variety of free-space laser applications. Thus, continued experimentation is likely to yield a number a number of rapidly reconfigurable sources in the NIR and MIR bands. Furthermore, integration of the EOBS into current laser systems has the potential to enhance the flexibility of next-generation laser sources.

REFERENCES

1. Zhai J.; Schroeck S.; Huang Y.; Messner W.C.; Stancil D.D.; Schlesinger T.E.; "Electro-optic scanner for optical disk fine tracking system" *SPIE* 3787, 194, July 1999
<http://dx.doi.org/10.1117/12.351645>
2. D. Scrymgeour, L. Tian, V. Gopalan, D. Chauvin, and K.L. Schepler, "Phased-array electro-optic steering of large aperture laser beams using ferroelectrics" *Appl. Phys. Lett.* **86**, 211113 (2005),
<http://link.aip.org/link/?APPLAB/86/211113/1>
3. J. David Zook, "Light Beam Deflector Performance: a Comparative Analysis," *Appl. Opt.* **13**, 875-887 (1974)
<http://www.opticsinfobase.org/abstract.cfm?URI=ao-13-4-875>
4. Yiyang Zuo, Madeleine Mony, Babak Bahamin, Etienne Grondin, Vincent Aimez, and David V. Plant, "Bulk electro-optic deflector-based switches," *Appl. Opt.* **46**, 3323-3331 (2007)
<http://www.opticsinfobase.org/ao/abstract.cfm?URI=ao-46-16-3323>
5. Yi Chiu; Gopalan, V.; Kawas, M.J.; Schlesinger, T.E.; Stancil, D.D.; Risk, W.P., "Integrated optical device with second-harmonic generator, electrooptic lens, and electrooptic scanner in LiTaO₃," *Lightwave Technology, Journal of*, vol.17, no.3, pp.462-465, Mar 1999
<http://ieeexplore.ieee.org/stamp/stamp.jsp?arnumber=749386&isnumber=16187>
6. D. Chauvin, "Electro-optic beam steering using Domain Engineered Lithium Tantalate", Master's Thesis, Dept. of the US Air Force, Air University, Mar 2005
<http://www.stormingmedia.us/71/7111/A711144.html>
7. Yi Chiu, Jie Zou, Daniel D. Stancil, and T. E. Schlesinger, "Shape-Optimized Electrooptic Beam Scanners: Analysis, Design, and Simulation," *J. Lightwave Technol.* **17**, 108- (1999)
<http://www.opticsinfobase.org/abstract.cfm?URI=JLT-17-1-108>
8. Fang, J.C.; Kawas, M.J.; Zou, J.; Gopalan, V.; Schlesinger, T.E.; Stancil, D.D., "Shape-optimized electrooptic beam scanners: experiment," *Photonics Technology Letters, IEEE*, vol.11, no.1, pp.66-68, Jan 1999
<http://ieeexplore.ieee.org/stamp/stamp.jsp?arnumber=736393&isnumber=15874>
9. Mahesh Krishnamurthi, Lili Tian, and Venkatraman Gopalan, "Design and simulation of planar electro-optic switches in ferroelectrics," *Appl. Phys. Lett.* **93**, 052912 (2008)
<http://link.aip.org/link/?APPLAB/93/052912/1>
10. L. E. Myers, R. C. Eckardt, M. M. Fejer, R. L. Byer, W. R. Bosenberg, and J. W. Pierce, "Quasi-phase-matched optical parametric oscillators in bulk periodically poled LiNbO₃," *J. Opt. Soc. Am. B* **12**, 2102-2116 (1995)
<http://www.opticsinfobase.org/abstract.cfm?URI=josab-12-11-2102>
11. P. A. Berry, and K. L. Schepler, "High-power, widely-tunable Cr²⁺:ZnSe master oscillator power amplifier systems," *Opt. Express* **18**, 15062-15072 (2010).
<http://www.opticsinfobase.org/oe/abstract.cfm?uri=oe-18-14-15062>
12. Rita D. Peterson, David Bliss, Candace Lynch, and David H. Tomich, "Progress in orientation-patterned GaAs for next-generation nonlinear optical devices" *Proc. SPIE* 6875, 68750D (2008), DOI:10.1117/12.766581
<http://spiedl.aip.org/getabs/servlet/GetabsServlet?prog=normal&id=PSISDG00687500000168750D000001&idtype=cvips&gifs=Yes>

13. V. Gopalan; M.J. Kaway; M.C. Gupta; T.E. Schlesinger; D.D. Stancil, "Integrated quasi-phase-matched second-harmonic generator and electrooptic scanner on LiTaO₃ single crystals," *Photonics Technology Letters, IEEE* , vol.8, no.12, pp.1704-1706, Dec. 1996
<http://ieeexplore.ieee.org/stamp/stamp.jsp?arnumber=544725&isnumber=11901>
14. Saleh, Bahaa, and Malvin Carl. Teich. Fundamentals of Photonics. Hoboken, NJ: Wiley-Interscience, 2007. p. 876. Print.
15. Powers, Peter E. *Fundamental Nonlinear Optics*. CRC Pr I Llc, 2010. Print.
16. Boyd, Robert W. Nonlinear Optics. Boston: Academic Press, 1992. Print.
17. Fejer, M.M.; Magel, G.A.; Jundt, D.H.; Byer, R.L.; , "Quasi-phase-matched second harmonic generation: tuning and tolerances," *Quantum Electronics, IEEE Journal of* , vol.28, no.11, pp.2631-2654, Nov 1992 doi: 10.1109/3.161322
<http://ieeexplore.ieee.org/stamp/stamp.jsp?tp=&arnumber=161322&isnumber=4215>
18. J. Casson, K. Gahagan, D. Scrymgeour, R. Jain, J. Robinson, V. Gopalan, and R. Sander, "Electro-optic coefficients of lithium tantalate at near-infrared wavelengths," *J. Opt. Soc. Am. B* 21, 1948-1952 (2004).
<http://www.opticsinfobase.org/abstract.cfm?URI=josab-21-11-1948>
19. Mendez, A.; Garcia-Cabanes, A.; Dieguez, E.; Cabrera, J.M., "Wavelength dependence of electro-optic coefficients in congruent and quasistoichiometric LiNbO₃," *Electronics Letters* , vol.35, no.6, pp.498-499, 18 Mar 1999
<http://ieeexplore.ieee.org/stamp/stamp.jsp?arnumber=756418&isnumber=16402>
20. Tian, L.; Gopalan, V., "Measurement of electro-optic coefficients of stoichiometric LiTaO₃ prepared by vapor transport equilibrium," *Lasers and Electro-Optics, 2005. (CLEO). Conference on Lasers and Electro-Optics*, vol.1, no., pp. 223-225 Vol. 1, 22-27 May 2005
<http://ieeexplore.ieee.org/stamp/stamp.jsp?arnumber=1572799&isnumber=33268>
21. A. Bruner, D. Eger, M. Oron, P. Blau, M. Katz, and S. Ruschin, "Temperature-dependent Sellmeier equation for the refractive index of stoichiometric lithium tantalate," *Opt. Lett.* 28, 194-196 (2003).
<http://www.opticsinfobase.org/abstract.cfm?URI=ol-28-3-194>
22. O. Gayer , Z. Sacks, E. Galun, A. Arie, "Temperature and wavelength dependent refractive index equations for MgO-doped congruent and stoichiometric LiNbO₃", *Appl. Phys. B* 91, 343–348 (2008),
<http://www.springerlink.com/content/93lg694k77335015/>
23. D. Jundt, "Temperature-dependent Sellmeier equation for the index of refraction, ne, in congruent lithium niobate," *Opt. Lett.* 22, 1553-1555 (1997).
<http://www.opticsinfobase.org/abstract.cfm?URI=ol-22-20-1553>
24. Inrad, Inc., "Lithium Niobate (LiNbO₃) Datasheet"
http://www.inrad.com/pdf/Inrad_datasheet_LNB.pdf
25. M. Nakamura, S. Higuchi, S. Takekawa, K. Terabe, T. Furukawa, K. Kitamura, "Optical Damage Resistance and Refractive Indices in Near-Stoichiometric MgO-Doped LiNbO₃", *Jpn. J. Appl. Phys.* 41 (2002) pp. L49-L51
<http://jap.ipap.jp/link?JJAP/41/L49/>

26. Shaolin Chen, Hongde Liu, Yongfa Kong, Ziheng Huang, Jingjun Xu, Guangyin Zhang, The resistance against optical damage of near-stoichiometric LiNbO₃:Mg crystals prepared by vapor transport equilibration, *Optical Materials*, Volume 29, Issue 7, March 2007, Pages 885-888, ISSN 0925-3467, DOI: 10.1016/j.optmat.2006.01.014.
<http://www.sciencedirect.com/science/article/B6TXP-4JHMYC-1/2/d1800c60aadd1d6d297b8a83369e5d7a>
27. J.M. O'Hare and R.J. Brecha, *Optical Radiation and Matter*, unpublished book used as a text at the University of Dayton (2004)
<http://campus.udayton.edu/~physics/pep/eop502/Optical%20Radiation%20and%20Matter.pdf>
28. M. C. Wengler, B. Fassbender, E. Soergel, and K. Buse, "Impact of ultraviolet light on coercive field, poling dynamics and poling quality of various lithium niobate crystals from different sources," *J. Appl. Phys.* 96, 2816 (2004)
http://jap.aip.org/japiau/v96/i5/p2816_s1
29. Sarangan, Andrew, "LIGHTS: Online Optical Simulation Software." Web. Spring 2010.
<<http://www.nano-fab.com/lights/>>
30. A.M. Sarangan, *Integrated Optics*, unpublished book used as a text at the University of Dayton (2007)
<http://131.238.119.245/sarangan/courses/604/604book.pdf>
31. R.S. Weis, T.K. Gaylord [*Appl. Phys. A* (Germany) vol.37 no.4 (1985) p.191-203]
<http://www.springerlink.com/content/g645525436r81w04/>
32. Wong, K. K. *Properties of Lithium Niobate*. London: INSPEC, 2002. Print.
33. Arnau, Antonio. *Piezoelectric Transducers and Applications*. New York, NY: Springer, 2008. Print.
34. AdvR Inc, "AdvR Electro-Optic Fiber Switch." *Welcome to AdvR Inc*. Web. 09 July 2009.
<<http://www.advr-inc.com/switch.html>>
35. F. Muhammad, P. Chandramani, J. Ekman, F. Kiamilev, V. Gopalan, E. Moore, and M. Weiler, "Compact Multipchannel 2KV Arbitray Waveform Generator for Ferroelectric Device Arrays," 2001 IEEE/LEOS Annual Meeting Conference Proceedings, Vol. 2, p. 818, (unpublished).
<http://ieeexplore.ieee.org/stamp/stamp.jsp?arnumber=00969066>
36. P. D. Henshaw, A. Sanchez, and R. B. McSheehy, "Digital beam switch for agile beam laser radar," *Appl. Opt.* **19**, 884-890 (1980)
<http://www.opticsinfobase.org/ao/abstract.cfm?URI=ao-19-6-884>
37. Qibiao Chen; Yi Chiu; Lambeth, D.N.; Schlesinger, T.E.; Stancil, D.D., "Guided-wave electro-optic beam deflector using domain reversal in LiTaO₃," *Lightwave Technology, Journal of*, vol.12, no.8, pp.1401-1404, Aug 1994
<http://ieeexplore.ieee.org/stamp/stamp.jsp?arnumber=317528&isnumber=7652>
38. J. Li; H.C. Cheng; M.J. Kawa; D.N. Lambeth; T.E. Schlesinger; D.D. Stancil, "Electrooptic wafer beam deflector in LiTaO₃," *Photonics Technology Letters, IEEE*, vol.8, no.11, pp.1486-1488, Nov. 1996
<http://ieeexplore.ieee.org/stamp/stamp.jsp?arnumber=541558&isnumber=11690>
39. M. Yamada; M. Saitoh; H. Ooki, "Electric-field induced cylindrical lens, switching and deflection devices composed of the inverted domains in LiNbO₃ crystals," *Appl. Phys. Lett.* **69**, 3659 (1996)
<http://link.aip.org/link/APPLAB/69/3659/1>

40. D. Scrymgeour, A. Sharan, V. Gopalan, K. T. Gahagan, R. Sander, J. M. Robinson, F. Muhammad, P. Chandramani and F. Kiamilev, "Cascaded Electro-optic scanning of laser light over large angles using domain microengineered ferroelectrics" *Appl. Phys. Lett.*, **81**, 3140-3 (2002).
<http://cat.inist.fr/?aModele=afficheN&cpsidt=13984098>
41. Davis, Scott R.; Rommel, Scott D.; Farca, George; Anderson, Michael H., "A new electro-optic waveguide architecture and the unprecedented devices it enables," *Proceedings of the SPIE*, Volume 6975, pp. 697503-697503-12 (2008)
http://spie.org/x648.html?product_id=783780
42. Mahesh Krishnamurthi, Mariola O. Ramirez, Sava Denev, Venkatraman Gopalan, Thomas M. Lehecka, Jeffrey G. Thomas, and Q. X. Jia, "Two dimensional dynamic focusing of laser light by ferroelectric domain based electro-optic lenses," *Appl. Phys. Lett.* 90, 201106 (2007)
<http://link.aip.org/link/?APPLAB/90/201106/1>
43. M. Krishnamurthi, M. Ramirez, L. Tian, and V. Gopalan, "Two-Dimensional Dynamic Focusing and Optical Switching of Laser Light by Ferroelectric Devices," in *Conference on Lasers and Electro-Optics/Quantum Electronics and Laser Science Conference and Photonic Applications Systems Technologies*, OSA Technical Digest (CD) (Optical Society of America, 2008), paper CThBB5.
<http://www.opticsinfobase.org/abstract.cfm?URI=CLEO-2008-CThBB5>
44. D. Zelmon, D. Small, and D. Jundt, "Infrared corrected Sellmeier coefficients for congruently grown lithium niobate and 5 mol.% magnesium oxide-doped lithium niobate," *J. Opt. Soc. Am. B* 14, 3319-3322 (1997).
<http://www.opticsinfobase.org/abstract.cfm?URI=josab-14-12-3319>
45. Fujiwara, T.; Takahashi, M.; Ohama, M.; Ikushima, A.J.; Furukawa, Y.; Kitamura, K., "Comparison of electro-optic effect between stoichiometric and congruent LiNbO₃," *Electronics Letters*, vol.35, no.6, pp.499-501, 18 Mar 1999
<http://ieeexplore.ieee.org/stamp/stamp.jsp?arnumber=756419&isnumber=16402>

APPENDIX A – A CATALOG OF FDM BEAM PROPAGATION SIMULATION RESULTS

This appendix contains the result of all FDM beam propagation simulations performed in the course of investigating the performance of the EOBS.

A.1 The Performance of All Channels at the Design Point

Recall that five EOBS steering channels were designed with different geometries suitable for steering beams of different qualities. Table A.1 summarizes each of these channels.

Table A.1 – The final design parameters of each channel.

Channel Number	D (μm)	α ($^\circ$)	Translation (μm)	Number of Cells	h (μm)	l (μm)	CL (μm)	Beta ($^\circ$)
1	255	30	775.16	48	392.57	1359.89	0.67224	0.056695
2	145	22.9	1071.52	48	290.39	1374.89	0.92859	0.077519
3	190	30	913.52	56	339.90	1177.46	0.58206	0.056695
4	170	30	1044.60	64	297.58	1030.86	0.50959	0.056695
5	175	30	497.25	44	299.69	1038.16	0.51320	0.056695

This section shows the optical field and the center of amplitude beampath for Gaussian beams propagating through each channel at the design point: $V_{\text{applied}} = -1005.6 \text{ Volts}$, $\text{Temp} = 20^\circ\text{C}$, $\lambda = 1064 \text{ nm}$, and $r_{33} = 30.8 \text{ pm/V}$.

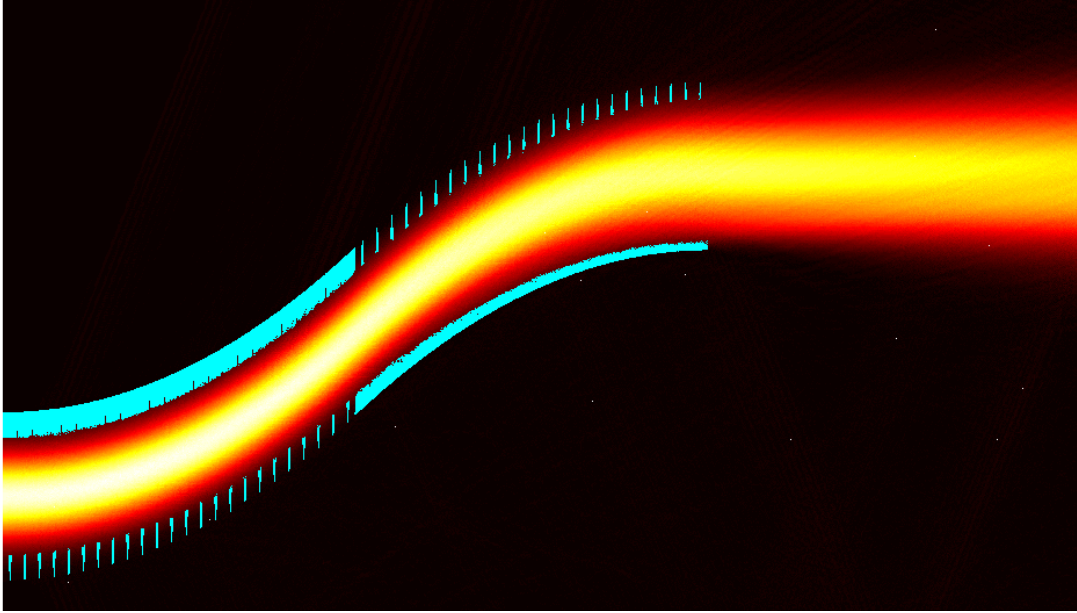


Figure A.1 – The optical field of a Gaussian beam propagating through Channel 1.

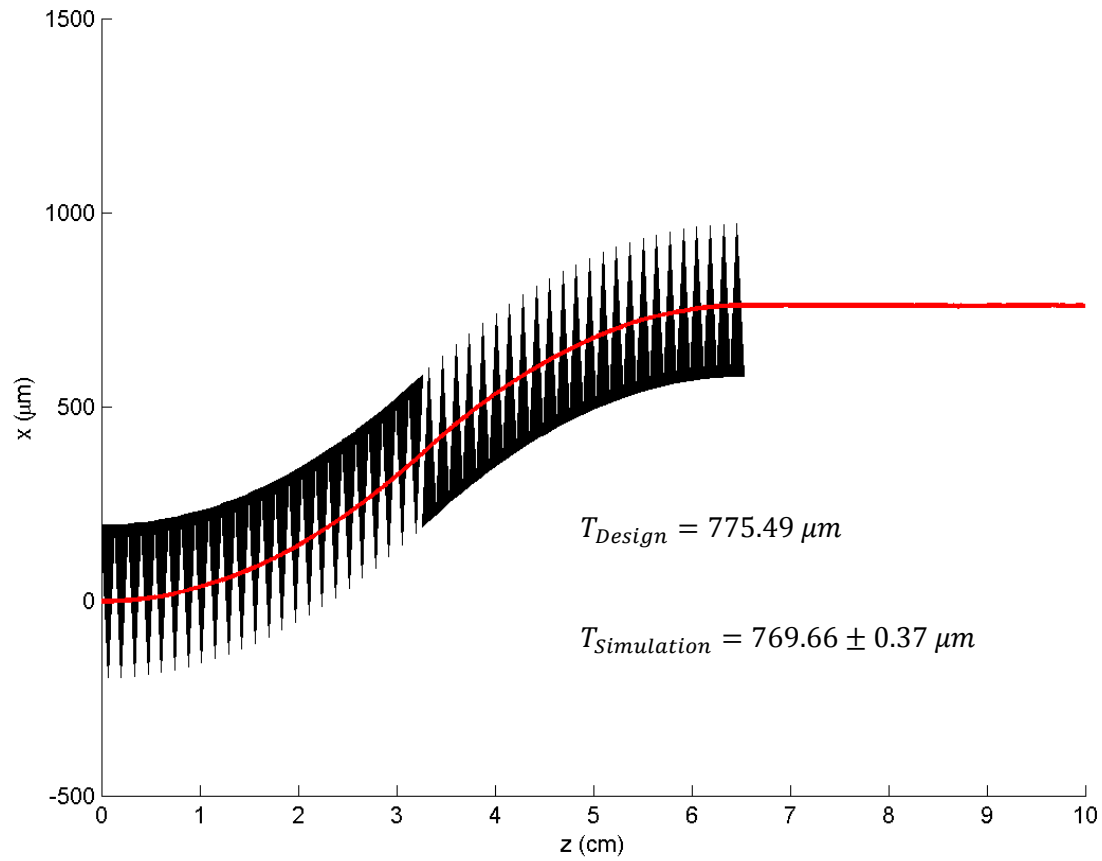


Figure A.2 – The center of amplitude beampath of a Gaussian beam in Channel 1.

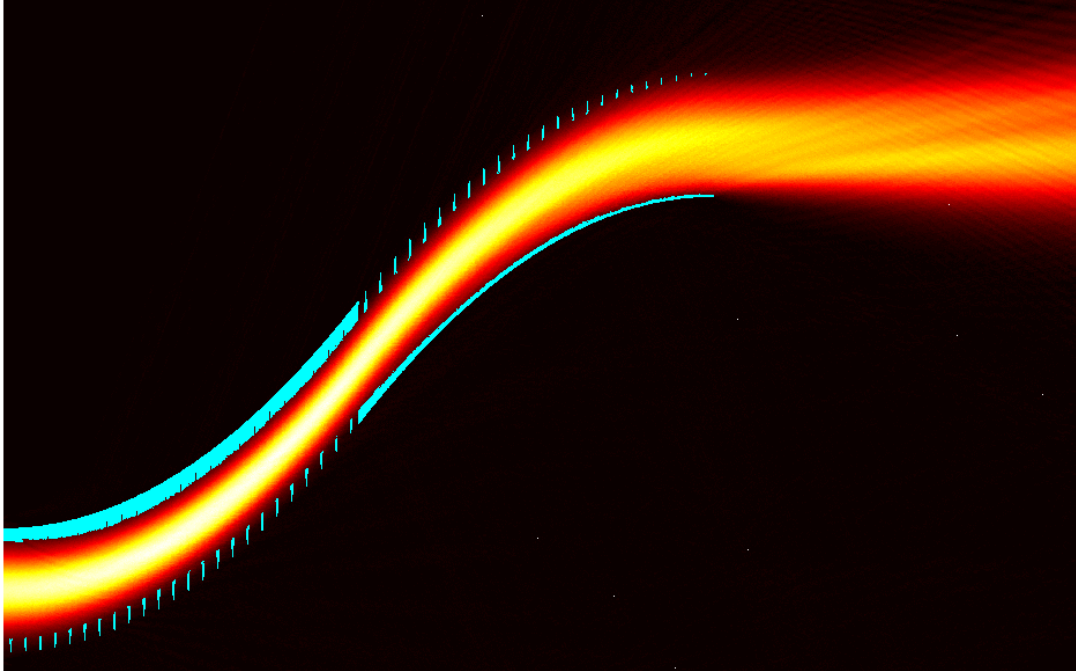


Figure A.3 – The optical field of a Gaussian beam propagating through Channel 2.

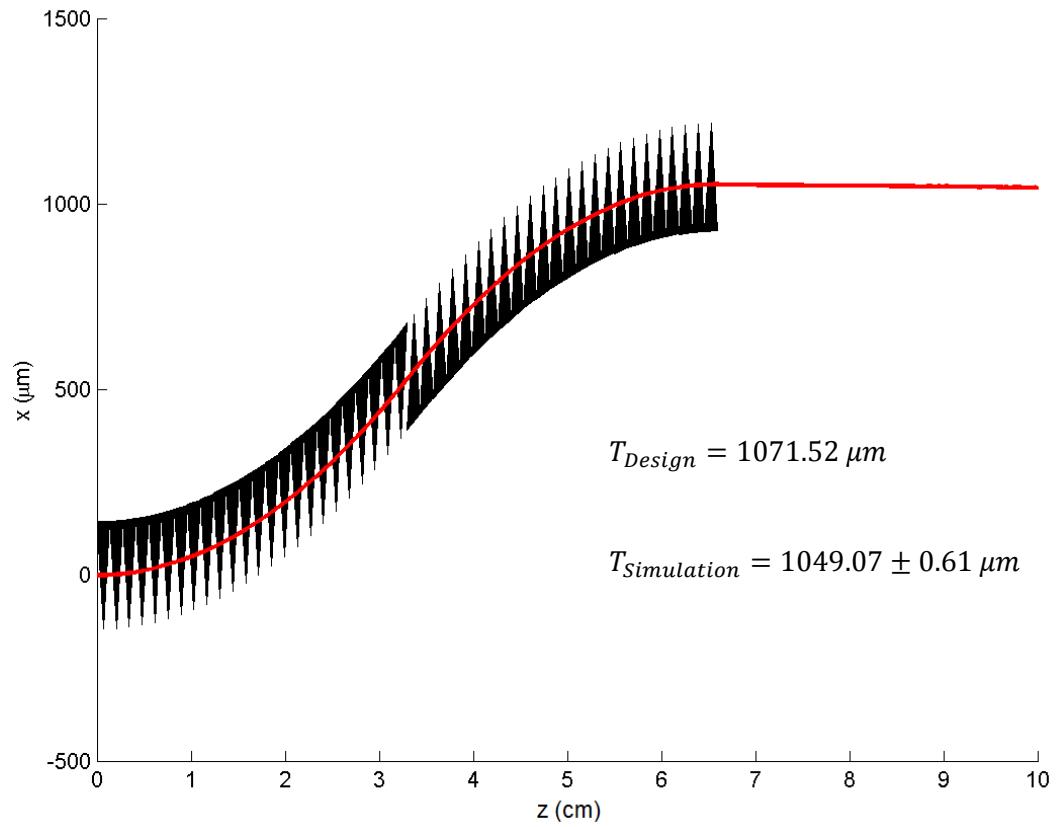


Figure A.4 – The center of amplitude beampath of a Gaussian beam in Channel 2.

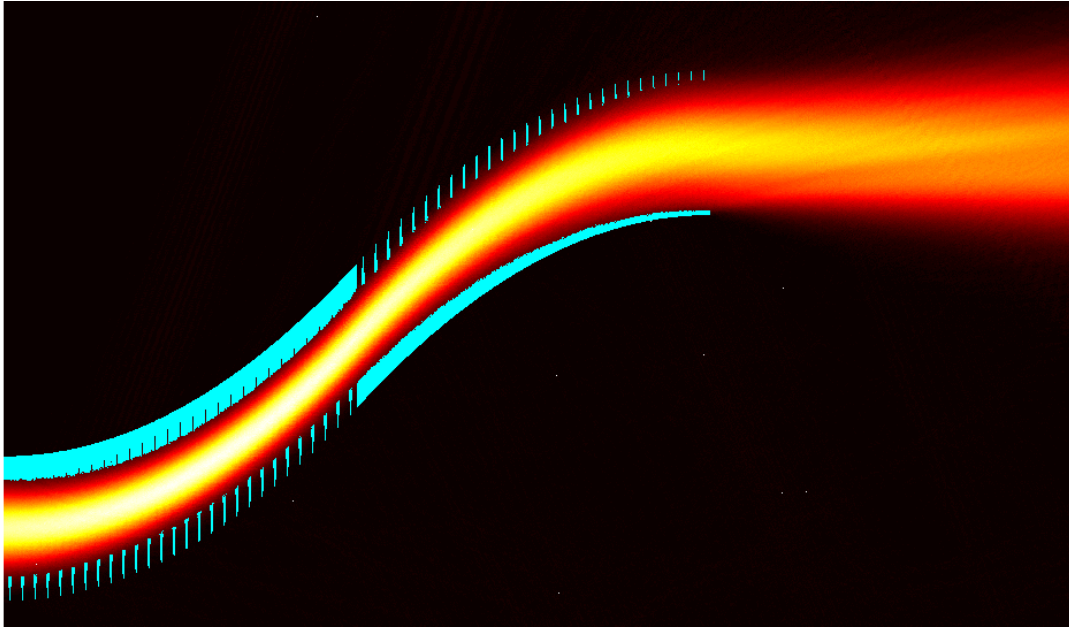


Figure A.5 – The optical field of a Gaussian beam propagating through Channel 3.

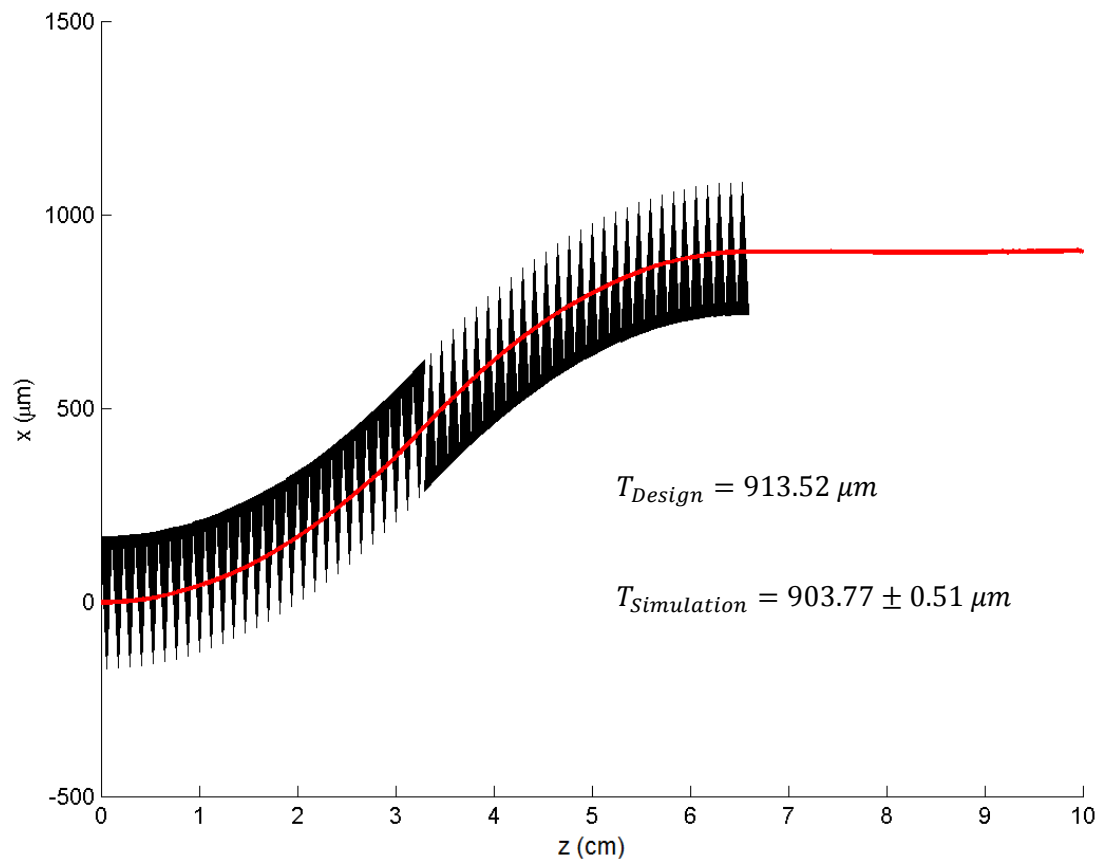


Figure A.6 – The center of amplitude beampath of a Gaussian beam in Channel 3.

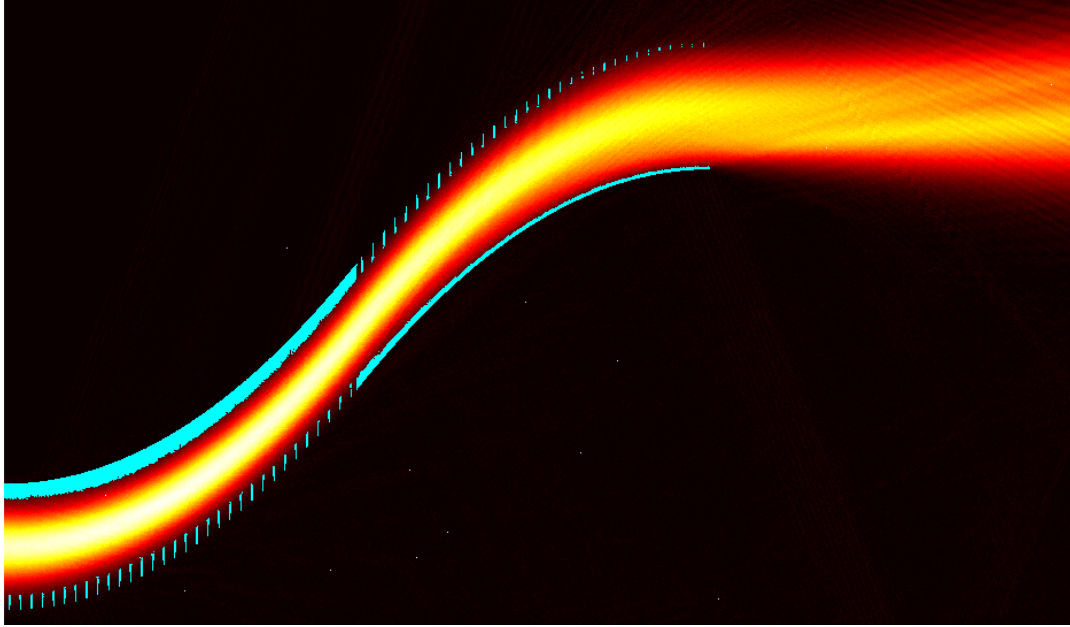


Figure A.7 – The optical field of a Gaussian beam propagating through Channel 4.

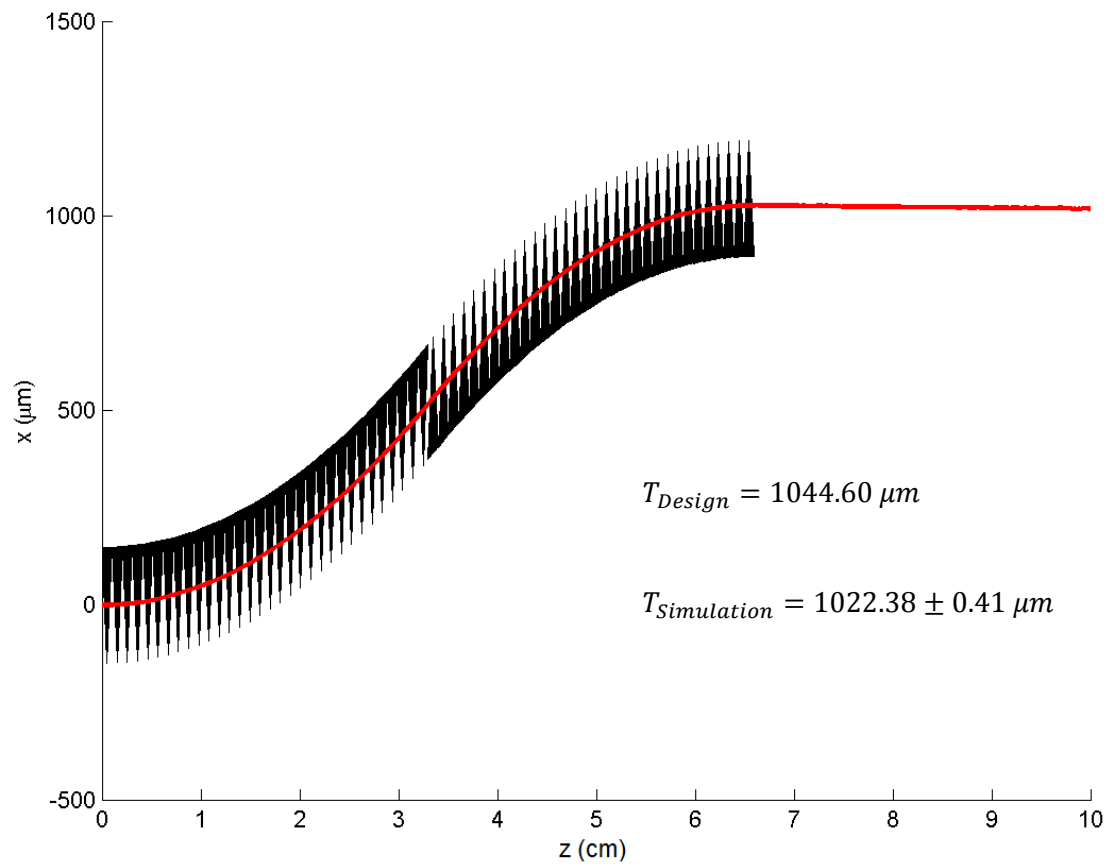


Figure A.8 – The center of amplitude beampath of a Gaussian beam in Channel 4.

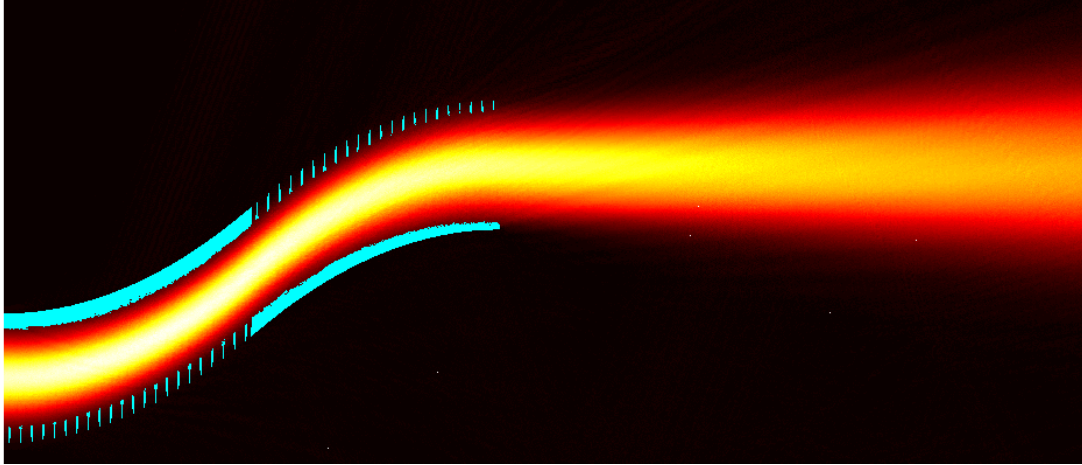


Figure A.9 – The optical field of a Gaussian beam propagating through Channel 5.

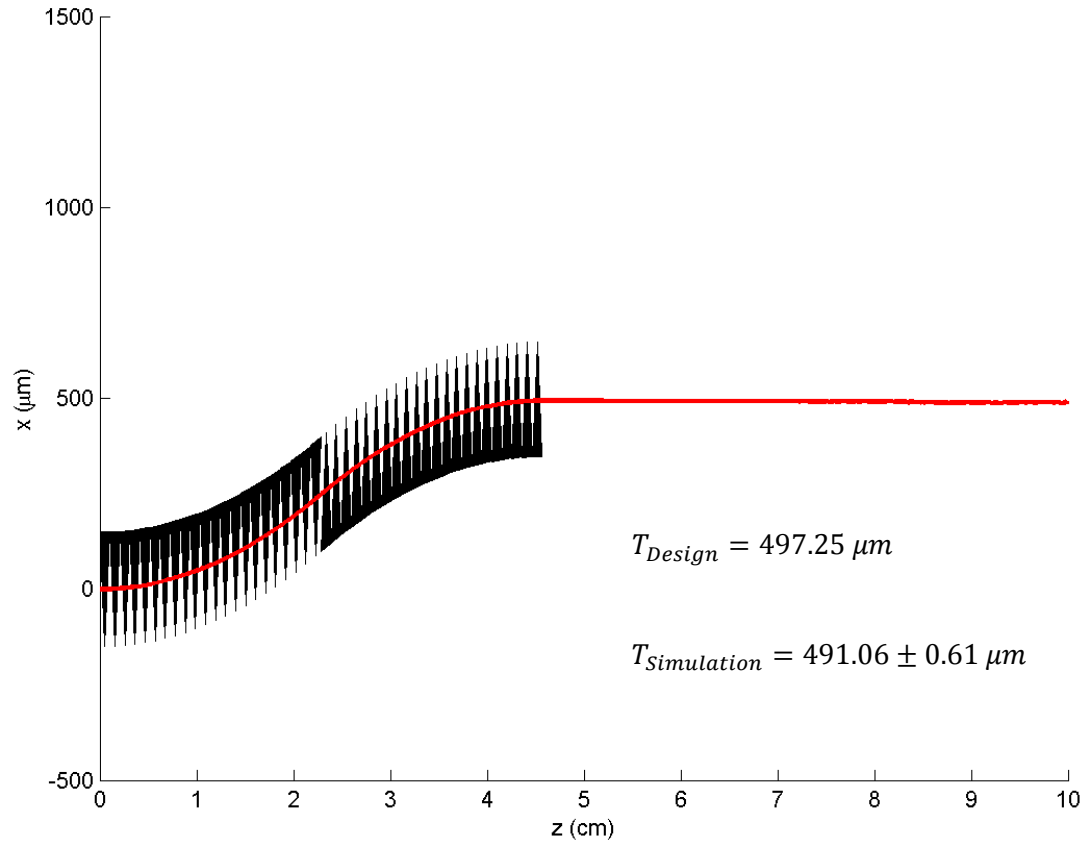


Figure A.10 – The center of amplitude beampath of a Gaussian beam in Channel 5.

A.2 Channel 1 Performance under Non-Design Conditions

Propagation of a Gaussian beam through Channel 1 was simulated at non-design conditions. The intent of this study was to develop a qualitative understanding of the relationship between environmental variables and EOBS steering performance. Thus, each simulation presented in this section was conducted for single parameter deviations from the design point.

A.2.1 The Effect of Uniform Deviations in Temperature

This section presents the effect of shifts in ambient temperature on the performance of EOBS channel 1. The EOBS was designed under the assumption that $T = 20^{\circ}\text{C}$. Here ambient temperature is assumed to take on values $0^{\circ}\text{C} \leq T \leq 50^{\circ}\text{C}$. The optical field propagating through Channel 1 is shown in separate figures for cases separated by $\Delta T = 5^{\circ}\text{C}$.

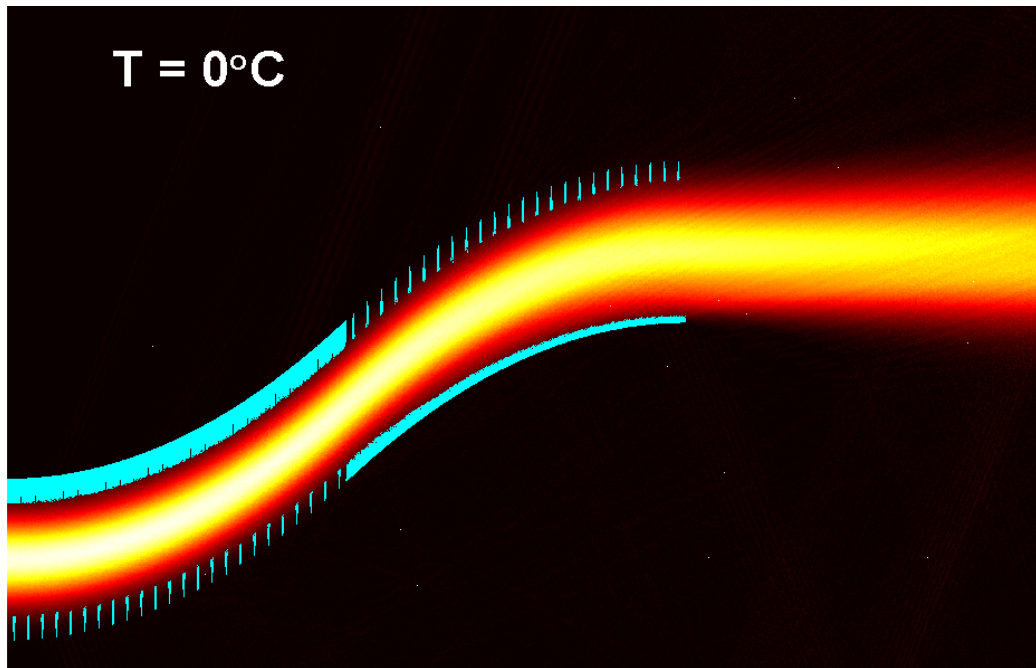


Figure A.11 – A Gaussian beam propagating through Channel 1 at $T = 0^{\circ}\text{C}$.

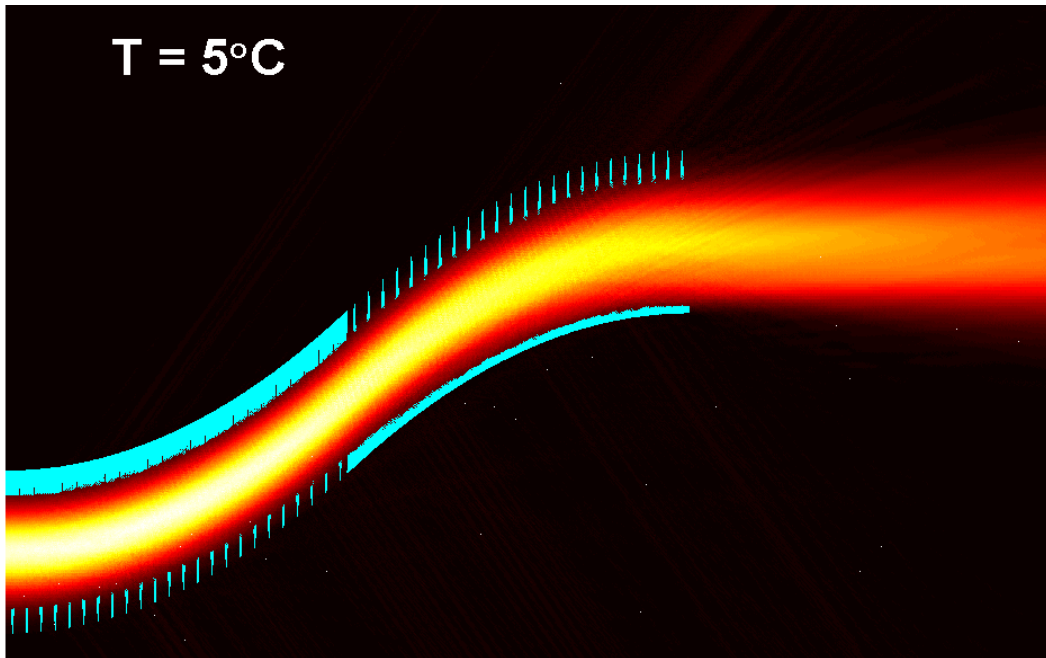


Figure A.12 – A Gaussian beam propagating through Channel 1 at $T = 5^{\circ}\text{C}$.

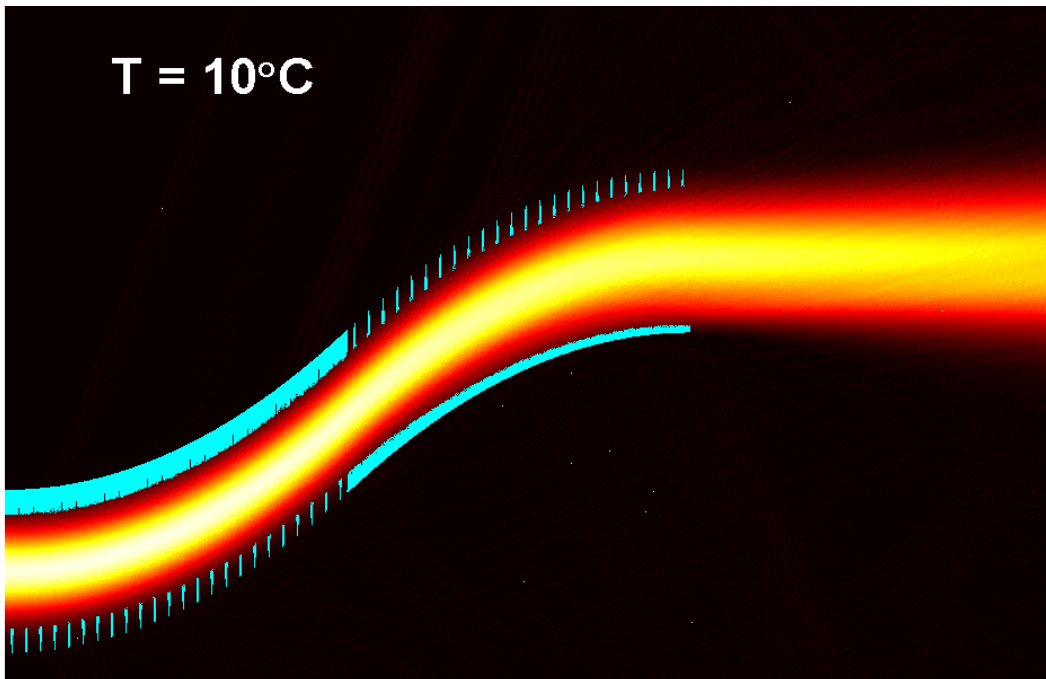


Figure A.13 – A Gaussian beam propagating through Channel 1 at $T = 10^{\circ}\text{C}$.

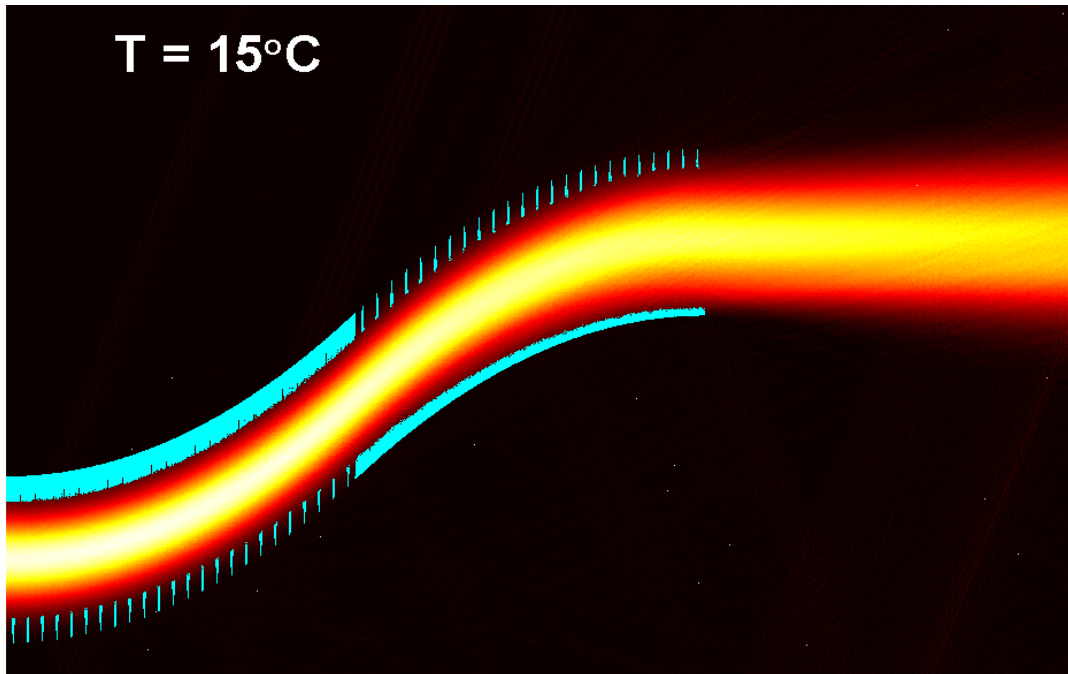


Figure A.14 – A Gaussian beam propagating through Channel 1 at $T = 15^{\circ}\text{C}$.

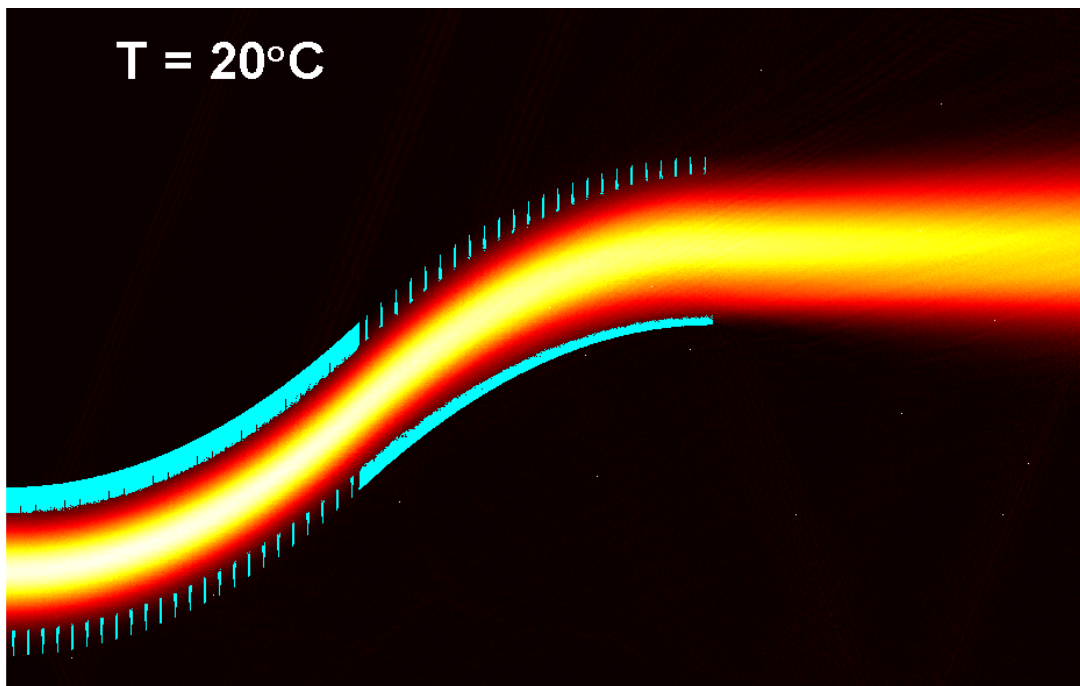


Figure A.15 – A Gaussian beam propagating through Channel 1 at $T = 20^{\circ}\text{C}$.
[Note that this is the design point for the ON state.]

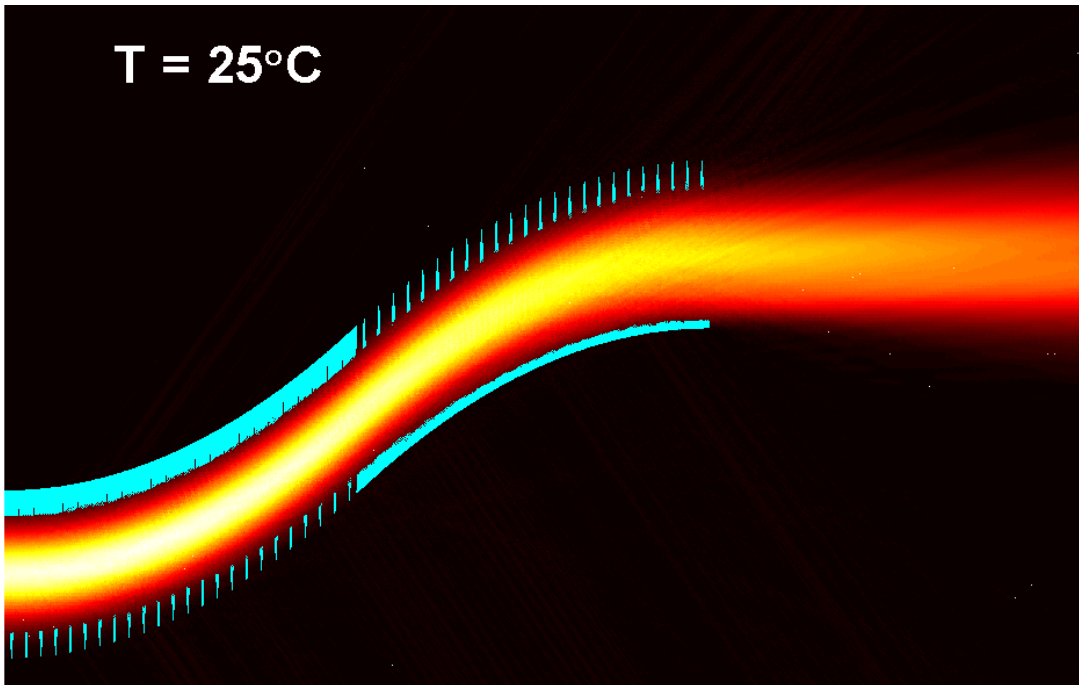


Figure A.16 – A Gaussian beam propagating through Channel 1 at $T = 25^\circ\text{C}$.

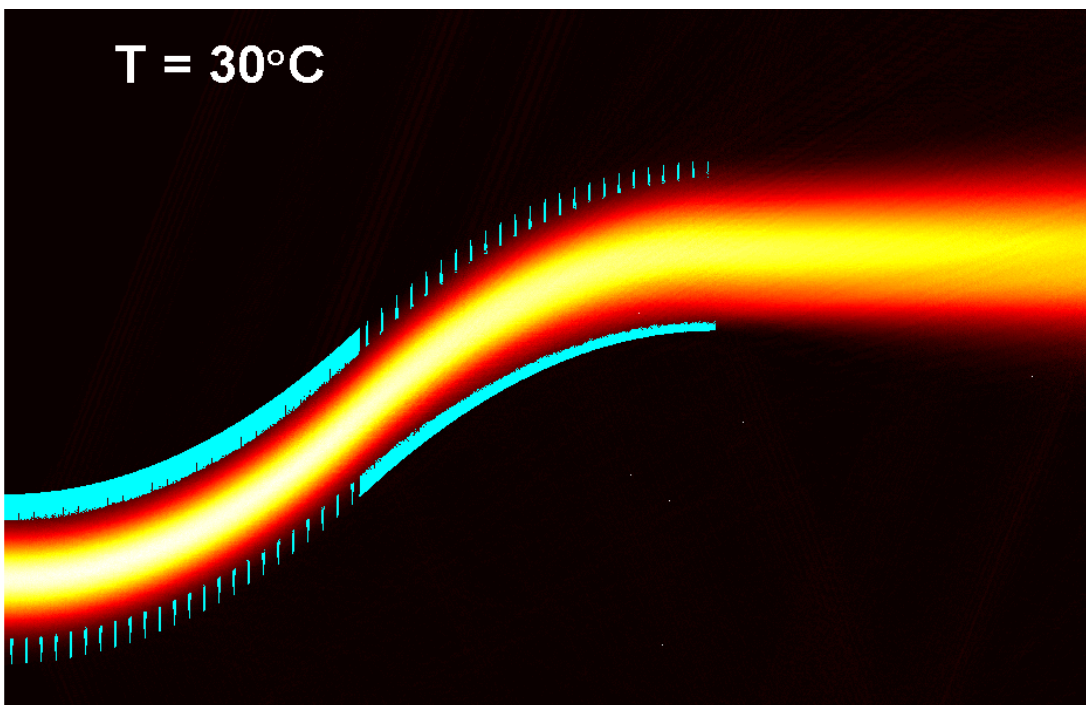


Figure A.17 – A Gaussian beam propagating through Channel 1 at $T = 30^\circ\text{C}$.

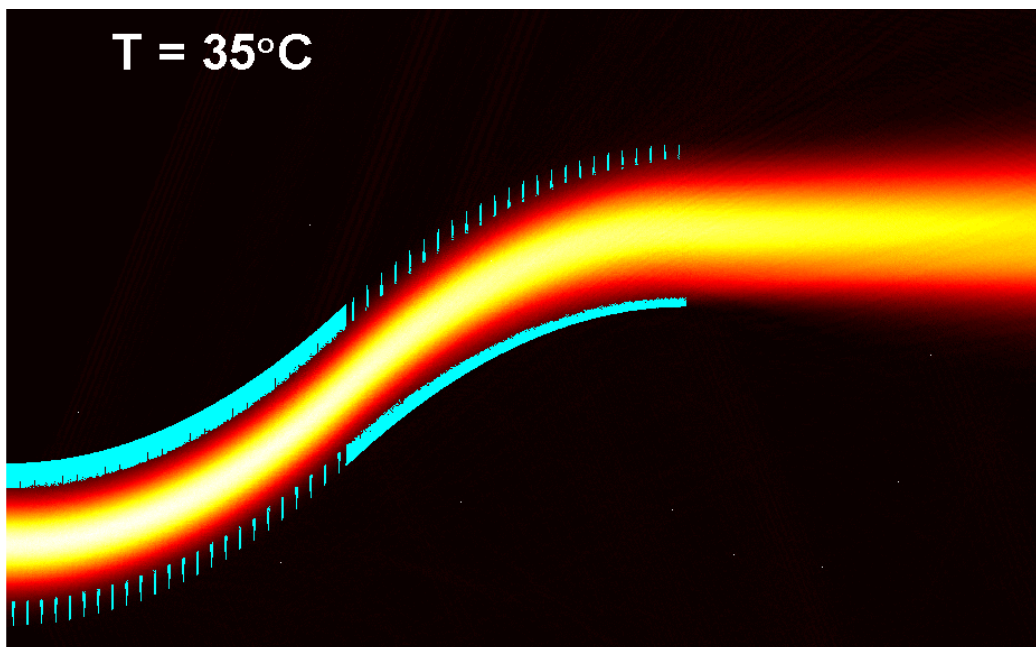


Figure A.18 – A Gaussian beam propagating through Channel 1 at $T = 35^{\circ}\text{C}$.

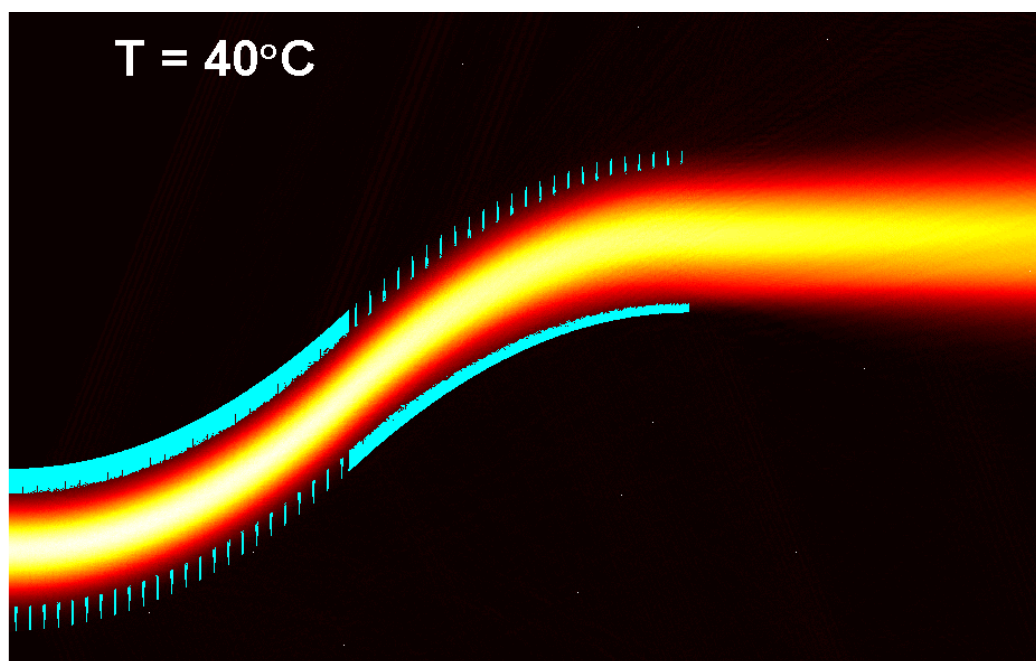


Figure A.19 – A Gaussian beam propagating through Channel 1 at $T = 40^{\circ}\text{C}$.

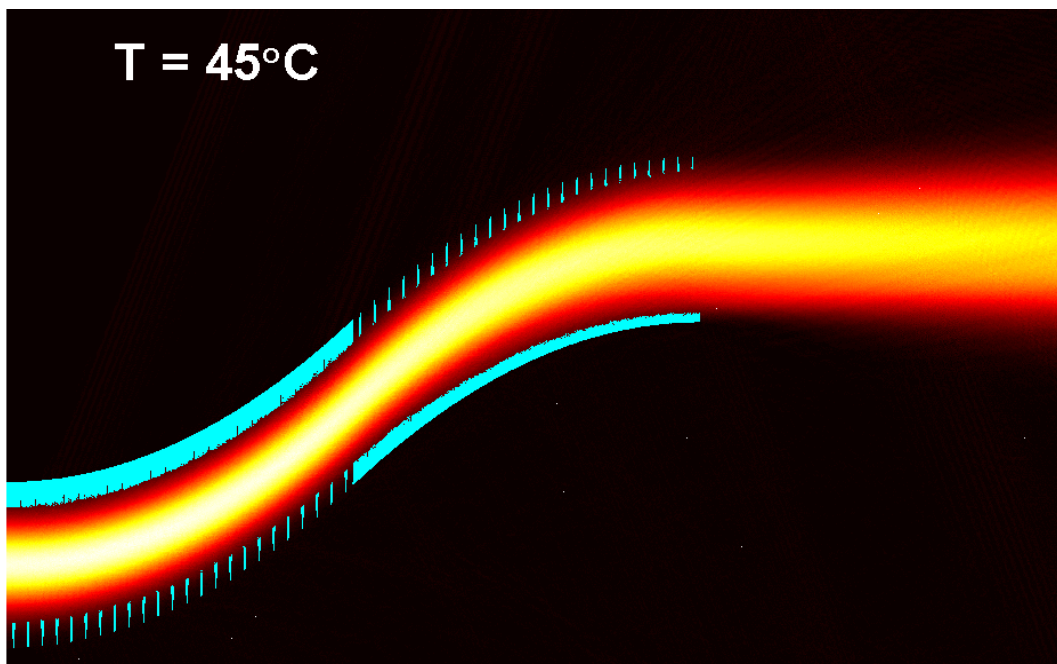


Figure A.20 – A Gaussian beam propagating through Channel 1 at $T = 45^{\circ}\text{C}$.

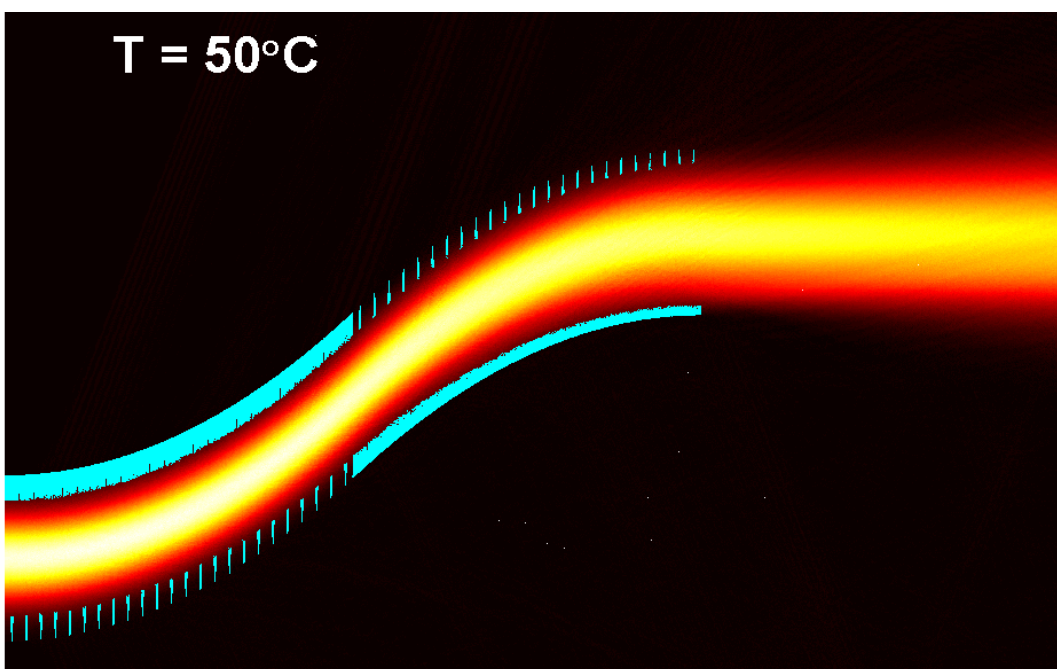


Figure A.21 – A Gaussian beam propagating through Channel 1 at $T = 50^{\circ}\text{C}$.

A.2.2 The Effect of Reductions in the Value of the Electro-Optic Coefficient

This section presents the effect of reductions in the electro-optic coefficient on the performance of EOBS Channel 1. The EOBS was designed under the assumption that $r_{33} = 30.8 \text{ pm/Volt}$. Here the electro-optic coefficient is assumed to take on values $0.8 \cdot r_{33} \leq r'_{33} \leq r_{33}$. The optical field propagating through Channel 1 is shown in separate figures for cases separated by $\Delta r'_{33} = 5\% \cdot r_{33}$.

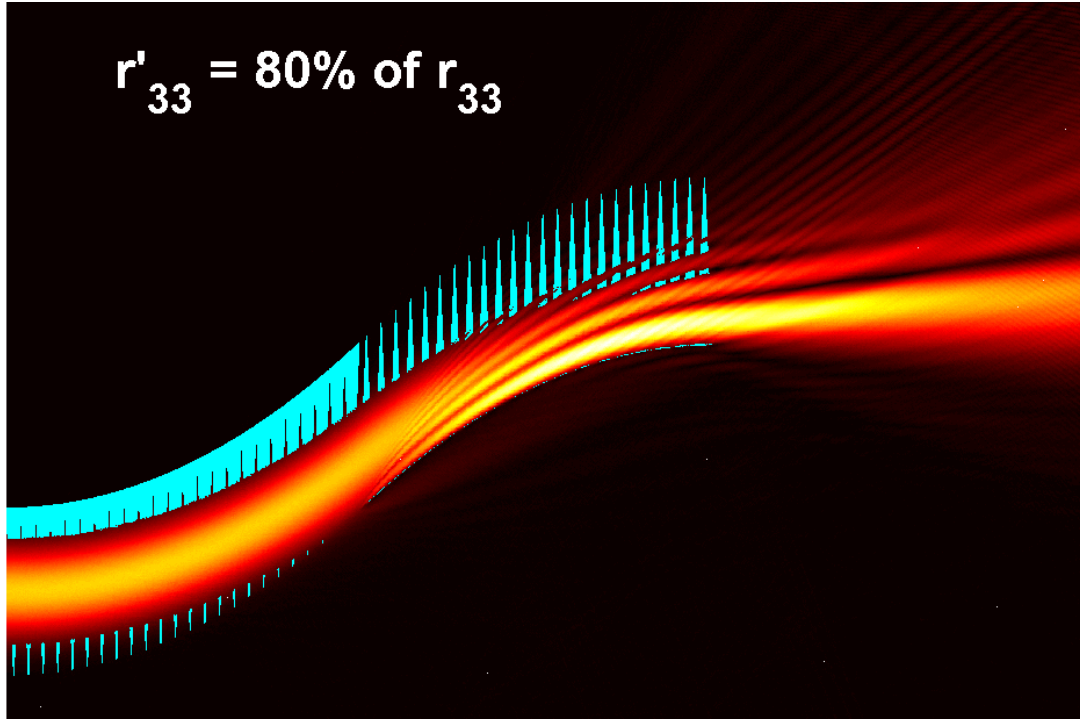


Figure A.22 – A Gaussian beam propagating through Channel 1 at $r'_{33} = 0.80 \cdot r_{33}$.

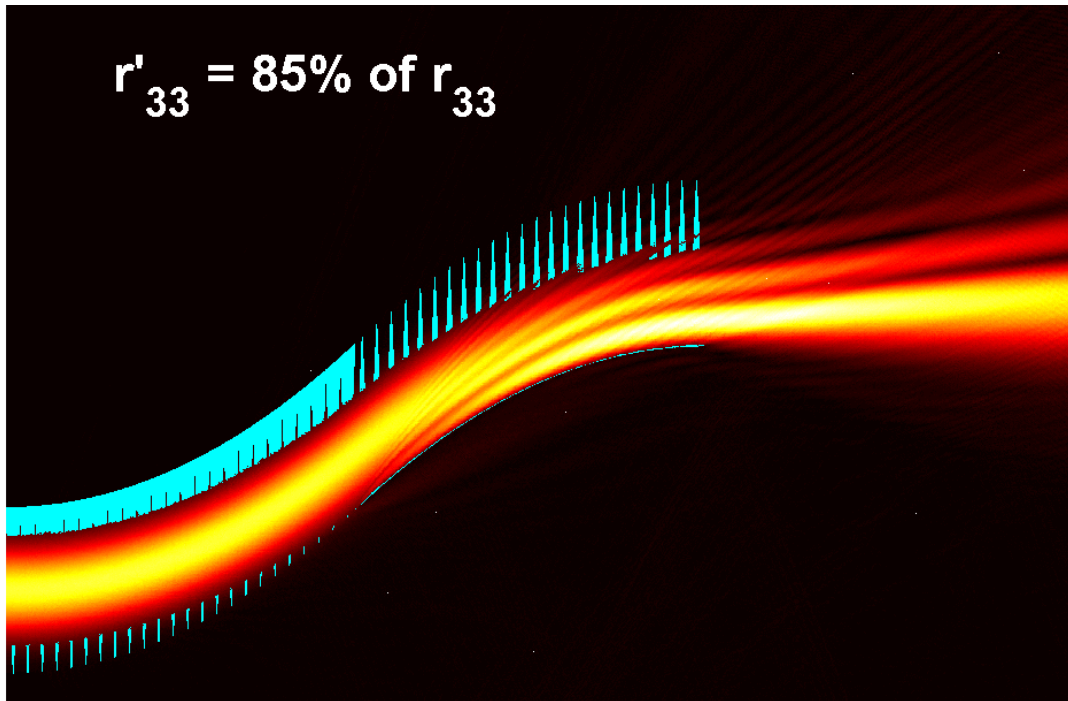


Figure A.23 – A Gaussian beam propagating through Channel 1 at $r'_{33} = 0.85 \cdot r_{33}$.

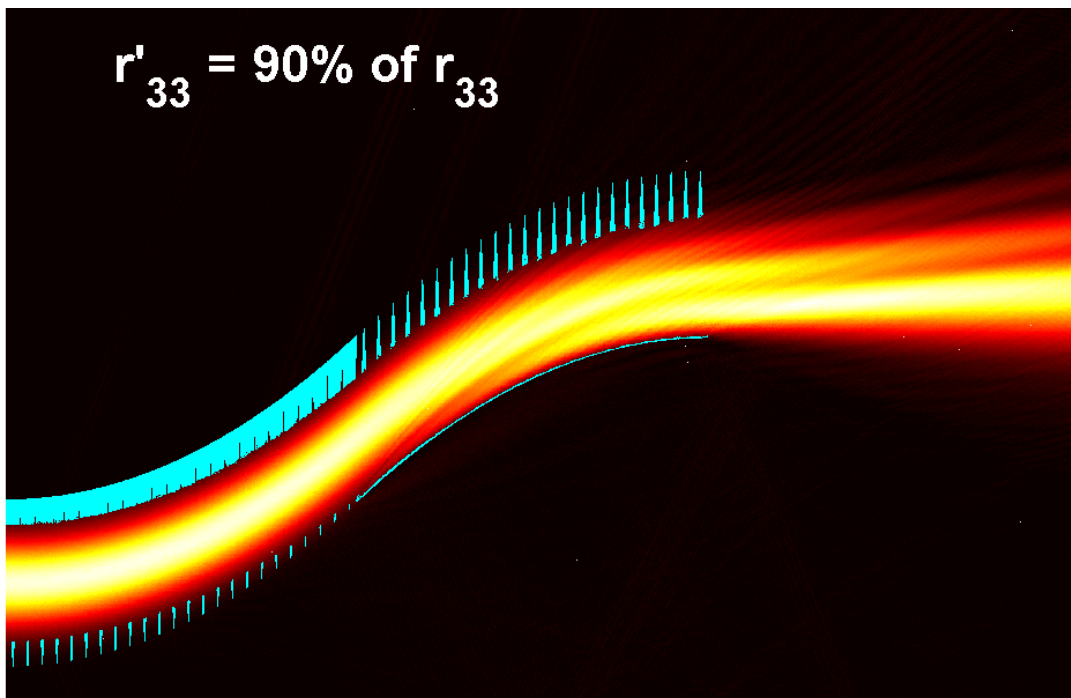


Figure A.24 – A Gaussian beam propagating through Channel 1 at $r'_{33} = 0.90 \cdot r_{33}$.

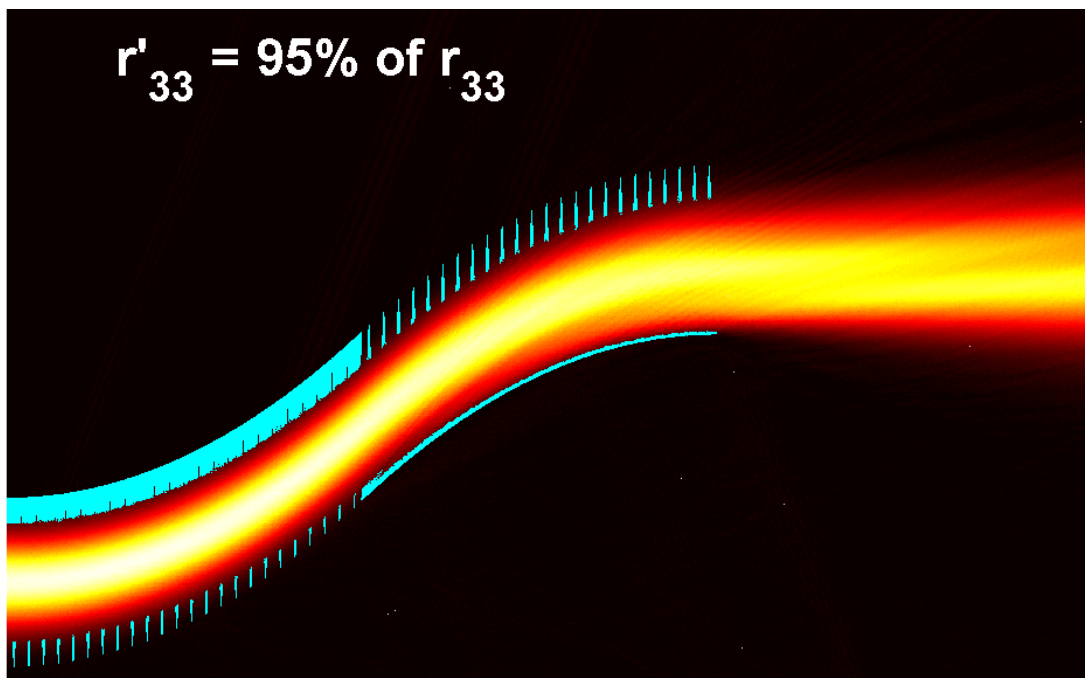


Figure A.25 – A Gaussian beam propagating through Channel 1 at $r'_{33} = 0.95 \cdot r_{33}$.

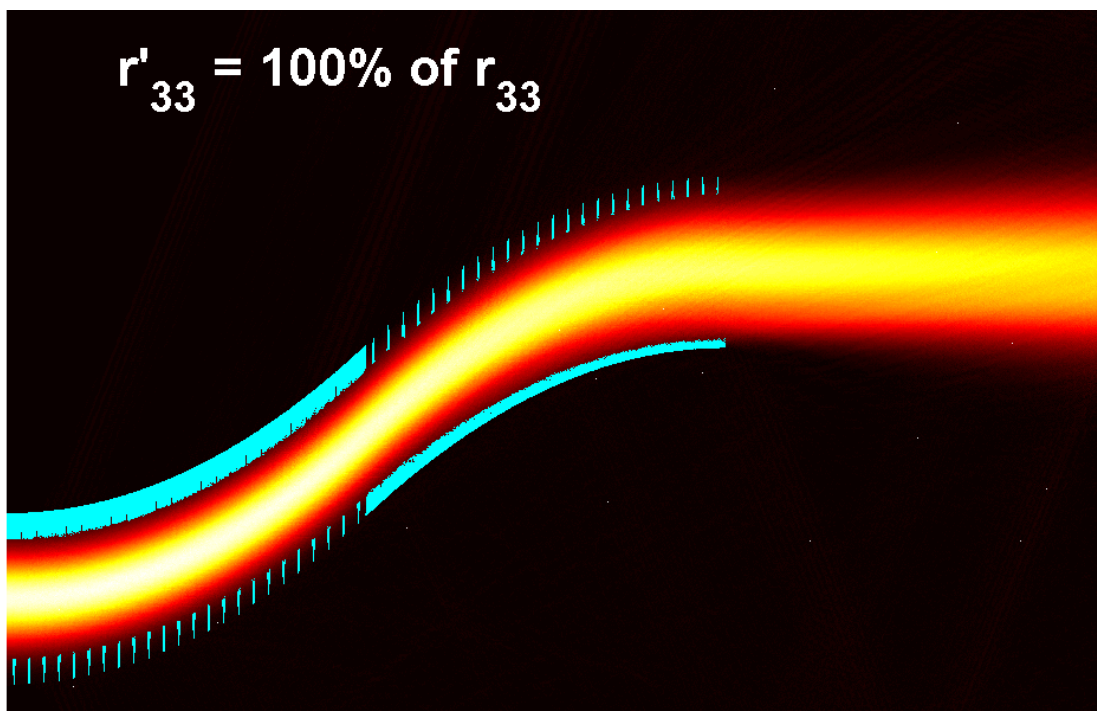


Figure A.26 – A Gaussian beam propagating through Channel 1 at $r'_{33} = r_{33}$.
[Note that this is the design point for the ON state.]

A.2.3 The Suitability of Channel 1 to Switch Beams at Various Wavelengths

This section demonstrates the ability of EOBS Channel 1 to steer beams at wavelengths that it was not designed to steer. The EOBS was designed under the assumption that $\lambda = 1064 \text{ nm}$. Here the wavelength is varied across the range $500 \text{ nm} \leq \lambda \leq 1500 \text{ nm}$. The optical field propagating through Channel 1 is shown in separate figures for cases separated by $\Delta\lambda = 500 \text{ nm}$.

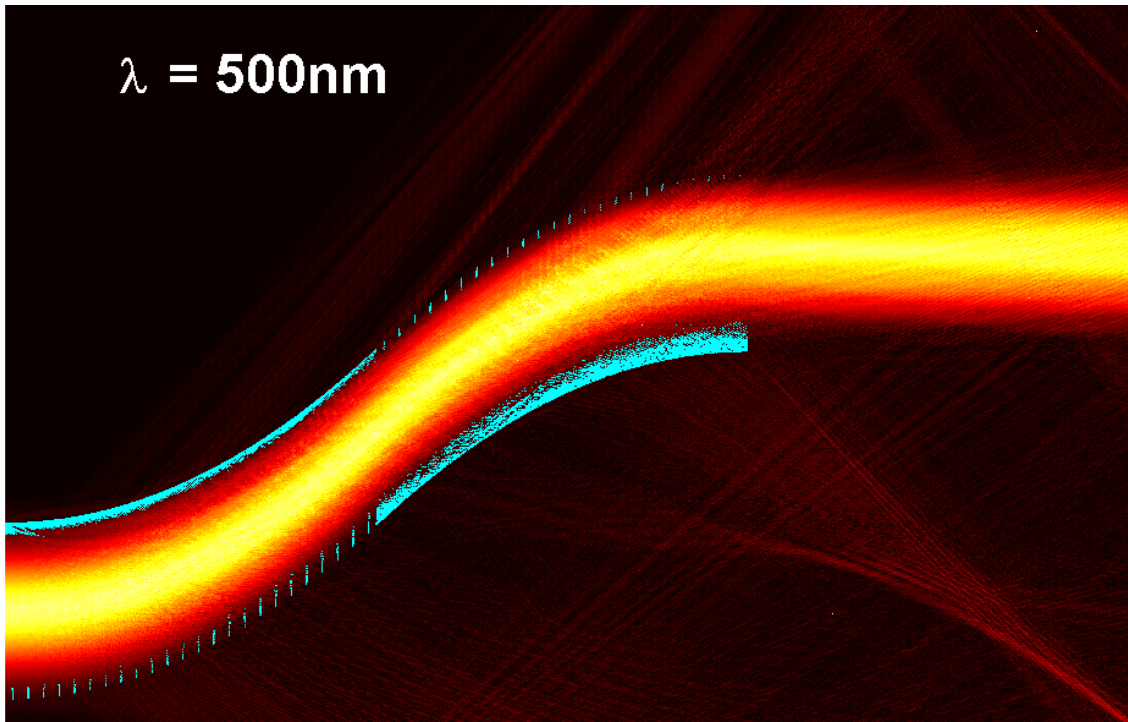


Figure A.27 – A Gaussian beam with $\lambda = 500 \text{ nm}$ propagating through Channel 1.

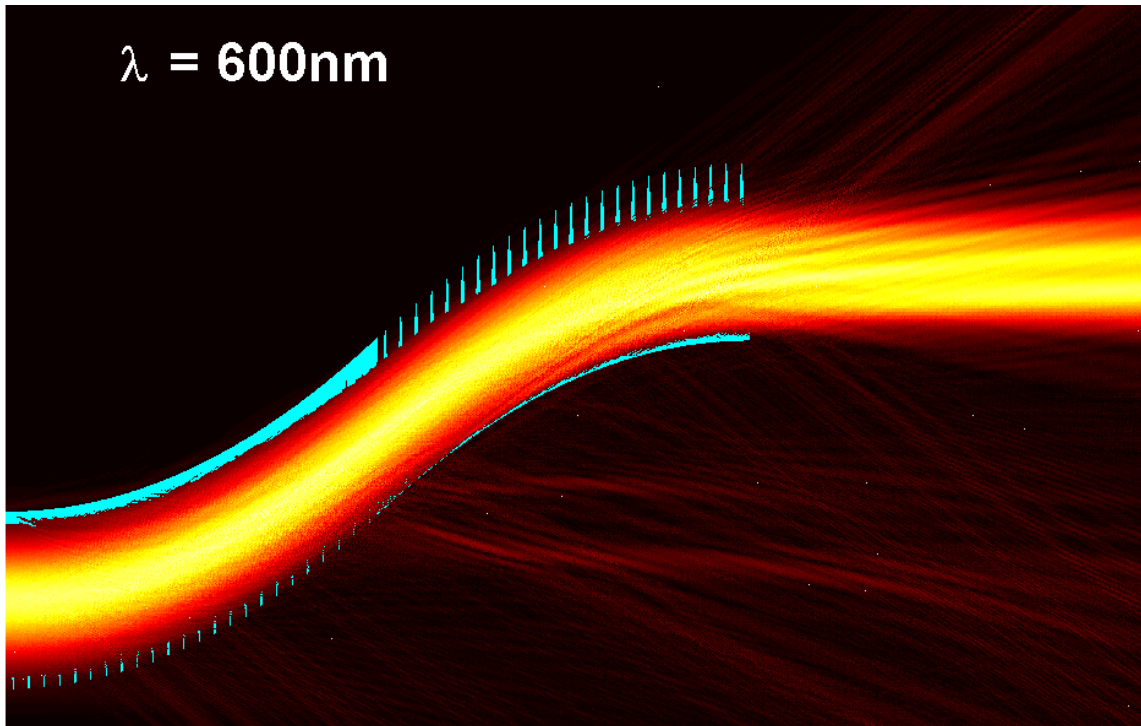


Figure A.28 – A Gaussian beam with $\lambda = 600 \text{ nm}$ propagating through Channel 1.

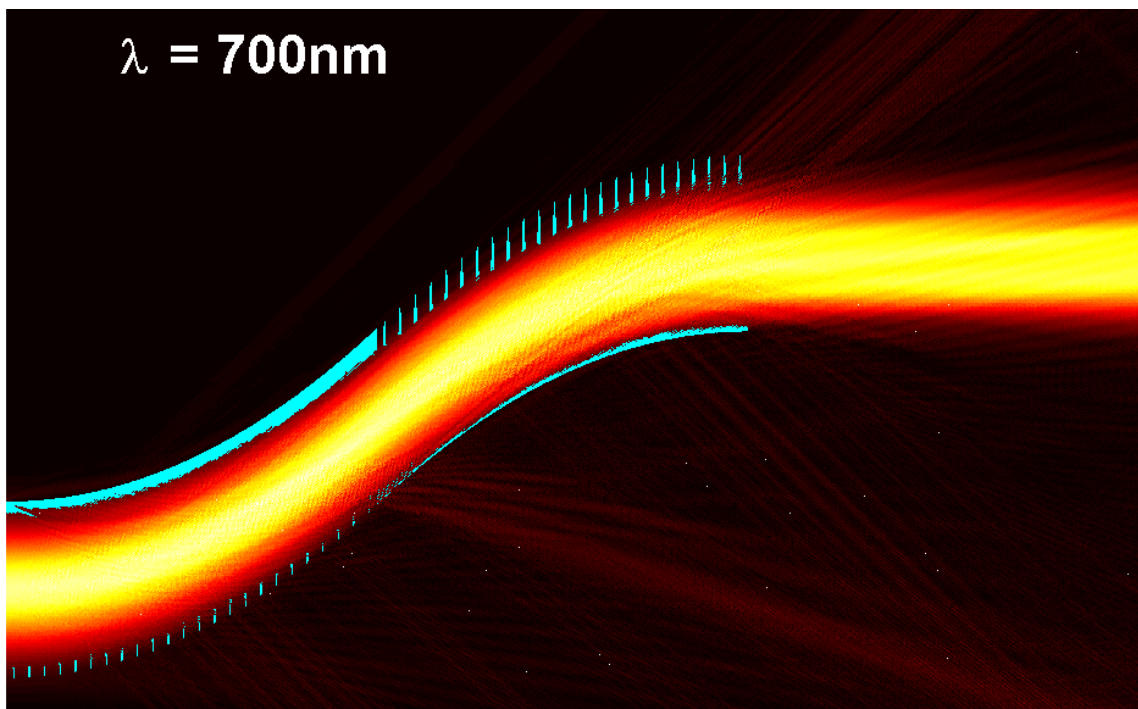


Figure A.29 – A Gaussian beam with $\lambda = 700 \text{ nm}$ propagating through Channel 1.

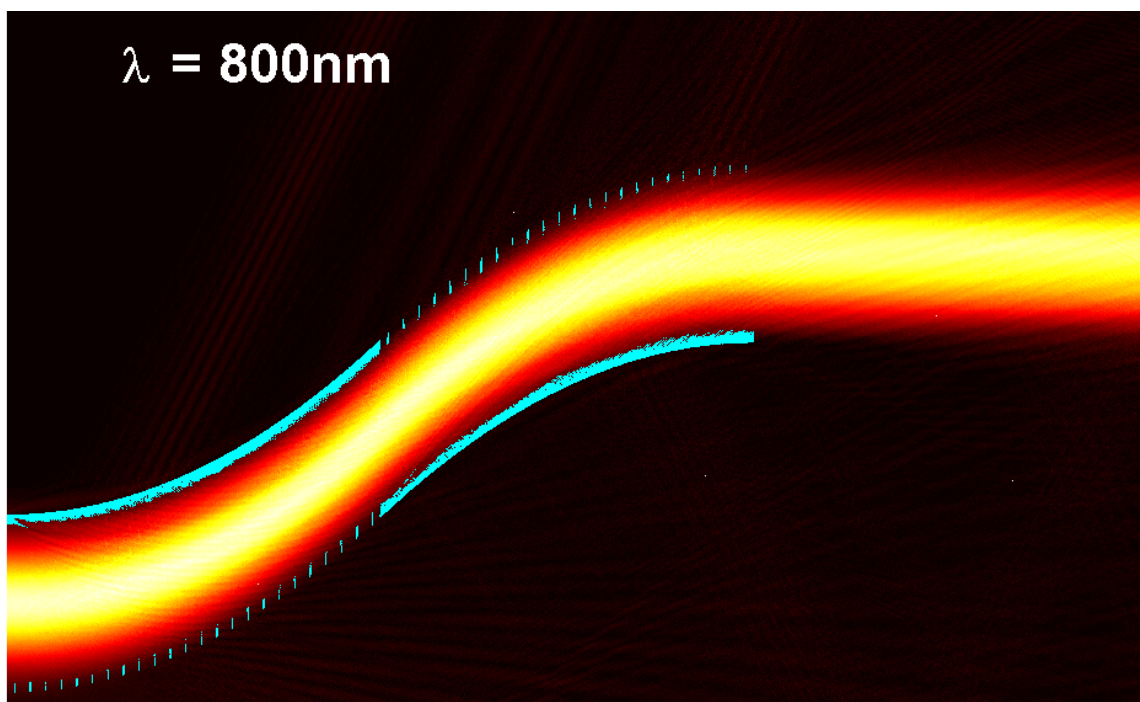


Figure A.30 – A Gaussian beam with $\lambda = 800\text{ nm}$ propagating through Channel 1.

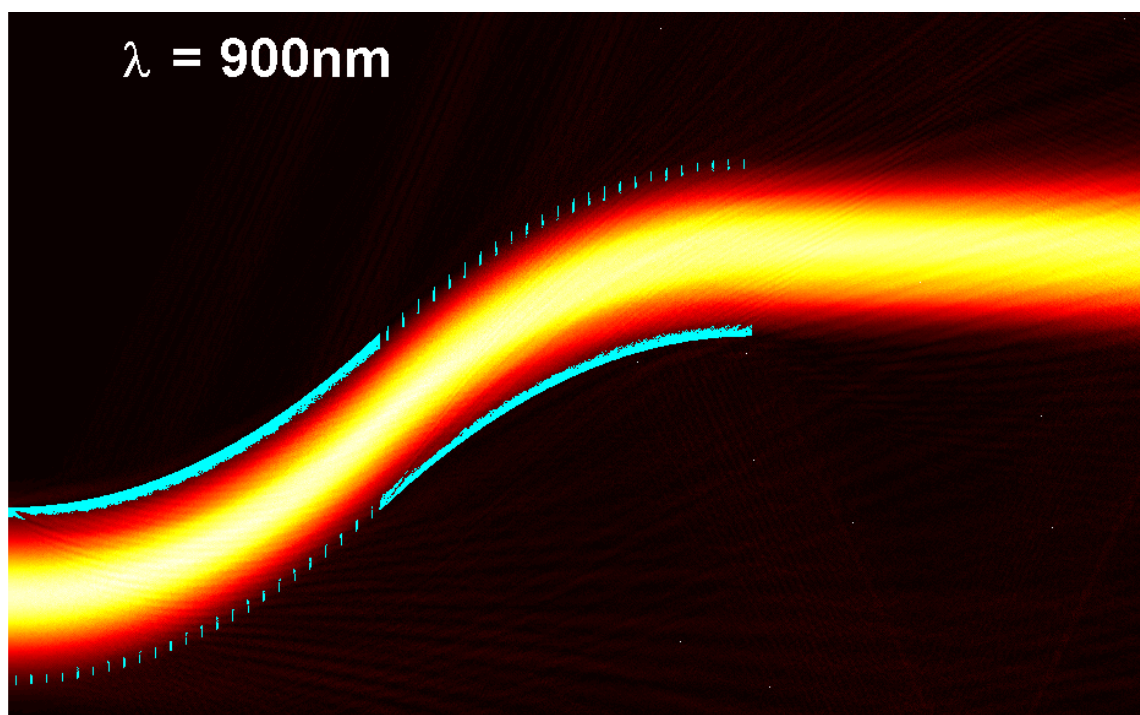


Figure A.31 – A Gaussian beam with $\lambda = 900\text{ nm}$ propagating through Channel 1.

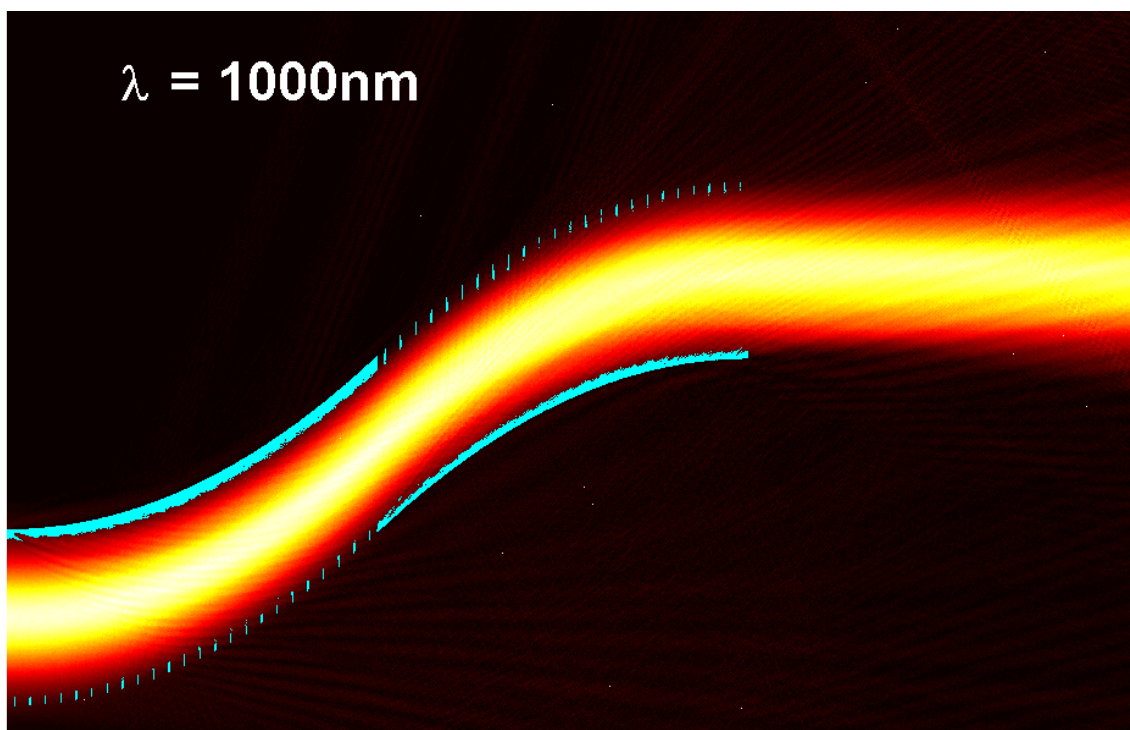


Figure A.32 – A Gaussian beam with $\lambda = 1000 \text{ nm}$ propagating through Channel 1.

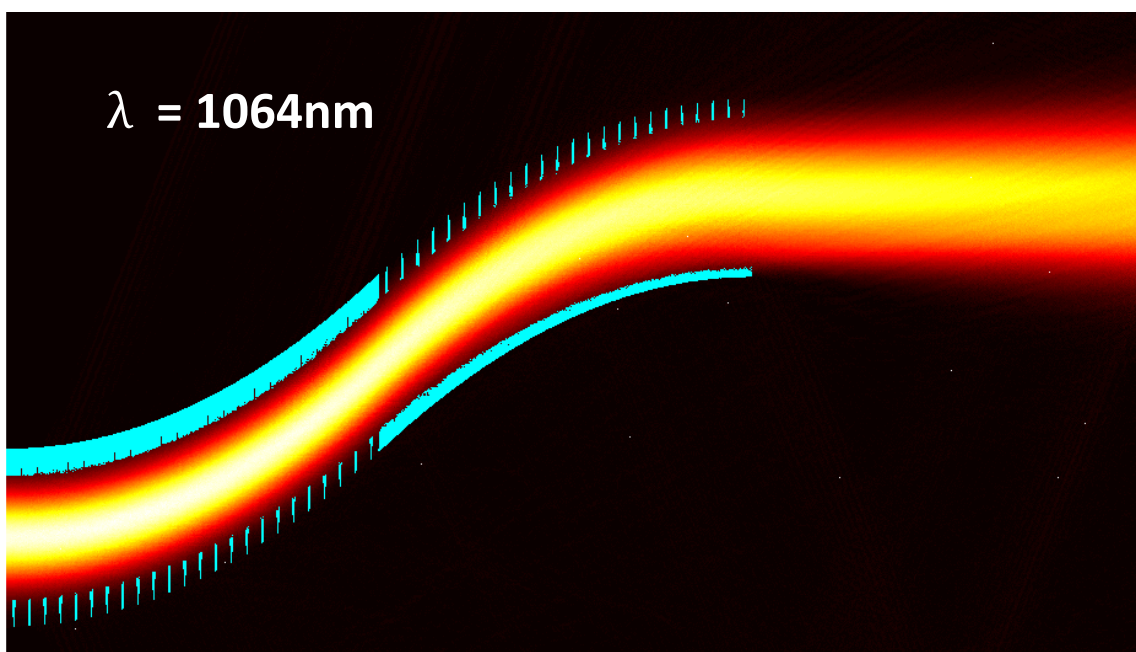


Figure A.33 – A Gaussian beam with $\lambda = 1064 \text{ nm}$ propagating through Channel 1.
[Note that this is the design point for the ON state.]

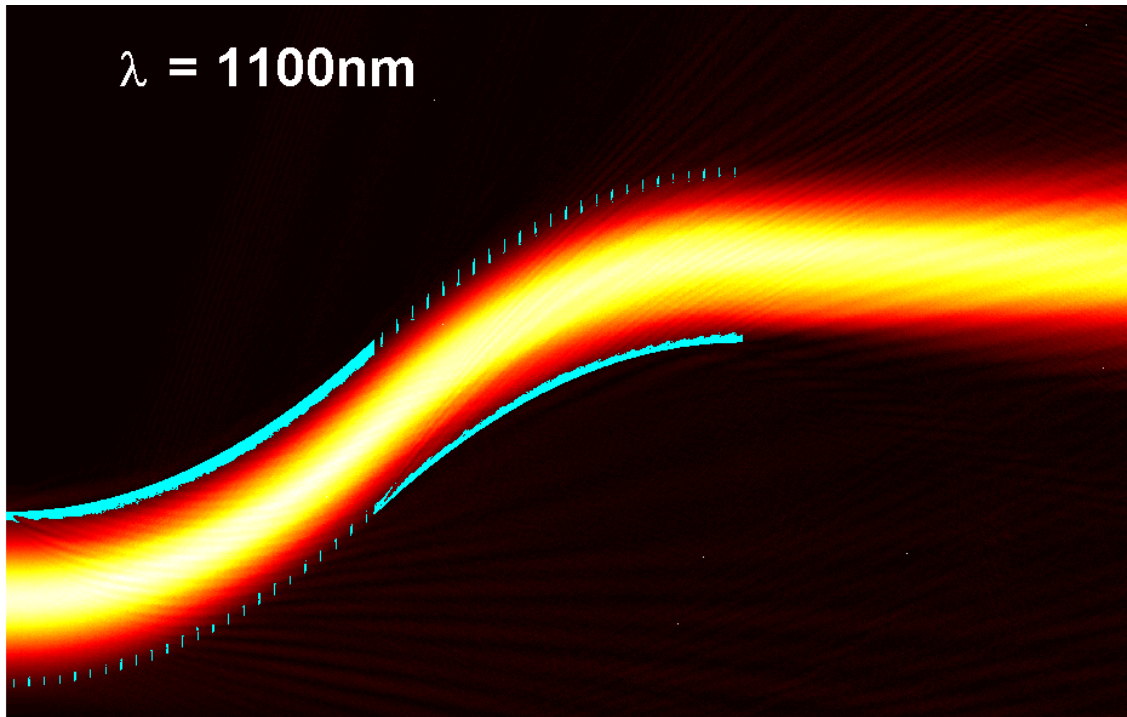


Figure A.34 – A Gaussian beam with $\lambda = 1100 \text{ nm}$ propagating through Channel 1.

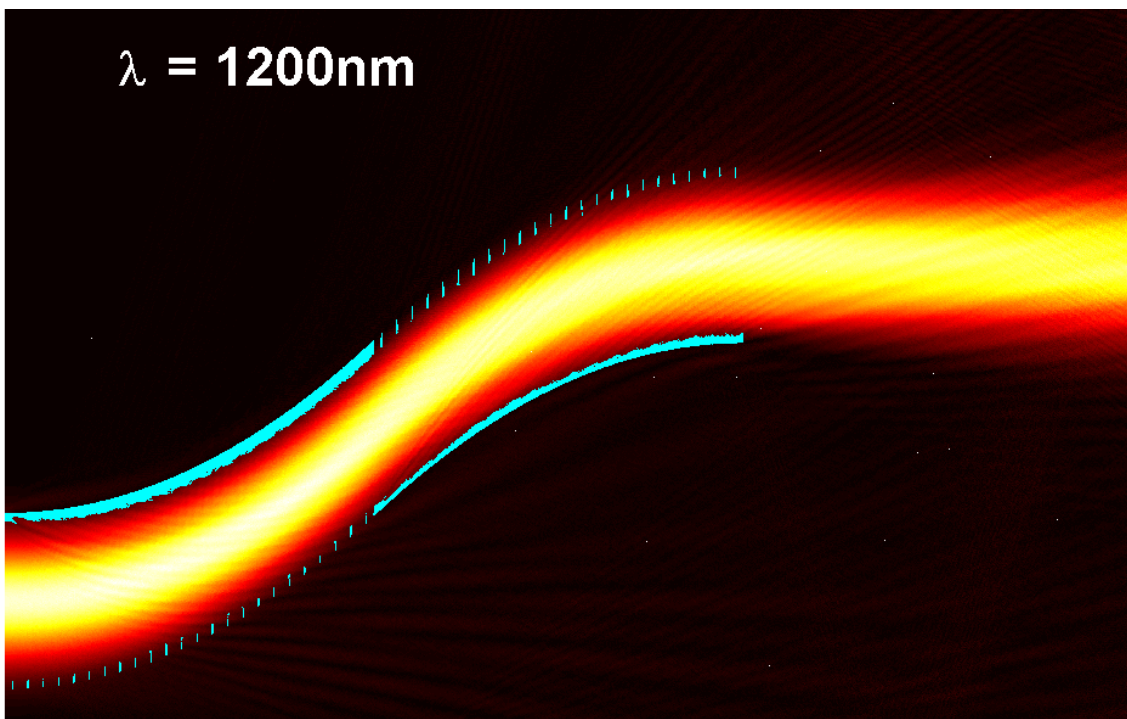


Figure A.35 – A Gaussian beam with $\lambda = 1200 \text{ nm}$ propagating through Channel 1.

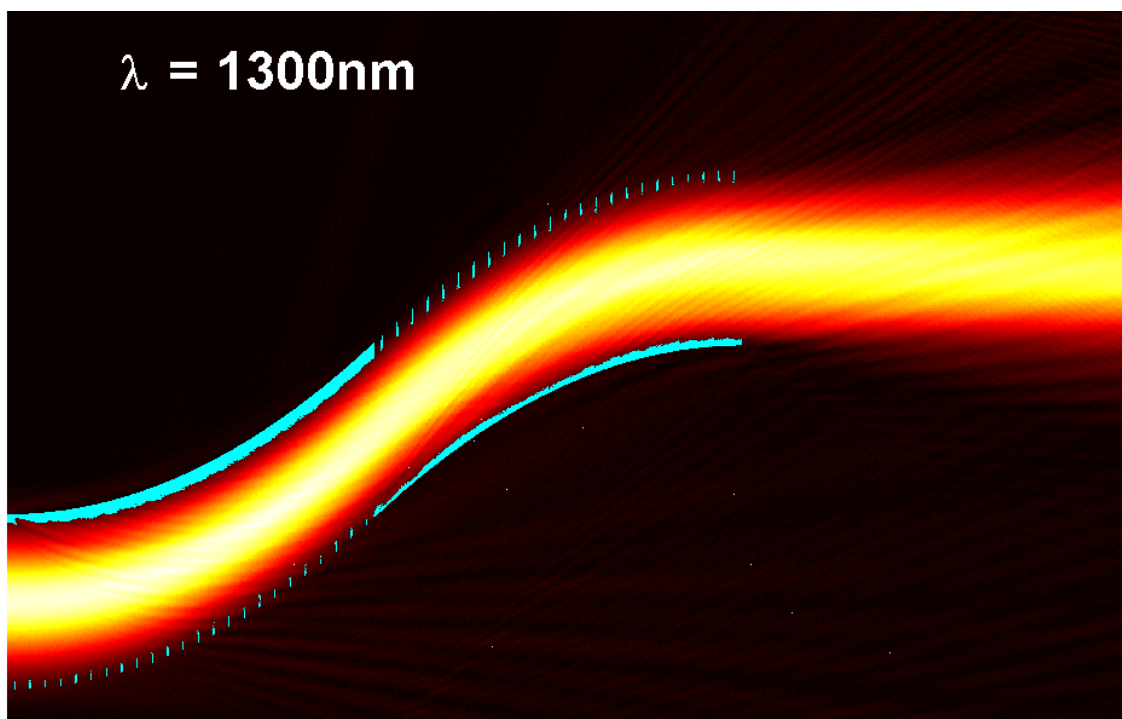


Figure A.36 – A Gaussian beam with $\lambda = 1300 \text{ nm}$ propagating through Channel 1.

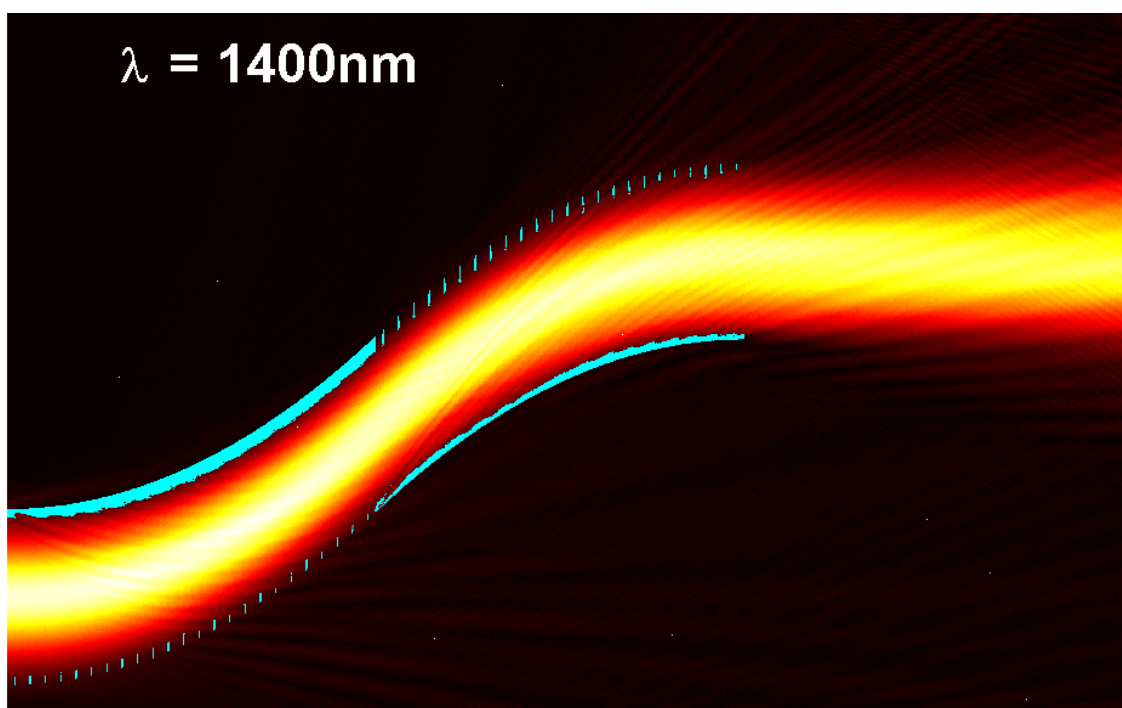


Figure A.37 – A Gaussian beam with $\lambda = 1400 \text{ nm}$ propagating through Channel 1.

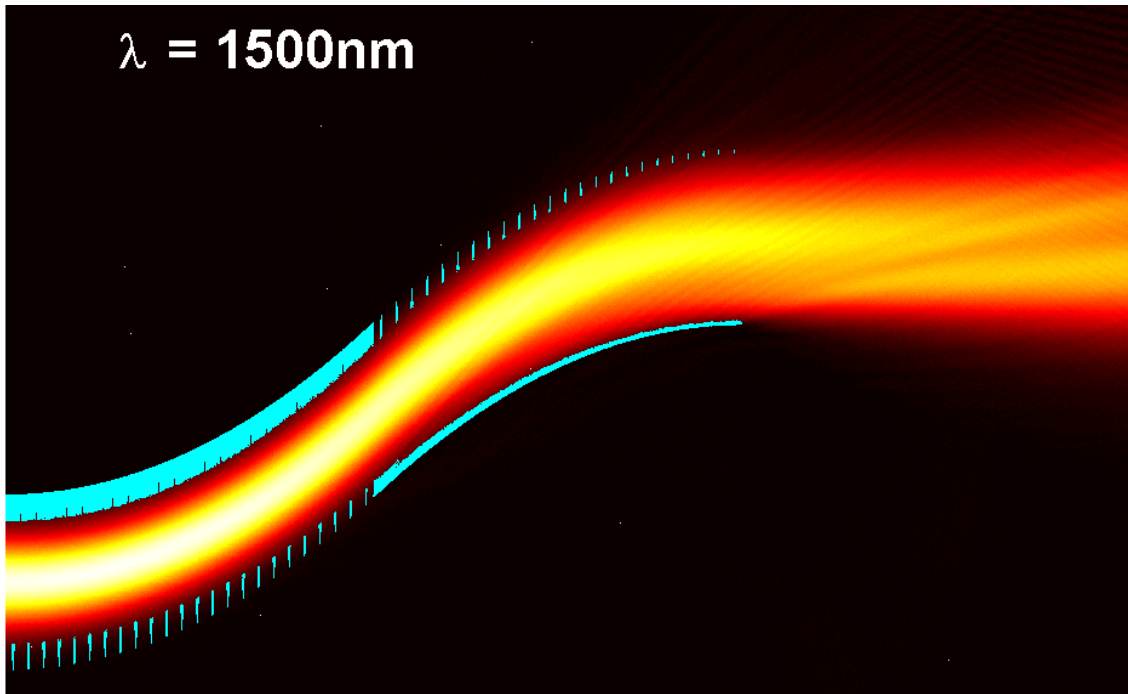


Figure A.38 – A Gaussian beam with $\lambda = 1500 \text{ nm}$ propagating through Channel 1.

A.2.4 The Response of Channel 1 to Various Applied Voltages

This section presents the beam steering response of EOBS channel 1 at voltages far from the design cases of $V_{ON} = -1000 \text{ Volts}$ and $V_{OFF} = 0 \text{ Volts}$. Here the voltage is varied across the range $-1500 \text{ Volts} \leq \lambda \leq 500 \text{ Volts}$. The optical field propagating through Channel 1 is shown in separate figures for cases separated by $\Delta V = 100 \text{ Volts}$.

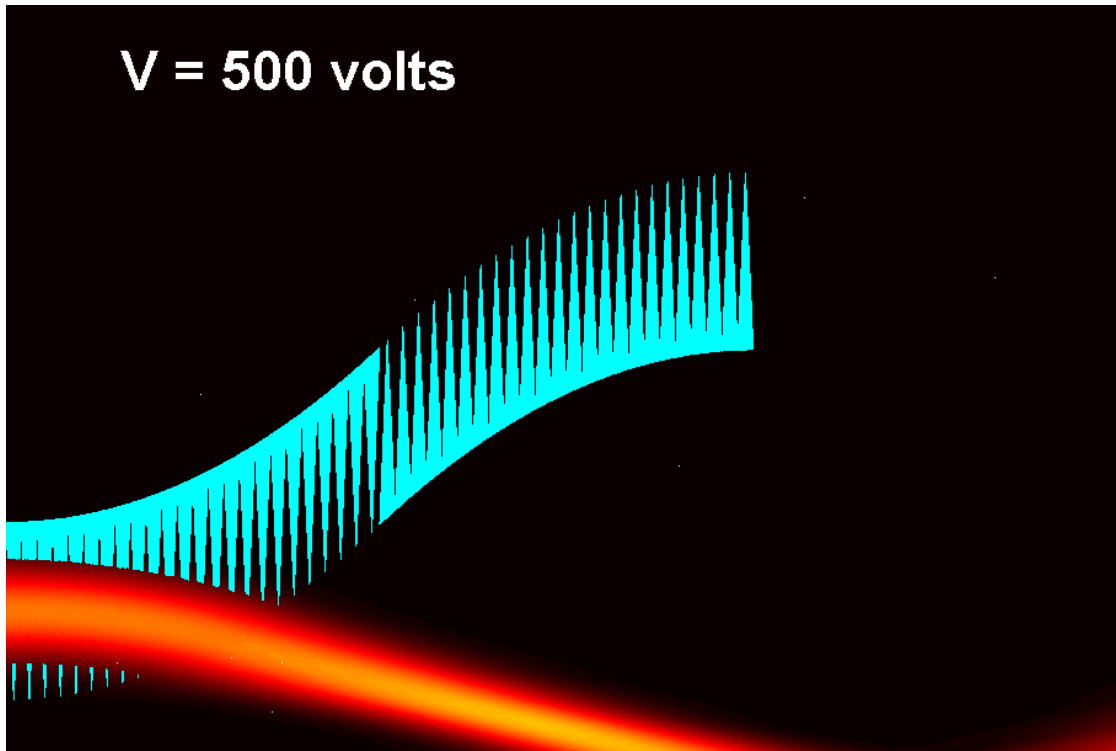


Figure A.39 – A Gaussian beam propagating through Channel 1 at $V_{\text{applied}} = 500 \text{ Volts}$.

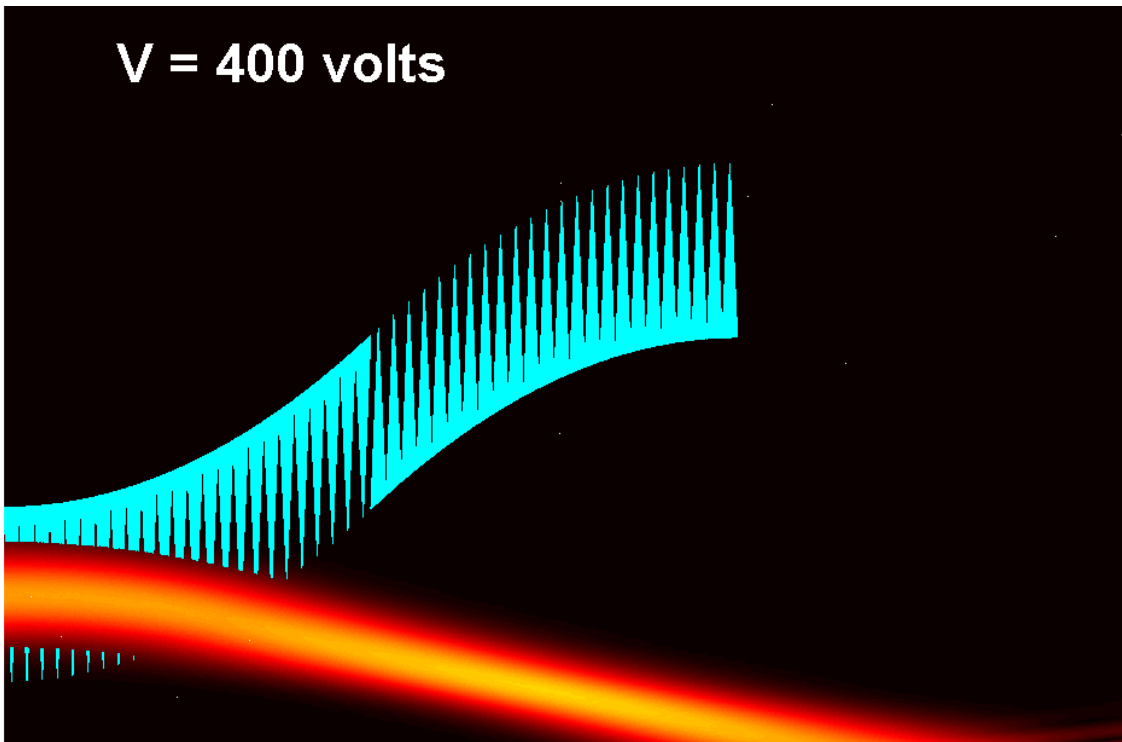


Figure A.40 – A Gaussian beam propagating through Channel 1 at $V_{\text{applied}} = 400 \text{ Volts}$.

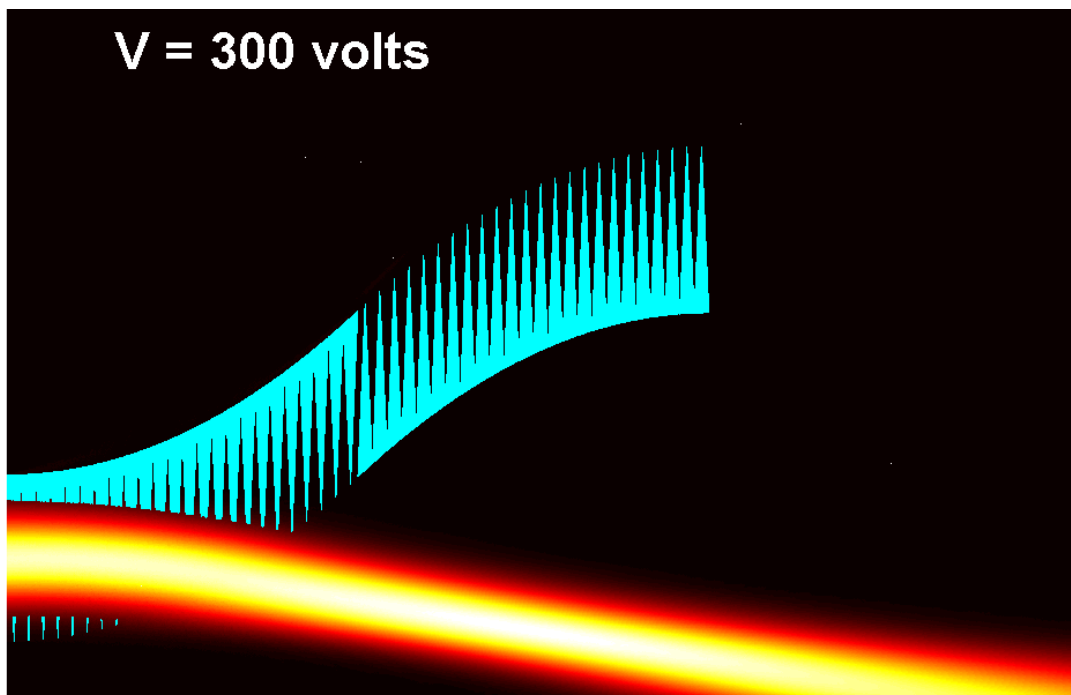


Figure A.41 – A Gaussian beam propagating through Channel 1 at $V_{\text{applied}} = 300 \text{ Volts}$.

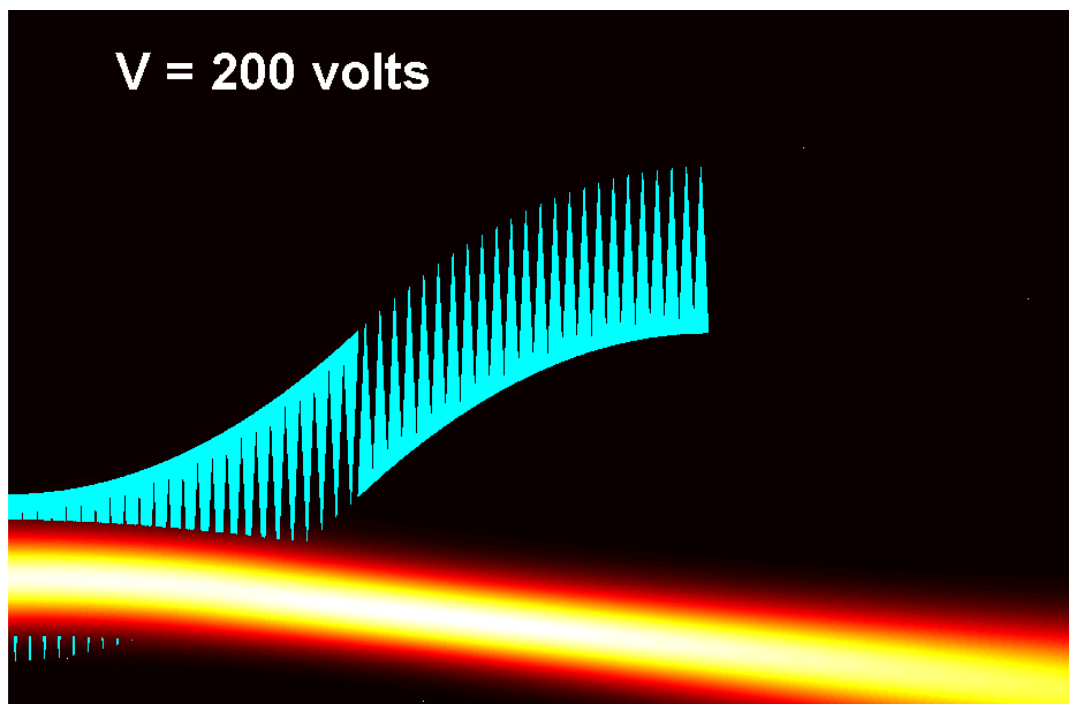


Figure A.42 – A Gaussian beam propagating through Channel 1 at $V_{\text{applied}} = 200 \text{ Volts}$.

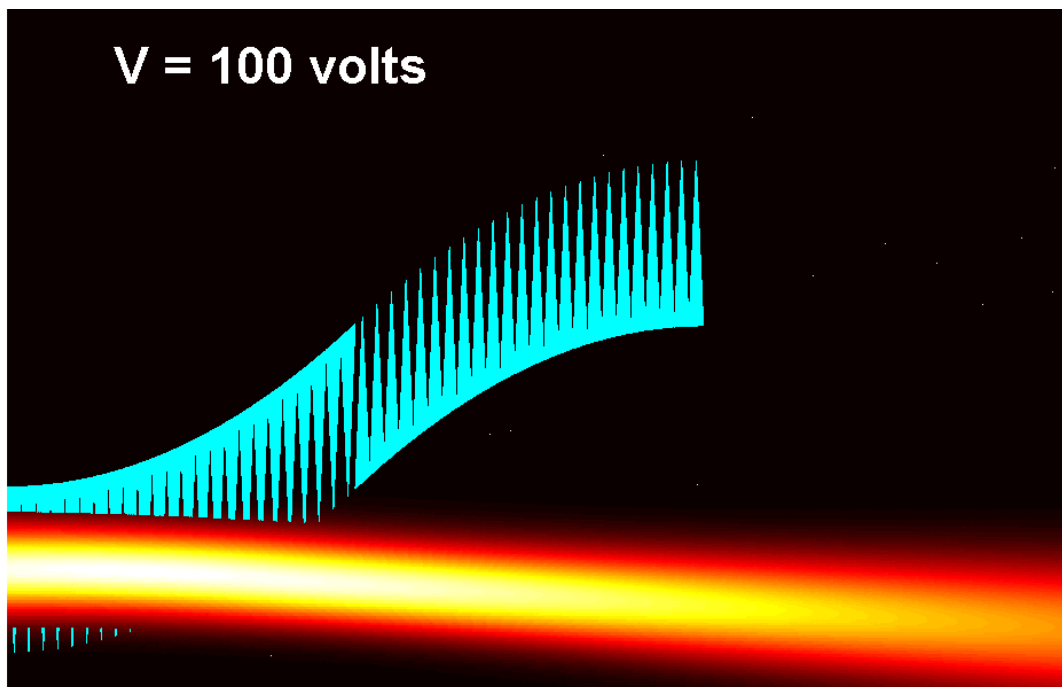


Figure A.43 – A Gaussian beam propagating through Channel 1 at $V_{applied} = 100$ Volts.

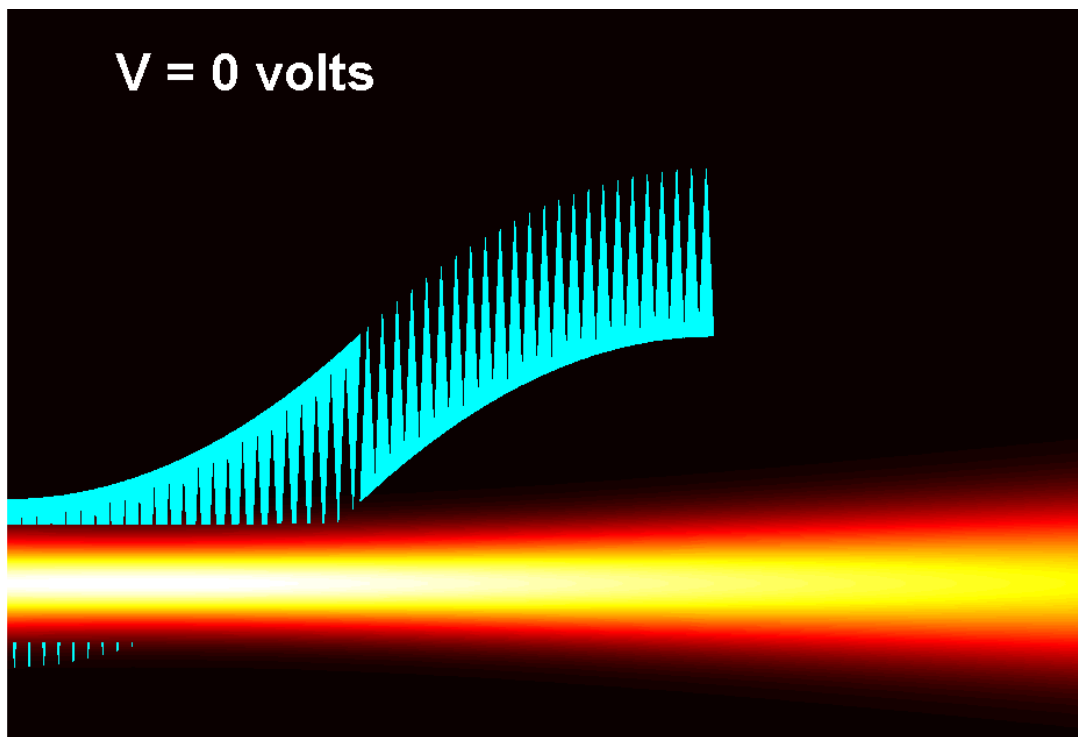


Figure A.44 – A Gaussian beam propagating through Channel 1 at $V_{applied} = 0$ Volts.
[Note that this is the design point for the OFF state.]

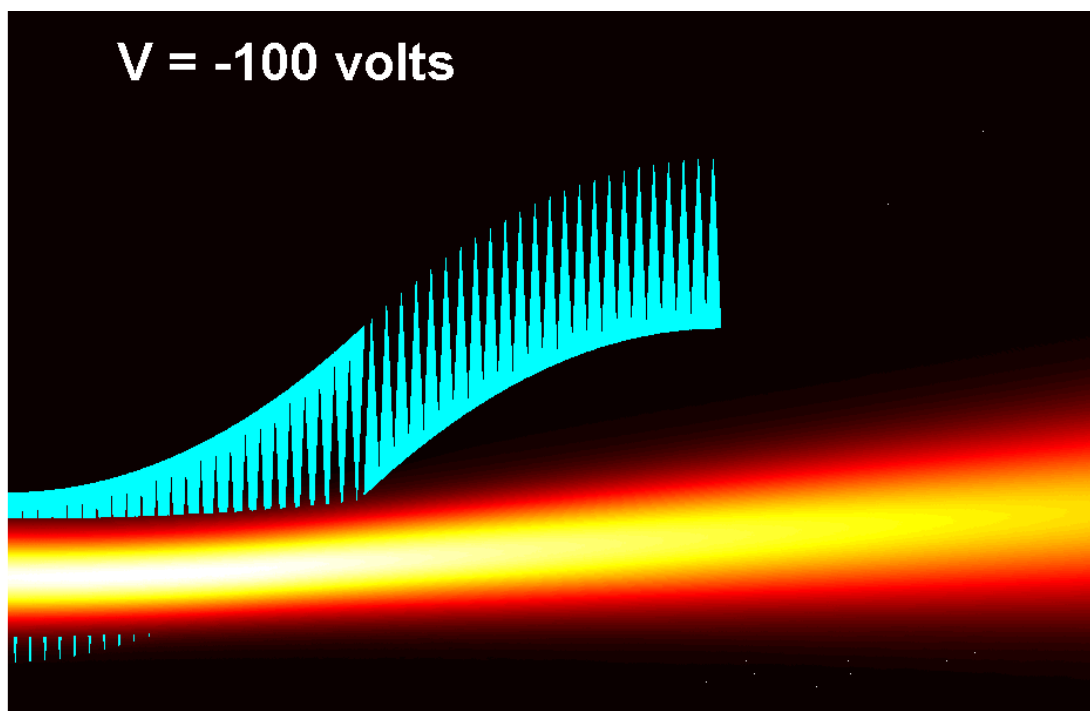


Figure A.45 – A Gaussian beam propagating through Channel 1 at $V_{\text{applied}} = -100$ Volts.

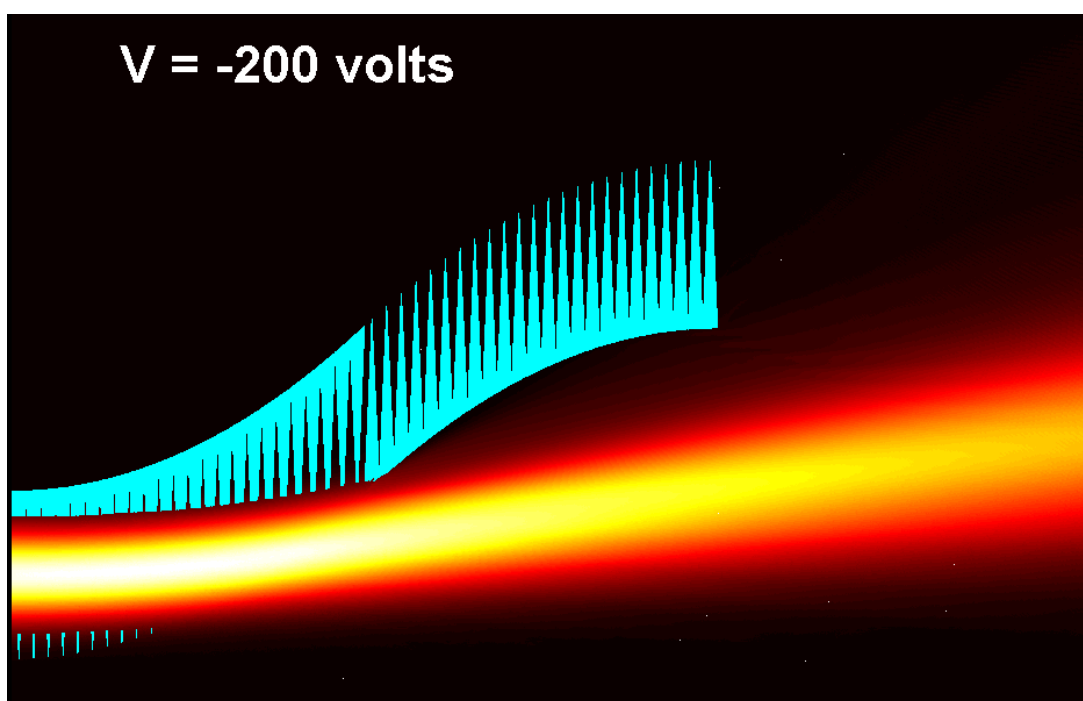


Figure A.46 – A Gaussian beam propagating through Channel 1 at $V_{\text{applied}} = -200$ Volts.

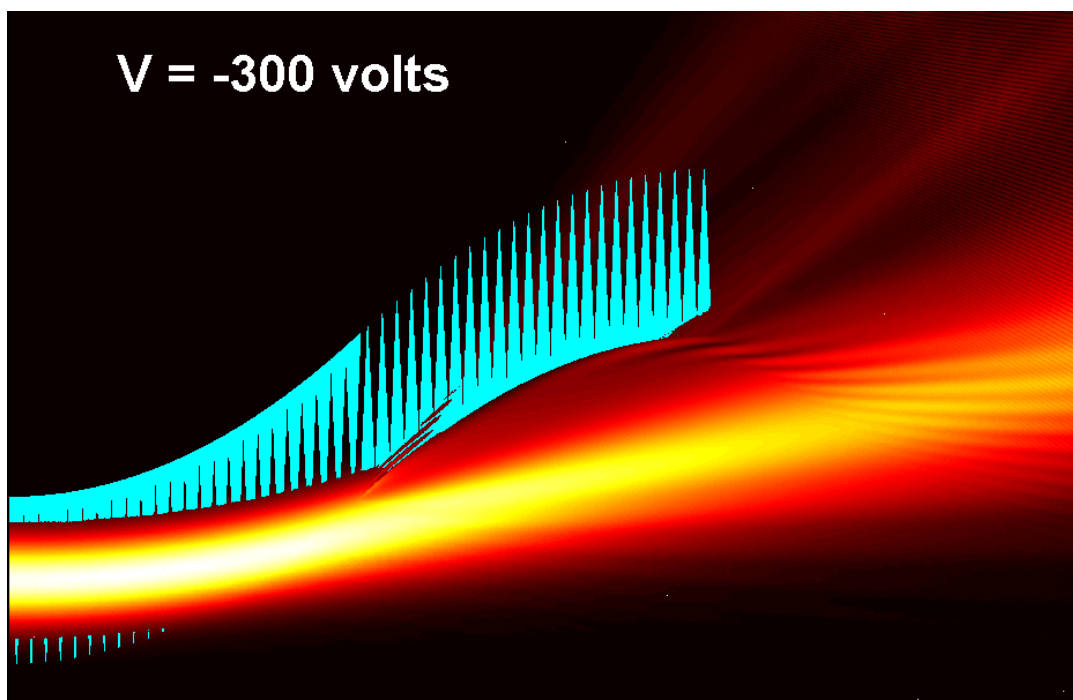


Figure A.47 – A Gaussian beam propagating through Channel 1 at $V_{\text{applied}} = -300 \text{ Volts}$.

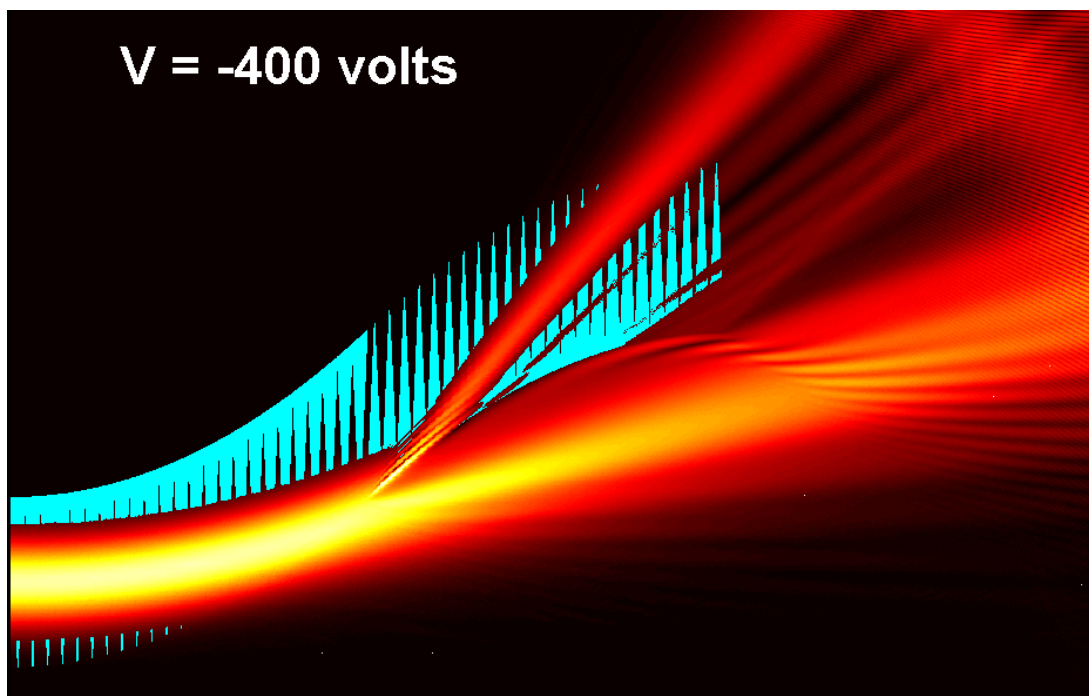


Figure A.48 – A Gaussian beam propagating through Channel 1 at $V_{\text{applied}} = -400 \text{ Volts}$.

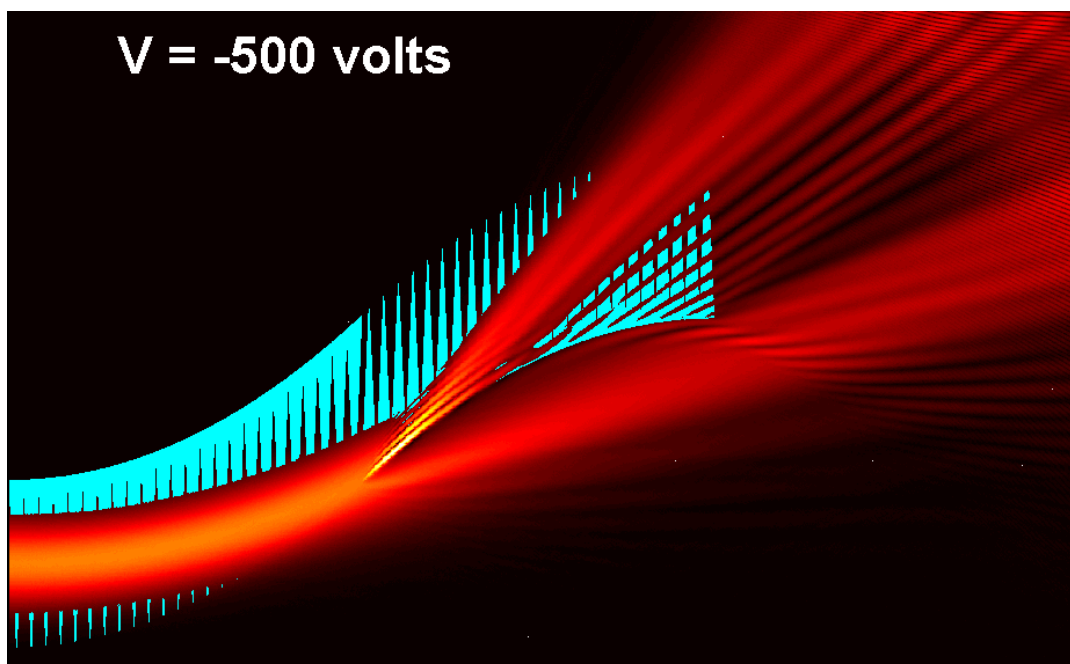


Figure A.49 – A Gaussian beam propagating through Channel 1 at $V_{\text{applied}} = -500 \text{ Volts}$.

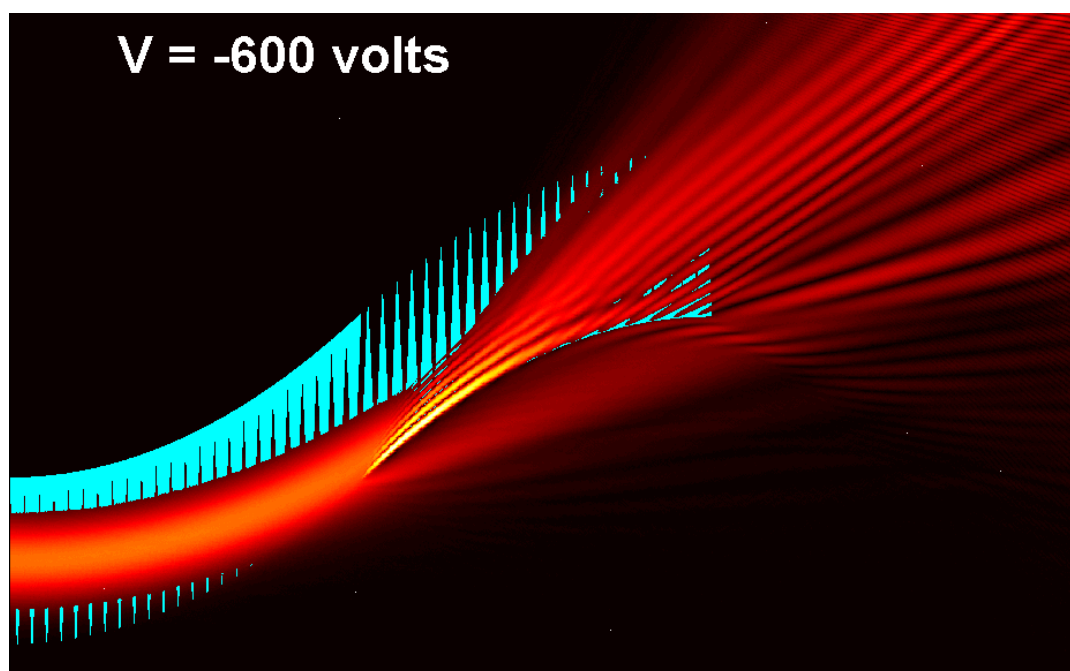


Figure A.50 – A Gaussian beam propagating through Channel 1 at $V_{\text{applied}} = -600 \text{ Volts}$.

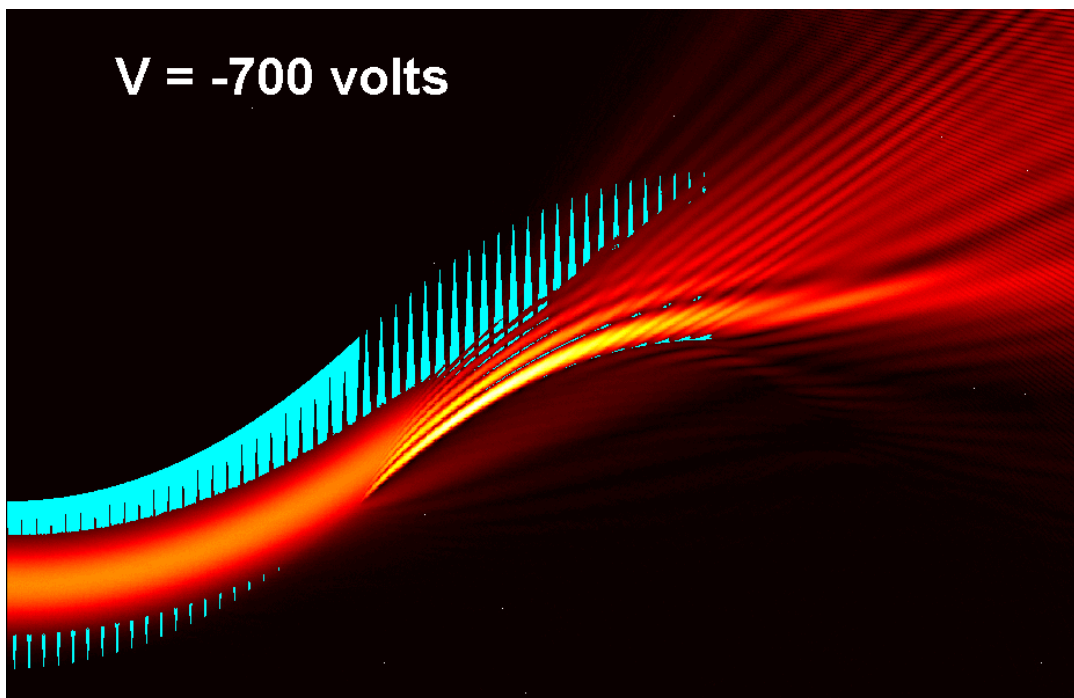


Figure A.51 – A Gaussian beam propagating through Channel 1 at $V_{\text{applied}} = -700 \text{ Volts}$.

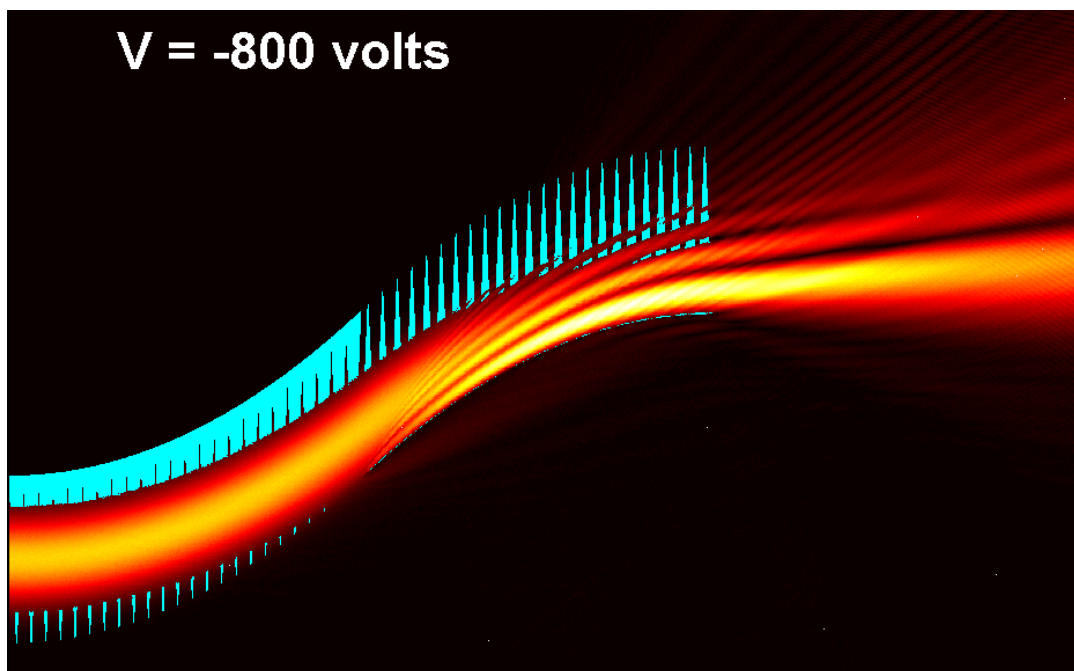


Figure A.52 – A Gaussian beam propagating through Channel 1 at $V_{\text{applied}} = -800 \text{ Volts}$.

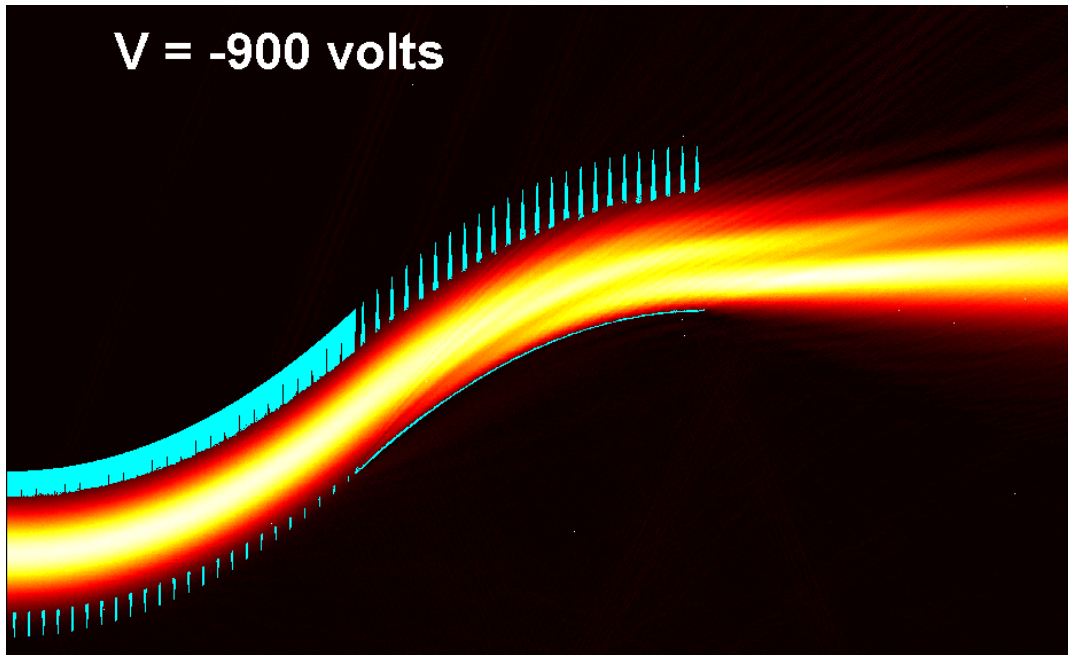


Figure A.53 – A Gaussian beam propagating through Channel 1 at $V_{\text{applied}} = -900 \text{ Volts}$.

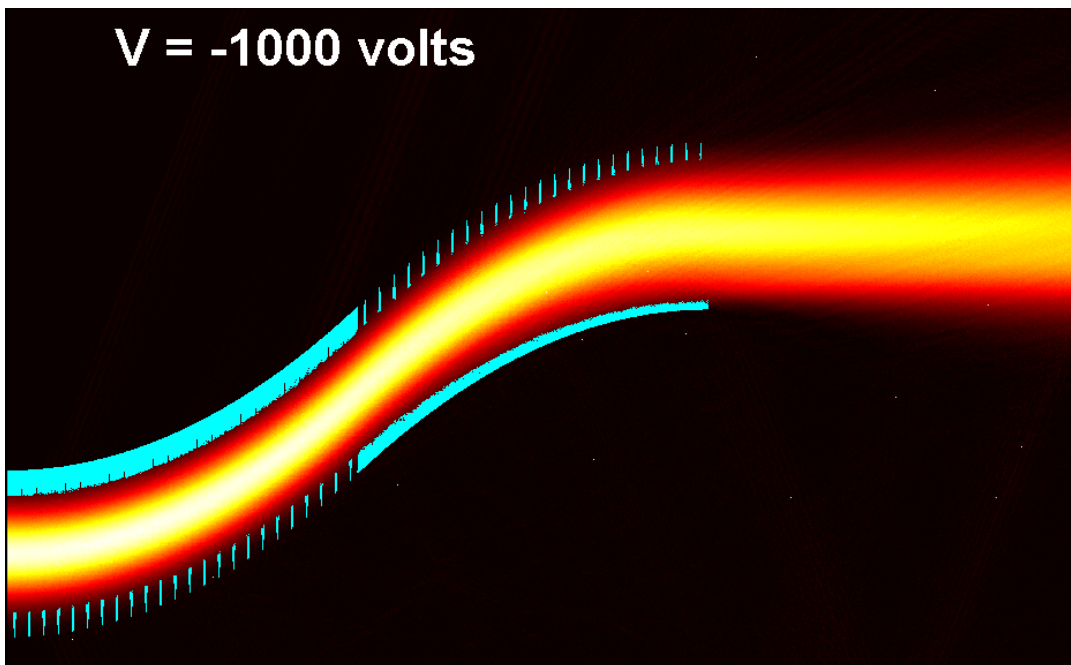


Figure A.54 – A Gaussian beam propagating through Channel 1 at $V_{\text{applied}} = -1000 \text{ Volts}$.
[Note that this is the design point for the ON state.]

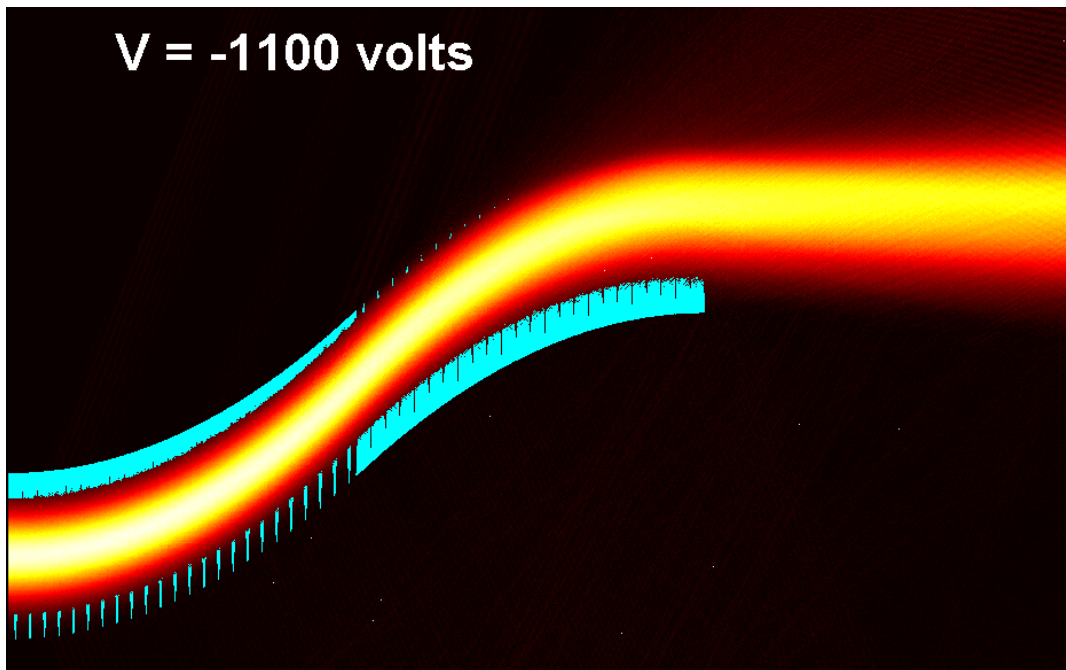


Figure A.55 – A Gaussian beam propagating through Channel 1 at $V_{\text{applied}} = -1100$ Volts.

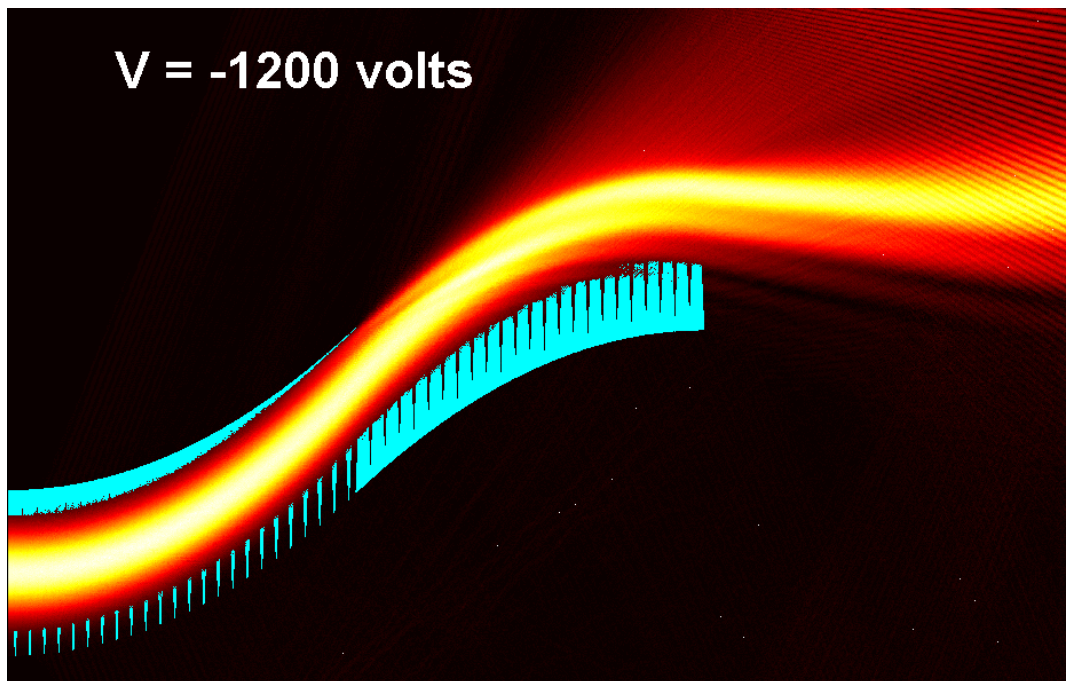


Figure A.56 – A Gaussian beam propagating through Channel 1 at $V_{\text{applied}} = -1200$ Volts.

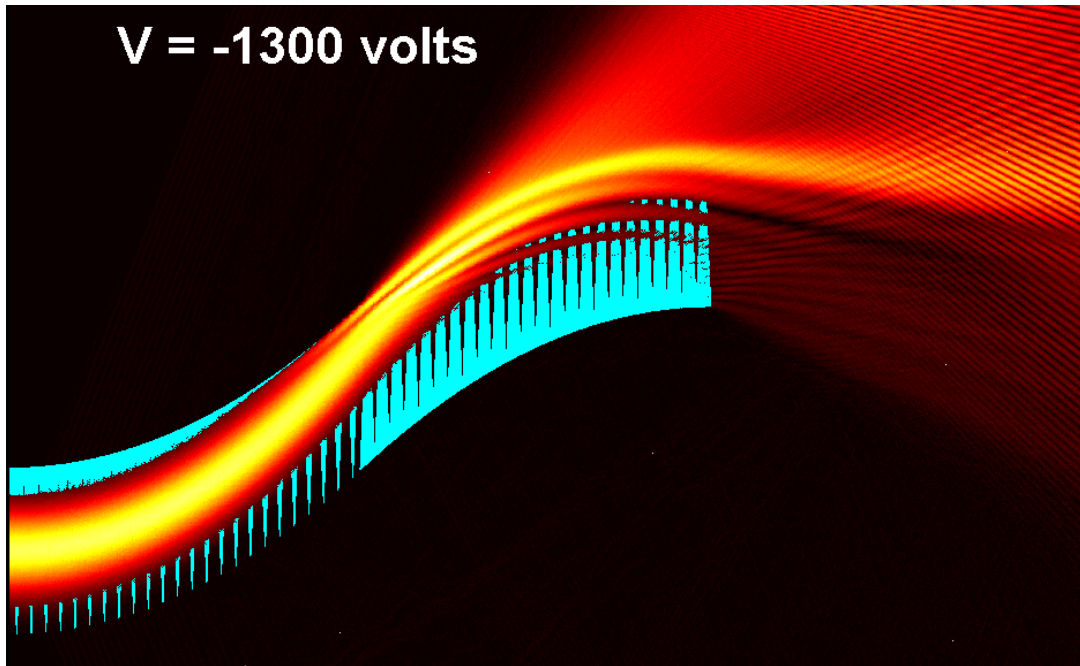


Figure A.57 – A Gaussian beam propagating through Channel 1 at $V_{\text{applied}} = -1300$ Volts.

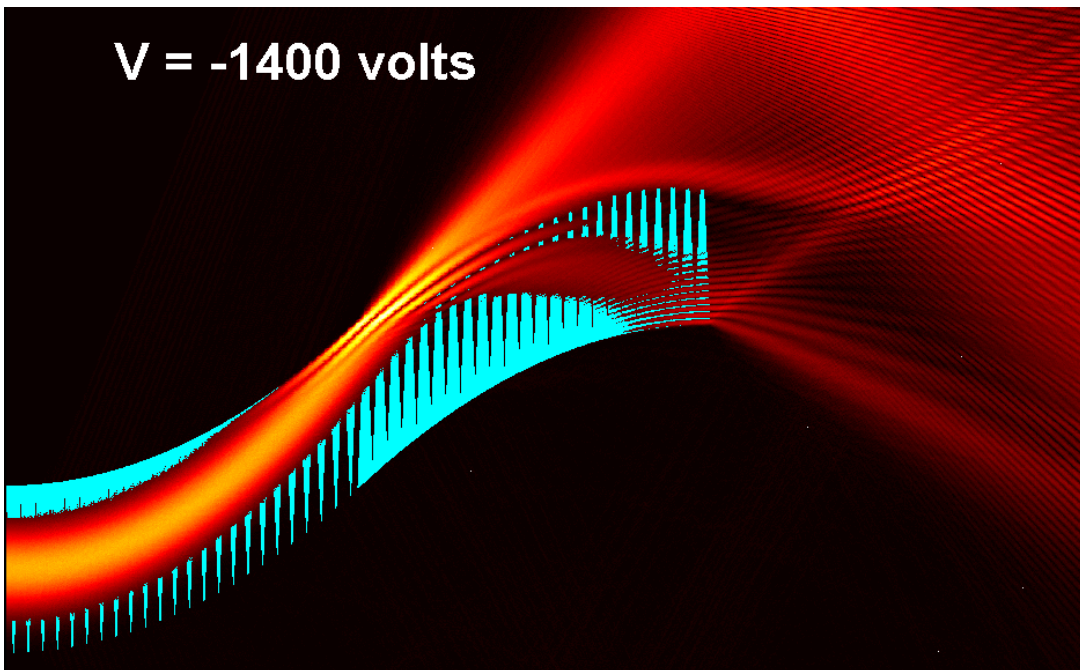


Figure A.58 – A Gaussian beam propagating through Channel 1 at $V_{\text{applied}} = -1400$ Volts.

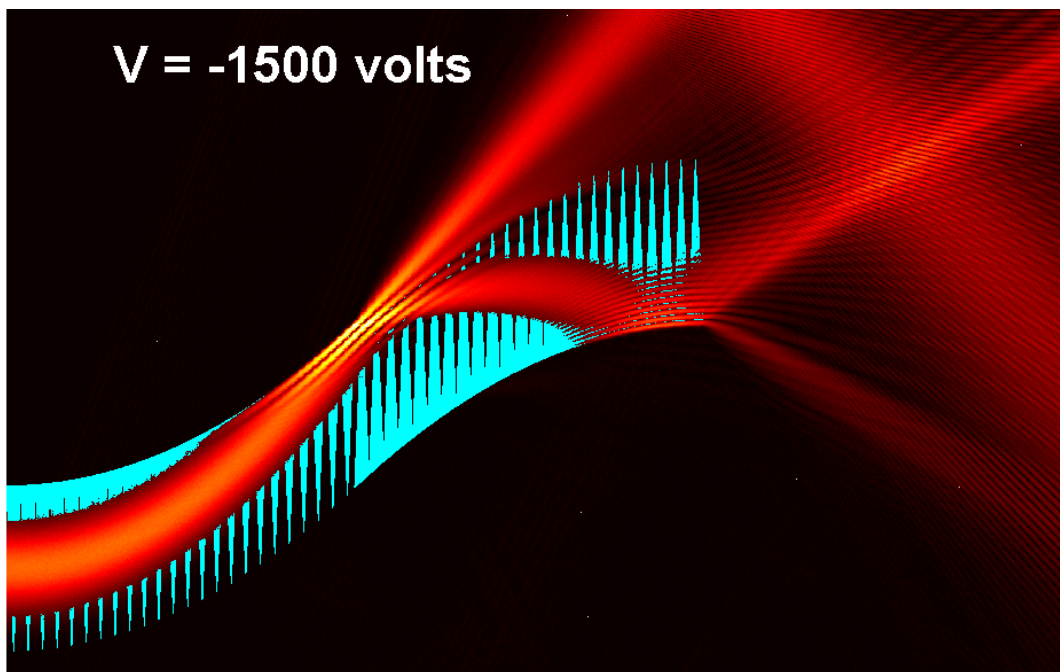


Figure A.59 – A Gaussian beam propagating through Channel 1 at $V_{\text{applied}} = -1500$ Volts.

APPENDIX B – VOLTAGE COMPENSATION FOR CHANGES IN ENVIRONMENTAL VARIABLES

Recall Snell's Law:

$$n_1 \sin(\theta_1) = n_2 \sin(\theta_2)$$

So for the first interface of the steering prism unit cell (see Figure 3.4):

$$n_{background} \sin(\theta_1) = n_{prism} \sin(\theta_2)$$

Which can be written more explicitly as:

$$(n_e - \Delta n_e) \sin(\theta_1) = (n_e + \Delta n_e) \sin(\theta_2)$$

Rearranging yields:

$$\theta_2 = \arcsin\left(\frac{n_e - \Delta n_e}{n_e + \Delta n_e} \sin(\theta_1)\right) = \arcsin\left(\frac{1 - \Delta n_e/n_e}{1 + \Delta n_e/n_e} \sin(\theta_1)\right)$$

Recall that $\Delta n_e \ll n_e$, so by the binomial approximation:

$$1 - \frac{\Delta n_e}{n_e} \approx \left(1 + \frac{\Delta n_e}{n_e}\right)^{-1}$$

Thus:

$$\frac{1 - \Delta n_e/n_e}{1 + \Delta n_e/n_e} = \frac{1}{\left(1 + \frac{\Delta n_e}{n_e}\right)^2} \approx \frac{1}{1 + \frac{2\Delta n_e}{n_e}}$$

Thus:

$$\theta_2 = \arcsin\left(\frac{\sin(\theta_1)}{1 + \frac{2\Delta n_e}{n_e}}\right)$$

Recall from Equation (3.8) that $|\Delta n_e| = \frac{1}{2} r_{33} n_e^3 \frac{V}{Z}$, thus:

$$\theta_2 = \arcsin\left(\frac{\sin(\theta_1)}{1 + n_e^3 r_{33} V / (n_e Z)}\right)$$

So:

$$\theta_2 = \arcsin\left(\frac{\sin(\theta_1)}{1 + \frac{r_{33}}{Z} V n_e^2}\right)$$

Recall that the deflection β (see Figure 3.5) imparted to a ray propagating through the prism is given by Equation (3.18):

$$\beta = \theta_3 + \alpha - 90^\circ = \sin^{-1} \left(\frac{n_e + \Delta n_e}{n_e - \Delta n_e} \sin(\theta_2) \right) + \alpha - 90^\circ$$

Thus, β can be expressed:

$$\beta = \sin^{-1} \left(1 + \frac{r_{33}}{Z} V n_e^2 \sin \left(\frac{\sin(\theta_1)}{1 + \frac{r_{33}}{Z} V n_e^2} \right) \right) + \alpha - 90^\circ$$

So, if the ray input angle θ_1 and prism base angle α remain constant, β is a function of r_{33} , Z , V , and $n(\lambda, T)$ only. By inspection, V is positioned in the expression for β such that any change in $n(\lambda, T)$, Z , or r_{33} can be compensated for by a reciprocal change in V . So it is possible to adjust the value of β to be exactly the value assumed when designing the EOBS channel. Thus, the EOBS can be made to function as designed by adjusting the control voltage, even if the environmental conditions vary from the design assumptions.

APPENDIX C – ERROR ANALYSIS FOR TRANSLATION MEASUREMENTS

Figure C.1 shows the geometry of the four point deflection angle measurement method. The optic axis lies in the z-direction, the x,y plane is the plane of the beam profiling camera. The math developed in this appendix was implemented in MATLAB routine M8.

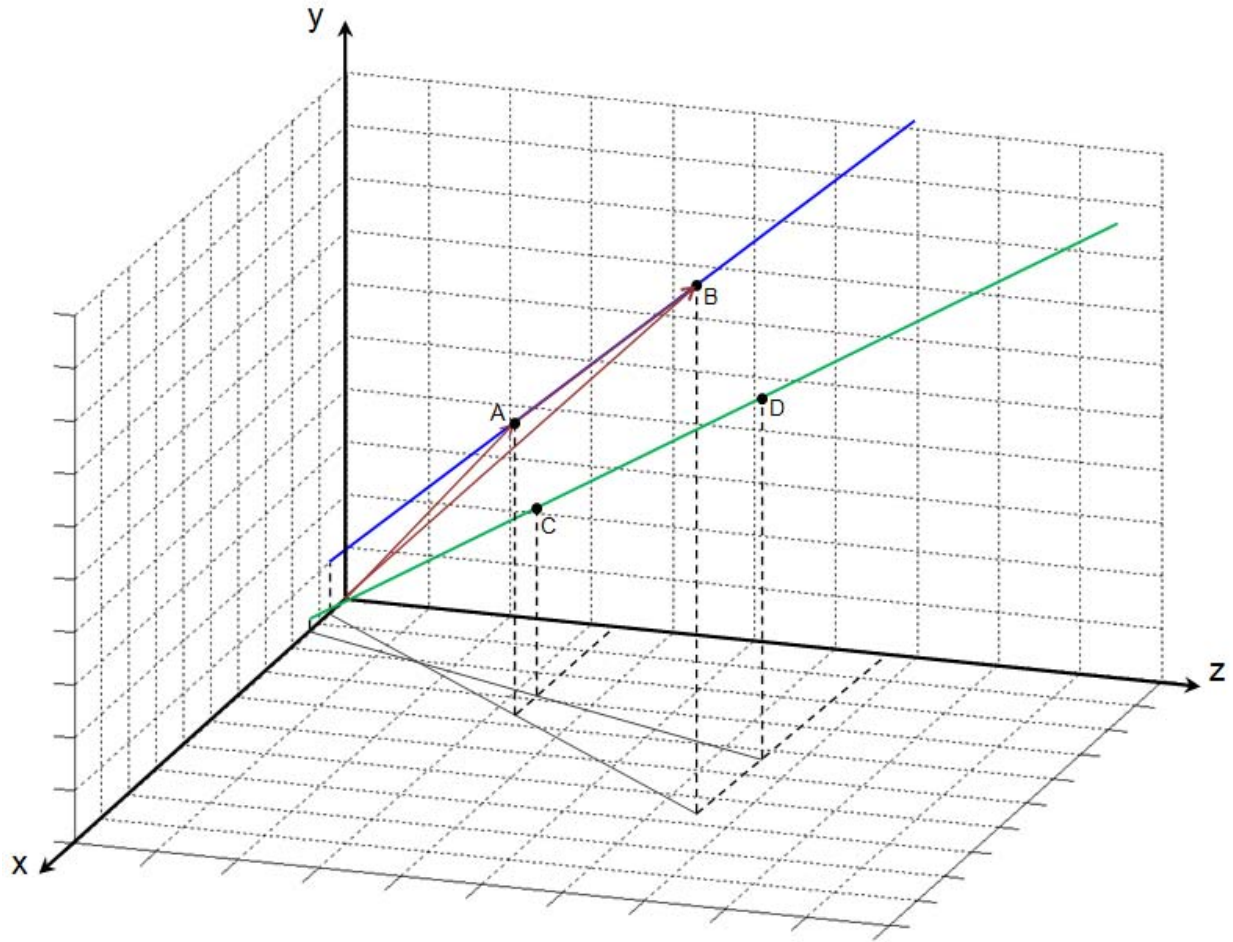


Figure C.1 – The geometry of the four-point determination of angular deflection.

Recall that the points under consideration take the form:

$$A: [x_A, y_A, z_A]$$

$$B: [x_B, y_B, z_B]$$

$$C_1: [x_C, y_C, z_C]$$

$$D_1: [x_D, y_D, z_D]$$

$$C_2: [x_C, y_C, z_C]$$

$$D_2: [x_D, y_D, z_D]$$

$$V_0 = 0 \pm 1 \text{ Volts}$$

$$V_1 = -900 \pm 1 \text{ Volts}$$

$$V_2 = -1000 \pm 1 \text{ Volts}$$

Table C.1 – The experimental data and uncertainty values (Center of Amplitude).

POINT	$V_{\text{applied}} [V]$	$\sigma_{V_{\text{applied}}} [V]$	$z (\mu m)$	$\sigma_z (\mu m)$	$x (\mu m)$	$\sigma_x (\mu m)$	$y (\mu m)$	$\sigma_y (\mu m)$
A	0	1	150000	333	2575.6	1.1998	1360.8	2.4315
B	0	1	165000	500	2584.3	3.097	1295.8	0.94994
C1	-900	1	150000	500	1590.7	1.2	1440	0.38376
D1	-900	1	165000	500	1449	1.797	1417.7	0.84538
C1	-1000	1	150000	500	1919.3	0.52302	1449.6	0.29989
D2	-1000	1	165000	500	1986.2	1.6861	1416.9	1.5162

Table C.2 – The experimental data and uncertainty values (Gaussian Filter).

POINT	$V_{\text{applied}} [V]$	$\sigma_{V_{\text{applied}}} [V]$	$z (\mu m)$	$\sigma_z (\mu m)$	$x (\mu m)$	$\sigma_x (\mu m)$	$y (\mu m)$	$\sigma_y (\mu m)$
A	0	1	150000	333	2575.6	1.1998	1360.8	2.4315
B	0	1	165000	500	2584.3	3.097	1295.8	0.94994
C1	-900	1	150000	500	1590.7	1.2	1440	0.38376
D1	-900	1	165000	500	1449	1.797	1417.7	0.84538
C1	-1000	1	150000	500	1919.3	0.52302	1449.6	0.29989
D2	-1000	1	165000	500	1986.2	1.6861	1416.9	1.5162

Recall:

$$\vec{B} = \vec{A} + \vec{AB}$$

Therefore:

$$\vec{AB} = \vec{B} - \vec{A}$$

which is of the form:

$$f(\Psi, \Gamma) = a\Psi \pm b\Gamma$$

which has a variance:

$$\sigma_f^2 = a^2\sigma_\Psi^2 + b^2\sigma_\Gamma^2$$

Thus:

$$\sigma_{\vec{AB}}^2 = \sigma_A^2 + \sigma_B^2 = \{\sigma_{x_A}^2 + \sigma_{x_B}^2, \sigma_{y_A}^2 + \sigma_{y_B}^2, \sigma_{z_A}^2 + \sigma_{z_B}^2\}$$

Similarly:

$$\vec{D} = \vec{C} + \vec{CD}$$

Therefore:

$$\vec{CD} = \vec{D} - \vec{C}$$

which is also of the form:

$$f(\Psi, \Gamma) = a\Psi \pm b\Gamma$$

which has a variance:

$$\sigma_f^2 = a^2 \sigma_\Psi^2 + b^2 \sigma_\Gamma^2$$

Thus:

$$\sigma_{\vec{CD}}^2 = \sigma_C^2 + \sigma_D^2 = \{\sigma_{x_C}^2 + \sigma_{x_D}^2, \sigma_{y_C}^2 + \sigma_{y_D}^2, \sigma_{z_C}^2 + \sigma_{z_D}^2\}$$

Recall:

$$\cos \theta = \frac{\vec{AB} \cdot \vec{CD}}{|\vec{AB}| |\vec{CD}|}$$

Note:

$$\vec{AB} \cdot \vec{CD} = x_{AB}x_{CD} + y_{AB}y_{CD} + z_{AB}z_{CD}$$

Terms $\xi_{AB}\xi_{CD}$ are of the form:

$$f = \Psi\Gamma$$

Which has a variance:

$$\sigma_f^2 = f^2 \left[\left(\frac{\sigma_\Psi}{\Psi} \right)^2 + \left(\frac{\sigma_\Gamma}{\Gamma} \right)^2 \right]$$

Thus:

$$\sigma_{\xi_{AB}\xi_{CD}}^2 = (\xi_{AB}\xi_{CD})^2 \left[\left(\frac{\sigma_{\xi_{AB}}}{\xi_{AB}} \right)^2 + \left(\frac{\sigma_{\xi_{CD}}}{\xi_{CD}} \right)^2 \right] = (\xi_{AB}\xi_{CD})^2 \left[\frac{\sigma_{\xi_{AB}}^2}{\xi_{AB}^2} + \frac{\sigma_{\xi_{CD}}^2}{\xi_{CD}^2} \right]$$

where $\xi = x, y, \text{ or } z$

$x_{AB}x_{CD} + y_{AB}y_{CD} + z_{AB}z_{CD}$ is of the form:

$$f(\Psi, \Gamma) = a\Psi \pm b\Gamma \pm c\Phi$$

which has a variance:

$$\sigma_f^2 = a^2 \sigma_\Psi^2 + b^2 \sigma_\Gamma^2 + c^2 \sigma_\Phi^2$$

Therefore:

$$\sigma_{\overrightarrow{AB} \cdot \overrightarrow{CD}}^2 = \sigma_{x_{AB}x_{CD}}^2 + \sigma_{y_{AB}y_{CD}}^2 + \sigma_{z_{AB}z_{CD}}^2$$

Also note:

$$|\overrightarrow{AB}| |\overrightarrow{CD}| = \sqrt{x_{AB}^2 + y_{AB}^2 + z_{AB}^2} \times \sqrt{x_{CD}^2 + y_{CD}^2 + z_{CD}^2}$$

Terms ξ_{AB}^2 and ξ_{CD}^2 are of the form:

$$f = a\Psi^{\pm b}$$

which has a variance:

$$\sigma_f^2 = f^2 b^2 \frac{\sigma_\Psi^2}{\Psi^2}$$

Thus:

$$\sigma_{\xi_{AB}^2}^2 = 4\xi_{AB}^2 \sigma_{\xi_{AB}}^2 \quad \& \quad \sigma_{\xi_{CD}^2}^2 = 4\xi_{CD}^2 \sigma_{\xi_{CD}}^2$$

where $\xi = x, y, \text{ or } z$

Also:

$$\text{Let } \Delta_{\overrightarrow{AB}} = x_{AB}^2 + y_{AB}^2 + z_{AB}^2 \quad \& \quad \text{Let } \Delta_{\overrightarrow{CD}} = x_{CD}^2 + y_{CD}^2 + z_{CD}^2$$

which are of the form:

$$f(\Psi, \Gamma) = a\Psi \pm b\Gamma \pm c\Phi$$

which has a variance:

$$\sigma_f^2 = a^2 \sigma_\Psi^2 + b^2 \sigma_\Gamma^2 + c^2 \sigma_\Phi^2$$

So:

$$\sigma_{\Delta_{\overrightarrow{AB}}}^2 = \sigma_{x_{AB}^2}^2 + \sigma_{y_{AB}^2}^2 + \sigma_{z_{AB}^2}^2 \quad \& \quad \sigma_{\Delta_{\overrightarrow{CD}}}^2 = \sigma_{x_{CD}^2}^2 + \sigma_{y_{CD}^2}^2 + \sigma_{z_{CD}^2}^2$$

Note that $|\overrightarrow{AB}| = \sqrt{x_{AB}^2 + y_{AB}^2 + z_{AB}^2}$ and $|\overrightarrow{CD}| = \sqrt{x_{CD}^2 + y_{CD}^2 + z_{CD}^2}$

which are of the form:

$$f = a\Psi^{\pm b}$$

which has a variance:

$$\sigma_f^2 = f^2 b^2 \frac{\sigma_\Psi^2}{\Psi^2}$$

Thus:

$$\sigma_{|\overrightarrow{AB}|}^2 = \frac{1}{4\Delta_{\overrightarrow{AB}}} \sigma_{\Delta_{\overrightarrow{AB}}}^2 \quad \& \quad \sigma_{|\overrightarrow{CD}|}^2 = \frac{1}{4\Delta_{\overrightarrow{CD}}} \sigma_{\Delta_{\overrightarrow{CD}}}^2$$

$|\overrightarrow{AB}| |\overrightarrow{CD}|$ is of the form:

$$f = \Psi \Gamma$$

which has a variance:

$$\sigma_f^2 = f^2 \left[\left(\frac{\sigma_\Psi}{\Psi} \right)^2 + \left(\frac{\sigma_\Gamma}{\Gamma} \right)^2 \right]$$

Thus:

$$\sigma_{|\overrightarrow{AB}| |\overrightarrow{CD}|}^2 = (|\overrightarrow{AB}| |\overrightarrow{CD}|)^2 \left[\frac{\sigma_{|\overrightarrow{AB}|}^2}{|\overrightarrow{AB}|^2} + \frac{\sigma_{|\overrightarrow{CD}|}^2}{|\overrightarrow{CD}|^2} \right]$$

Also:

$$\text{Let } \mathcal{R} = \frac{\overrightarrow{AB} \cdot \overrightarrow{CD}}{|\overrightarrow{AB}| |\overrightarrow{CD}|}$$

which is of the form:

$$f = \frac{\Psi}{\Lambda}$$

which has a variance:

$$\sigma_f^2 = f^2 \left[\left(\frac{\sigma_\Psi}{\Psi} \right)^2 + \left(\frac{\sigma_\Gamma}{\Gamma} \right)^2 \right]$$

Thus:

$$\sigma_{\mathcal{R}}^2 = \mathcal{R}^2 \left[\frac{\sigma_{\overrightarrow{AB} \cdot \overrightarrow{CD}}^2}{(\overrightarrow{AB} \cdot \overrightarrow{CD})^2} + \frac{\sigma_{|\overrightarrow{AB}| |\overrightarrow{CD}|}^2}{(|\overrightarrow{AB}| |\overrightarrow{CD}|)^2} \right]$$

Also, recall that in general:

$$\sigma_f^2 = \left(\frac{\partial f}{\partial A} \sigma_A \right)^2 + \left(\frac{\partial f}{\partial B} \sigma_B \right)^2 + \dots = \left(\frac{\partial f}{\partial A} \right)^2 \sigma_A^2 + \left(\frac{\partial f}{\partial B} \right)^2 \sigma_B^2 + \dots$$

Further recall:

$$\frac{d}{dr} \arccos(r) = -\frac{1}{\sqrt{1-r^2}}$$

Therefore:

$$\sigma_\theta^2 = \sigma_{\arccos(\mathcal{R})}^2 = \frac{\sigma_{\mathcal{R}}^2}{1 - \mathcal{R}^2}$$

Equivalently:

$$\sigma_\theta^2 = \frac{\mathcal{R}^2}{1 - \mathcal{R}^2} \left[\frac{\sigma_{\overrightarrow{AB} \cdot \overrightarrow{CD}}^2}{(\overrightarrow{AB} \cdot \overrightarrow{CD})^2} + \frac{\sigma_{|\overrightarrow{AB}| |\overrightarrow{CD}|}^2}{(|\overrightarrow{AB}| |\overrightarrow{CD}|)^2} \right]$$

Consider $f(\mathcal{R}) = \frac{\mathcal{R}^2}{1 - \mathcal{R}^2}$ and note:

$$\lim_{\mathcal{R} \rightarrow 1} f(\mathcal{R}) = \infty$$

Also recall that \mathcal{R} is a measure of the similarity of \overrightarrow{AB} and \overrightarrow{BC} . The beam displacements measured here are far smaller than the distance between measurement planes. Thus, \overrightarrow{AB} and \overrightarrow{BC} are quite similar and $\mathcal{R} \rightarrow 1$. Consequently, the small errors in camera position are mapped to large values of σ_θ^2 . The measured displacement angles are typically $\theta \approx 0.5^\circ$. The asymptotic behavior of $f(\mathcal{R})$ leads to experimental error values of $\sigma_\theta \approx \pm 10^\circ$ and $\sigma_{translation} \approx 5000\mu m$, which are clearly nonsensical. Consequently, the error σ_θ was approximated by the following worst-case analysis.

The angles θ_1 and θ_2 were calculated for values of z_1 and z_2 at all combinations of the extremes of the uncertainties of these values. Table C.3 shows the results:

Table C.3 – The worst-case scenario analysis of angular experimental error.

$z_1 (\mu m)$	$z_2 (\mu m)$	$\theta_1 (^\circ)$	$\theta_1 \text{ \%Error}$	$\theta_2 (^\circ)$	$\theta_2 \text{ \%Error}$
149667	164667	-0.59727	0.02%	0.25428	0.01%
149667	165000	-0.58430	2.16%	0.24876	2.16%
149667	165333	-0.57197	4.22%	0.24350	4.23%
150000	164667	-0.61063	2.25%	0.25998	2.25%
150000	165000	-0.59717	0.00%	0.25425	0.00%
150000	165333	-0.58430	2.16%	0.24876	2.16%
150333	164667	-0.62481	4.63%	0.26602	4.63%
150333	165000	-0.61063	2.25%	0.25998	2.25%
150333	165333	-0.59717	0.00%	0.25425	0.00%

Note that the relative error of the calculation compared to the error free case (shown in bold) has a maximum value of 4.63%. From this calculation, the standard error of the measurement of the angle between vectors was assumed to be $\sigma_{\theta_n} = 5.0\% \cdot \theta_n$. The remainder of the error propagation analysis is performed under this assumption.

Recall:

$$V_{control} = V_1 - \theta_1 \cdot \frac{V_2 - V_1}{\theta_2 - \theta_1}$$

Also:

$$\text{Let } S = \theta_1 \cdot \frac{V_2 - V_1}{\theta_2 - \theta_1}$$

Note that $V_2 - V_1$ and $\theta_2 - \theta_1$ are of the form:

$$f(\Psi, \Gamma) = a\Psi \pm b\Gamma$$

which has a variance:

$$\sigma_f^2 = a^2\sigma_\Psi^2 + b^2\sigma_\Gamma^2$$

Thus:

$$\sigma_{V_2-V_1}^2 = \sigma_{V_1}^2 + \sigma_{V_2}^2 \quad \& \quad \sigma_{\theta_2-\theta_1}^2 = \sigma_{\theta_1}^2 + \sigma_{\theta_2}^2$$

Also note that S is of the form :

$$f = \frac{\Psi}{\Lambda} \Phi$$

which has a variance:

$$\sigma_f^2 = f^2 \left[\left(\frac{\sigma_\Psi}{\Psi} \right)^2 + \left(\frac{\sigma_\Gamma}{\Gamma} \right)^2 + \left(\frac{\sigma_\Phi}{\Phi} \right)^2 \right]$$

Thus:

$$\sigma_S^2 = S^2 \left(\frac{\sigma_{\theta_1}^2}{\theta_1^2} + \frac{\sigma_{V_2-V_1}^2}{(V_2 - V_1)^2} + \frac{\sigma_{\theta_2-\theta_1}^2}{(\theta_2 - \theta_1)^2} \right)$$

Recall:

$$V_{control} = V_1 + S$$

which is of the form:

$$f(\Psi, \Gamma) = a\Psi \pm b\Gamma$$

which has a variance:

$$\sigma_f^2 = a^2 \sigma_\Psi^2 + b^2 \sigma_\Gamma^2$$

Thus:

$$\sigma_{V_{control}}^2 = \sigma_{V_1}^2 + \sigma_S^2$$

Recall:

$$\Delta x_i = x_{V_2} + \frac{V_{control} - V_1}{V_2 - V_1} (x_{V_2} - x_{V_1}) - x_{V_0}$$

And:

$$\Delta y_i = y_{V_2} + \frac{V_{control} - V_1}{V_2 - V_1} (y_{V_1} - y_{V_2}) - y_{V_0}$$

Also:

$$\text{Let } \mathcal{K} = \frac{V_{control} - V_1}{V_2 - V_1} (x_{V_2} - x_{V_1})$$

$$\text{Let } \mathcal{Z} = \frac{V_{control} - V_1}{V_2 - V_1} (y_{V_2} - y_{V_1})$$

Note that $V_{control} - V_1$, $x_{V_2} - x_{V_1}$, and $y_{V_2} - y_{V_1}$ are of the form:

$$f(\Psi, \Gamma) = a\Psi \pm b\Gamma$$

which has a variance:

$$\sigma_f^2 = a^2 \sigma_\Psi^2 + b^2 \sigma_\Gamma^2$$

Thus:

$$\sigma_{V_{control}-V_1}^2 = \sigma_{V_{control}}^2 + \sigma_{V_1}^2$$

$$\sigma_{x_{V_2}-x_{V_1}}^2 = \sigma_{x_{V_2}}^2 + \sigma_{x_{V_1}}^2$$

$$\sigma_{y_{V_2}-y_{V_1}}^2 = \sigma_{y_{V_2}}^2 + \sigma_{y_{V_1}}^2$$

Also note that \mathcal{K} and \mathcal{Z} are of the form :

$$f = \frac{\Psi}{\Lambda} \Phi$$

which has a variance:

$$\sigma_f^2 = f^2 \left[\left(\frac{\sigma_\Psi}{\Psi} \right)^2 + \left(\frac{\sigma_\Gamma}{\Gamma} \right)^2 + \left(\frac{\sigma_\Phi}{\Phi} \right)^2 \right]$$

Thus:

$$\sigma_{\mathcal{K}}^2 = \mathcal{K}^2 \left(\frac{\sigma_{V_{control}-V_1}^2}{(V_{control} - V_1)^2} + \frac{\sigma_{V_2-V_1}^2}{(V_2 - V_1)^2} + \frac{\sigma_{x_{V_2}-x_{V_1}}^2}{(x_{V_2} - x_{V_1})^2} \right)$$

$$\sigma_{\mathcal{Z}}^2 = \mathcal{Z}^2 \left(\frac{\sigma_{V_{control}-V_1}^2}{(V_{control} - V_1)^2} + \frac{\sigma_{V_2-V_1}^2}{(V_2 - V_1)^2} + \frac{\sigma_{y_{V_2}-y_{V_1}}^2}{(y_{V_2} - y_{V_1})^2} \right)$$

Recall:

$$\Delta x_i = x_{V_2} + \mathcal{K} - x_{V_0}$$

$$\Delta y_i = y_{V_2} + \mathcal{Z} - y_{V_0}$$

which are of the form:

$$f(\Psi, \Gamma) = a\Psi \pm b\Gamma \pm c\Phi$$

which has a variance:

$$\sigma_f^2 = a^2 \sigma_\Psi^2 + b^2 \sigma_\Gamma^2 + c^2 \sigma_\Phi^2$$

Therefore:

$$\sigma_{\Delta x_i}^2 = \sigma_{V_1}^2 + \sigma_{\mathcal{K}}^2 + \sigma_{x_0}^2$$

$$\sigma_{\Delta y_i}^2 = \sigma_{V_1}^2 + \sigma_{\mathcal{Z}}^2 + \sigma_{y_0}^2$$

Finally:

$$Translation_{overall} = \sqrt{\Delta x^2 + \Delta y^2}$$

Note that Δx^2 and Δy^2 are of the form:

$$f = a\Psi^{\pm b}$$

which has a variance:

$$\sigma_f^2 = f^2 b^2 \frac{\sigma_\Psi^2}{\Psi^2}$$

Thus:

$$\sigma_{\Delta x^2}^2 = 4\Delta x^2 \sigma_{\Delta x}^2$$

$$\sigma_{\Delta y^2}^2 = 4\Delta y^2 \sigma_{\Delta y}^2$$

Note that $\Delta x^2 + \Delta y^2$ is of the form:

$$f(\Psi, \Gamma) = a\Psi \pm b\Gamma$$

which has a variance:

$$\sigma_f^2 = a^2 \sigma_\Psi^2 + b^2 \sigma_\Gamma^2$$

So:

$$\sigma_{\Delta x^2 + \Delta y^2}^2 = \sigma_{\Delta x^2}^2 + \sigma_{\Delta y^2}^2$$

Note that $\sqrt{\Delta x^2 + \Delta y^2}$ is of the form:

$$f = a\Psi^{\pm b}$$

which has a variance:

$$\sigma_f^2 = f^2 b^2 \frac{\sigma_\Psi^2}{\Psi^2}$$

So:

$$\sigma_{Translation_{overall}}^2 = \frac{\sigma_{\Delta x^2 + \Delta y^2}^2}{4(\Delta x^2 + \Delta y^2)}$$

From which it can be calculated (M8) that for the Center of Amplitude Data:

$$\sigma_{Translation_{overall}} = \sqrt{\sigma_{Translation_{overall}}^2} = \pm 13.87 \mu m$$

And for the Filtered Gaussian Data:

$$\sigma_{Translation_{overall}} = \sqrt{\sigma_{Translation_{overall}}^2} = \pm 13.77 \mu m$$

Thus, for EOBS Channel 1, the experimentally determined value of the overall translation is:

$$Translation_{overall} = 759.30 \pm 13.87 \mu m$$

APPENDIX D – EQUIPMENT AND VENDOR INDEX

1. AdvR Inc., 'EOBS and OPG Chips,'
<http://www.advr-inc.com/>
2. Teem Photonics, 'Nanopulse Series Q-Switch Microchip Laser,'
<http://www.teemphotonics.com/products/microchipfamily.html>
3. Spectra-Physics, 'T-Series Q-Switched DPSS Laser,'
<http://search.newport.com/i/1/q1/Products/q2/Lasers/q3/Q-Switched+DPSS+Lasers/x1/pageType/x2/section/x3/chapter/nav/1/>
4. MATLAB, [Computer math package for numerical computations],
<http://www.mathworks.com/products/matlab/>
5. TurboCAD, [Computer aided drafting software], 'TurboCAD 15 Deluxe,'
<http://www.turbocad.com/>
6. Power Designs, 'TW5005D ± 40 VDC Supply'
7. EMCO High Voltage Corporation, 'C30N HV Amplifier,'
<http://www.emcohighvoltage.com/>
8. Hewlett-Packard, '3325B Function Generator'
9. Trek Inc., '50/750 HV Amplifier,'
http://www.trekinc.com/products/HV_Amp.asp
10. Crystal Technology, Inc., '5%MgO:CLN,'
<http://www.crystaltechnology.com/products/MagnesiumDoped.html>
11. Fluke Electronics, 'Fluke 45 Multi-meter,'
<http://us.fluke.com/fluke/USEN/Bench-Instruments/Bench-Multimeters/Fluke-45.htm?PID=56082>
12. Ophir-Spircon, 'SP620U Beam Profiling Camera and Beam-Gage Software,'
<http://www.ophiropt.com/laser-measurement-instruments/beam-profilers/products/industrial-applications/the-cameras/SP620U>
13. Yamaju Ceramics Co., '5%MgO:CLN,'
<http://www.yamajuceramics.co.jp/english/product/index.html>
14. Yokogawa Electric Corporation, 'AQ6370B Optical Spectrum Analyzer,'
<http://tmi.yokogawa.com/products/optical-measuring-instruments/optical-spectrum-analyzer/aq6370b-optical-spectrum-analyzer/>
15. 5Spice, '5Spice Analysis Software,'
www.5spice.com

APPENDIX E – A CATALOG OF MATLAB CODE

MATLAB Routine M1

Gayer_Sellmeier.m

```
%% Gayer_Sellmeier.m
%% Author: Jonathan W. Evans

%% Initial Setup
close all
clear all
clc

%% Physical Parameters
lambda = linspace(0.5,4,401); % Pump Wavelength
Temp = 20; % Ambient Temperature ©

%% Gayer et al Sellmeier Equation
a1 = 5.756;
a2 = 0.0983;
a3 = 0.2020;
a4 = 189.32;
a5 = 12.52;
a6 = .0132;

b1 = 2.860e-6;
b2 = 4.700e-8;
b3 = 6.113e-6;
b4 = 1.516e-4;

f = (Temp-24.5)*(Temp+570.82);

%Sellmeier Equation
n_e = sqrt(a1 + b1*f + (a2+b2*f)./(lambda.^2-(a3+b3*f)^2) +
(a4+b4*f)./(lambda.^2-a5^2) - a6*lambda.^2);

%% Evaluation and Plotting
figure('Color','White')
plot(lambda,n_e,'LineWidth',2);
xlabel('\lambda (\mu m)');
ylabel('n [Refractive Index]');
axis([0.5 4 2 2.3])
```


MATLAB Routine M2

QPM_TuningCurve.m

%% QPM_TuningCurve.m

%% Author: Jonathan W. Evans

%% Initial Setup

clc

clear all

close all

%% Physical Parameters

lambda1 = 1.064; % Pump Wavelength

Temp = 20; % Ambient Temperature (C)

%% Sellmeier Coefficients

a1 = 5.756;

a2 = 0.0983;

a3 = 0.2020;

a4 = 189.32;

a5 = 12.52;

a6 = .0132;

b1 = 2.860e-6;

b2 = 4.700e-8;

b3 = 6.113e-6;

b4 = 1.516e-4;

f = (Temp-24.5)*(Temp+570.82);

%% Tuning Curve Calculation

n = 1; % Counting Index for the For Loop

for l2 = linspace(1.2,2*lambda1-.001,4001)

LAMBDA = linspace(10,50,401); % QPM Period

lambda2(n) = l2;

lambda3(n) = (1/lambda1-1/lambda2(n))^-1 ;

% Gayer Sellmeier Equation for Each Wavelength

n1 = sqrt(a1 + b1*f + (a2+b2*f)./(lambda1.^2-(a3+b3*f)^2) +
(a4+b4*f)./(lambda1.^2-a5^2) - a6*lambda1.^2);

n2 = sqrt(a1 + b1*f + (a2+b2*f)./(lambda2(n).^2-(a3+b3*f)^2) +
(a4+b4*f)./(lambda2(n).^2-a5^2) - a6*lambda2(n).^2);

n3 = sqrt(a1 + b1*f + (a2+b2*f)./(lambda3(n).^2-(a3+b3*f)^2) +
(a4+b4*f)./(lambda3(n).^2-a5^2) - a6*lambda3(n).^2);

LAMBDA = (-n2./lambda2(n) - n3./lambda3(n) + n1./lambda1).^-1; % OPG
Grating Period

LL(n) = LAMBDA; % The Array Storing Each Period Value

n = n+1;

end

%% Evaluation and Plotting

figure('Color','White')

plot(LL,lambda2,'r','LineWidth',2)

hold on

```
plot(LL,lambda3,'','LineWidth',2)
xlabel('\Lambda [Poling Period] (\mum)')
ylabel('\lambda [Wavelength] (\mum)')
```

MATLAB Routine M3

Optimal_5pMgOCLN_EOBS_Spec.m

%% Optimal_5pMgOCLN_EOBS_Spec.m

%% Author: Jonathan W. Evans

%% Calculate the Optimal Geometry of an EOBS Steering Channel

%% Initial Setup

clc

clear all

close all

%Environmental Parameters =====

lambda = 1.064; % microns

Temp = 20; % Degrees C

%=====

%Independent Geometric Variables =====

%full_beam_width = 100; % Laser Beam Width (microns)

device_length = (6.6)*10000; % Linear Extent of Poled Region

T = 500*1e-6; % Substrate Thickness (meters)

%=====

%Material Parameters =====

a1 = 5.756;

a2 = 0.0983;

a3 = 0.2020;

a4 = 189.32;

a5 = 12.52;

a6 = .0132;

b1 = 2.860e-6;

b2 = 4.700e-8;

b3 = 6.113e-6;

b4 = 1.516e-4;

f = (Temp-24.5)*(Temp+570.82);

%Sellmeier Equation

n_e = sqrt(a1 + b1*f + (a2+b2*f)./(lambda.^2-(a3+b3*f)^2) +
(a4+b4*f)./(lambda.^2-a5^2) - a6*lambda.^2);

n = n_e;

r = 30.8*10^-12; % r @ lambda = 633 microns (M/V)

%=====

%Electric Field & Effects: =====

V = -1000;

d_n = -.5*V*(n^3)*r/T; % change in index of refraction
(unitless)

nm = n-d_n;

np = n+d_n;

%=====

```

%Pre-Calculations =====
MAT_ALPHA = zeros(1,881);
MAT_TRANS = zeros(1,881);
index = 2;
DataTable = zeros(881,71);
PTD_SPEC = zeros(25,11);
Diameters = zeros(1,71);
%=====

for full_beam_width = linspace(50,400,71);
    Diameters(1,index-1) = full_beam_width;

    %Beam Divergence =====
    w0 = full_beam_width/2; % Radius at Beam waist (@
device center)
    zR = (pi/lambda)*w0^2; % Rayleigh Range
    z = (device_length+1000)/2;
    z = z/n; % compensated maximum beam
path length
    M2 = 1.76; % maximum beam divergence
    W = w0*sqrt(1+M2*(z/zR)^2); % Waist Equation
    %=====

    %Calculations =====
    x = 1;
    for alpha = 1:.1:89;
        Trans = 0;
        alpha = alpha*pi/180;

        %\\Geometry =====
        I0 = pi/2 - alpha;
        I1 = asin(nm*sin(I0)/np);
        I2 = pi - I1 - 2*alpha;
        I3 = asin(np*sin(I2)/nm);
        Beta = I3 + alpha - pi/2;

        %\\Cell Dimensions =====
        h = 2*sqrt(2)*W;
        l = 2*h*cot(alpha);

        %\\Cell Count =====
        Max_Cell_Num = floor(device_length/l);
        NUM = (Max_Cell_Num - mod(Max_Cell_Num,2))/2;

        %\\More Geometry =====
        a = .5*h*csc(alpha);
        B = pi - 2*alpha;
        C = pi/2 - I1;
        A = pi - B - C;
        c = a*sin(C)/sin(A);
        e = c*cos(alpha);
        f = c*sin(alpha);
        g = h*cot(alpha) - e;
        j = g*tan(Beta);
    end
end

```

```

%\\Translation and Compenstation Length=====
Y = j + f -.5*h;
CL = (.5*h-(.5*h-Y)*cos(Beta))*cos(Beta);

%\\Overall Translation =====
for N = 0:NUM-1;
    TT = Y*cos(N*Beta) + (1+(.5*h-Y)*sin(Beta))*sin(N*Beta);
    Trans = Trans + TT;
end

for N = 1:NUM;
    TT = -Y*cos(N*Beta) + (1+(.5*h-Y)*sin(Beta))*sin(N*Beta);
    Trans = Trans + TT;
end

%\\Losses =====
r1 = sin(I1-I0)/sin(I1+I0);
r2 = sin(I3-I2)/sin(I3+I2);
R1 = r1^2;
R2 = r2^2;
T1 = 1-R1;
T2 = 1-R2;
Ri = 1-(T1*T2)^2;

%\\Precalc =====
alpha = (alpha*180/pi);
MAT_ALPHA(x) = alpha;
MAT_TRANS(x) = Trans;

%\\Sort and Record =====
if ((Trans > PTD_SPEC(25,3)) & (alpha > 29.9) & (alpha < 30.1))
    PTD_SPEC = circshift(PTD_SPEC,[1 0]);
    PTD_SPEC(1,1) = full_beam_width;
    PTD_SPEC(1,2) = alpha;
    PTD_SPEC(1,3) = Trans;
    PTD_SPEC(1,4) = 2*NUM;
    PTD_SPEC(1,5) = h;
    PTD_SPEC(1,6) = l;
    PTD_SPEC(1,7) = CL;
    PTD_SPEC(1,8) = Beta*180/pi;
    PTD_SPEC(1,9) = n;
    PTD_SPEC(1,10) = d_n;
    PTD_SPEC(1,11) = 100*Ri;
    PTD_SPEC = sortrows(PTD_SPEC,-3);
end
x = x +1;
end
DataTable(:,index) = MAT_TRANS;
index = index + 1;
end

DataTable(:,1) = MAT_ALPHA;

```

```

xlswrite('C:\EVANS\EOBS_Calc.xls',DataTable,'Niobate_PTD','A2');
xlswrite('C:\EVANS\EOBS_Calc.xls',PTD_SPEC,'Optimal_LN','A2');
xlswrite('C:\EVANS\EOBS_Calc.xls',Diameters,'Niobate_PTD','B1');

%% Evaluation and Plotting
disp('DONE!')
idx = find(DataTable(:,1) == 10);
DATA = DataTable(idx:size(DataTable,1),2:size(DataTable,2));
x = 10:.1:89;
y = linspace(50,400,71);
[X,Y] = meshgrid(x,y);
X=X';
Y=Y';
figure('Color','white')
mesh(Y,X,DATA);
ylabel('Prism Base Angle \alpha (\circ)');
xlabel('Nominal Beam Diameter d0 (\mu m)');
zlabel('Overall Translation (\mu m)');
title(['Beam Translation in 5%MgO:CLN']);
view([2 1 .8]);
axis([0 400 0 100 0 1200])

```

MATLAB Routine M4

Build_GaussianBeam.m

%% Build_GaussianBeam.m

%% Author: Jonathan W. Evans

%% Build Gaussian Expression in Amplitude in Phase for FDM Simulation

function

[Amplitude,Phase,X,Y]=Build_GaussianBeam(x_low,x_high,y_low,y_high,zphase,h_cell,beam_diameter,wavelength,path,graphs)

%% Create a Coordinate Space

```
xdim = x_high-x_low;
x = linspace(x_low,x_high,2000);
y = linspace(y_low,y_high,1000);
[X,Y] = meshgrid(x,y);
x=x';
y=y';
z = zphase;
```

%% Geometric Parameters of the Beam

```
x0 = h_cell/2;
y0 = 0;
D_0 = beam_diameter;
w_0 = D_0/2;
r2 = (X-x0).^2 + (Y-y0).^2;
```

%% Physical Parameters of the Radiation

```
E_0 = 1;
lambda = wavelength;
k = 2*pi/lambda;
z_R = (pi*w_0^2)/lambda;
```

%% The Gaussian Beam Equations

```
wz2 = w_0^2*(1+(z/z_R).^2);
wZ = sqrt(wz2); % Beam Radius at z
Rz = z.*(1+(z_R./z).^2); % Radius of Curvature at z
Zetaz = atan(z/z_R); % Guoy Phase at z2
```

%% Assembling the Gaussian Expression

```
E1 = E_0*w_0./wZ;
E2 = exp(-r2./wz2);
E3 = exp(-i*k*z - i*k*r2./(2*Rz) + i*Zetaz);
Erz = E1.*E2.*E3;
Erz = 100*Erz/max(max(real(Erz)));
```

%% Separating Amplitude and Phase

```
Amplitude = abs(Erz);
Phase = atan(imag(Erz)./real(Erz));
```

%% Diagnostic Graphs

```
if (graphs == 1)
    figure('Color','White')
```

```

    mesh(X,Y,sqrt(Amplitude.^2));
    view(2)
    axis([x_low x_high -xdim/2 xdim/2])
end

%% Data Export
dlmwrite([[path],['\X-Grid.txt']],x,' ')
dlmwrite([[path],['\Y-Grid.txt']],y,' ')
dlmwrite([[path],['\X-Field.txt']],zeros(size(X)),' ')
dlmwrite([[path],['\Y-Field.txt']],Amplitude,'delimiter','
','precision','%10.12f')
dlmwrite([[path],['\Phase.txt']],Phase,'delimiter',' ','precision','%10.12f')

```


MATLAB Routine M5

Index.mat

'Channel1_T'	''
'ELECTRO_OPTIC'	'Channel1_20r'
'ELECTRO_OPTIC'	'Channel1_15r'
'ELECTRO_OPTIC'	'Channel1_10r'
'ELECTRO_OPTIC'	'Channel1_5r'
'ELECTRO_OPTIC'	'Channel1_0r'
'TEMPERATURE'	'Channel1_0C'
'TEMPERATURE'	'Channel1_5C'
'TEMPERATURE'	'Channel1_10C'
'TEMPERATURE'	'Channel1_15C'
'TEMPERATURE'	'Channel1_20C'
'TEMPERATURE'	'Channel1_25C'
'TEMPERATURE'	'Channel1_30C'
'TEMPERATURE'	'Channel1_35C'
'TEMPERATURE'	'Channel1_40C'
'TEMPERATURE'	'Channel1_45C'
'TEMPERATURE'	'Channel1_50C'
'WAVELENGTH'	'Channel1_500nm'
'WAVELENGTH'	'Channel1_600nm'
'WAVELENGTH'	'Channel1_700nm'
'WAVELENGTH'	'Channel1_800nm'
'WAVELENGTH'	'Channel1_900nm'
'WAVELENGTH'	'Channel1_1000nm'
'WAVELENGTH'	'Channel1_1100nm'
'WAVELENGTH'	'Channel1_1200nm'
'WAVELENGTH'	'Channel1_1300nm'
'WAVELENGTH'	'Channel1_1400nm'
'WAVELENGTH'	'Channel1_1500nm'
'SELLMEIER'	'Channel1_m9n'
'SELLMEIER'	'Channel1_m6n'
'SELLMEIER'	'Channel1_m3n'
'SELLMEIER'	'Channel1_0n'

'SELLMEIER'	'Channel1_p3n'
'SELLMEIER'	'Channel1_p6n'
'SELLMEIER'	'Channel1_p9n'
'VOLTAGE'	'Channel1_500V'
'VOLTAGE'	'Channel1_400V'
'VOLTAGE'	'Channel1_300V'
'VOLTAGE'	'Channel1_200V'
'VOLTAGE'	'Channel1_100V'
'VOLTAGE'	'Channel1_0V'
'VOLTAGE'	'Channel1_-100V'
'VOLTAGE'	'Channel1_-200V'
'VOLTAGE'	'Channel1_-300V'
'VOLTAGE'	'Channel1_-400V'
'VOLTAGE'	'Channel1_-500V'
'VOLTAGE'	'Channel1_-600V'
'VOLTAGE'	'Channel1_-700V'
'VOLTAGE'	'Channel1_-800V'
'VOLTAGE'	'Channel1_-900V'
'VOLTAGE'	'Channel1_-1000V'
'VOLTAGE'	'Channel1_-1100V'
'VOLTAGE'	'Channel1_-1200V'
'VOLTAGE'	'Channel1_-1300V'
'VOLTAGE'	'Channel1_-1400V'
'VOLTAGE'	'Channel1_-1500V'

Index_Trials.mat

'Channel1_T'
'ELECTRO_OPTIC'
'TEMPERATURE'
'WAVELENGTH'
'SELLMEIER'
'VOLTAGE'

Table E.1 – The content of Index.mat and Index_Trials.mat.

LIGHTS_Analysis.m

```

%% LIGHTS_Analysis.m
%% Author: Jonathan W. Evans

%% Analyze field data returned from LIGHTS FDM BeamProp Simulation

%% Initial Setup
clear all
clc
close all

%% Import Tables listing simulation names

```

```

Index = importdata('C:\Users\Jon\MATLAB\Beam_Prop\Index.mat');
Index_Trials = importdata('C:\Users\Jon\MATLAB\Beam_Prop\Index_Trials.mat');

%% Make Movie Frames
for k = 1:size(Index,1);
    Trial = char(Index(k,1));
    Simulation = char(Index(k,2));

    % Calculate Beam Statistics
    [z_std,z_avg,theta,z,centroid] =
BeamProp_Results_Import(Trial,Simulation,1,1);
    centroid1(k,:) = centroid;

    close all
    clc
end

%% Make Movie Files
for a = 1:size(Index_Trials,1);
    Trial = char(Index_Trials(a,1));
    k1 = find(strcmp((Index(1:size(Index,1),1)),Trial));
    mov2 = avifile(['C:\Users\Jon\MATLAB\Beam_Prop\Results\Channel
1\Tweakage\'],[Trial],['\'],[Trial],['_Sweep.avi']], 'compression', 'None', 'fps
',5);
    mov1 = avifile(['C:\Users\Jon\MATLAB\Beam_Prop\Results\Channel
1\Tweakage\'],[Trial],['\'],[Trial],['_SweepSlow.avi']], 'compression', 'None',
'fps',1);

    i = 1;
    for k = min(k1):max(k1);
        Trial = char(Index(k,1));
        Simulation = char(Index(k,2));
        IMAGE = imread(['C:\Users\Jon\MATLAB\Beam_Prop\Results\Channel
1\Tweakage\'],[Trial],['\'],[Simulation],['\LaserView.png']]);
        F(i) = im2frame(IMAGE);
        i=i+1;
    end

    %Slow Movie
    mov1 = addframe(mov1,F);
    mov1 = close(mov1);

    %Foward and Back Again at Normal Speed
    mov2 = addframe(mov2,F);
    mov2 = addframe(mov2,flip1r(F));
    mov2 = close(mov2);
end

```

BeamProp_Results_Import.m

```

%% BeamProp_Results_Import.m
%% Author: Jonathan W. Evans

%% Plot Field data from LIGHTS within EOBS structure

```

```

function [z_std,z_avg,theta,z,centroid] =
BeamProp_Results_Import(Trial,Simulation,plot,beamonly)

%% Setup
close all

%% Global Variables
global Index
global count

%% Data Paths
path = strcat('C:\Users\Jon\MATLAB\Beam_Prop\Results\Channel
1\Tweakage\',Trial,'\','Simulation','\field\');
path2 = strcat('C:\Users\Jon\MATLAB\Beam_Prop\Results\Channel
1\Tweakage\',Trial,'\','Simulation','\');

%% Import Data
x = importdata([path],['xgrid.txt']);
z = importdata([path],['zgrid.txt']);
Field = importdata([path],['y_field_mag_at_z=0.00000.txt']);

%% Create a Coordinate Space
[X,Z] = meshgrid(x,z);
xt=x';

%% Data Processing
% Large-Windowed Center of Amplitude
q=200;
for a = 1:2000;
    M = max(Field(a,:));
    idx = find(Field(a,')==M);
    if idx <= 200
        idx =201;
    elseif idx>=1800
        idx = 1799;
    end
    %% Center of Amplitude Equation
    centroid(a) = sum(Field(a,(idx-q):(idx+q)).*xt((idx-
q):(idx+q)))/sum(Field(a,(idx-q):(idx+q)));
end

% Small-Windowed Center of Amplitude
q = 95;
for n=1:5;
    for a = 1:2000;
        idx = find(x==round(centroid(a)));
        if idx <= 96
            idx = 96;
        elseif idx>=1904
            idx = 1904;
        end
        centroid(a) = sum(Field(a,(idx-q):(idx+q)).*xt((idx-
q):(idx+q)))/sum(Field(a,(idx-q):(idx+q)));
    end
end

```

```

% Averaging the Center of Amplitude data
for a = 6:1995;
    centroid(a) = mean(centroid(a-5:a+5));
end

maxx = max(max(Field))/exp(1)^2;

%% Plot Prisms Too
if beamonly == 1;
    Build_EOBS(1,maxx,'cyan','black');
    hold on;
end

%% Plotting
mesh(Z,X,Field);
view(2);
colormap('hot');
maximize;

% Add some comment text to the image
path2 = strcat('C:\Users\Jon\MATLAB\Beam_Prop\Results\Channel
1\Tweakage\',Trial,'\Simulation,\'');

index = strfind(Simulation, '_');
if strcmp(Trial, 'WAVELENGTH')
    TEXT = [['\lambda = '],[Simulation(index+1:size(Simulation,2))]]

text(10000,1200,maxx,TEXT,'Color','white','FontWeight','Bold','FontSize',22)
elseif strcmp(Trial, 'TEMPERATURE')
    TEXT = [['T = '],[Simulation(index+1:size(Simulation,2)-1)],['\circ C']]

text(10000,1200,maxx,TEXT,'Color','white','FontWeight','Bold','FontSize',22)
elseif strcmp(Trial, 'ELECTRO_OPTIC')
    index2 = strfind(Simulation, 'r');
    TEXT = [['r'_'_3_3 = '],[num2str(100-str2num(Simulation(index+1:index2-
1)))],['% of r_3_3']]

text(10000,1200,maxx,TEXT,'Color','white','FontWeight','Bold','FontSize',22)
elseif strcmp(Trial, 'VOLTAGE')
    TEXT = [['V = '],[Simulation(index+1:size(Simulation,2)-1)],[' volts']]

text(10000,1200,maxx,TEXT,'Color','white','FontWeight','Bold','FontSize',22)
elseif strcmp(Trial, 'SELLMEIER')
    if strcmp(Simulation(index+1:size(Simulation,2)), 'm3n')
        TEXT = 'n'_'_e = 99.7% of n_e'
    elseif strcmp(Simulation(index+1:size(Simulation,2)), 'm6n')
        TEXT = 'n'_'_e = 99.4% of n_e'
    elseif strcmp(Simulation(index+1:size(Simulation,2)), 'm9n')
        TEXT = 'n'_'_e = 99.1% of n_e'
    elseif strcmp(Simulation(index+1:size(Simulation,2)), 'p3n')
        TEXT = 'n'_'_e = 100.3% of n_e'
    elseif strcmp(Simulation(index+1:size(Simulation,2)), 'p6n')
        TEXT = 'n'_'_e = 100.6% of n_e'
    elseif strcmp(Simulation(index+1:size(Simulation,2)), 'p9n')
        TEXT = 'n'_'_e = 100.9% of n_e'

```

```

elseif strcmp(Simulation(idex+1:size(Simulation,2)), '0n')
    TEXT = 'n' '_e = 100.0% of n_e'
end

text(10000,1200,maxx,TEXT, 'Color', 'white', 'FontWeight', 'Bold', 'FontSize', 22)
end

% OUTPUT Image (Movie Frame)
saveas(gcf, strcat(path2, 'LaserView.png'));
clc

%% Plot the Center of Amplitude Path of the Beam
if plot == 1;
    Plot_CenterofAmplitude(Simulation,Trial)
end

%% Calculate Parameters of Interest
z_std = std(centroid(1500:1700));
z_avg = mean(centroid(1500:1700));

c_min = mean(centroid(1500:1510));
z_min = 1505;

c_max = mean(centroid(1700:1710));
z_max = 1705;

delta_x = (c_max-c_min);
delta_z = (z_max-z_min);
theta = atand(delta_x/delta_z);

%% Record Simulated Beam Statistics
Stats(1,1:8)='z_avg = ';
Stats(2,1:11)='    z_std = ';
Stats(3,1:11)='    theta = ';
Stats(1,9:(9+length(num2str(z_avg)))-1) = num2str(z_avg);
Stats(2,12:(12+length(num2str(z_std)))-1) = num2str(z_std);
Stats(3,12:(12+length(num2str(theta)))-1) = num2str(theta);

dlmwrite(strcat(path2, 'Stats.txt'), Stats, '')

```

Plot_CenterofAmplitude.m

```

%% Plot_CenterofAmplitude.m
%% Author: Jonathan W. Evans

function [] = Plot_CenterofAmplitude(Simulation,Trial)

%% Start
clc
close all
global Index
global count

%% Data Import

```

```

path = strcat('C:\Users\Jon\MATLAB\Beam_Prop\Results\Channel
1\Tweakage\',Trial,'\','Simulation','\field\');
path2 = strcat('C:\Users\Jon\MATLAB\Beam_Prop\Results\Channel
1\Tweakage\',Trial,'\','Simulation','\');

x = importdata([path],['xgrid.txt']);
z = importdata([path],['zgrid.txt']);
Field = importdata([path],['y_field_mag_at_z=0.000000.txt']);

xt=x';

%% Data Processing
% Large-Windowed Center of Amplitude
q=200;
for a = 1:2000;
    M = max(Field(a,:));
    idx = find(Field(a,')==M);
    if idx <= 200
        idx =201;
    elseif idx>=1800
        idx = 1799;
    end
    %% Center of Amplitude Equation
    centroid(a) = sum(Field(a,(idx-q):(idx+q)).*xt((idx-
q):(idx+q)))/sum(Field(a,(idx-q):(idx+q)));
end

% Small-Windowed Center of Amplitude
q = 95;
for n=1:5;
    for a = 1:2000;
        idx = find(x==round(centroid(a)));
        if idx <= 96
            idx = 96;
        elseif idx>=1904
            idx = 1904;
        end
        centroid(a) = sum(Field(a,(idx-q):(idx+q)).*xt((idx-
q):(idx+q)))/sum(Field(a,(idx-q):(idx+q)));
    end
end

% Averaging the Center of Amplitude data
for a = 6:1995;
    centroid(a) = mean(centroid(a-5:a+5));
end

%% Plotting
Build_EOBS(1,0,'Black','White');
hold on
plot(z,centroid,'r','LineWidth',2);
axis([0 1e5 -500 1500])
saveas(gcf,strcat(path2,'PowerCentroid.png'));

```

Build_EOBS.m

```
%% Build_EOBS.m
%% Author: Jonathan W. Evans

%% Plot EOBS Prisms from Geometric Calculations of Traingle Point Locations
function []=Build_EOBS(channel,height,color,figurecolor)

SPEC = xlsread('C:\Users\Jon\DATA\PTD_CALC.xls','CLN Channels','A57:H61');
M = size(SPEC,1);
p = zeros(100,6*M);
Translation = zeros(1,M);

NUM = zeros(1,M);

for z = channel%1:M;

    D_0 = SPEC(z,1);
    alpha = SPEC(z,2);
    Trans = SPEC(z,3);
    NUM(z) = SPEC(z,4)/2;
    h = SPEC(z,5);
    l = SPEC(z,6);
    CL = SPEC(z,7);
    Beta = SPEC(z,8)*pi/180;

    points = zeros(2*NUM(z),6);

% Stage #1
    points(1,1) = 0;
    points(1,2) = h/2;
    points(1,3) = l;
    points(1,4) = h/2;
    points(1,5) = l/2;
    points(1,6) = -h/2;

    for q = 2:NUM(z)
        points(q,1) = points(q-1,3);
        points(q,2) = points(q-1,4) + CL;
        points(q,3) = points(q,1) + l*cos((q-1)*Beta);
        points(q,4) = points(q,2) + l*sin((q-1)*Beta);
        points(q,5) = (points(q,1) + points(q,3))/2 + h*sin((q-1)*Beta);
        points(q,6) = (points(q,2) + points(q,4))/2 - h*cos((q-1)*Beta);
    end

%Stage #2
    points(NUM(z)+1,1) = points(NUM(z),3) + h*sin(NUM(z)*Beta);
    points(NUM(z)+1,2) = points(NUM(z),4) + CL - h*cos(NUM(z)*Beta);
    points(NUM(z)+1,3) = points(NUM(z)+1,1) + l*cos(NUM(z)*Beta);
    points(NUM(z)+1,4) = points(NUM(z)+1,2) + l*sin(NUM(z)*Beta);
    points(NUM(z)+1,5) = points(NUM(z),3) + cos(NUM(z)*Beta)*l/2;
    points(NUM(z)+1,6) = points(NUM(z),4) + CL + sin(NUM(z)*Beta)*l/2;

    v = 1;
    for q = NUM(z)+2:2*NUM(z)
```

```

        points(q,1) = points(q-1,3);
        points(q,2) = points(q-1,4) - CL;
        points(q,3) = points(q,1) + l*cos((NUM(z)-v)*Beta);
        points(q,4) = points(q,2) + l*sin((NUM(z)-v)*Beta);
        points(q,5) = (points(q,1) + points(q,3))/2 - h*sin((NUM(z)-v)*Beta);
        points(q,6) = (points(q,2) + points(q,4))/2 + h*cos((NUM(z)-v)*Beta);
        v = v+1;
    end

% Organize
slab = char('s 0.000614602632 0.000614602632 250 -250 ');
channel = slab;

for q = 1:2*NUM(z)
    p(q,(z-1)*6+1) = points(q,1);
    p(q,(z-1)*6+2) = points(q,2);
    p(q,(z-1)*6+3) = points(q,3);
    p(q,(z-1)*6+4) = points(q,4);
    p(q,(z-1)*6+5) = points(q,5);
    p(q,(z-1)*6+6) = points(q,6);

    a = 0;
    b = length(num2str(char('s 0.000614602632 0.000614602632 250 -250
'))));
    slab(1,(a+1):(a+b+1)) = char('s 0.000614602632 0.000614602632 250 -
250 ');
    %a = b;
    for w = [2 1 4 3 6 5];
        a = length(slab(1,:));
        b = length(num2str(points(q,w)));
        slab(1,(a+1):(a+b)) = num2str(points(q,w));
        slab(1,a+b+1) = char(' ');
    end
    a = 0;
    b = length(num2str(slab));
    channel(q,(a+1):(a+b)) = slab;
    slab = char('s 0.000614602632 0.000614602632 250 -250 ');
end

Y = .5*h + (CL/cos(Beta)-.5*h)/cos(Beta);
Translation(z) = (points(2*NUM(z),4) + cos(Beta)*h/2 - cos(Beta)*Y) -
(points(1,2) - h/2);
dlmwrite(['C:\Users\Jon\MATLAB\Beam_Prop\Input\Channel
'],[num2str(z)],['\Channel '],[num2str(z)],['.txt']],channel,'')
end

%% Plotting
figure('Color',figurecolor)
xlabel('z (mm)')
ylabel('x (\mum)')
hold on
for z = 1:size(SPEC,1);
    for q = 1:NUM(z)
        fill3(p(q,((z-1)*6+1):2:((z-1)*6+5)),p(q,((z-1)*6+2):2:((z-
1)*6+6)),linspace(height,height,3),color,'EdgeColor',color)
    end
end

```



```

    for q = (NUM(z)+1):2*NUM(z);
        fill3(p(q,((z-1)*6+1):2:((z-1)*6+5)),p(q,((z-1)*6+2):2:((z-
1)*6+6)),linspace(height,height,3),color,'EdgeColor',color)
    end
    axis([0 10e4 -500 1500])
end

```

MATLAB Routine M6

Two_Point_Trajectory.m

```
%% Two_Point_Trajectory.m
%% Author: Jonathan W. Evans

%% Plot beam trajectories from two-point vector definitions

%% Initial Setup
clear all
close all
clc

%% Various Experiments to Process
TOC(1,:) = mat2cell('S:\DATA\Spiricon\Gen1Chip.xlsx');
TOC(2,:) = mat2cell('S:\DATA\Spiricon\7 June 2010\Annealed Chip\Positive
Voltages\Centroid_Data.m');
TOC(3,:) = mat2cell('S:\DATA\Spiricon\7 June 2010\NonAnnealed Chip\Positive
Voltages\TRIAL 1\Centroid_Data.m');
TOC(4,:) = mat2cell('S:\DATA\Spiricon\7 June 2010\NonAnnealed Chip\Positive
Voltages\TRIAL 2\Centroid_Data.m');
TOC(5,:) = mat2cell('S:\DATA\Spiricon\8 June 2010\Annealed Chip\Negative
Voltages\Centroid Location.txt');
TOC(6,:) = mat2cell('S:\DATA\Spiricon\8 June 2010\Annealed Chip\Negative
Voltages\Filtered Peak Location.txt');

%% Create z Axis Coordinates
z = linspace(0,20,501);

%% Process the trajectory for each data set
for q = 1:length(TOC)

    if q == 1;
        z1 = 19*1e-2;
        z2 = 20*1e-2;
    else
        z1 = 15*1e-2;
        z2 = 16.5*1e-2;
    end

    if strfind(mat2str(cell2mat(TOC(q,:))),'.xlsx')
        data = xlsread(mat2str(cell2mat(TOC(q,:))), 'B2:C14');
    else
        data = importdata(mat2str(cell2mat(TOC(q,:))));
    end

    % Vector Algebra
    figure
    hold on
    f = 1;
    for i=1:2:length(data)

        x1(f) = data(i,1)*1e-6;
        x2(f) = data(i+1,1)*1e-6;
        y1(f) = data(i,2)*1e-6;
```

```

y2(f) = data(i+1,2)*1e-6;

y(f,:) = (z-z1).*(y2(f)-y1(f))./(z2-z1) + y1(f);
x(f,:) = (z-z1).*(x2(f)-x1(f))./(z2-z1) + x1(f);

A = [x1(1) y1(1) z1];
B = [x2(1) y2(1) z2];
C = [x1(f) y1(f) z1];
D = [x2(f) y2(f) z2];

AB = B-A;
CD = D-C;
mag_AB = sqrt(AB(1)^2 + AB(2)^2 + AB(3)^2);
mag_CD = sqrt(CD(1)^2 + CD(2)^2 + CD(3)^2);

theta(q,f) = acosd(dot(AB,CD)/(mag_AB*mag_CD));

f = f+1;
end

% Plotting Logic
if (q < 5)
    plot3(z,-y(1,:),x(1,:),z,-y(2,:),x(2,:),z,-y(3,:),x(3,:),z,-
y(4,:),x(4,:),z,-y(5,:),x(5,:),z,-y(6,:),x(6,:))
    plot3(z1,-y1(1),x1(1),'o',z1,-y1(2),x1(2),'o',z1,-
y1(3),x1(3),'o',z1,-y1(4),x1(4),'o',z1,-y1(5),x1(5),'o',z1,-y1(6),x1(6),'o')
    plot3(z2,-y2(1),x2(1),'o',z2,-y2(2),x2(2),'o',z2,-
y2(3),x2(3),'o',z2,-y2(4),x2(4),'o',z2,-y2(5),x2(5),'o',z2,-y2(6),x2(6),'o')
    legend('V_appl_i_e_d = 0 V','V_appl_i_e_d = 100
V','V_appl_i_e_d = 200 V','V_appl_i_e_d = 300 V',...
'V_appl_i_e_d = 400 V','V_appl_i_e_d = 500 V');
else
    plot3(z,-y(1,:),x(1,:),z,-y(2,:),x(2,:),z,-y(3,:),x(3,:),z,-
y(4,:),x(4,:),z,-y(5,:),x(5,:),z,-y(6,:),x(6,:))
    plot3(z,-y(7,:),x(7,:),z,-y(8,:),x(8,:),z,-y(9,:),x(9,:),z,-
y(10,:),x(10,:),z,-y(11,:),x(11,:))
    plot3(z1,-y1(1),x1(1),'o',z1,-y1(2),x1(2),'o',z1,-
y1(3),x1(3),'o',z1,-y1(4),x1(4),'o',z1,-y1(5),x1(5),'o',z1,-y1(6),x1(6),'o')
    plot3(z2,-y2(1),x2(1),'o',z2,-y2(2),x2(2),'o',z2,-
y2(3),x2(3),'o',z2,-y2(4),x2(4),'o',z2,-y2(5),x2(5),'o',z2,-y2(6),x2(6),'o')

    plot3(z1,-y1(7),x1(7),'o',z1,-y1(8),x1(8),'o',z1,-
y1(9),x1(9),'o',z1,-y1(10),x1(10),'o',z1,-y1(11),x1(11),'o')
    plot3(z2,-y2(7),x2(7),'o',z2,-y2(8),x2(8),'o',z2,-
y2(9),x2(9),'o',z2,-y2(10),x2(10),'o',z2,-y2(11),x2(11),'o')
    legend('V_appl_i_e_d = 0 V','V_appl_i_e_d = 100
V','V_appl_i_e_d = 200 V','V_appl_i_e_d = 300 V',...
'V_appl_i_e_d = 400 V','V_appl_i_e_d = 500
V','V_appl_i_e_d = 600 V','V_appl_i_e_d = 700 V',...
'V_appl_i_e_d = 800 V','V_appl_i_e_d = 900
V','V_appl_i_e_d = 1000 V');
end

view(0,180);
xlabel('z (cm)')

```

```

        ylabel('-y (\mum)')
        xlabel('x (\mum)')
        axis([10e-2 20e-2 -4.4*76881e-6 0 0 4.4*1024*1e-6])
    end

%% OUTPUT
clc
theta = -(theta')
xlswrite('S:\DATA\Spiricon\Beam Steering
Predictions2.xlsx',theta,'Sheet1','E2:I7')

```

MATLAB Routine M7

Points.mat

'0V_15CM'
'0V_165CM'
'100V_15CM'
'100V_165CM'
'200V_15CM'
'200V_165CM'
'300V_15CM'
'300V_165CM'
'400V_15CM'
'400V_165CM'
'500V_15CM'
'500V_165CM'
'600V_15CM'
'600V_165CM'
'700V_15CM'
'700V_165CM'
'800V_15CM'
'800V_165CM'
'900V_15CM'
'900V_165CM'
'1000V_15CM'
'1000V_165CM'

Table E.2 – The content of Points.mat.

HDF5_Spiricon_FrameStats.m

```
%% HDF5_Spiricon_FrameStats.m
%% Author: Jonathan W. Evans

%% Import and average beam data over 40 seperate frames

%% Initial Setup
clear all
close all
clc

%% Get Screen Size
scrsz = get(0, 'ScreenSize');

%% Import Dataset Names
list = importdata('C:\Users\Jon\MATLAB\Beam_Prop\Points.mat')

folder = '\\Nas\Public\SWAP\Evans Swap\DATA\Spiricon\8 June 2010\Annealed
Chip\Negative Voltages\';
```

```

%% Camera Info
xdim = 1024;
ydim = 768;
pixelsize = 4.4;

q = 1:length(list);

%% Import a Frame
for h = 1:40
    path = strcat(folder,cell2mat(list(q)),'\');
    DATA =
hdf5read(strcat(path,cell2mat(list(q)),'.binary.bgData'),strcat('/BG_DATA/',m
at2str(h),'/DATA'))/40;
    data = double(DATA);

    for k = 0:ydim-1
        start = k*xdim+1;
        finish = (k+1)*xdim;
        BEAM_DATA(k+1,:) = data(start:finish);
    end

    BEAM_DATA = flipud(BEAM_DATA);

    x = linspace(0,pixelsize*(xdim-1),xdim);
    y = linspace(0,pixelsize*(ydim-1),ydim);
    [X,Y] = meshgrid(x,y);

    % Find Data Peak
    [i,j] = find(BEAM_DATA==max(max(BEAM_DATA)));
    peak(h,1) = mean(j)*pixelsize;
    peak(h,2) = mean(i)*pixelsize;

    % Find Data Centroid within a window centered at the peak
    u = (i-100:1:i+100);
    v = (j-100:1:j+100);

    [U,V] = meshgrid(v*pixelsize,u*pixelsize);

    num_x = sum(sum(U.*BEAM_DATA(u,v)));
    num_y = sum(sum(V.*BEAM_DATA(u,v)));
    den = sum(sum(BEAM_DATA(u,v)));

    centroid(h,1) = num_x/den;
    centroid(h,2) = num_y/den;

    % Perform Gaussian Filtering
    F = GaussFilter(100,.3);
    D = filter2(F,BEAM_DATA);
    D = D/max(max(D));

    [i,j] = find(D==max(max(D)));
    fpeak(h,1) = j*pixelsize;
    fpeak(h,2) = i*pixelsize;

```

```

        disp(strcat('Frame #',mat2str(h),' finished!'))
    end

    clc
    disp('Writing Files...')

    %% Average the Beam Locations
    x_f_avg = mean(fpeak(:,1));
    y_f_avg = mean(fpeak(:,2));
    x_c_avg = mean(centroid(:,1));
    y_c_avg = mean(centroid(:,2));

    x_f_std = std(fpeak(:,1));
    y_f_std = std(fpeak(:,2));
    x_c_std = std(centroid(:,1));
    y_c_std = std(centroid(:,2));

    %% OUTPUT
    Center_Stats = [x_c_avg,x_c_std,y_c_avg,y_c_std];
    Filter_Stats = [x_f_avg,x_f_std,y_f_avg,y_f_std];
    dlmwrite(strcat(path,'Center Stats.txt'),Center_Stats,' ')
    dlmwrite(strcat(path,'Filter Stats.txt'),Filter_Stats,' ')

    disp('DONE!')

```

MATLAB Routine M8

Propagation_of_Errors.m

```
%% Propagation_of_Error.m
%% Author: Jonathan W. Evans

%% Examine the propagation of experimental error through the process of
%% interpolating the overall translation measurement

%% Initial Setup
clear all
clc

%% Data Import
% Center of Amplitude Data
error_table = xlsread('S:\Uncertainty.xls','Sheet1','A1:I8')
% Gaussian Filter Data
error_table = xlsread('S:\Uncertainty.xls','Sheet1','A13:I18')

%% Physically
theta2 = .25477;
theta1 = -.59857;
V0 = 0;
V1 = -900;
V2 = -1000;
sv_0 = 1;
sv_2 = 1;
sv_1 = 1;

%% Point A
A = [error_table(1,5) error_table(1,7) error_table(1,3)];
sx_A = error_table(1,6)^2;
sy_A = error_table(1,8)^2;
sz_A = error_table(1,4)^2;

%% Point B
B = [error_table(2,5) error_table(2,7) error_table(2,3)];
sx_B = error_table(2,6)^2;
sy_B = error_table(2,8)^2;
sz_B = error_table(2,4)^2;

%% Point C
C = [error_table(3,5) error_table(3,7) error_table(3,3)];
sx_C = error_table(3,6)^2;
sy_C = error_table(3,8)^2;
sz_C = error_table(3,4)^2;

%% Point D
D = [error_table(4,5) error_table(4,7) error_table(4,3)];
sx_D = error_table(4,6)^2;
sy_D = error_table(4,8)^2;
sz_D = error_table(4,4)^2;

%% Point E
```



```

E = [error_table(5,5) error_table(5,7) error_table(5,3)];
sx_E = error_table(5,6)^2;
sy_E = error_table(5,8)^2;
sz_E = error_table(5,4)^2;

%% Point F
F = [error_table(6,5) error_table(6,7) error_table(6,3)];
sx_F = error_table(6,6)^2;
sy_F = error_table(6,8)^2;
sz_F = error_table(6,4)^2;

%% Vector Algebra
AB = B-A;
sx_AB = sx_A + sx_B;
sy_AB = sy_A + sy_B;
sz_AB = sz_A + sz_B;

CD = D-C;
sx_CD = sx_C + sx_D;
sy_CD = sy_C + sy_D;
sz_CD = sz_C + sz_D;

EF = F-E;
sx_EF = sx_E + sx_F;
sy_EF = sy_E + sy_F;
sz_EF = sz_E + sz_F;

%% VECtor Uncertainties
ABdotCD = dot(AB,CD);
ABdotEF = dot(AB,EF);

sx_ABCD = (AB(1)*CD(1))^2*(sx_AB/(AB(1)^2)+sx_CD/(CD(1)^2));
sy_ABCD = (AB(2)*CD(2))^2*(sx_AB/(AB(2)^2)+sx_CD/(CD(2)^2));
sz_ABCD = (AB(3)*CD(3))^2*(sx_AB/(AB(3)^2)+sx_CD/(CD(3)^2));

sx_ABEF = (AB(1)*EF(1))^2*(sx_AB/(AB(1)^2)+sx_EF/(EF(1)^2));
sy_ABEF = (AB(2)*EF(2))^2*(sx_AB/(AB(2)^2)+sx_EF/(EF(2)^2));
sz_ABEF = (AB(3)*EF(3))^2*(sx_AB/(AB(3)^2)+sx_EF/(EF(3)^2));

s_ABdotEF = sx_ABEF + sy_ABEF + sz_ABEF;
s_ABdotCD = sx_ABCD + sy_ABCD + sz_ABCD;

%% More Vector Uncertainties
Delta_AB = AB(1)^2 + AB(2)^2 + AB(3)^2;
Delta_CD = CD(1)^2 + CD(2)^2 + CD(3)^2;
Delta_EF = EF(1)^2 + EF(2)^2 + EF(3)^2;

mag_AB = sqrt(Delta_AB);
mag_CD = sqrt(Delta_CD);
mag_EF = sqrt(Delta_EF);

mag_ABCD = mag_AB*mag_CD;
mag_ABEF = mag_AB*mag_EF;

```

```

sx2_AB = 4*AB(1)^2*sx_AB;
sy2_AB = 4*AB(2)^2*sy_AB;
sz2_AB = 4*AB(3)^2*sz_AB;

sx2_CD = 4*CD(1)^2*sx_CD;
sy2_CD = 4*CD(2)^2*sy_CD;
sz2_CD = 4*CD(3)^2*sz_CD;

sx2_EF = 4*EF(1)^2*sx_EF;
sy2_EF = 4*EF(2)^2*sy_EF;
sz2_EF = 4*EF(3)^2*sz_EF;

sx_DeltaAB = sx2_AB + sy2_AB + sz2_AB;
sx_DeltaCD = sx2_CD + sy2_CD + sz2_CD;
sx_DeltaEF = sx2_EF + sy2_EF + sz2_EF;

s_magAB = .25*sx_DeltaAB/Delta_AB;
s_magCD = .25*sx_DeltaCD/Delta_CD;
s_magEF = .25*sx_DeltaEF/Delta_EF;

s_magABCD = mag_ABCD^2*(s_magAB/mag_AB^2 + s_magCD/mag_CD^2);
s_magABEF = mag_ABEF^2*(s_magAB/mag_AB^2 + s_magEF/mag_EF^2);

R_ABCD = ABdotCD/mag_ABCD;
R_ABEF = ABdotEF/mag_ABEF;

theta1 = -acosd(R_ABCD)
theta2 = acosd(R_ABEF)

sR_ABCD = (R_ABCD)^2*(s_ABdotCD/ABdotCD^2 + s_magABCD/mag_ABCD^2); %< in this
expression the second quantity is too large
sR_ABEF = (R_ABEF)^2*(s_ABdotEF/ABdotEF^2 + s_magABEF/mag_ABEF^2);

%% Interpolation Uncertainties
s_theta1 = (.05*theta1)^2;
s_theta2 = (.05*theta2)^2;
s_theta21 = s_theta1 + s_theta2;
s_theta21^.5
sV_21 = sv_2 + sv_1;

S = theta1*(V2-V1)/(theta2-theta1);
s_S = S^2*(s_theta1/theta1^2 + sV_21/(V2-V1)^2 + s_theta21/(theta2-
theta1)^2);

V_control = V1 - S;
sV_control = sv_1 + s_S;

K = (V_control-V1)*(E(1)-C(1))/(V2-V1);
Z = (V_control-V1)*(E(2)-C(2))/(V2-V1);

%% More Interpolation Uncertainties
delta_xi = C(1) + K - A(1);
delta_yi = C(2) + Z - A(2);

```

```

sV_C1 = sV_control + sv_1;
sx_21 = sx_E + sx_C;
sy_21 = sy_E + sy_C;

sK = K^2*(sV_C1/(V_control-V1)^2 + sV_21/(V2-V1)^2 + sx_21/(E(1)-C(1))^2);
sZ = Z^2*(sV_C1/(V_control-V1)^2 + sV_21/(V2-V1)^2 + sy_21/(E(2)-C(2))^2);

s_delta_xi = sv_1 + sK + sx_A;
s_delta_yi = sv_1 + sZ + sy_A;

%% Overall Translation Measurement Error
Trans = sqrt(delta_xi^2 + delta_yi^2)
s_dx2 = 4*delta_xi^2*s_delta_xi;
s_dy2 = 4*delta_yi^2*s_delta_yi;
s_dx2dy2 = s_dx2 + s_dy2;

s_Trans = .25*s_dx2dy2/(Trans^2);
error = sqrt(s_Trans)

```